Mechanical Behaviour of Irradiated Tungsten for Fusion Power

James S. K.-L. Gibson

Hilary Term 2015

Supervisors: Dr. David E.J. Armstrong & Prof. Steve G. Roberts

Preface

This thesis describes works carried out by the author in the Department of Materials, University of Oxford from October 2011 to April 2015 under the supervision of Dr. David E.J. Armstrong and Prof. Steve G. Roberts.

No part of this thesis has been previously submitted for a degree at this or any other university. The work of other authors has been drawn upon and has been referenced and acknowledged in the text. A list of references is given at the end of the thesis.

Some work from this thesis has been reported at the following conferences and in the following publications:

Conferences

- Gordon Research Seminar, Boston, USA - High Temperature Nanoindentation of Ion-Irradiated Tungsten, July 2014. *Invited speaker.*
- MRS Spring 2014, San Francisco, USA - High Temperature Nanoindentation of Ion-Irradiated Tungsten, April 2014.
- UNTF 2014, Oxford, UK - High Temperature Nanoindentation of Helium-Implanted Tungsten, April 2014.
- Tungsten Workshop, Oxford, UK - Micro-Mechanical Tests in Tungsten, September 2013.
- PFMC 2013, Julich, Germany - Effects of Helium Ion Implantation on the Mechanical Properties of Tungsten, May 2013.
- TMS 2013, San Antonio, USA - The Change in the Mechanical Properties of Ion-Irradiated Tungsten, March 2013.

Publications

- D.E.J. Armstrong, et al. 'Small-scale characterisation of irradiated nuclear materials: Part II nanoindentation and micro-cantilever testing of ion irradiated nuclear materials', Journal

of Nuclear Materials 2015

- J. Gibson, et al. 'High Temperature Nanoindentation of Helium-Implanted Tungsten', Materials Science and Engineering:A 625 2014
- J. Gibson, et al. 'The Micro-Mechanical Properties of Ion-Irradiated Tungsten', Physica Scripta T159 2014
- M. Rieth, et al. 'A Brief Summary of the Progress on the EFDA Tungsten Materials Program', Journal of Nuclear Materials 442(1-3) 2013
- M. Rieth, et al. 'Recent Progress in Research on Tungsten Materials for Nuclear Fusion Applications in Europe', Journal of Nuclear Materials 432(1-3) 2013

Abstract

Tungsten will be a key material for the plasma-facing components in future fusion devices. Its mechanical performance under neutron irradiation will strongly influence the lifetime of these devices. Pure tungsten has been subjected to a variety of irradiating species - tungsten ions, helium ions and fission neutrons - between 500°C and 900°C and the change in mechanical properties measured by micro-mechanical testing methods.

Pure tungsten has been ion-irradiated using self-ions and helium ions at 500°C and 800°C. Nanoindentation has been performed on all specimens, and the 800°C specimens have been tested at temperatures up to 750°C using high-temperature nanoindentation. The irradiation temperature has no effect on the hardening of tungsten. Hardening from self-ion irradiation has not saturated by 4.5 dpa with an increase in hardness of 3.3 GPa. The hardening from helium implantation is only 0.73 GPa, and a comparison with literature shows that this hardening only depends on the concentration of the injected helium. The difference is likely due to the much smaller defect size of helium-vacancy clusters when compared to dislocation loops. High-temperature nanoindentation shows that helium-implanted tungsten softens rapidly, with the hardening from the radiation damage becoming negligible above 450°C. Self-ion implanted tungsten does not soften by 650°C, again likely due to the size difference of the defects.

Micro-mechanical tests - namely micro-cantilever bending - have been used to investigate the plastic and fracture characteristics of tungsten before and after irradiation. Plastic behaviour is dominated by size effects due to the 3 μm depth of the implanted layers, which makes nanoindentation a better method for investigating radiation damaged layers. In fracture testing, fracture is rarely seen. Using the yield stress to calculate fracture toughness, the hardening from irradiation damage results in an increase in fracture toughness from 2.2 MPa$\sqrt{m}$ to 6.0 MPa$\sqrt{m}$. The work of deformation at 1% is also increased after irradiation from 7.2×10^{-11} Nm to 2.8×10^{-10} Nm, implying that the implanted damage is not leading to an increase in embrittlement by reducing K_{1c}.

Neutron irradiated tungsten also shows an increase in fracture toughness after irradiation from 6.5 MPa$\sqrt{m}$ to 14.5 MPa$\sqrt{m}$. However, the BDTT increases by ∼100°C in poly-crystal tungsten and ∼500°C in single-crystal tungsten. The difference in BDTT does not exist in the unimplanted

material. The change after irradiation is likely due to the fine ($\sim$3 μm) grain size and 900°C irradiation temperature causing a significant amount of the displacement damage to be absorbed at the grain boundaries. The hardness of neutron irradiated and ion irradiated tungsten is very close: 10.4 GPa and 11.2 GPa respectively, demonstrating the ions are likely well-representing the neutron damage in pure tungsten.

Acknowledgements

I would like to thank my supervisors, Dave Armstrong and Steve Roberts for their support and guidance over the course of the project. Their input and discussions have made the project run surprisingly smoothly.

I have made good use of collaborations with KIT, and I am grateful for the help from (in no particular order): Hans-Christian Schneider, Jonas Groten, Thomas Kreuter, Ruth Schwaiger, Jan Hoffmann, and Steffen Antusch.

Similarly, my thanks to other members of the department and elsewhere for the huge amount of support and training on all the instruments: Ian Lloyd, Laurie Walton, Yina Huang, Gareth Hughes, Steve Lett, Gabriella Chapman, Neil Young, Greg Cook, Graham Wyatt, Chris Hardie, Alex Cackett, and Adrian Harris.

My thanks to Nianhua Peng, Yves Serruys, Johannes von Borany, and Wolfgang Jacob for the use of the ion-implantation facilities without which I would have no materials to test.

Finally, my thanks to my families old and new: Angela, Greg and Charles Gibson as well as Ruth, Andrew, David and Alice MacArthur. A special thank you to Kate for putting up with me and my disappearance all times of the day or night when a microscope was calling.

Glossary of Abbreviations

ASTM	American Society for Testing and Materials
BCC	Body Centred Cubic
BDTT	Brittle-to-Ductile Transition Temperature
CBN	Cubic Boron Nitride
CFC	Carbon Fibre Composite(s)
CSM	Continuous Stiffness Measurement
CVD	Chemical Vapour Deposition
DD	Dislocation Dynamics
DEMO	DEMOnstration Reactor
DFT	Density Functional Theory
DPA	Displacements per Atom
EBSD	Electron Backscatter Diffraction
EDM	Electric Discharge Machining
FE(M)	Finite Element (Modelling)
FIB	Focussed Ion Beam
FPY	Full Power Year
GND	Geometrically Necessary Dislocations
HFIR	High-Flux Isotope Reactor
HFR	High-Flux Reactor
HZDR	Helmholtz-Zentrum Dresden-Rossendorf
ITER	International Thermonuclear Experimental Reactor
JANNuS	Joint Accelerators for Nanoscience and Nuclear Studies
JET	Joint European Torus
MATLAB	MATrix LABoratory
MD	Molecular Dynamics
ODS	Oxide Dispersion Strengthened
PFC	Plasma Facing Component(s)
PID	Proportional Integral Derivative
PKA	Primary Knock-On Atom
RAF	Reduced Activation Ferritic
SEM	Scanning Electron Microscopy
SRIM	Stopping Range of Ions in Matter
TDS	Thermal Desorption Spectroscopy
TEM	Transition Electron Microscopy
UFG	Ultra-Fine Grained
UHP	Ultra High Purity

Contents

Chapter 1

Introduction

Over the last forty years world energy usage has increased by over 250%[1] and will continue to increase, largely driven by the industrialisation of second and third-world countries. Most of the increased energy demand will be met by an increase in fossil fuel consumption, with China alone having expanded at a rate of three coal-fired power stations per week in 2010.[2] Although much progress has been made in 'clean-coal' and carbon-capture technologies, these fossil power stations draw on increasingly dwindling resources and lead to increased carbon dioxide emissions and climate change. In many countries, there also exists a strong socio-economic pressure to move towards low-carbon, low-pollution methods of energy production whilst retaining a reasonable cost per kilowatt-hour.

Nuclear fission has expanded considerably since 1960 and now produces nearly 3 TW of power globally per year, around 14% of the total output.[3] However, this method produces long-lived radioactive waste and there are also constant fears over the safety of such reactors, notably highlighted by the Fukushima disaster in 2011.[4]

Renewable energy production is likely to form a large part of future energy portfolios. Renewables produce low-carbon energy, however due to their relatively low power output per device (e.g. < 3 MW per wind turbine[5]) they take up lots of space. Additionally, the energy that they produce can be more than four times more expensive than traditional fossil-fuel based technologies[6] and are arguably only currently economically viable due to significant government subsidies.[7] Due to the intermittent nature of energy generation their cost is further increased by the additional industrialisation required to produce electricity to fulfil either base-load or sudden demand. Storage of the generated energy is often obtained using methods such as batteries, flywheels or pumped water storage.[8]

In contrast, a nuclear fusion reactor would be a low-carbon, low-pollution, highly efficient and intrinsically safe method of producing large amounts of continuous energy. However, these reactors still require considerable research and development in several areas - including plasma physics

and high-temperature, radiation-resistant materials - before they can generate electrical energy for consumer use.

This thesis will investigate the mechanical properties of tungsten after irradiation to help evaluate the lifetime of tungsten components in commercial fusion reactors. Tungsten is arguably the key material for successful high-temperature operation of a commercial reactor, particularly for components such as the divertor.

Chapter 2

Literature Review

2.1 The Materials Requirements for Nuclear Fusion

For a commercial nuclear fusion reactor to operate, it must output more power than it requires in input. Whilst JET has shown that a deuterium-tritium fusion reaction is possible,[9] a self-sustaining, power generating reaction is not possible on these small scales. The critical parameter for power generation is the triple product, given by the product of temperature, reactant density and confinement time.[10] Of these, only the confinement time is readily adjustable by increasing the volume of the plasma. As such, to test the viability of commercial fusion power, larger reactors are required. These requirements are to be met by ITER, in 2019, followed by DEMO post-2030.[11] Tungsten is to be used as a material for the divertor in these reactors[12] and is a significant candidate for the plasma-facing tiles in the tokamak walls in DEMO and beyond.[13] The divertor, shown in figure 2.1, is responsible for extracting heat from the fusion reaction to generate electricity as well as the removal of helium ash and impurities from the plasma.[12]

Figure 2.1: Proposed tungsten divertor design for ITER.[12]

In order to produce a commercial power plant, significant progress is required in materials research. The plasma-facing components see operating temperatures up to 800°C for most first-

wall components, with neutron damage resulting in up to 120 displacements per atom (dpa) over an estimated five-year operational lifetime.[14] Helium levels are expected to reach 1200 appm in first-wall steels,[14] although levels will vary slightly with changes in alloy composition.

In the divertor, the design parameters require materials to withstand steady state heat fluxes of 5 MW/m^2, with transient events from edge localised modes resulting in heat fluxes over twice this.[15,16] Additionally, neutron collisions will impart 10 MW/m^2 of heat.[17] Furthermore, there is a desire to limit the amount of radioactive waste produced by fusion power and therefore only low-activation elements are suitable.[18,19] This limits engineering materials to the following seven elements: C, Si, Fe, V, Cr, W and Ta.

These candidate materials have an operating temperature window in which they provide the required mechanical properties for their application. The lower temperature limits are strongly influenced by radiation hardening and the intrinsic brittle-to-ductile transition temperature (BDTT) for body-centred cubic (BCC) metals. The upper temperature limits are controlled by creep, void swelling and corrosion issues.

Only two candidate materials are suitable for the high-temperature conditions of the divertor: SiC-CFC (carbon-fibre composites) or tungsten. SiC materials have a range of ∼650-950°C, while tungsten has a window of ∼1000-1200°C.[20]

CFC materials are easily shaped, have excellent thermal conductivity (200-500 W/mK), result in little plasma contamination (12% allowable plasma concentration) and have a reasonable fracture toughness.[21] However, CFC materials are very sensitive to radiation damage and plasma exposure. At 800°C, the thermal conductivity of CFC components is reduced to 33% of the unirradiated value at only 1 dpa.[22] Carbon-based materials also have high levels of tritium retention, shown in figure 2.2. After 1000 plasma discharges, 70g of tritium was retained in CFC materials. Beryllium and tungsten materials retained 2g.[23] Tritium is a fuel for a fusion reactor, and due to its radioactivity only very limited amounts are permitted on a site at any time. This means that inventories must be kept as low as possible.

The biggest drawback for carbon-based plasma-facing components (PFCs) is the erosion rates due to the plasma, also shown in figure 2.2. This is extremely fast, with rates of a few microns per pulse reported.[24] This causes problems due to re-deposition of (potentially tritium-contaminated) carbon over the other components inside the vacuum vessel. Most importantly, this means that the

carbon-based armour requires regular repair or replacement. This results in significant downtime for the reactor, severely limiting its commercial application. These drawbacks mean that carbon components are unlikely to be used long-term in fusion reactors.

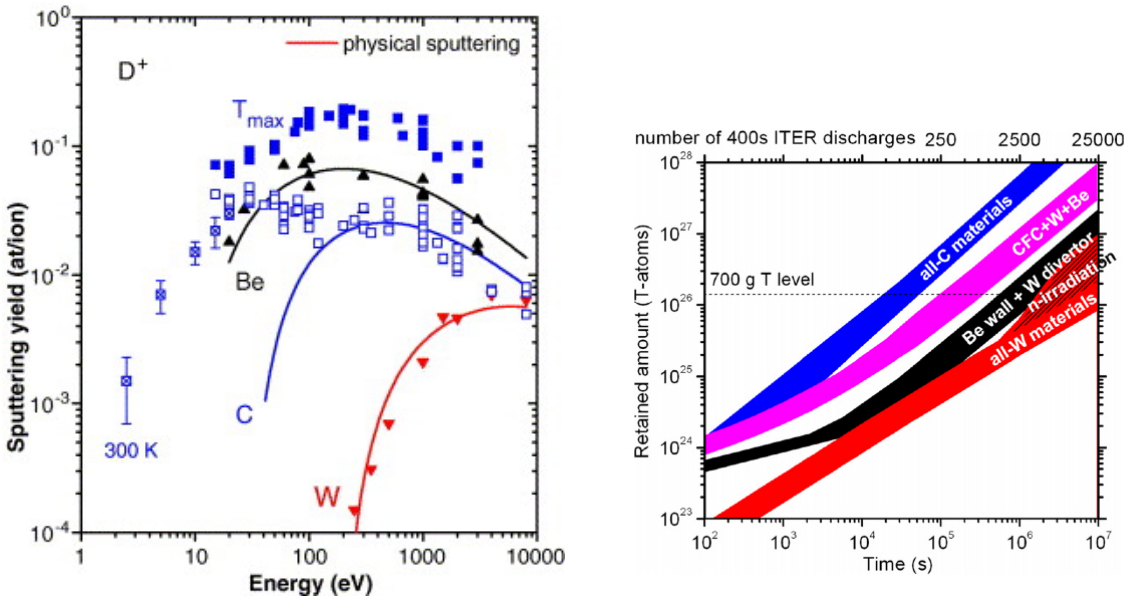

Figure 2.2: Sputter yield for candidate PFC materials, and their levels of tritium retention in ITER.[25] CFC materials show fast erosion rates and high levels of tritium retention, making them unsuitable for commercial reactors.

Tungsten-based PFCs require significant development before they can be used. Tungsten is very well suited for PFCs, due to its high melting point (3422°C), good thermal conductivity (174 W/mK at 25°C), low tritium inventory (10-100 times lower than carbon), resistance to plasma erosion and neutron displacements and the ability to retain these properties even after accumulating radiation damage.[14, 26–29] It is these beneficial properties that have led to the ITER organisation using a full-tungsten divertor for operation from launch.[30, 31]

However, the chief drawback of tungsten is the low fracture toughness, with polycrystalline alloys typically showing a fracture toughness below 10MPa$\sqrt{m}$ with intergranular crack paths. Fracture behaviour also depends strongly on trace contaminants and prior thermomechanical treatment.[32–34] The poor ductility of tungsten results in an inability to carry out the deep drawing

required to form structural components for the divertor. Additionally, in the plasma-facing tiles flaking or shattering may introduce heavy ions into the plasma, quenching the fusion reaction, as well as exposing other structural components of the reactor to increased thermal and fast-neutron fluxes.

In service, the fracture toughness of tungsten components will be lowered due to irradiation,[35] reducing fracture toughness by up to a factor of ten.[36] Therefore, these parts must have sufficient ductility to prevent failure even after significant degradation. As a result, a central theme in the research of tungsten for fusion power is increasing the ductility, formability and fracture toughness of the material.

In order to judge the level to which the ductility must be increased, and assess the feasibility of the current component designs it is necessary to understand how these properties change during the lifetime of the material. In particular, the effects of implanted helium must be considered. 3.5 MeV helium ions are a major output from the fusion reaction but will be exhausted into the divertor so as not to quench the fusion reaction. The mechanical behaviour of tungsten after both neutron and energetic helium irradiation is therefore an essential factor in determining the feasibility of a nuclear fusion power plant. The 14 MeV neutrons penetrate the full thickness of the tungsten armour, while the 3.5 MeV helium ions reach a depth of around 5 μm when implanted into tungsten.

2.2 Tungsten as an Engineering Material

In order to understand the effects of radiation damage on the mechanical properties of tungsten, it is necessary to first understand the mechanical behaviour of the material in its unirradiated condition. Tungsten traditionally has not been used as a structural material, instead finding more common use in light-bulb filaments, X-ray targets and tungsten inert gas welding.[37] These applications rely on functional, rather than mechanical, properties of the material such as its high melting point and electronic structure. The lack of structural use is partly because tungsten displays a common transition from brittle fracture at low temperatures to ductile failure at high temperatures; this is due to its BCC structure. The brittle to ductile transition temperature depends on strain rate, as well as several additional factors detailed herein, but it is typically between 100-200°C, rising to around 1000°C at high strain rates.[38] The poor fracture toughness at low temperature – typically

10 MPa$\sqrt{m}$[33,34] – and high BDTT of tungsten has been well-documented in single and poly-crystals.[38–40] This mechanical behaviour is controlled by the mobility of dislocations,[32] which depends on both intrinsic and extrinsic influences.

2.2.1 Intrinsic Factors Affecting Mechanical Properties

The intrinsic mobility of dislocations in a material is given by the Peierls stress. It is a measure of the stress required to move a dislocation through a perfect crystal at 0K and is determined by the atomic bond strength, dislocation width, shear modulus and Poisson's ratio.[41] The strong bonding and non-close-packed, BCC structure of tungsten give rise to a high Peierls stress, and hence a low intrinsic dislocation mobility. In tungsten, glide of screw dislocations occurs via the nucleation of kinks in the dislocation line into the neighbouring Peierls valley. This is a thermally activated process, therefore the mobility of dislocations, and hence the BDTT,[38] follows an Arrhenius relationship. The relationship has a corresponding activation energy, E_{BDT} (equation 2.2.1) where T_{BDT} is the brittle-to-ductile transition temperature, k is the Boltzmann constant, $\dot{\varepsilon}$ is the strain rate and A is a constant.

$$T_{BDT} = \frac{E_{BDT}}{k}\left(ln\left(\frac{\dot{\varepsilon}}{A}\right)\right) \tag{2.2.1}$$

Edge and screw dislocations have different activation energies (E_{BDT}) for glide. Although crack-tip deformation behaviour controlled by edge dislocation mobility has been reported by Gumbsch,[38] the majority of work agrees that screw dislocations control the plasticity and brittle-to-ductile transition (BDT) of tungsten, and that the findings by Gumbsch[38] were due to the specific crystallography of the specimens.[40,42] This is because screw dislocations are significantly less mobile than edge dislocations,[43] hence their motion will generally be the rate-controlling component of crystal plasticity. Specifically,[40] it is the energy of the double-kink formation of screw dislocations that determines the value of E_{BDT} in tungsten. The value of E_{BDT} varies depending on sample purity, but values of 1.05eV for pure tungsten – rising to 1.45eV for less pure sintered material due to dislocation-solute interaction – have been reported.[39,40] These high values of E_{BDT} (c.f. 0.096eV in Fe-3wt.%Si[44]) are important for two reasons: firstly, that the behaviour of the material is sensitive to impurities; secondly, the BDTT is sensitive to strain rate.

By introducing a high dislocation density into a material, the stress required to move dislocations through the material is increased.[45] This increases the yield strength, however fracture toughness is decreased and the BDTT is shifted to higher temperatures.[46] A very low dislocation density, whilst not providing significant resistance via dislocation-dislocation interactions, will not have many mobile dislocations. This results in a higher stress required to either unpin immobile dislocations, or nucleate new ones. It is the middle ground – a moderate dislocation density of $\sim 10^8$ lines/m^2 – that will give rise to the highest dislocation mobility and ductility, as recognised by Margevicius et al.[33]

It can be seen that the mechanical behaviour of tungsten is intrinsically poor, primarily due to its brittle behaviour and high BDTT. This is due to the low mobility of dislocations present within the material. Additionally, the processing of tungsten will influence the dislocation mobility, and hence the ductility of tungsten. Grain boundary behaviour - particularly intergranular fracture - will also have a significant effect on properties, discussed below.

2.2.2 Extrinsic Factors Affecting Mechanical Properties

The processing of tungsten will affect two main properties of the material: purity and grain size. The link between purity and mechanical behaviour has long been investigated. Typically, for materials with a BCC structure:

1. The small, asymmetric interstitial cavity size allows interstitial impurities – for example carbon, nitrogen and oxygen – to pin both edge and screw dislocations.[33] This is due to the small stress field around the intersitial atom relaxing by the atomic diffusion to the dislocation core.[47]

2. Substitutional solute atoms act to disrupt dislocation glide, increasing flow stresses.[39]

3. Deleterious solute atoms such as phosphorus can segregate to grain boundaries, leading to embrittlement and intergranular failure.[34]

The majority of tungsten alloys are made via powder processing routes. These routes can lead to significant concentrations of dissolved gasses[48] and can also introduce large numbers of impurities into the material because of the high surface area to volume ratio of the powders. This

is an important issue, as bulk impurity concentrations of only a few ppm can fully saturate the grain boundaries of a typical polycrystalline material when segregation occurs,[49] often leading to intergranular failure.

However, it is likely that tungsten fails intergranularly regardless of contamination. In detailed work on high-purity, polycrystalline tungsten by Margevicius[33] intergranular failure is seen. The minimum concentration of phosphorus required to cause grain boundary embrittlement is not known, so it cannot be conclusively stated that phosphorus-embrittlement is not occurring. Transgranular failure has been seen even with phosphorous levels as low as 20 ppm,[34] significantly lower than the <120 ppm present in Margevicius' work. The current design for divertor armour calls for 99.96wt% pure tungsten, i.e. 400 ppm of impurities, therefore for all engineering applications it can be assumed that the failure of tungsten will be intergranular.

Additionally, recent work has investigated the brittle-to-ductile transition in polycrystalline tungsten,[40] involving material with oxygen and phosphorus impurities in the <20 ppm range. In a comparison between high-purity tungsten and sintered, deformed tungsten it was found that the impure sintered material was more brittle, with the BDTT ∼80K higher than the high-purity tungsten over all strain rates. It was also noted that 'intergranular fracture was not observed in this [impure] material, implying that the effects of any impurities on the fracture process are via modification of the behaviour of the 'bulk' materials, rather than grain boundary segregation'. This supports the argument that contamination may not be the root cause of intergranular failure.

Finally, Gludovatz et al. have carried out an extensive characterisation of the influence of impurities on the fracture behaviour of tungsten.[50] Ten samples of tungsten were mechanically tested, with systematic variations of grain size and impurity content present. They found that both intergranular and transgranular fracture was present in all samples. Although insoluble impurities like oxygen, carbon and phosphorus were seen covering high angle grain boundaries, the authors show that the weakening of grain boundaries due to the impurities does not always result in intergranular failure.

This occurs because of two factors: firstly, due to the high density of grain boundaries present in fine-grained materials or materials with elongated grains from thermomechanical treatment, the levels of impurities in commercially-pure tungsten are low enough that impurities are too sparsely distributed along grain boundaries to cause weakness. Secondly, the influence of grain character -

grain size, size distribution, texture and internal dislocation density - is a dominating effect over the influence of impurities.

Gludovatz et al. further show that the fracture type of tungsten depends on the microstructure,[51] with deformed and recrystallized tungsten showing transgranular and intergranular failure dominating, respectively. In fusion applications, the high working temperatures of the PFCs and additional heating from plasma instabilities will likely lead to recrystallization over the working component lifetime and hence intergranular failure will again be favoured.

As demonstrated, the grain boundaries in tungsten control the crack path during failure, leading to intergranular or transgranular fracture being favoured. Prior to fracture, the traditional role of grain boundaries in a structural material is to strengthen the material against deformation by inhibiting dislocation glide. This is characterised by the well-known Hall-Petch relationship:[52,53]

$$\sigma_y = \sigma_0 + \frac{k_y}{\sqrt{d}} \tag{2.2.2}$$

Where σ_y is the yield stress of the specimen, σ_0 is the lattice resistance to dislocation motion and d is the grain size. k_y characterises the ability of grain boundaries to resist dislocation motion, and hence yield. The net result is that a fine-grained material will be stronger than a coarse-grained material.

However, Giannattasio[40,54] determined that in pure tungsten, grain boundaries are not the controlling factor for dislocation mobility. The activation energy for the glide of screw dislocations is sufficiently high that it is the still the nucleation of kink-pairs – not slip-transfer across grain boundaries – that is deformation-controlling. This was true even in fine-grained tungsten, with a mean grain size of 30 μm.

Despite the minimal contribution of grain boundaries to strengthening, grain shape can play an important role in the mechanical behaviour of tungsten. A comparison between ITER-grade rolled plate and pure tungsten produced by HIP with an equiaxed grain structure showed that the fracture strength of the equiaxed material is 2.7 times higher.[55]

In summary, tungsten is a brittle material due to the low mobility of dislocations. The purity of the material has a strong effect on the BDTT, but is unlikely to affect the intergranular failure mode seen in fracture. Finally, while grain boundaries in the material do not affect the inital yield

strength of tungsten, they will inhibit dislocation glide during plastic deformation.

2.3 Development of Tungsten for Fusion Power

As previously discussed, the main goal for tungsten development is increasing the initial ductility of the material, without compromising on thermal conductivity, recrystallisation and creep behaviour. There are two main ductilisation strategies employed in tungsten development: alloying to increase the ductility of the material itself and producing composite materials to enhance ductility through external contributions.

Rhenium is known to have a ductilising effect on tungsten,[39,56] but its cost and irradiation embrittlement due to the formation of σ and χ phases has ruled out its use for fusion energy applications. It is only tantalum, vanadium, molybdenum and titanium that remain as elements forming a solid solution with tungsten. Alloys of W-1%Ta, W-5%Ta, W-5%V, W-25%Mo and W-50%Mo have undergone Charpy tests from 400-1100°C.[57] The results show that all the alloys are more brittle than pure tungsten, i.e. the BDTT is higher. Four-point bend tests have been carried out on the same W-1%Ta and W-5%Ta material at much slower strain rates (3.30×10^{-5} s^{-1}) with similar results.[58] These alloys show brittle, intergranular failure along high-angle grain boundaries. It therefore appears that tungsten is most ductile in an un-alloyed condition, and an enhancement of fracture toughness must be gained through other means.

One potential method is that of tungsten-fibre reinforced tungsten composites. This allows 'pseudo-toughening' through controlled crack deflection at the engineered fibre/matrix interfaces producing internal energy dissipation by interface debonding and friction. Three-point bend tests of this material shows stable crack propagation whereas pure CVD tungsten failed catastrophically.[59,60]

Some success has been made by He et al. in producing tungsten-fibre reinforced tungsten-copper composites.[61] By infiltrating the copper at high temperatures, a stronger, more ductile material is formed. However, it still suffers from the same limitations as other composite-based materials: that scaling up production for bulk, reactor-scale components is exceedingly difficult.

Several attempts have been made to braze ductile tungsten foils together to produce a bulk component while simultaneously attaching the foils to heat sink materials such as copper. Kuru-

mada et al. joined tungsten to copper using titanium and copper brazing foils.[62] This produced a component with a boundary shear strength of 310 MPa - higher than that of the base material at 214 MPa. However, upon thermal cycling between 5-15 MWm^{-2} (∼600-1000°C), thermal cracking occurred in the tungsten leading to melting and loss of the brazing alloy. The limiting factor in the component design was therefore the fracture toughness of the tungsten itself. However, this method introduces copper components - that are extremely weak above a few hundred degrees - into an environment in which tungsten is being used largely because of its high melting point.

Reiser et al.[63] have carried out significant testing on tungsten foils and bulk pipe and charpy test structures formed from laminates. In particular, sections of pipe show ductile deformation and 20 J of energy dissipation at room temperature. Pipe formed from tungsten rod shows highly brittle failure with 0 J of dissipation at 300°C. The mechanical properties of tungsten components are therefore significantly improved with this methodology, however Reiser also uses a relatively low-temperature braze (Ag-28wt%Cu) that limits the high-temperature applications.

Nemeth et al. studied the BDTT of UFG tungsten foil,[64] as UFG materials show an attractive combination of elevated strength as well as pseudo-plasticity from grain delamination. In the UFG foils, the BDT was seen to occur at ∼77 K regardless of strain rate. After annealing to a coarse-grained microstructure, the BDT was seen at ∼400 K. The authors propose that because thermally-activated screw dislocation is not possible at cryogenic temperatures, edge dislocations must control the onset of plasticity in the UFG sample, although this not not directly observed. However, given the propensity of grain boundaries in tungsten to fail, it seems more likely that the grain boundary delamination is dominating the failure behaviour before plasticity is relevant.

Saito et al. successfully used hot isostatic pressing to bond tungsten and high-purity copper.[65] Joining to dispersion-strengthened copper failed due to the formation of an oxide layer, but was possible with the presence of a high-purity copper layer. Tensile tests showed that the dispersion-strengthened copper resulted in a slightly stronger component, however the material was not tested under fusion-relevant thermal loads as with Kurumada's work.[62] It is therefore unclear how effective these components will be in practise.

Finally, Kalin et al. successfully joined both monocrystalline and polycrystalline tungsten to ODS-EUROFER97 steel.[66] A novel design is used to reduce failure due to thermal stress. The tungsten is brazed to a tantalum spacer using a titanium-chromium-based braze, and the tantalum

subsequently attached to the steel using an iron-tantalum-based brazing alloy. During thermal cycling from 25-750°C no joints failed, and the microstructure remained stable. The technique and materials are being further developed to reduce the high-activation materials present in the brazing alloys.

Enhancement of ductility is not the only materials engineering required for enhancing tungsten. The top of the operating temperature window is limited by recrystallisation and creep. To reduce thermal loading on plasma facing materials, plasmas are often deliberately seeded with impurity atoms such as nitrogen[67] in order to radiate energy and reduce the heat load on the divertor. By increasing the recrystallisation temperature of tungsten, impurity concentrations can be reduced and engineering proposals simplified.[20] In order to do so, powder processed W, W-Ti, W-V and W-Ta alloys have been produced with grain sizes ranging between 20 nm and 500 nm, and reinforced with Y_2O_3, La_2O_3 or TiC nanoparticles. These alloys have a high density ($\sim 6 \times 10^{22}$ m^{-3}) of small oxide particles with sizes below 50 nm. However, the alloying additions again result in poor fracture toughnesses, with the DBTT of these ODS alloys typically above 1100°C. However pure ODS tungsten, W-2%Y_2O_3, is fully ductile above 300°C in three-point bend and tensile testing, showing total elongation up to 10%.[68,69] Fan et al.[70]also developed ODS tungsten alloys, and showed that fine grained W-TiC and W-ZrC composites endured a heat flux 100% higher than pure tungsten and also had higher tensile strengths. These ODS tungsten alloys are therefore a promising candidates for further materials testing.

To summarise the development of tungsten: alloying tungsten increases the BDTT of the material, although small additions of ODS particles can be included successfully. Tungsten composite materials show promise, but are difficult to produce at the reactor scale. Finally, brazes to join tungsten to heat-sinks still require development to produce tough, low-activation joints. Additionally, there has been very little investigation into the mechanical properties of these materials, particularly with respect to degradation from irradiation.

2.4 Radiation Damage: Description and Effects in Tungsten

There are three main types of radiation damage in a fusion reactor: a flux of 14 MeV neutrons, implantation of hydrogen and helium,[71] and transmutation. These will be described, and observations from neutron and ion irradiation analysed. Their effects on the mechanical properties will then be examined, and a comparison between neutron and ion irradiation made.

2.4.1 Displacement Damage

Upon impacting the material, neutrons and other particles cause atomic displacements and subsequent knock-on displacements, as shown in figure 2.3.[72] Lattice displacements are formed by the incident particle knocking an atom from its lattice site. This primary knock-on atom then travels through the material and produces further atomic displacements.

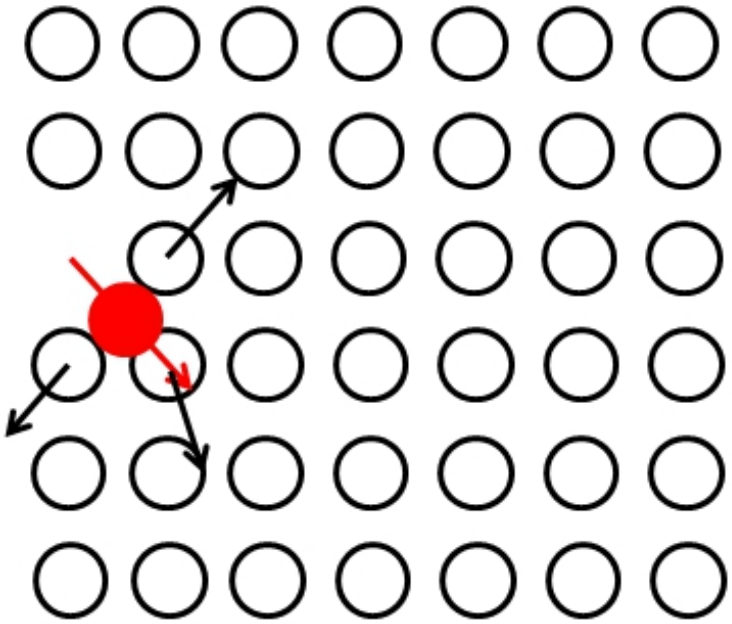

(a) Having been struck by an incident particle, the primary knock-on atom (PKA) (shown in red) travels through the material causing a cascade of atomic displacements.

Figure 2.3: Displacement damage from high-energy primary knock-on atoms.[72]

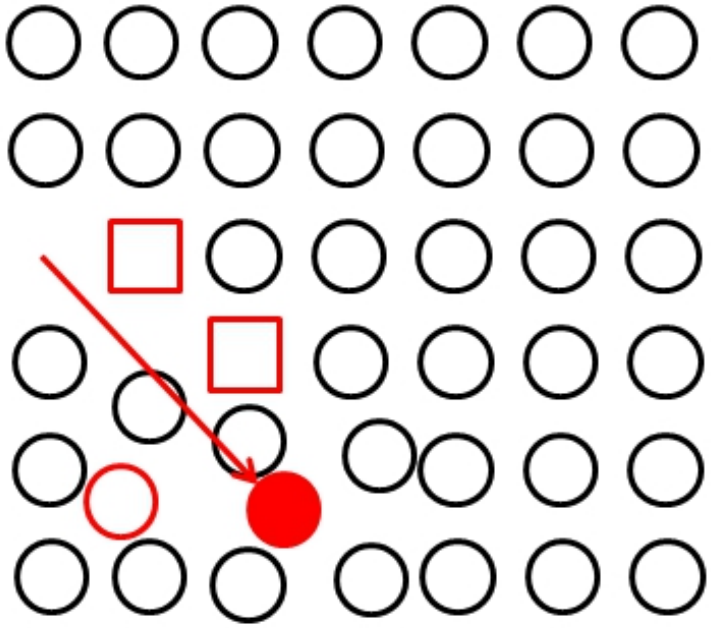

(b) The atomic displacements result in vacant lattice sites (red squares) and interstitial atoms (red circles). The majority of these defects will recombine to reform a perfect lattice.

Figure 2.3: Displacement damage from high-energy primary knock-on atoms (cont.)[72]

The lattice displacements result in many dislocation loops within the material that cause strain localisation, blocking dislocation motion and increasing the BDTT. The vacancies created can also cluster into voids, causing a decrease in thermal conductivity and a change in the dimensions of plasma-facing materials.[73] As Frankel pairs are formed from displacement cascades, they can be efficiently created either by neutron or ion irradiation;[74, 75] both methods produce a high-energy primary knock-on atom. In ion-irradiation of iron, loops are not seen until doses above 10^{16} ions/m^{-2} when cascade overlap becomes significant. This corresponds to approximately 0.01 dpa,[76] well below the damage levels investigated herein. Void diameter will increase with dose, although as shown by figure 2.4 this increase is not linear with damage levels.

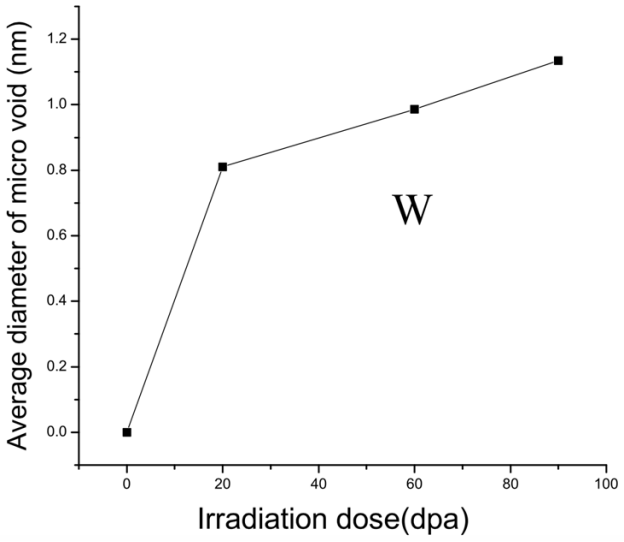

Figure 2.4: Void diameter with dpa levels. From tungsten irradiated by 85 MeV flourine ions at room temperature.[77]

Neutron-based experiments in the literature typically report irradiation levels in one of two ways: fluence or damage. Kinetic Monte Carlo calculations by Troev[78] allow a conversion between the two. They calculate 2.85 dpa in tungsten per full power year (FPY) of ITER operation under a neutron flux of 2.5×10^{22} n/cm^2. Their modelled cascades produced single vacancies and divacancies. Ideally, displacements per atom provide a way of comparing radiation damage from different sources: fusion neutrons, fission neutrons and ion irradiation. Therefore, damage levels in this thesis will be referred to in terms of dpa. It should be noted however that although dpa is widespread measure of damage in materials, it does not fully capture the effects of radiation damage: transmutation, solute clustering and defect recombination will all affect the final microstructure of the material and hence its mechanical properties.

Yi has carried out extensive TEM characterisation of radiation damage in tungsten.[75,79] This work has characterised pure tungsten and W-Re, W-Ta and W-V alloys that were implanted with 2 MeV W+ ions at temperatures ranging from 300°C to 750°C for damage levels up to 4.5 dpa. Loop analysis showed the presence of both $\frac{1}{2}\langle111\rangle$ loops and $\langle100\rangle$ loops, with the $\frac{1}{2}\langle111\rangle$ loops being more thermally stable. High irradiation temperatures and doses favoured the production of interstitial loops compared with vacancy loops. In-situ annealing of irradiated thin foils was also performed to investigate the thermal stability of radiation damage in tungsten. The majority of

the change in damage was completed within 15 minutes of annealing, largely through the loss via coalescence of <2 nm loops.

It is important to compare both methods of creating displacement damage with the fusion neutron damage expected from DEMO and commercial fusion reactors. Figure 2.5 shows a comparison between various neutron spectra for irradiating materials. The important plots in this figure are the 'DEMO Helium-Cooled Pebble Bed Blanket' (DEMO HCPB) as this is the spectrum to which experiments should be matched, and the fission reactor 'HFR-F8'. HFR-F8 is a typical fission source, and is also the reactor that irradiated the neutron irradiated tungsten investigated within this thesis. It can be seen that the fission spectrum is similar, but approximately five times lower than the DEMO spectrum for neutron energies up to ∼5 MeV. Above this, the fission spectrum decreases sharply, with the fusion spectrum extending up to 14 MeV. This means that the high energy knock-on atoms will not be present, potentially leading to different damage morphologies. This is also shown in the graph of damage production function ($W(T)$) in figure 2.6, which characterises the entire PKA spectrum. It shows that for the HFR irradiation the damage produced happens at much lower knock-on energies, potentially affecting the displacement damage produced.

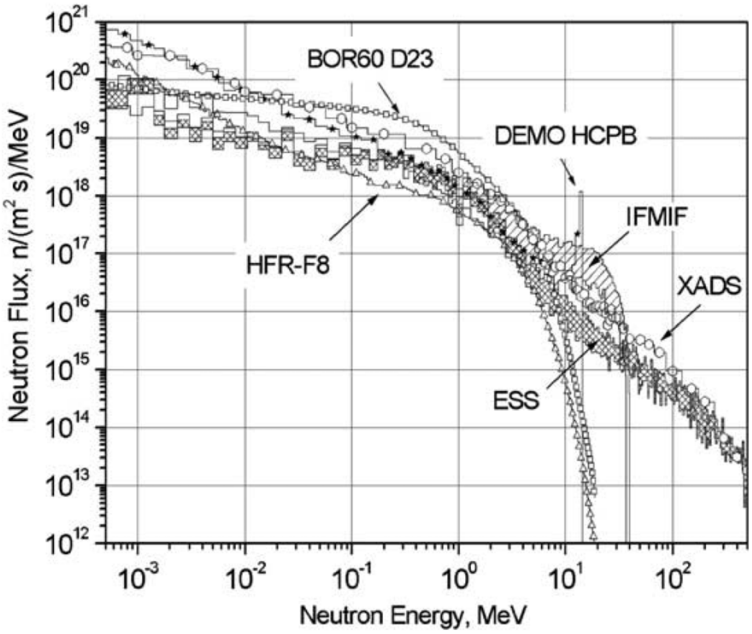

Figure 2.5: Neutron spectrum for fission and fusion neutrons. The spectra from the DEMO fusion reactor and the HFR reactor used to irradiate the tungsten in this thesis are very close except for the 14 MeV peak in DEMO. From:[80]

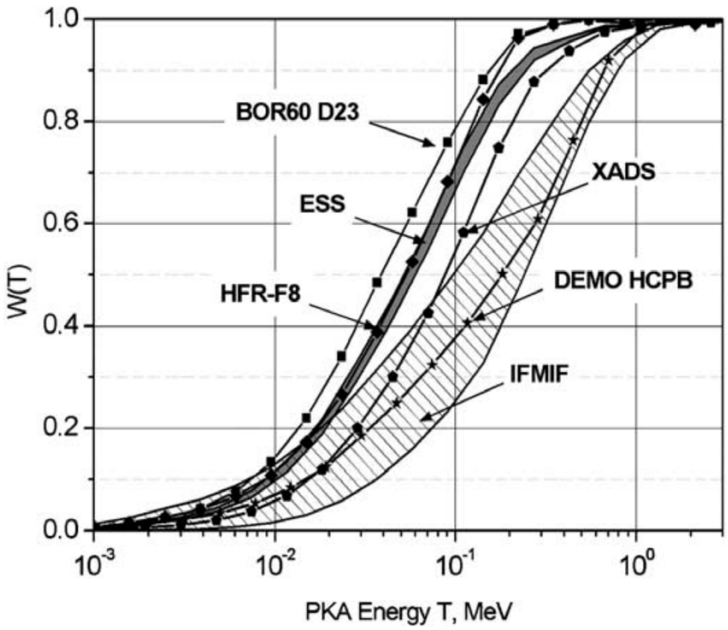

Figure 2.6: Damage profile in iron for fission and fusion neutrons. The fission neutrons (HFR) produce their damage at lower PKA energies than the DEMO spectrum, potentially influencing the damage structure produces. From:[80]

The effect of PKA energy can clearly be seen in Ryazanov's work on sub-cascade formation.[81] Figure 2.7 shows the sub-cascade generation rate for HFIR (a typical fission neutron source), ITER and DEMO. It is obvious that the generation rates are significantly different between the fission and fusion neutron sources. Sub-cascades are similar to low-energy cascades in size and shape, leading to an increase in damage production once sub-cascade formation begins.[82] An increase in sub-cascade generation may therefore over-estimate the amounts of damage present: the extra cascades present from fission neutrons may lead to an increased defect concentration when compared with that produced by fusion neutrons.

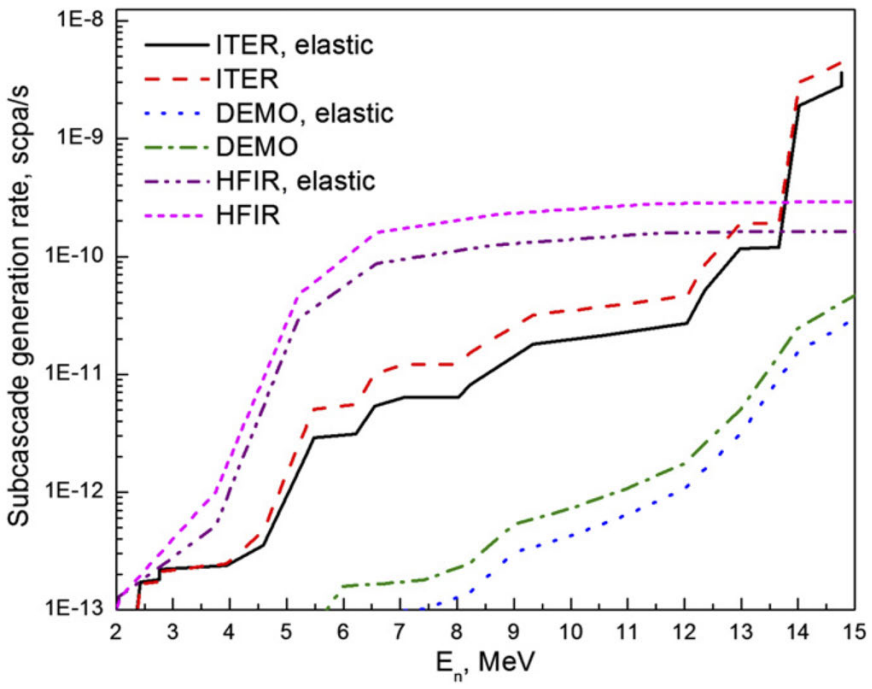

Figure 2.7: Generation rates of sub-cascades vs neutron energy spectrum for tungsten for elastic and inelastic nuclear channels. In inelastic channels, energy from the incident particles of the nuclear reactions can raise the reaction products to an excited state. The fission (HFIR) spectrum produces a substantially different subcascade generation rate than the fusion spectra, which may overestimate the damage produced. From:[81]

Similar results have been produced by Sawan in a comparison of the High Flux Isotope Reactor (HFIR) at Oak Ridge with Magnetic Confinement Fusion.[83] The HFIR produces a lower dpa (26.1 vs 19.5) and much lower helium concentration (12.9 appm vs 0.02) for same fast neutron fluence. Therefore, the displacement per atom ratios fall from 0.6 He atoms and 1.8 H atoms per dpa in fusion to 0.0008 He atoms and 0.003 H atoms per dpa at the HFIR. This demonstrates both that the high-energy region of the fusion neutron spectrum largely produces hydrogen and helium, and that fission neutron irradiation poorly reproduces the gas effects in fusion.

Ion irradiation has an advantage in representing fusion neutron damage as it can be used to produce lattice displacements in a material in much shorter time frames compared with fission neutron irradiation, with several dpa per day readily obtainable. Additionally, hydrogen and helium implantation can be used to reproduce the transmutation products from fusion neutrons. Figure 2.8 shows a plot of damage fraction against PKA energy for several neutron profiles (black) and ion implantations from the JANNuS[84] facility. Although the ion irradiations do not exactly match

the profiles for neutron irradiation, it can be seen that heavy ions - such as gold or tungsten (not shown) - match the initial portions of the DEMO spectrum relatively closely. From these data, it can be assumed that heavy ions are reasonably representative of fusion neutrons. Despite the potential difficulties due to sub-cascade generation, the high energy PKAs do not form substantially different damage structures to those produced at lower energies.

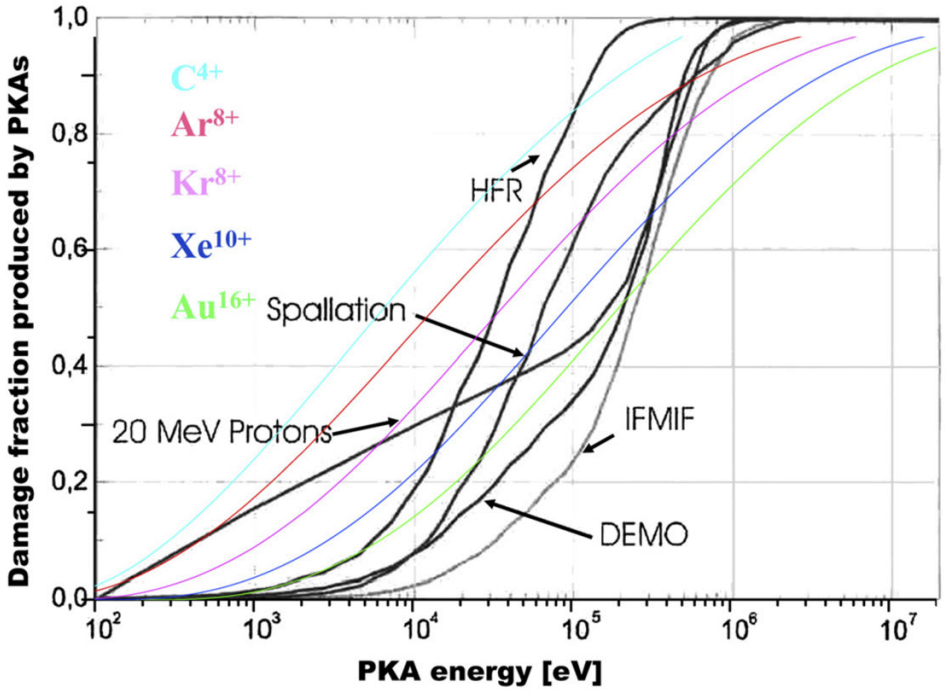

Figure 2.8: Damage profiles of neutron irradiation and ion irradiation at the JANNuS facility. The heavy ions produce a close match to the fusion spectrum over the initial portion, hence tungsten self-ion irradiation should produce a close match to neutron irradiation.[85]

Perhaps more importantly than the effects of sub-cascades, dose rate effects and a rate difference of six orders of magnitude between fusion neutrons and ion irradiation,[86–88] means that care must be taken in using ion irradiation data. Garner et al.[89]concluded that when comparing two radiation environments, differences in dose rate are dominant in determining of the response of an alloy. Hardie observed that the change in dose rate affects the clustering behaviour of chromium.[90] It is possible that the effects are reduced in pure materials, supported by the lack of a dose rate effect in pure iron.[76] Nevertheless, ion irradiation may be best suited to studying the underlying mechanisms of radiation damage, so that property changes can be determined from predictive models.[91]

In summary, neither fission neutrons nor heavy ions will exactly match the expected damage from 14 MeV fusion neutrons. As such, care must be taken in informing engineering designs directly from current experimental tests. Fission neutrons are a slightly worse match to the damage profile than heavy ions, but are a good match in dose rate: 6×10^{-8} dpa/s in this work and 10^{-7} to 10^{-8} dpa/s expected in fusion irradiation.[86] However, due to the long time scales, expense and limited testing options available when dealing with neutron-irradiated materials it is necessary to use ion irradiation to carry out the systematic studies necessary for predictive models to be generated and the underlying fundamentals of radiation damage science to be understood.

2.4.2 Hydrogen and Helium Effects

Hydrogen and helium will be present in PFCs due to two mechanisms: implantation and transmutation. Hydrogen and helium ions from the plasma will be implanted in the material through the mechanism outlined above (figures 2.3(a) and 2.3(b)). However, they can also be produced through nuclear reactions that result in the production of protons and alpha particles, in small, but roughly equal proportions.[92] The presence of these dissolved gasses can result in the formation of nanometre-sized bubbles,[93,94] especially at grain boundaries, leading to a 'foamy' structure and a significant reduction in the cross-section of components.

The use of dual or triple-beam irradiation facilities such as JANNuS, DuET[95] or the HZDR ion beam centre[96] allows heavy ions, hydrogen and helium to be implanted simultaneously to closely represent fusion conditions.

With hydrogen, thermal desorption experiments have shown that implanted deuterium is swiftly desorbed at low temperatures, with the majority of the deuterium leaving tungsten at temperatures below 550°C.[97] Furthermore, the low activation energy for hydrogen diffusion in tungsten of 0.39 eV means only hydrogen trapped in defects remains within the material.[97] DFT modelling[98] shows hydrogen does not cluster strongly, so that the formation of hydrogen blisters in tungsten can only take place in the vicinity of a defect or a solute atom. It should be noted however that in fusion the simultaneous neutron irradiation can produce a significant defect density.

For tungsten samples loaded with a hydrogen beam containing 1 at% helium, bubbles are formed at surface temperatures above 1000°C.[99] However, thermal desorption spectroscopy shows that

hydrogen is still rapidly released above 300°C. Long-term desorption (10^5 s) still shows release of hydrogen at these time scales due to the depth of hydrogen diffusion into the bulk of the samples.

Sekimura[100] has also shown that in BCC vanadium: 'swelling is found to be enhanced [during triple-beam irradiation]... These results cannot be explained by simply adding the helium and hydrogen effects observed in the dual beam irradiation experiments, since hydrogen does not contribute to swelling under dual beam irradiation.' There is therefore a synergistic effect of the hydrogen and helium implantation on the microstructure. A similar effect has also been seen in triple beam irradiated austenitic stainless steel[101] that results in a microstructure consisting of significantly fewer dislocation loops but more dislocation lines due to the interaction of dislocations with the injected gases.

Due the the rapid desorption of hydrogen and the higher concentrations of helium present due to the plasma exhaust, it is helium that is the concerning gaseous species during reactor operation. Fortunately, the rate of helium production in tungsten through transmutation is extremely low, such that grain boundary embrittlement in this manner would take over 300 years.[102] As such, it is helium implantation from the plasma that is most important for tungsten materials. Work on helium in tungsten is complex, as the produced damage is affected by fluence, implantation energy and implantation temperature, but general behaviour can be seen as helium levels in the material are increased from single helium atoms to novel 'nanofuzz' structures seen at very large fluences (figure 2.9).

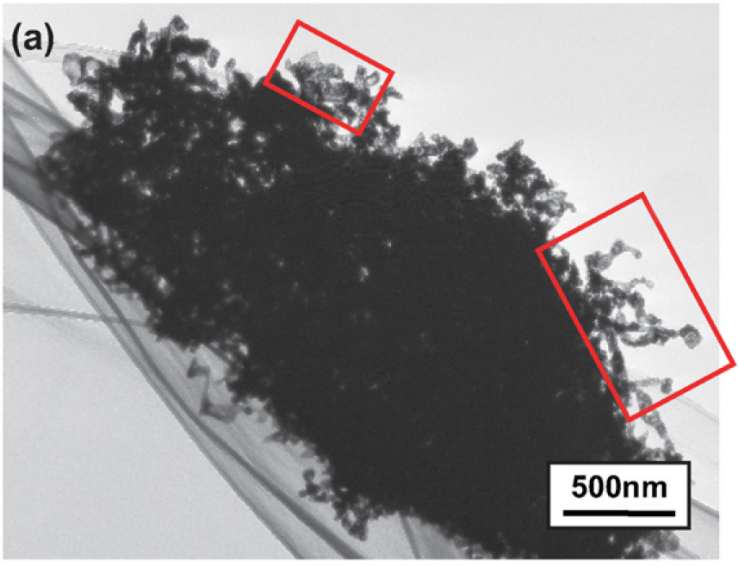

Figure 2.9: 'Nanofuzz' structure after exposure to an extremely high helium ion fluence of 4×10^{27} m^2 at 1300°C.[103]

There has been much modelling work studying helium in tungsten. At low energies, below the displacement threshold energy of tungsten, it was determined that helium sits at the tetrahedral interstitial sites in tungsten.[104,105] Unsurprisingly, as an interstitial atom, the diffusivity of helium is very rapid. In damage-free tungsten the helium migration energy is only 0.28 eV, therefore it is highly mobile from 110 K.[106] In practise, this means if the helium is not trapped during irradiation it will migrate and release from the surface.

Unfortunately, this trapping can occur even in defect-free material. Becquart and Domain[107] use DFT calculations to show that there is a strong He-He binding energy of 1 eV between two He atoms in interstitial positions. This leads to an extremely strong tendency for multiple helium atoms to be trapped in stable clusters. The strong attraction between helium atoms further favours the interstitial tetrahedral sites. This trapping is purely elastic,[98] leading to binding only at close separation distances.

Even once clustered, MD simulations performed in tungsten[108] indicate that small helium clusters are very mobile. 2He clusters perform a 1D motion along ⟨111⟩ directions at low temperatures and can migrate as fast as a single helium atom. As the temperature increases, the motion becomes more and more 3D-like. As cluster size increases however, Li et al. used MD simulations to show that when the cluster size is greater than five, cluster mobility is near-zero.[109]

However, these results are only for clusters of pure helium; they do not describe the motion of helium-vacancy or helium-interstitial clusters that form during an irradiation event. Indeed, in Li's simulation of an 800 keV helium implantation, all the implanted helium formed He-v or He-I clusters. The binding between helium and the generated vacancies is very strong. Yang[110] determined a He-v binding energy of 4.58 eV and dissociation energy of 4.65 eV that compared favourably with experiment (4.5-4.6 eV). It is therefore the behaviour of helium-vacancy clusters that is important for tungsten. Interestingly, the vacancies themselves also have a lower migration energy without helium, i.e. helium traps vacancies as well as vacancies trapping helium. This has been determined from DFT models by Gonzalez et al.[105] The migration of helium-free monovacancies is found to occur between 250°C and 300°C,[111] therefore helium-vacancy clusters will be the important species during fusion conditions as operating temperatures will be above this. These helium-vacancy clusters spontaneously form near free surfaces due to Frenkel pair formation - that is easier near surfaces - producing a vacancy to form a helium-vacancy cluster. The interstitial then moves as a $\langle 111 \rangle$ crowdion.[112]

These helium-vacancy interactions can be studied through the retention properties of tungsten. Hashimoto carried out a comparison of the helium retention properties of single-crystal and polycrystalline tungsten.[113] In a single implantation and annealing experiment there was no observed difference between the two types of tungsten. However, when the same test was carried out in a 1000-step annealing process - mimicking pulsed reactor operation - the single-crystal sample retained only 5% of the implanted helium, while the polycrystalline sample retained 30%. TEM analysis suggested that the helium was trapped in cavities that form at grain boundaries in the polycrystalline sample but in the bulk in the single-crystal material. The increased trapping sites at grain boundaries therefore led to increased helium retention in polycrystalline materials.

Debelle et al. have studied helium behaviour and vacancy defect distribution in helium implanted tungsten.[114] Firstly, they note the actual helium implantation distribution is less spiky than SRIM[115] (Stopping Range of Ions in Matter) predicts, a difference 'usually found and attributed to an incorrect evaluation of the 'straggling phenomena' by the SRIM program'. This affects light ions more strongly: for self-ions, TEM observations of radiation damage in tungsten[74] have shown that SRIM-predicted tungsten ions ranges match the damage structures observed in tungsten. Secondly, Debelle carried out a reactor-appropriate implantation of helium to 1×10^{16}

ions/cm^2 (approximately 600 appm), followed by an anneal at 1200°C or 1500°C. A spike of 'over-concentration' compared to the as-implanted helium profile is seen after annealing at 1500°C due to the formation of helium bubbles. Finally, no helium desorption, with a relative precision of 3%, was observed in any annealing conditions.

The conclusion of helium-bubble formation at 1500°C is well supported. Takamura[116] estimated an effective diffusion coefficient of 1×10^{-9} m^2/s for helium. This assumes the helium is in tungsten containing a large concentration of vacancy trapping sites, in the temperature range ~575-1425 K. As such, in Debelle's one hour annealing stages a helium migration of over 6 μm could have occurred. The fact that no migration was observed - as no desoption was observed - well-supports the conclusion of the precipitation of helium bubbles. Gilliam et al.[117] used similar implantation conditions (1.3 MeV, 5×10^{16} ions/cm^2) and did not observe any change in helium retention after flash annealing at 2000°C. They also attributed their results to the formation of helium bubbles.

Bubble formation has been studied by Iwakiri et al. in the TEM.[118] Two main effects are seen: firstly, up to 600°C, fine bubbles of a few nanometres in size were formed. Once vacancy migration is increased, the bubble number density decreases but the bubble size increases. Also seen is the relationship between the fluence required for bubble formation and temperature. Bubbles are seen at a flux of $>10^{19}$ atoms/m^2 at 800°C and $>10^{21}$ atoms/m^2 at 500°C, i.e. increased vacancy and/or helium mobility favours the formation of bubbles.

Hofmann et al. have done extensive characterisation of a 300°C, 3000 appm helium-implanted W-1%Re alloy[119] that demonstrates the significant elastic strains from implanted helium. They use micro-Laue diffraction to measure an out-of-plane lattice strain of 1.5×10^{-3} that results in a hydrostatic strain of 2.620×10^{-3}. This gives in-plane stresses of 0.32 GPa and out-of-plane stress of 0.81 GPa due to the implanted defects and in the in-plane case also the boundary condition requiring continuity of the material at the interface between the implanted layer and the substrate. These significant stresses likely explain the significant hardening seen in indentation experiments.[120] Using DFT, they also show that the helium-vacancy clusters likely contain a pair of helium atoms.

From these results, the following scheme can be drawn: during irradiation, highly stable helium-vacancy complexes are created. Increasing damage results in small voids, followed by helium bubbles and finally a 'nanofuzz' structure shown in figure 2.9 at fluences above 1×10^{22} ions/cm^2,[121]

although the exact fluence depends on the helium energy. Void and bubble formation is enhanced at higher temperatures, due to the increased mobility of vacancies. During annealing above 1500°C, helium-vacancy complexes migrate and coalesce to form bubbles, since these are only observed later when increasing the implantation fluence. Grain boundaries act as nucleation sites for bubbles when a critical concentration is reached, in particular at high implantation fluences.[113,117] Thus, bubble growth may be favoured by bubble migration along grain boundaries. Furthermore, during the thermal treatments, grain growth might have occurred. A dragging effect of helium by the moving grain boundaries could also have contributed to the bubble growth.[122] Bubbles can also be grown at extremely high fluxes, $>10^{19}$ atoms/m^2 depending on temperature.

As discussed, during reactor operation the plasma-facing components will be subject to displacement damage from fusion neutrons at the same time as helium implantation. It is therefore prudent to study the interaction between hydrogen or helium with significant levels of displacement damage.

Yoshida et al. show that similar effects - vacancy stabilisation by helium - occur under these conditions. They have conducted a dual beam irradiation of tungsten[93] with copper and helium ions. With 3 dpa of damage, a combination of interstitial loops and voids from vacancy agglomeration were seen. If low energy (below the displacement threshold) helium ions are also introduced no voids are seen; the helium ions stabilise individual vacancies and prevent void formation.

Concerning a combination of hydrogen and displacement damage, Shimada's work on deuterium retention in neutron and ion irradiated tungsten[86] suggests that ion irradiation may not accurately capture the behaviour of neutrons. Neutron irradiated samples were damaged to 0.025 dpa under a fast neutron fluence of 1.1×10^{24} neutrons/m^2. Ion irradiated samples were irradiated using iron, tungsten and hydrogen ions up to 3 dpa. All materials were then exposed to a deuterium plasma, and deuterium retention measured using thermal desorption spectroscopy (TDS) up to 900°C. It was found that no ion choice fully captured the TDS spectrum from the neutron irradiated material, although the iron and tungsten irradiations were relatively close to the low and high temperature parts of the spectrum respectively. Additionally, the levels of deuterium retention for the 0.025 dpa neutron irradiated sample were only reached by 3 dpa in the ion irradiated materials. The authors decline to give a reason for this behaviour, as the results are not statistically significant enough to draw absolute conclusions.

Oya et al. also compared the behaviour of deuterium retention for ion irradiated tungsten with neutron irradiated tungsten.[123] The ion damage levels of 0.025-3 dpa were compared with neutron irradiated tungsten with damage levels of 0.025 dpa. The desorption peaks are shown in figure 2.10 and do not closely match: ion irradiated samples show two sharp peaks below 300°C, while the neutron irradiated sample shows a much broader spectrum and a third peak around 500°C. This peak is attributed to deuterium trapping by a void or vacancy cluster, with the broad spectrum due to deuterium diffusion. The authors conclude that 'the deuterium trapping and desorption mechanism for the neutron irradiated tungsten differs from that of the ion irradiated one.' As a TDS spectrum will depend on the defects present in the material, these data suggest that ion irradiation may not accurately capture the behaviour of neutrons.

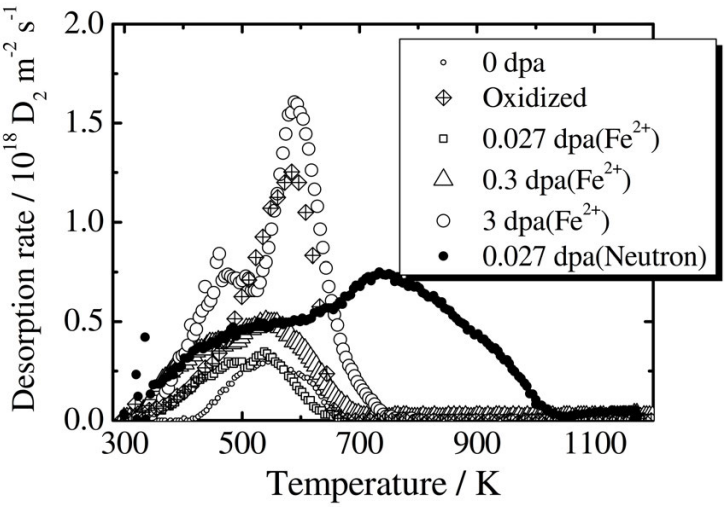

Figure 2.10: Deuterium thermal desorption spectrum for Fe^{2+}-irradiated tungsten and neutron-irradiated tungsten. The spectra depend on the defect population in the material, and do not closely match between the ion spectrum and neutron spectrum. [123]

2.4.3 Transmutation

Transmutation effects occur when atoms absorb the incident neutrons and new elements or isotopes are formed through nuclear decay. It is this process that produces 'active' specimens, one of the two big barriers to testing irradiated materials. The other barrier to widespread testing of neutron irradiated material is the low rate at which damage accumulates. To produce even moderate damage in a material requires years of exposure, which is not practical for multiple tests of a wide variety

of materials.

Ion irradiation does not produce any transmutation within the damaged materials. Therefore, to produce a complete picture of the behaviour of tungsten using ion irradiation requires many alloys with a wide variety of compositions to be produced, irradiated and examined.

Transmutation of tungsten will produce rhenium and osmium, as well as small amounts of tantalum via β decay. Modelling work using a FISPACT inventory code and Monte Carlo neutron transport simulations[124] (figure 2.11) predicts up to ~4 at% rhenium and ~1 at% osmium formed after five years. These elements can lead to the formation of brittle, intermetallic σ and χ phases, to the detriment of the mechanical properties of the PFCs. It is important to note these predicted compositions will gradually change as the FISPACT database improves. For example, work by Cottrell et al. in 2006 predicted up to 3% osmium.[125] It is therefore not possible to work on the exact alloy present at the end-of-life stage, further emphasising the need for predictive models and the understanding of fundamental processes.

Starting composition (at%)	Transmutation products	Concentration of product in appm (in brackets, at%) after irradiating for		
		1 year	3 years	5 years
W (100)	W	9.89×10^5 (98.9)	9.63×10^5 (96.3)	9.40×10^5 (94.0)
	Re	9.06×10^3 (0.91)	2.59×10^4 (2.59)	3.80×10^4 (3.80)
	Os	5.58×10^2 (0.06)	5.28×10^3 (0.53)	1.38×10^4 (1.38)
	He	6.65×10^0 (<0.01)	2.00×10^1 (<0.01)	3.36×10^1 (<0.01)
	H	1.51×10^1 (<0.01)	4.56×10^1 (<0.01)	7.63×10^1 (<0.01)
Ta (100)	Ta	9.32×10^5 (93.2)	7.56×10^5 (75.6)	6.15×10^5 (61.5)
	W	6.37×10^4 (6.37)	2.32×10^5 (23.2)	3.67×10^5 (36.7)
	Hf	4.37×10^3 (0.44)	1.15×10^4 (1.15)	1.67×10^4 (1.67)
	He	2.88×10^0 (<0.01)	1.03×10^1 (<0.01)	2.00×10^1 (<0.01)
	H	1.64×10^1 (<0.01)	5.07×10^1 (<0.01)	8.68×10^1 (<0.01)
Re (100)	Re	8.73×10^5 (87.3)	6.65×10^5 (66.5)	5.08×10^5 (50.8)
	Os	1.22×10^5 (12.2)	3.20×10^5 (32.0)	4.69×10^5 (46.9)
	W	5.67×10^3 (0.57)	1.50×10^4 (1.50)	2.15×10^4 (2.15)
	He	3.58×10^0 (<0.01)	1.14×10^1 (<0.01)	1.98×10^1 (<0.01)
	H	1.89×10^1 (<0.01)	5.81×10^1 (<0.01)	9.82×10^1 (<0.01)

Figure 2.11: Transmutation response for tungsten and its main transmutation products.[124]

Herschitz and Seidman used atom probe tomography to study radiation-induced segregation in neutron irradiated tungsten-rhenium alloys after 8.6 dpa (4×10^{26} neutrons/m^2).[126] They showed homogeneous precipitation of intermetallic species after irradiation in both W-10at%Re and W-25at%Re, with voids also forming in the 25% alloy.

Tanno et al.[127] investigated the effect of transmutation elements in neutron irradiated tungsten alloys using TEM. It was found that both rhenium and osmium prevent void swelling, possibly by interrupting defect cluster formation. The interruption effects of osmium are much stronger than those of rhenium as no voids were observed in the TEM in alloys containing osmium. Precipitates were seen in W-Re after 0.4 dpa at 750°C and were confirmed to be Re_3W. In W-3%Os, and W-5%Re-3%Os precipitates were only seen after 1.54 dpa at 750°C, illustrating that osmium suppresses precipitate formation.

Fukuda et al.[128] also looked at neutron-irradiated tungsten in the TEM. Pure tungsten and W-Re alloys up to W-26%Re were irradiated up to 1 dpa at 500°C and 800°C. σ and χ intermetallic phases were seen even in pure tungsten. Rhenium contributed towards smaller precipitates with lower number density.

Young-Won used resistivity measurements in an annealing study of several samples of neutron irradiated tungsten with varying purities.[129] The results show that annealing-out of the radiation damage does not strongly depend on material purity. Transmutation-induced rhenium production accounts for the inability to fully recover the unirradiated resistivity levels; 'if it is reasonably assumed that rhenium atoms play an important role in trapping interstitials during irradiation.' The rhenium impurities themselves also increase the resistivity levels as the impurities cause scattering, reducing the electron mean free path. The level of radiation damage in this study is slightly unclear: a fluence of 4.5×10^{-15} neutrons/m^2 is stated, which corresponds to a damage level of approximately 9×10^{-41} dpa. This is an impossibly small damage level (1 displacement in $\sim 10^{10}$ m^3 of tungsten), therefore assuming the negative sign is an error, 4.5×10^{15} neutrons/m^2 corresponds to 0.01 dpa.

2.5 Radiation Damage Summary

Neither fission neutrons nor heavy ions accurately represent a fusion neutron spectrum. While the PKA energies of ions and fusion neutrons are slightly closer than with fission neutrons, the dose rates are substantially different. This means that care must be taken in interpreting results from either type of irradiation campaign. However, both methods will produce displacement damage in a crystal lattice, producing large numbers of Frenkle pairs that then form $\frac{1}{2}\langle 111 \rangle$ loops and

⟨100⟩ dislocation loops. Neither method will produce hydrogen or helium in the material unless it is deliberately implanted, but there are limited data showing that helium implanted above the displacement threshold of tungsten will produce a similar microstructure - helium-stabilised vacancies - as simultaneous lattice displacements and helium formation. At very high temperatures, well above expected operating temperatures, these helium-vacancy clusters can coalesce into stable bubbles. However bubbles will still form at large enough fluences. Finally, neutrons will produce transmutation products consisting mainly of rhenium, osmium and tantalum. These act to prevent void formation, but cluster to produce intermetallics that strongly embrittle the material.

2.6 Mechanical Properties of Neutron Irradiated Tungsten

As fission neutrons closely simulate the damage produced by fusion neutrons, it is important to examine previous work on neutron irradiated material. However, data on the mechanical properties of irradiated tungsten are scarce. As mentioned, the irradiation produces radioactive samples that must be tested in a hot cell, severely limiting the number and types of test that can be performed.

Hardness values of neutron irradiated tungsten have been measured in Japan[127, 130] (figure 2.12). While there is little data available with which to make a comparison, the values obtained represent a 50-100% increase in hardness after irradiation. Hasegawa's most recent work is a study of tungsten and tungsten-rhenium alloys.[131] This too contains some extremely high reported hardnesses: one sample of tungsten nearly doubling in hardness after an 800°C irradiation to only 0.98 dpa. This is an extremely large figure, as ion irradiated materials with similar damage levels show hardness increases of only ∼10%.[132, 133] Even if the data are accurate, more research is needed as indentation does not give any indication of the fracture behaviour of tungsten. The fracture stress and fracture toughness are the critical parameters in determining component lifetime, although not the sole factors: fatigue in particular will play an important role in determining component life.

Vickers hardnesses have been measured for pure tungsten and a W-0.5TiC alloy by Kurishita et al.[134] For neutron irradiation to a fluence of 2×10^{24} neutrons/m^2 at 600°C (0.03 dpa), pure tungsten exhibits an increase in hardness of 19%, much lower than the values from Tanno and Hasegawa above. No irradiation hardening is seen in the TiC-containing material and the void density, as measured by bright-field TEM, decreases significantly ($\sim 28 \times 10^3$ voids/μm^3 vs

125×10^3 voids/μm^3). The UFG material is also more resistant to 3 MeV helium irradiation. The critical fluence for exfoliation and surface cracking at 550°C is about 2×10^{22} He/m^2 for commercially available tungsten and above 2×10^{23} He/m^2 for UFG W-0.3TiC. The increase in radiation resistance due to an increase in sink density is well known, and is one of the major motivators in the development of ODS materials.

It is therefore unclear as to precisely the hardening effect neutron irradiation has on tungsten. Although the Japanese studies used to construct figure 2.12 and table 2.1 all show a hardening effect of >50%, this does not match with the data from Kurishita and ion irradiation. Fukada's work showing the hardness of unimplanted tungsten[135] determines a Vickers hardness value of ~400 (3.9 GPa). This is a high value for pure tungsten, which has a hardness of ~2.5 GPa for large indents.[136, 137] The sole paper that mentions the measurements of hardness[135] specifies an indentation load of 200g, corresponding to a depth of ~5.4 μm and therefore well outside the depths where a size-effect in the hardness would be seen.

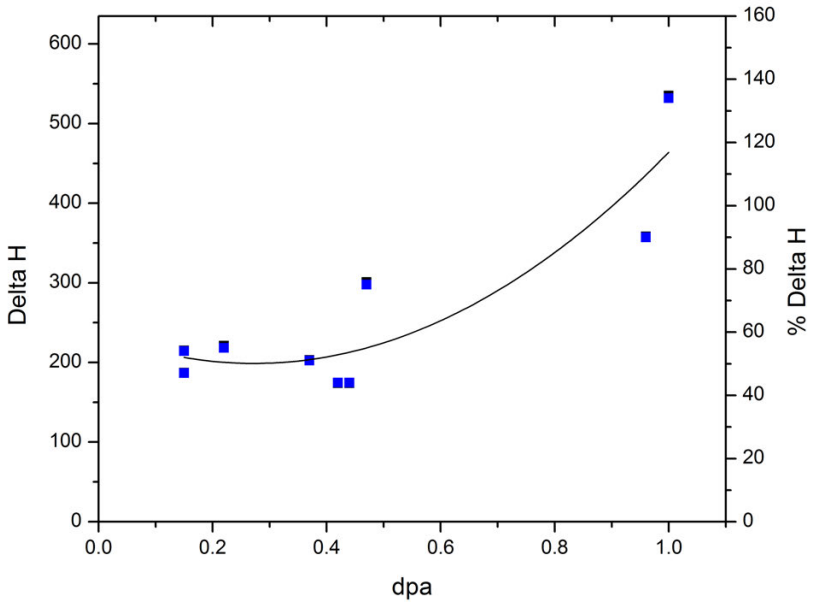

Figure 2.12: Change in hardness with dose for neutron-irradiated pure tungsten. Redrawn from:[130, 131, 135, 138] for pure tungsten irradiated at 500-800°C where the similar levels of vacancy mobility mean similar damage structures are produced. Specific references are given in table 2.1. A Vickers hardness value of 400 was used as the unirradiated value to calculate the percentage increase in hardness.[135]

dpa	ΔH	$\%\Delta H$	Irradiation Temperature (°C)	Reference
0.15	187	47	600	[135]
0.22	221	55	800	[135]
0.44	174	44	531	[135]
0.47	301	75	583	[135]
0.42	174	44	756	[135]
0.15	215	54	600	[138]
1.0	535	134	500	[138]
0.37	203	51	500	[130]
0.96	358	90	538	[130]
0.22	221	55	800	[131]
1.54	333	83	750	[131]
0.96	333	83	538	[131]
0.9	521	130	500	[131]
0.98	730	183	800	[131]

Table 2.1: Values used to construct figure 2.12.

Various authors have produced tensile tests of neutron irradiated tungsten.[36, 73, 139] Elongations of ∼0 were obtained for irradiations performed at 400°C and 500°C and fluences of 0.5-1.5×10^{26} neutrons/m^2 (<2 dpa). In comparison, unirradiated high-purity single crystals show elongations of 10-15% above 350°C,[140] and four-point bend tests on pure, single-crystal tungsten show plastic strains at fracture of up to 5%.[40] This demonstrates the severe degradation of properties radiation damage causes, emphasising the need to make initial components and materials as ductile as possible.

Krautwasser noted severe embrittlement in unnotched bend bars of tungsten irradiated at 300°C to a fluence of 0.5×10^{26} neutrons/m^2 (∼1 dpa),[141] with a shift in the BDTT of 13.7°C per 10^{24} neutrons/m^2 for fluences up to 5×10^{24}. If this trend continued, this would correspond to an overall shift of nearly 1400°C by 1 dpa. The rate of embrittlement was also found to be much more rapid in a W-10%Re alloy (31°C per 10^{24} neutrons). This is presumably due to the precipitation of intermetallic phases. As the bend bars were unnotched, it is not possible to extract a value of fracture toughness from these tests. Like the tensile tests above, this demonstrated the severe

embrittlement of tungsten under neutron irradiation.

Finally, Zinkle,[20] in his analysis of tungsten operating temperature windows states: 'Since mechanical properties data are not available for pure tungsten or its alloys irradiated at high temperatures, an accurate estimate of the DBTT versus irradiation temperature cannot be made. The minimum operating temperature which avoids severe radiation hardening embrittlement is expected to be 900-1000°C, scaling from the limited molybdenum alloy database.' This shows more data on the properties of neutron irradiated tungsten are critical.

2.7 Mechanical Properties of Ion Irradiated Tungsten

Ion irradiation has been used since 1970 to simulate the type of damage seen from neutron irradiation.[142] However, while neutrons typically penetrate several millimetres into a material, ions typically have a penetration depth between 100 nm and 10 μm, depending on atomic number and ion energy.[132] As such, there are very few mechanical property data from these studies, with the majority of research using TEM or atom probe tomography to investigate microstructural changes. Although recent advances in nanoindentation are beginning to allow mechanical properties of these damaged layers to be determined, nanoindentation will only determine material hardness and modulus rather than the full suite of mechanical properties.

With respect to tungsten, there are few published papers investigating the mechanical properties of ion irradiation. Of most relevance is the work by Armstrong[132,143] that covers the properties of W, W-5wt%Ta and W-5wt%Re after self-ion irradiation from 0.07 to 33 dpa at 300°C. The irradiations were carried out at the National Ion Beam Centre at the University of Surrey. The damaged layer was 300 nm thick, and therefore hardness and modulus data were determined using nanoindentation. By examining the differential of load-displacement^2 curves in unimplanted and ion-implanted material the depth at which the ion-implanted properties dominate could be determined. It was shown that the properties could be determined from depths of 100-200 nm, a significant difference from work on coatings that found indentation depths of 10% of the coating thickness were required.[144] Due to the thin depth of implanted material, no micromechanical tests incorporating plastic or fracture data could be carried out.

Armstrong saw that pure tungsten increases in hardness and saturates at 0.4 dpa, with a

hardness increase of 0.7-0.9 GPa (∼12%). This was backed up by TEM examination, showing no increase in dislocation loop density above 0.4 dpa. In the W-5Ta material, the hardness increased rapidly from 7.3 GPa to 8.8 GPa at 0.07 dpa, saturating at 11 GPa with damage levels of 13 dpa. No saturation was seen in the W-5Re material, with hardness increasing to 10.2 GPa at 33 dpa. Atom probe tomography was used in the W-5Re material, to show that at 13 dpa and above, clustering of the rhenium atoms in the material is observed; a precursor to σ-phase formation. As noted by the authors, it is unclear why the tantalum-alloyed material reaches higher values of hardness. The phase diagram for the system predicts full solid solubility across the entire composition range, and atom probe tomography did not show any atomic clustering.[145] Despite this, the work gives very strong evidence that the hardening of tungsten and its alloys after irradiation is due to a combination of dislocation loop formation and atomic clustering leading to precipitate formation.

Work on an ODS tungsten alloy (W-2Y_2O_3) by Battabya[146] can be compared with Armstrong's work[120] as they both assess a saturated, heavy-ion irradiated sample (5 dpa and 13 dpa respectively) with low helium levels (75 vs 300 appm respectively). Armstrong measured a hardness increase of 30%, while Battabya measures 15%. Although this may be an artefact of simultaneous (Battabya) vs sequential (Armstrong) irradiation, it is probable that the presence of ODS particles reduced the hardening effect of radiation damage, as with ODS steels and neutron-irradiated tungsten.[134]

Battabya has also compared ion-irradiated pure tungsten and W-2Y_2O_3 irradiated with self-ions at JANNuS.[147] Radiation loops are present in the tungsten grains whereas in yttria particles, radiation-induced damage appeared as voids. This means the particles are acting for vacancy sinks as expected. Berkovich hardness values are slightly higher for unirradiated ODS-W (4.8 vs 4.5 GPa). After irradiation at 300°C or 700°C, the hardness of both samples was 5.5 GPa. However, Battabya carried out the indents under a load of 1 N that resulted in indent depths of 2.8 μm, i.e. the depth of irradiated layer. This is not a valid method for the testing of irradiated layers: Armstrong[143] showed that hardnesses measured at these depths are dominated by the unimplanted substrate.

In his most recent work, Armstrong showed the importance of microstructure as radiation damage sinks in self-ion irradiated tungsten.[148] He compared the hardness of rolled or annealed W-5wt%Re sheet from 0.07 to 13 dpa. Hardening is seen to saturate in the rolled material at

0.4 dpa. In the annealed material, the relative hardness change is over four times higher and saturation does not occur by 13 dpa. This is attributed to the increased number of dislocations in the nanostructured, rolled material that allow for the recombination of vacancies without the formation of dislocation loops.

Arsenlis et al. used dislocation dynamics modelling in BCC iron to show a transition from homogenous deformation to highly localised plastic flow creating dislocation free channels.[149] This occurs at a loop density above 8.15×10^{21} m^{-3}. Comparing with Armstrong's work,[143] this roughly corresponds to a damage level of 0.5 dpa. This result has important implications: if the damage levels are directly applicable to tungsten then it means that slip will be highly localised throughout most of the reactor operation.

2.8 Mechanical Properties of Helium Irradiated Tungsten

Helium implanted in the material will be present in the form of helium-vacancy complexes or helium bubbles. These will act to inhibit dislocation glide, strongly influencing the mechanical properties of tungsten.

Much of the work present in the literature involves exposing tungsten to extremely high levels of helium - much higher than components will see during operating conditions. Similarly, much of the work only considers helium implantation at very low energies and does not consider the increased trapping seen in defects caused by neutron or heavy ions irradiation.[150–153] Therefore, relevant work will involve studies of both helium implantation and microstructural damage, with helium levels consisting of approximately 10 appm per dpa.[14] This corresponds to ∼150 appm after five years of operation.

It is currently unknown whether there is a difference between simultaneous irradiation and helium implantation of pre-damaged materials. There is also little on the effect of helium on the mechanical properties of tungsten. Armstrong showed the potent hardening effect of helium and its interaction with defects generated in self-ion irradiation.[143] However, this work only considers the interaction of defects sequentially, not simultaneously as in fusion systems. Additionally, the irradiations were performed at 300°C, below the 450-500°C at which vacancy migration becomes significant enough to affect damage formation.[79, 116]

Beck carried out an implantation of 3000 appm helium into high purity tungsten, W-Ta and W-Re alloys and measured the increased hardnesses with nanoindentation.[154] Significant changes in hardness are seen: a 107% increase in pure tungsten and 88% and 92% in the W-5wt%Ta and W-5wt%Re samples respectively. TEM micrographs show no helium bubbles are present in the material, suggesting the implanted helium is trapped in small helium-vacancy clusters below the resolution limit of the TEM. This work also records an apparent increase in modulus of the materials after implantation of ∼20%. This is unusual, as the presence of implanted helium should not affect the elastic modulus of a material.[119] The only recorded influence of irradiation on elastic modulus is work by Thompson on copper[155] that only results in a 2% increase. It is likely that this is an error due a change in pile-up around the nanoindenter tip resulting in an incorrect calculation of the contact area during indentation. Although the actual increases in hardness should be lower, even a 20% reduction of the determined increases still represents a very strong hardening effect from the implanted helium.

Oi[156] investigated helium irradiation of tungsten using nanoindentation and positron-annihilation spectroscopy. They show a slight increase in the hardening effect of helium at 600°C compared to room temperature. The PAS shows that at 600°C, large He_nV_m complexes are formed with a low helium-vacancy ratio (i.e. $m >> n$). At room temperature, small vacancy clusters with a large amount of helium are formed and are preferentially found at pre-existing defects. This is as expected, the higher irradiation temperature generates and allows the diffusion of vacancies that are known to be strongly bound by helium.

Liu et al. have attempted to model from first-principles a tensile test for pure tungsten and for tungsten with a single helium atom impurity (figure 2.13). They determine the ideal UTS of tungsten along the [001] direction is 29.1 GPa, falling to 28.2 GPa with the presence of a helium atom - a difference of 3.1%.[104] This value is extremely high, and unlike the previously discussed work in section 2.4.2, the authors determine that the most stable site for the helium atom is a substitutional site. They subsequently conduct the tensile test with the helium atom in this position. This may explain why experimental results discussed above - a significant hardening effect[143, 154, 156] - contradict this prediction.

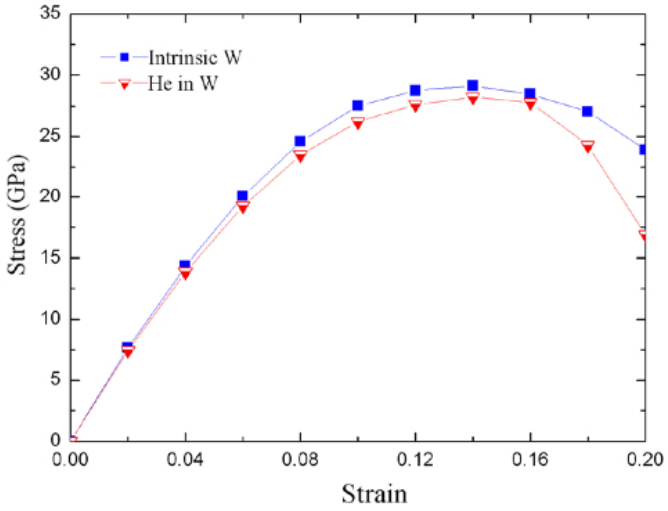

Figure 2.13: Stress-strain curve for a modelled tensile test of tungsten in the [001] direction with and without the presence of a single helium atom. The presence of the helium produces a softening in the material, unlike experimentally-observed hardening.[104]

2.9 Ions vs Neutrons

As ion or neutron irradiation are the only methods for forming damaged microstructures in tungsten, it is prudent to compare how well the ions represent neutrons. As discussed in section 2.4.2, deuterium retention has been compared by two authors in ion-irradiated and neutron-irradiated tungsten.[86, 123] Both show that the TDS spectra from the neutron-irradiated material does not match that from the ion-irradiated material.

However, with regards to changes in the microstructure, Tanigawa[157] showed that in reduced-activation ferritic-martensitic steels, the size distribution of precipitates 'changed by ion irradiation just the same as it was observed in neutron irradiated RAFs.' This seems reasonable, as the method of damage formation - the creation of high-energy primary knock on atoms - is similar in both cases. These data are also promising as the microstructure will have a direct effect on the mechanical properties of the materials.

It is possible that the difference in deuterium retention comes from a change in dose rate, and hence data comparing the effects of dose rate are crucial. In some ion irradiated systems - Fe-Cr and SiC - the indentation hardness has been shown to vary with dose rate.[76, 88] However, for pure

iron[76] dose rate effects are not seen. Irradiation at 300°C produces an increase in hardness of 0.75 GPa at a dose rate of 6×10^{-4} dpa/s and 3×10^{-5} dpa/s. At 400°C and 500°C, there was no measured irradiation hardening, indicating the radiation-induced defects annihilate by recombination at and above 400°C. A dose-rate effect is seen in the Fe-Cr samples, indicating that the dose-rate effect is due to elemental clustering rather than changes in loop structure or density.

Nevertheless, the difference in these tests was only a factor of twenty; in a fusion reactor rates are up to six orders of magnitude slower than typical ion irradiation rates. Thus, it is probably that ion irradiation cannot be extrapolated directly to determine the mechanical properties of neutron irradiated materials. However, it is still a useful tool for two reasons: firstly, it provides a method to assess the underlying mechanisms of radiation damage in materials. Secondly, as fission irradiation campaigns are not widely available, it provides the only alternative method of producing a radiation-damaged microstructure.

2.10 Tungsten Irradiation Summary

Tungsten and its alloys embrittle strongly under irradiation. Although hardness levels are seen to saturate under ion irradiation, the transmutation elements produced under neutron irradiation show clustering that continues to increase with damage, producing increased levels of embrittlement. Additionally, helium has been shown to have a potent hardening effect on tungsten materials.

Due to the low transmutation rate of tungsten, helium will almost solely be present as a result of implantation from the plasma. While many exotic structures exist for high helium fluxes ($> 10^{19}$ ions/m^2), expected helium levels are much lower than this (10 appm per dpa, 150 appm after five years) and hence embrittlement from dislocation pinning is the expected behaviour.

Hydrogen is weakly trapped in tungsten, and is therefore expected to desorb at relatively low temperatures (<500°C). It is unlikely to have a significant effect on the mechanical properties of tungsten, however care must be taken as radiation swelling of vanadium has shown a synergistic effect when hydrogen and helium are co-implanted.

There are very few data from neutron irradiated tungsten. Some basic, but inconsistent data exist up to 1 dpa, but no measurements of fracture toughness, BDTT or strain-rate dependence have been measured on these or any higher-dpa samples where clustering of transmutation elements

may be important.

There also exists the ongoing question as to how well ion-irradiated materials relate to neutron irradiated ones. Nevertheless, ion-irradiation remains a useful tool for analysing the fundamental mechanisms behind radiation damage.

2.11 Micromechanical Testing

Regardless of the irradiation conditions - ion or neutron - small-scale testing will be required. For neutron-irradiated materials, there is a desire to limit the volume of material tested to reduce radioactive limits. For ion irradiation, only shallow damaged layers are produced. As such, it will always be necessary to employ specialist techniques in order to extract data from the damaged region. The recent developments in focussed ion beam systems have allowed a significant advancement in small-scale testing. Test pieces can be fabricated with geometries that allow testing in compression,[158,159] bending[160–163] and tension.[164] Compressive techniques, typically the compression of micro-pillars, have been used for a number of years to investigate the effects of scale[158] and FIB damage.[165,166] However, the technique is difficult to use to extract mechanical properties due to strong substrate effects[158] and the lack of fracture events. It is therefore of little relevance to the project.

Tensile techniques have been performed by Kiener et al. on copper samples.[164] A FIB was used to produce micro-tensile specimens 0.5-8 μm long, which were subsequently tested using a micro-indenter mounted inside an SEM using specially adapted micromanipulater grippers. This technique provides an interesting method to investigate small-scale deformation behaviour, and is capable of extracting all the relevant mechanical properties. However, the fabrication of samples is extremely complicated and time-consuming. Similarly, the testing is complex and requires equipment that is not routinely available. Other techniques - namely cantilever testing - may allow the same level of mechanical analysis in a much less complicated test environment, and hence micro-tensile testing is not a technique that will be used in this project.

Micro-cantilever tests have been shown to produce data in good agreement with bulk measurements for elastic,[72,167] plastic[162] and fracture properties[168–170] of materials. As tungsten cannot be easily etched using lithographic methods, it is necessary to use a focussed ion beam (FIB) in

order to manufacture micro-cantilevers. In much of the work, simple beam theory has been used to convert load-displacement data into stress-strain data. As the cantilevers are attached to a bulk of identical material, the 'fixed' end is not truly fixed and stress fields propagate into the bulk areas. This leads to calculated values of modulus ∼10% lower than true values.[72] Finite element modelling can be used to account for these erroneous assumptions, producing values much closer to literature data.

The biggest drawback to micro-cantilever testing is the instrument time required to produce and test specimens. It is therefore not practical to apply this technique to a wide variety of materials and irradiation conditions. Nanoindentation - while only producing values of hardness and modulus - is a very rapid and simple technique. It can therefore be used to determine 'interesting' samples after irradiation that can subsequently be analysed in more detail using cantilevers, examples of which are shown in figure 2.14.

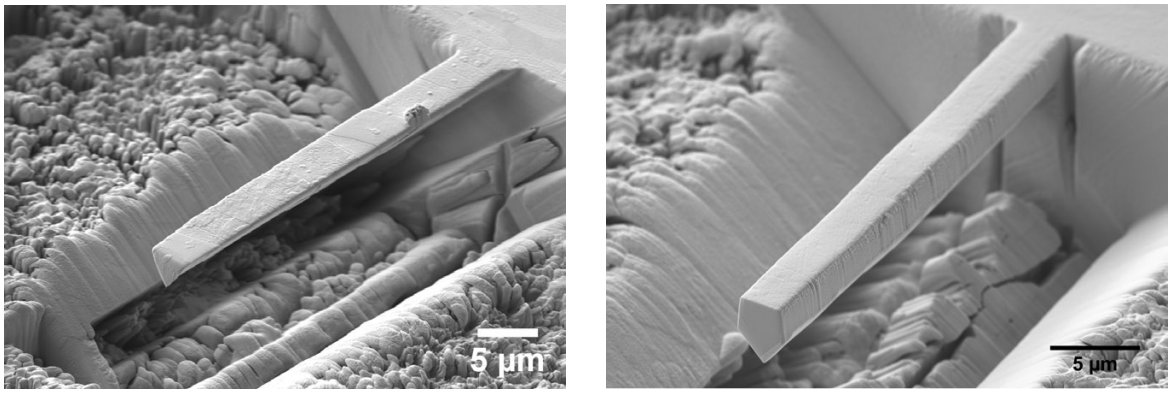

(a) Triangular beam for elastic-plastic tests. (b) Pentagonal beam for fracture tests.

Figure 2.14: Typical micro-cantilevers produced by FIB-machining.

2.11.1 Nanoindentation

Hardness testing is a standard technique for determining the mechanical properties of materials, and has been used for many years via Brinell[171] and Vickers[172] indentation. These methods rely on measuring the residual impression from a well-defined tip driven into the surface of a material at a given force. In order to accurately determine the size of these indents they must be larger than a few tens of microns, thereby limiting the size or depth of features that can be measured.

The alternative - using SEM imaging to accurately determine indent area - removes the speed and simplicity of the technique.

Nanoindentation is a fundamentally similar technique, involving the penetration of a sharp tip into a material in order to determine mechanical data. Initially, a modified micro-hardness tester was used[173] in order to study nitrogen implantation into stainless steel. Currently there are many available commercial nanoindentation systems (e.g. from Keysight, MicroMaterials and Hysitron), with recent developments allowing testing to be carried out from cryogenic temperatures up to ~700°C with continuous measurements of load, modulus and hardness with depth.[174] The use of unloading measurements allow elastic properties to be measured, and time-dependent properties such as creep can be determined by the use of continuous-load segments.

However, there still exists a significant problem with indentation-based measurements. The shape and size of the elastic and plastic zones around the nanoindenter tip are very complex.[175] They vary with local crystallography,[176] indenter shape[177] and contact area.[171] This means it is only possible to measure hardness and elastic modulus using nanoindentation, both of which require some estimation based on empirical observation explained below.[178] In particular, the yield stress is very difficult to measure due to the complex stress fields around a sharp tip. A spherical tip can be used to evaluate values of yield stress,[179] however the stress-strain behaviour is very different and comparisons with uniaxial values are difficult. Values of fracture toughness can theoretically be determined for very brittle materials, such as amorphous carbon.[180] However, in these tests the measured values of 10 MPa$\sqrt{m}$ were not in good agreement with literature values of 5-6 MPa$\sqrt{m}$ due to the unknown development of sub-surface cracks.

In order to understand the limitations of nanoindentation as a technique, it is necessary to review the methods by which values are determined. A typical load-displacement curve is given in figure 2.15. The most widely used method for data analysis is the Oliver and Pharr method.[178] This relies on three key parameters: the maximum load (P_{max}), the depth at the maximum load (h_{max}) and the initial unloading contact stiffness ($S = \frac{dP}{dh}$) (figure 2.15).

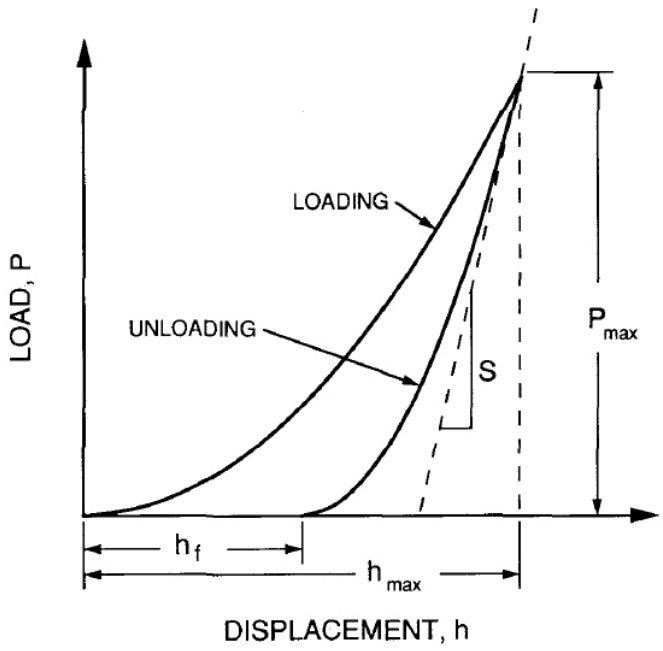

Figure 2.15: Typical load-displacement curve obtained via nanoindentation.[178]

During indentation, the measured displacement is a combination of the elastic and plastic deformation of the material under the indenter. During the unloading segment of the curve the elastic deformation relaxes, and an empirical equation can be fitted to the curve at this point. Oliver and Pharr[178] show, using experimental data, that this equation is a power law given by:

$$P = B(h - h_f)^m \tag{2.11.1}$$

where B and m are the empirical constants, with m lying between 1.2 and 1.6.[178] P, h and h_f are shown in figure 2.15.

To calculate the unloading contact stiffness, S, equation 2.11.1 is differentiated and P_{max} and h_{max} are substituted.

$$S = \frac{dP}{dh} = \beta \frac{2}{\sqrt{\pi}} E_r \sqrt{A} \tag{2.11.2}$$

β is a dimensionless parameter based on the indenter tip, A is the projected area of elastic contact and E_r is the reduced modulus given by:

$$\frac{1}{E_r} = \frac{1-\nu^2}{E} + \frac{1-\nu_i^2}{E_i} \tag{2.11.3}$$

where E and ν and the Young's modulus and Poisson's ratio, respectively, of the specimen and E_i and ν_i are those of the indenter.

The elastic modulus of the specimen can therefore be calculated if the contact area at maximum indentation can be measured. The Oliver and Pharr approach assumes that this area can be related to the indentation depth via an area function. This area function is known for tips of specific geometry, such as a typical Berkovich indenter. A more accurate result can be made by treating the total measured compliance as the sum of sample and indenter compliance. The indenter compliance is then accounted for by fitting of experimental results of deep indents in soft materials.

As this approach requires no imaging of the indents produced, it allows very rapid processing of experimental data and is the standard method included in many commercial nanoindenter systems. However, as shown above, this method relies on many empirical data-fitting steps. It also does not account of the 'pile-up' of material around the indenter tip. This is a common effect in elastic-plastic materials[178] and results in an increase in the contact area and a subsequent overestimation of hardness and modulus.

A secondary consideration is that this method assumes elastic isotropy, which is not the case for most materials. Fortunately, tungsten does not show significant deviation from isotropic behaviour,[181] and additionally often has a fine grain size due to the powder manufacturing routes. This means that many grains will be sampled by the elastic strain field during deformation, resulting in an averaging of the elastic response of the sample. The field has a radius of approximately seven times the indent depth.[182]

In summary, nanoindentation is a quick and simple way to generate reasonably accurate values for elastic properties. However, the technique relies on several empirical assumptions and does not generate data on the true yield stress or fracture properties of materials. It is therefore insufficient for a complete analysis of the mechanical properties of tungsten after irradiation.

2.11.2 High Temperature Nanoindentation

High temperature nanoindentation is a recent addition to the micro-mechanical testing toolbox. While high temperature hardness tests have been carried out since 1953,[183] the first publication of nanoindentation at elevated temperature was not until 1996[184] on silicon at 600°C.

A selection of published work on high temperature nanoindentation is detailed in table 2.2. The majority of work is carried out in air at temperatures below 400°C on non-oxidising materials. The testing of an iron-aluminide[185] resulted in significant surface oxidation. Not only does tungsten oxidise strongly above ∼300°C, these temperatures are not particularly relevant for the operating temperatures of a fusion reactor. As such, testing in vacuum at higher temperatures is required.

Year	Material	T_{max}	Reference
2003	Iron-Aluminide	400°C	[185]
2004	Platinum	200°C	[186]
2006	Fused Silica	400°C	[174]
2007	Gold Metallic Glass	140°C	[187]
2008	Nickel Superalloy	400°C	[188]
2008	Nickel Superalloy	400°C	[189]
2009	Aluminium	115°C	[190]
2009	Silicon	150°C	[191]
2010	Fused Silica and Copper	500°C	[192]
2011	Fused Silica and Gold	300°C	[184]
2012	Steel	250°C	[193]
2012	Al-SiC Multilayers	300°C	[194]
2012	Gold and Nickel	665°C	[195]
2013	Nanocrystalline Nickel	300°C	[196]
2013	Ni-10Pd	400°C	[197]

Table 2.2: High temperature nanoindentation data reported in the literature, ordered by year published.

Of the work detailed in table 2.2, only the work by Trenkle[192] and Korte[195] was carried out in vacuum. Trenkle's work demonstrates the further difficulty of extending high-temperature nanoindentation into vacuum, measuring thermal drift rates of 37 nm/s on copper at 300°C. Drift as high as this does not allow accurate determination of material properties. For comparison, rates of <0.05 nm/s are typical at room temperature, and <0.15 nm/s at elevated temperature.[184]

Korte et al. have carried out indentation experiments into gold and a single crystal Ni-superalloy in vacuum. Instead of a standard Berkovich indenter, a flat punch was used. Although this did

not allow measurements of hardness to be obtained, the authors state it represents 'a worst case scenario' for thermal drift due to the 'much more rapid increase in cross section at the beginning of the experiment, compared with the steady increase in pyramidal indentation'. Despite this, drift rates of -0.25 nm/s and 0.26 nm/s were measured before and after the experiment, respectively. Given the temperature of 665°C, these represent the lowest drift rates (where the authors provide the data) obtained so far during high-temperature nanoindentation in vacuum or atmosphere.

2.11.3 Micro-Cantilever Testing

As shown, nanoindentation data does not provide a complete characterisation of the mechanical properties of irradiated layers. Micro-cantilevers are likely the best geometry to use for this, but it is necessary to examine the extent they can be used and how applicable the results are to reactor-scale behaviour. Cantilevers typically have two geometries: triangular and pentagonal cross-sections, which are used for elastic-plastic tests and fracture tests respectively.

Elastic Behaviour

Armstrong's work measuring anisotropy in the Young's modulus of polycrystalline copper[72] demonstrates the validity of micro-cantilevers in investigating elastic properties. Nine measurements of modulus with crystal orientation were detailed, all of which lie in the range of values for single-crystal data reported in the literature. Not only does this demonstrate numerical validity, it shows that individual grains in a polycrystalline material can be examined using micro-mechanical methods in order to determine single-crystal data.

This work also demonstrated several methods that attempt to account for the non-static 'fixed' end of the cantilever. Armstrong showed that the flexure of the fixed end scales with L^2, where L is the distance from the fixed end to the loading point. The deflection given by simple beam theory scales as L^3, and therefore dominates for longer cantilevers. It was found that the L^3 term dominates for aspect ratios greater than six. Armstrong also showed that for cantilevers tested by a single indentation, the calculated modulus from the loading curve was 6% lower than that determined from the unloading curve. This was due to the embedding of the tip into the cantilever.

Gong and Wilkinson[162] further developed this technique by deflecting their cantilevers a second time within the elastic limit. They found that on the second indentation the difference between the

loading and unloading moduli was only 0.3%. Using a series of indents towards the fixed end of the cantilever, modulus values of 125, 122 and 117 GPa were calculated using simple beam theory. By using an FE model to capture the majority of the beam flexure - the authors specify '99%' - these data produced values of 132, 132 and 130 GPa. This reduction in scatter, and closer agreement with literature data, demonstrates that FE modelling is essential in producing quantitative data as even for aspect ratios greater than six the bulk deflections result in an underestimation of modulus of 5%.

Plastic Behaviour

There are very few data regarding plasticity measurements using micro-cantilevers. Motz et al. used micro-cantilevers to measure the size-dependence of the flow stress in copper.[160] They found that as the cantilever thickness increased, the flow stress tended to 260 MPa, very close to the value obtained from their macroscopic sample of 227 MPa. However, both these values are extremely high for single crystal copper, with typical values of 10-50 MPa more commonly reported.[198–200]

While it is difficult to explain why the macroscopic value is so high, it is not unusual for the plasticity of small-scale samples to be increased compared to bulk-scale specimens. Firstly, it is possible that a dislocation starvation effect occurs due to the high surface area to volume ratio.[201] Secondly, plastic strain gradients in materials are accommodated by geometrically necessary dislocations (GNDs), dislocations that are necessary to support the curvature in the crystal lattice. As the beam thickness decreases, the resultant reduction in dislocation sources results in dislocations being confined to fewer glide planes. The average distance from these sources to the neutral axis of the bending beam decreases, leading to more frequent pile-ups and a resultant rise in the flow stress due to work hardening. Dislocation dynamics modelling[162] in titanium confirms this, and agrees well with the observed variation in yield stress with $\frac{1}{\text{Beam Thickness}}$. The values of flow stress do not reach their bulk values until the beam is nearly $8\mu m$ thick - much thicker than it is possible to create using ion implantation techniques. Therefore it will be necessary to account for these size effects in the cantilevers in order to calculate bulk properties.

Finally, Gong et al. have investigated the critical resolved shear stress of prismatic slip in titanium.[162] The FIB-machined cantilevers in this work closely followed Schmidt's law, and values of the critical resolved shear stress were well described by a work-hardening power law again based

upon dislocation pile-up at the neutral axis of the cantilever. Due to the triangular cross-section of the cantilevers used, leading to plasticity initiating at the bottom corner of the triangle, the flow stress in this work varies with $\frac{1}{(\text{Beam Thickness})^{1.1}}$.

Fracture Behaviour

The initial use of cantilevers to investigate fracture behaviour was conducted by Di Maio and Roberts to measure the fracture toughness of a thin WC coating.[168] They manufactured a cantilever with a pentagonal cross-section, with a sharp pre-notch milled near the fixed end. In order to validate the method, the same technique was applied to silicon. They tested four cantilevers, and determined an average fracture toughness of 1.1 MPa$\sqrt{m}$, in close agreement with literature values of 0.83-0.95 MPa$\sqrt{m}$. The authors attributed the extra toughness due to an extra load needed 'to nucleate a sharp crack at the bottom of the notch'.

Massel also used pentagonal micro-cantilevers to measure the fracture toughness of TiN films,[202] measuring a fracture toughness of 2.6 ± 0.3 MPa$\sqrt{m}$, in excellent agreement with bulk values of 2.3-2.7 MPa$\sqrt{m}$. These results showed that the fracture of micro-cantilevers produced quantitative results in very close agreement with bulk data.

Armstrong also used these cantilevers to measure the fracture toughness of grain boundaries in bismuth embrittled copper.[203] EBSD was used to locate grain boundaries with a specific orientation, and cantilevers milled along these boundaries. The small specimen size resulted in yield over fracture, meaning that only weak grain boundaries could be analysed.

Wurster et al. have demonstrated an important result in their comparison of naturally cracked cantilevers and cantilevers notched using a FIB. They note 'that the essential fracture behaviour of such micro samples is not significantly affected by the FIB-notching [using currents of 50 pA to 100 pA]'.[201] This significantly simplifies the manufacturing process as samples can be notched in the FIB once manufacture is complete.

However, there is evidence that the toughness of materials increases with decreasing specimen size.[204] As for the 'smaller is stronger' observation in plasticity measurements, this is due to increased dislocation density with decreasing specimen size. If the dislocations act to shield the crack tip - i.e. reduce the effective stress intensity at the crack tip below that due to the applied

stress on the sample - then the increased number of dislocations per unit volume in small-scale testing will increase the measured fracture toughness value.

It is important to note the fracture toughnesses measured above are all lower than the fracture toughness of tungsten (~10 MPa$\sqrt{m}$). Irwin's estimate of plastic zone size is given by:[205]

$$r_y = \frac{1}{2\pi}\left(\frac{K}{\sigma_y}\right)^2 \tag{2.11.4}$$

For tungsten, using a value of 10 MPa$\sqrt{m}$ for K[40,54] and 1.25 GPa for σ_y,[206] r_y comes out to 10 μm. This is much larger than the depth of most ion-irradiation damaged layers and typical cantilever sizes, hence fracture may not be seen unless the material is significantly embrittled.

2.11.4 Small-Scale Considerations

It is clear that micro-mechanical testing techniques, particularly the testing of micro-cantilevers, can be a useful technique for determining the mechanical response of materials on the micro-scale. However, there are clear size effects present in the work studied. Due to the general rule of 'smaller is stronger', these effects must be accounted for when examining engineering materials as failure to do so would lead to a dangerous overestimation of the strength of a material. It is also necessary to show that the techniques used to manufacture small-scale specimens do not introduce any systematic error.

Size Effects

In nanoindentation experiments, it is common to see the 'indentation size effect' shown in figure 2.16. This manifests itself through an increase in the measured hardness at shallow indent depths, typically below 300 nm.[158,207–209] In nanoindentation studies of tungsten,[210] the apparent hardness is seen to increase below 2 μm, and becomes significantly higher below 1 μm. These large depths are unusual, and it is likely that this early effect is due to a blunt, poorly characterised tip.

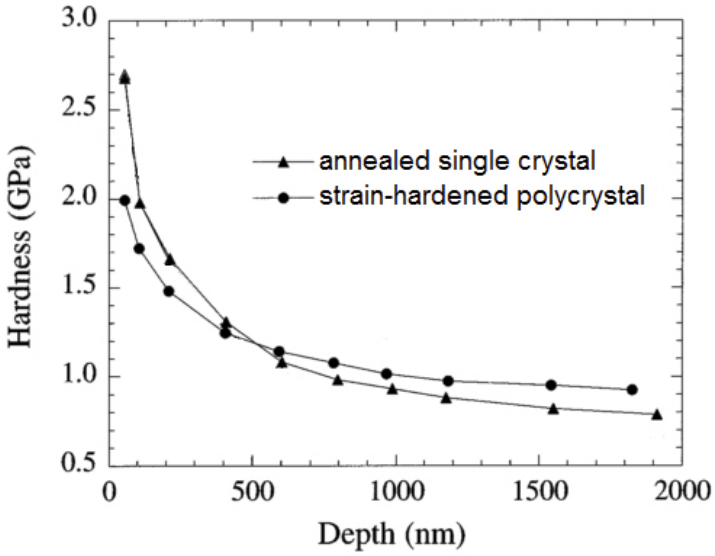

Figure 2.16: Indentation size effect in copper seen by McElhaney et al. The apparent strength of the copper significantly increases below 750 nm.[211]

The indentation size effect is described as Nix and Gao[208] as occurring because the density of geometrically necessary dislocations under an indent is proportional to d^{-1}, where d is the diameter of the indent. Therefore, as the indent depth decreases, so too does the indent diameter; this increases the dislocation density, which therefore increases the measured hardness via work hardening.

This model begins using the Taylor relation, relating the flow stress (σ) to the square root of the dislocation density:

$$\sigma = \sqrt{3}\alpha G b \sqrt{\rho_T} \tag{2.11.5}$$

Where α is the Taylor factor (varying between 0.1 and 0.5), G is the shear modulus, b is the Burger's vector and ρ_T is the total dislocation density, i.e. the sum of the GND density (ρ_G) and the statistically stored dislocation density (ρ_S).

The model assumes that all the GNDs are located in a hemispherical region with a radius equal to the radius of the contact area, and therefore ρ_G is given by:

$$\rho_G = \frac{3\tan^2\theta}{2bh} \tag{2.11.6}$$

Therefore, through simple substitution the depth-dependent hardness of a material varies as:

$$\begin{aligned} H &= H_0\sqrt{1+\frac{h^*}{h}} \\ H_0 &= 3\sqrt{3}\alpha G b\sqrt{\rho_S} \\ h^* &= \frac{3\tan^2\sigma}{2b\rho_S} \end{aligned} \tag{2.11.7}$$

H_0 is the macroscopic hardness and h^* is the length scale below which hardness appreciably increases.[212] This model has been shown to break down at very shallow indent depths in copper, iridium and magnesium oxide,[211, 212] as shown in figure 2.17. This is most likely because at very small plastic zone sizes (below ∼150 nm), the mutual repulsion from the stress fields around similar dislocations prevents the plastic zone from contracting further. This causes the model to overestimate hardness for these small indents. The Nix-Gao model also does not fully capture the behaviour of dislocations. As a continuum model, it does not account for the formation of dislocation cells and networks that are created during deformation. It also fails to account for stochastic 'pop-in' events seen during the early stages of nanoindentation, where dislocation sources are homogeneously nucleated due to the extremely high stresses under the indenter tip. Despite this, for reasonably-sized indents the model allows the extraction of bulk, macro-scale values of hardness from nanoindentation experiments. When looking at radiation-damaged microstructures where both damage and size effects contribute to hardening, it is important to note that the Nix-Gao law is a multiplicative increase in the measured hardness and the size effect hardening cannot simply be subtracted from the measured result.

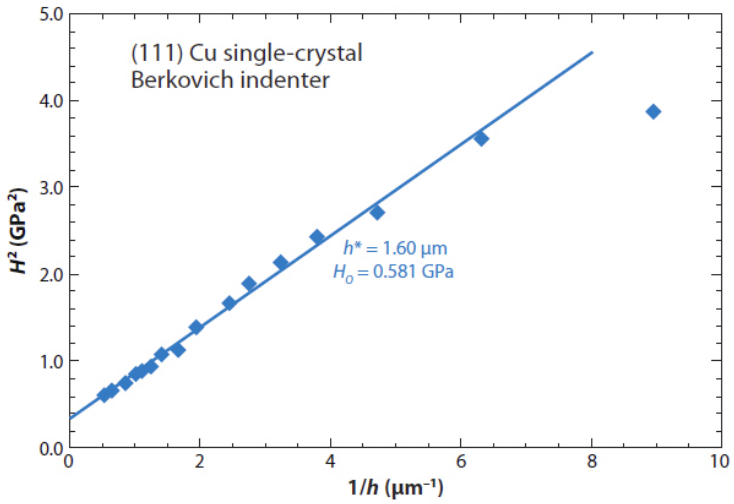

Figure 2.17: At shallow indent depths (high values of $\frac{1}{h}$), the Nix-Gao model breaks down and overestimates the value of hardness (H). Plot taken from McElhaney et al.[211]

In microcantilever experiments, a size effect is also seen when the thickness of a cantilever is reduced to the order of one micron. This has been shown in many systems via modelling using strain-gradient theory[213] and experimental work in thin films[214,215] and epoxy micro-cantilevers.[216] It is interesting that size effects manifest themselves in the epoxy cantilevers that will not contain dislocations. The size effect present in this work is simply due to the strain gradients that are present within the bent beams. This demonstrates that there can be multiple factors - obstacle density, strain gradients, dislocation source density - influencing the size effect in mechanical tests. As a universal size effect law accounting for these factors does not exist, size effects must be examined on a per-method, per-material basis.

Haque et al. determined a characteristic length scale of 4.5 μm for thin aluminium films,[217] which the authors note 'is similar to the values for copper and nickel reported in the literature.' As the possible size of ion-implanted layers is of the order of three micrometers, these size effects will have to be accounted for during experimental data analysis.

Size effects vary with temperature, shown in LiF nanopillars.[218] Due to the different components of plasticity - 'the lattice resistance, the forest hardening; and the size-dependent contribution as a result of the operation of single-arm dislocation sources' - that have different temperature variations, a size effect manifested at high (250°C) temperature that was not present at room

temperature.

Strain-Rate Sensitivity (SRS)

TEM of helium-implanted tungsten does not show any visible bubbles in the material,[154] and atom probe tomography is ineffective in detecting light elements. As such, other methods of determining the damage structure within the material are necessary. The strain-rate sensitivity of a material - how the measured hardness changes with strain-rate - can be used to determine an 'activation volume'. This volume is characteristic of the deformation process, and hence the damage structure of the material.

This has been carried out via α-particle irradiation of nanocrystalline Ni.[219] Irradiation to levels of 0.1 dpa produces dislocation loops and dislocation networks, thereby reducing the domain size. This produces an increase in hardness from 2.8 to 3.6 GPa and a corresponding increase in strain-rate sensitivity, m, from 0.03 to 0.13 and decrease in the activation volume, V, from 30 b^3 to 7 b^3, where b is the Burgers' vector.

In nanoindentation, the strain-rate sensitivity, m, is given by:[220]

$$m = \frac{d(ln\ H)}{d(ln\ \dot{\epsilon}_{indentation})} \tag{2.11.8}$$

m can also be written as:[221]

$$m = \frac{3\sqrt{3}kT}{V \cdot H} \tag{2.11.9}$$

Where k is the Boltzmann constant, T the absolute temperature and V the activation volume for plastic deformation.

Strain-rate sensitivity can be determined in indentation by constant-load nanoindentation,[222] tests at multiple strain rates[223] and strain-rate jump tests.[224] Multiple authors[221,222] note the importance of minimising drift during indentation. In nanocrystalline nickel,[221] drift accounts for a change in the SRS factor from 0.019 to 0.052 - a difference of 270%. In constant load nanoindentation,[222] high loads - therefore short test times - produce low drift rates (<0.05 nm/s) that match constant strain-rate data well. As the constant load produces a constantly changing strain rate, m can be determined from a single indent.

Although not determined via nanoindentation, m has been shown to change with temperature, increasing from 0.03 to 0.15 from room temperature to 300°C in nanocrystalline nickel foils.[196] This was attributed to thermally-activated deformation mechanisms.

However, the indentation size effect makes it difficult to study radiation damaged layers. Connolly,[225] in a study of ODS-steels, was not able to study the strain rate sensitivity of the materials due to size effects that were present in shallow indents despite the unirradiated condition.

FIB Damage

A concern when conducting tests using FIB-milled specimens is the effect of gallium damage. This effect has been investigated using compression of micro-pillars.[165, 166] Bei and Shim compared FIB-machined micro-pillars to 'virgin' pillars created through chemical methods, producing a pillar that was free from damage. They found that the pillars free from damage had strengths very close to their theoretical strength, however FIB-produced pillars had yield strengths around ten times lower: 0.85 GPa compared with 9.2 GPa. This work showed that one effect of the beam is to introduce many dislocation sources into the pillar.

As a major effect of irradiation is to introduce dislocations in the material - indeed this is one of the causes of irradiation hardening - it is unlikely that any gallium damage will significantly alter the mechanical behaviour of irradiated tungsten. Additionally, as the critical dimension of cantilevers is greater than that of pillars, it is unlikely that FIB damage contributes greatly to the mechanical properties of the beam.[226]

A second effect of FIB damage was seen in the initial work by McCarthy.[227] It was found that when a pure silicon cantilever was thinned to less than 0.3 μm, deflection of the cantilever occurred. Although the specific beam conditions are not given in the paper, typical beam values (>100 nA at 30 keV) result in an amorphous damaged layer of 30 nm,[164] i.e. 10% of the cantilever thickness, and this could, in principle, result in a residual stress large enough to produce the observed deflection.

Recently, Maass et al. investigated Au micropillars by in-situ Laue diffraction and found that FIB milling introduced strain gradients in small (<2 μm) pillars, which activated plastic deformation on a geometrically hard slip system during compression. A larger (10 μm) pillar showed less streaking in the Laue spots (implying a smaller strain gradient) and deformed on the geometrically expected (softer) slip system.[228]

Hütsch[229] prepared microcompression specimens in magnesium using lathe and annular milled pillars. Lathe milling involves making a large diameter pre-ring, before tilting the specimen to a small angle and forming the final pillar using a series of small rectangular cuts and rotations. The annular method involves using circular ring patterns at gradually reducing beam currents so as to form a pillar more quickly and without tilting. Due to the increased imaging required to form pillars through lathe milling the pillars showed surface cracking consistent with a hard surface layer formed via ion damage. The annular method was therefore deemed to be better for studying mechanical properties. As the 'polishing' of micro-cantilevers only involves a single imaging step, they are likely to show the same behaviour as the annular pillars; reliable mechanical data.

2.12 Literature Review Summary

This literature review has shown that tungsten is a key material for commercial fusion power. The degradation of mechanical properties through accumulated radiation damage limits the lifetime of tungsten components, and hence the running costs and uptime of a fusion power plant. The radiation damage - lattice displacements, hydrogen and helium implantation and transmutation - can be simulated using either fission neutron irradiation or heavy ion irradiation. While an overall more representative technique, neutron irradiations are time-consuming and produce radioactive specimens. Therefore, it is preferable to use ion irradiation to simulate and understand the effects of radiation damage to inform predictive models.

Ion irradiation produces shallow damage layers in materials, of the order of a few microns. This requires specialist testing techniques in order to extract mechanical property data. The two most suitable techniques for this are nanoindentation and micro-cantilever testing. Nanoindentation allows a quick and simple assessment of the change in modulus and hardness of materials after irradiation, which subsequently allows estimates of other properties such as yield stress. However, to fully analyse the mechanical response - including true yield stress and fracture toughness - of an ion irradiated layer, micro-cantilevers should be machined and tested. These cantilevers have been shown to be suitable in determining the elastic, plastic and fracture properties of materials. However, care must be taken when applying the results of these tests to bulk materials, as micro-mechanical testing shows a strong size effect, with smaller test pieces generally being stronger and

tougher than their bulk counterparts.

These tests can be extended to determine additional information about the structure and behaviour of damage by testing at high temperatures and potentially at varying strain rates.

2.13 Research Goals

This thesis aims to add to the knowledge on the effects of radiation damage on the mechanical properties of tungsten, as well as the ability of ion irradiation to represent neutron damage in tungsten. In particular, the following points will be considered:

- Chapter 4 addresses the effect of radiation damage on the mechanical properties of tungsten, focussing in particular on the behaviour of implanted helium. Implantations were carried out at reactor-relevant temperatures in order to form defect structures most similar to those formed in reactors.

- Chapter 5 focusses on testing at elevated temperatures to determine the in-service mechanical properties of irradiated tungsten. A method is also detailed so as to allow the testing of thin layers at elevated temperatures in vacuum.

- Chapter 6 covers the use of micro-cantilever testing to determine true yield stresses and fracture toughness values of tungsten after irradiation. Additionally, an analysis of the size effects present in tungsten materials is performed to determine the validity of small-scale testing in tungsten and attempts made to extract reactor-relevant mechanical property data from ion-damaged layers.

- Chapter 7 provides unique data on the fracture toughness and the BDTT of neutron-irradiated tungsten. Micro-mechanical tests are used to allow a comparison of neutron and ion irradiated tungsten, so as to determine how well ions represent neutrons despite the difference in dose rate and PKA energy.

Chapter 3

Experimental Techniques

The data within this thesis were obtained using focussed ion beam (FIB) machining, scanning electron microscopy (SEM) and nanoindentation. SEM is a standard technique and only basic secondary electron imaging was performed, therefore an in-depth discussion of the method is not necessary. However, the FIB-machining and the nanoindentation - particularly at elevated temperatures - will be reviewed.

3.1 Focussed Ion Beam

The focussed ion beam (FIB) is a relatively recent development in the field of electron microscopy. Although the first scanning ion beam system was produced in 1979,[230] they were not widespread until 1993 when more than 150 commercial systems were in use.[231]

Current commercial systems use a gallium liquid metal ion source, with accelerating voltages between 5 and 30 keV.[232] Gallium flows from a reserve to the tip of a needle where Ga^+ ions are extracted due to a large potential difference between the needle and an extractor electrode.

Typical emission currents from the tip are around 2 μA, with apertures used to define beam currents between 1 pA and 16 nA. These currents equate to spot sizes of 10 nm to 500 nm. The beam is then rastered over the sample and secondary electrons collected to form an image, as with an SEM.

Upon impacting the sample, the gallium ions can experience inelastic collisions with sample electrons that results in secondary electron generation. Alternatively, elastic collisions with atoms in the sample can displace or eject the atoms from the surface. It is these atomic ejections that are the primary purpose of the FIB. By focusing the beam and repeatedly scanning across a selected area, sub-micrometer machining can be achieved. This machining can be used to produce small mechanical test specimens, allowing the mechanical properties of ion-implanted layers to be measured.

3.1.1 Micro-Cantilevers

It has been established in section 2.11.3 that micro-cantilevers are the most appropriate micro-mechanical test geometry for this work. Cantilevers allow the elastic, plastic and fracture behaviour of implanted layers to be tested without the need for specialist testing apparatus. These are manufactured in the following way:

- A 'U'-shaped trench is milled in the surface of the specimen (figure 3.1(a)) using a large beam current of 4 - 7 nA.
- The sample is tilted to 30-45° and the underside of the cantilever is cut away (figure 3.1(b)).
- The sample is rotated by 180° and the other side of the beam is removed (figure 3.1(c)). These undercuts also use a 4 - 7 nA current.
- A smaller beam aperture (typically 240-1000 pA) is selected for fine milling (figure 3.1(d)).
- The redeposited material from the previous steps is removed to produce a free-standing beam (figure 3.1(e)).
- For fracture testing cantilevers, the sides of the beam are milled away to produce a pentagonal cross-section and a notch put in near the fixed end using very low currents (<10 pA)(figure 3.1(f)).

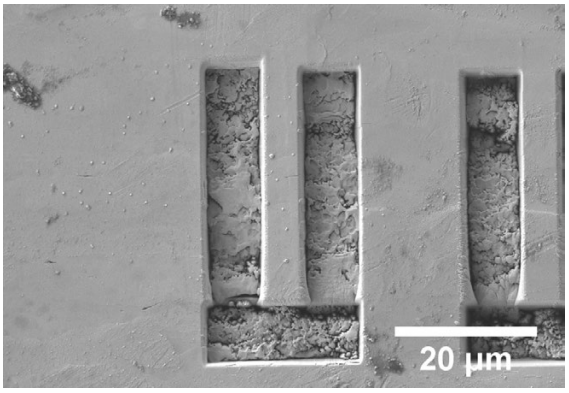

(a)

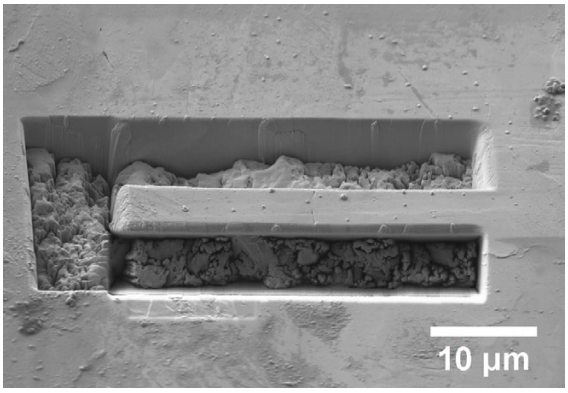

(b)

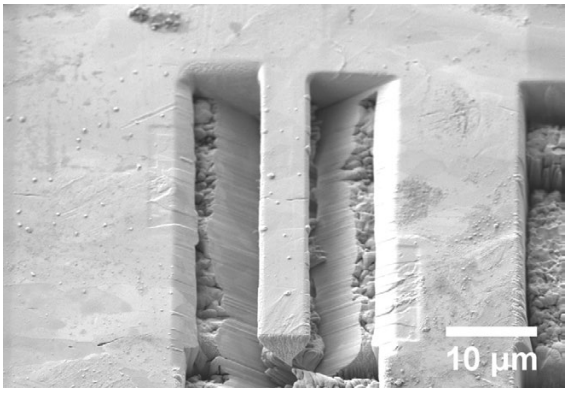

(c)

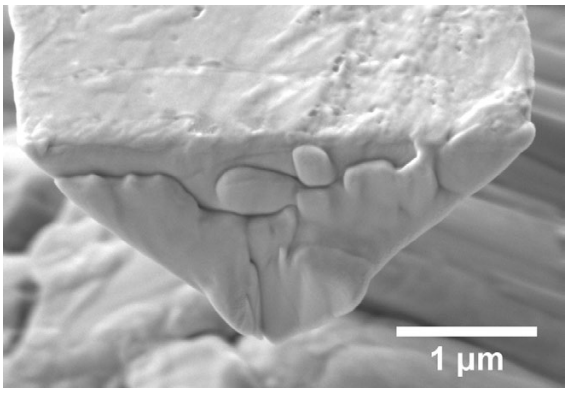

(d) Rough cuts (figures 3.1(a)–3.1(c)) to produce a triangular beam with significant amounts of re-deposited material.

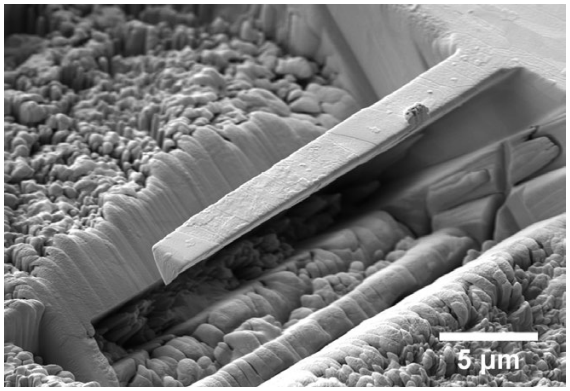

(e) Rough beam polished to a triangular beam for elastic-plastic testing.

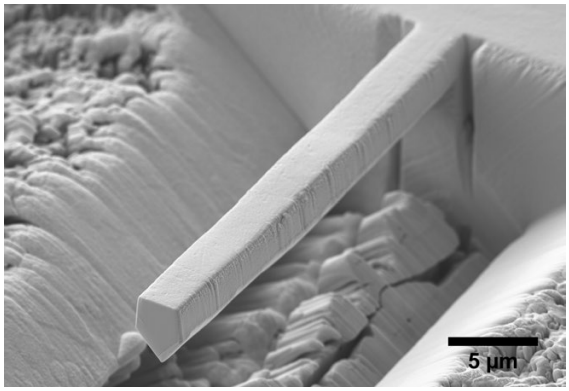

(f) Rough beam polished to a pentagonal beam for fracture testing.

Figure 3.1: SEM images showing different stages during the manufacture of micro-cantilevers.

3.2 Nanoindenter

Two room-temperature nanoindenters were used in this work: an MTS Nanoindenter XP (MTS NANO, Oakridge, TN, USA) and an Agilent G200 Nanoindenter (Agilent Technologies, Wokingham, UK). Both systems operate in an identical way, briefly explained herein.

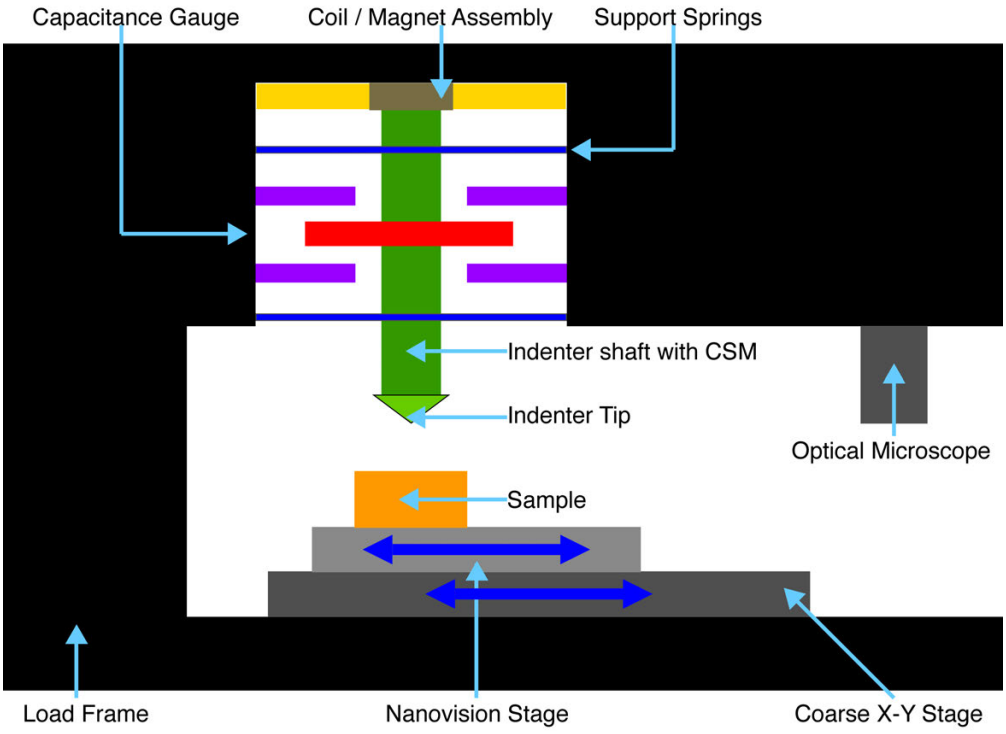

Figure 3.2: Schematic representation of the room-temperature nanoindentation system.

Figure 3.2 shows the important components in the nanoindenter. The coil-magnet assembly applies a known load to the shaft and hence the nanoindenter tip. The displacement of the shaft is measured using the capacitive plates. An overall resolution of 50 nN in force and 0.01 nm in depth is available. Typically, a constant strain rate of 0.05 s^{-1} was used for the indentation experiments and a constant displacement rate of 0.05 nm/s for the micro-cantilever experiments.

Fundamentally, the instrument is load-controlled; the constant displacement rate is obtained via a rapid feedback loop using a proportional-integral-derivative controller (PID controller). The applied load causes a measured displacement. The PID controller then adjusts the loading rate so that the displacement rate is kept constant.

The nanoindenters both allow a continuous stiffness measurement[178, 233] (CSM) to be performed throughout the experiment. This measures modulus and hardness throughout the indentation, allowing both properties to be plotted against indentation depth. A small sinusoidal load (typically 2 nm at 39 Hz) is placed on top of the main load signal, effectively resulting in multiple load-unload tests at increasing depth. However, the CSM method is much faster and more accurate than large-scale load-unload tests due to the reduced effect of thermal drift.

The final aspect of the nanoindenters is the nanopositioning stage that is used to generate topographical maps of the samples, particularly the micro-cantilever beams. The indenter tip is brought into contact with the sample surface and held at a constant load (typically 0.5 μN). A piezoelectric stage then rasters the sample under the tip and the x-y position of the tip is plotted against the tip displacement. The resultant profile allows the indenter tip to be placed to a positional accuracy of 2 nm - essential for micro-mechanical tests as the low loads required to deflect the beam (and the blunt indenter tip used) typically do not leave a visible indent on the beam. The distance between the load point and the fixed end is therefore dependent on this positional accuracy.

3.3 Hot Nanoindenter

The hot nanoindenter was manufactured by MicroMaterials (Wrexham, UK) and was largely developed in Oxford to produce the system now sold as the NanoTest Xtreme. The principle of operation is similar to the room temperature systems: a sharp tip is driven into the surface of the material under a known load and the tip displacement is measured using a pair of capacitive plates. However, in the MicroMaterials nanoindenters this system is mounted horizontally with the tip on a pendulum assembly, rather than the vertical arrangement of the room temperature systems. A schematic representation of the system is shown in figure 3.3(a), with a comparison photo in figure 3.3(b). As the arc involved in the pendulum is so small - especially over the depth of a typical indent - the slight vertical movement of a pendulum is negligible and the load-displacement data are identical to those collected at room temperature in the G200 or Nanoindenter XP.

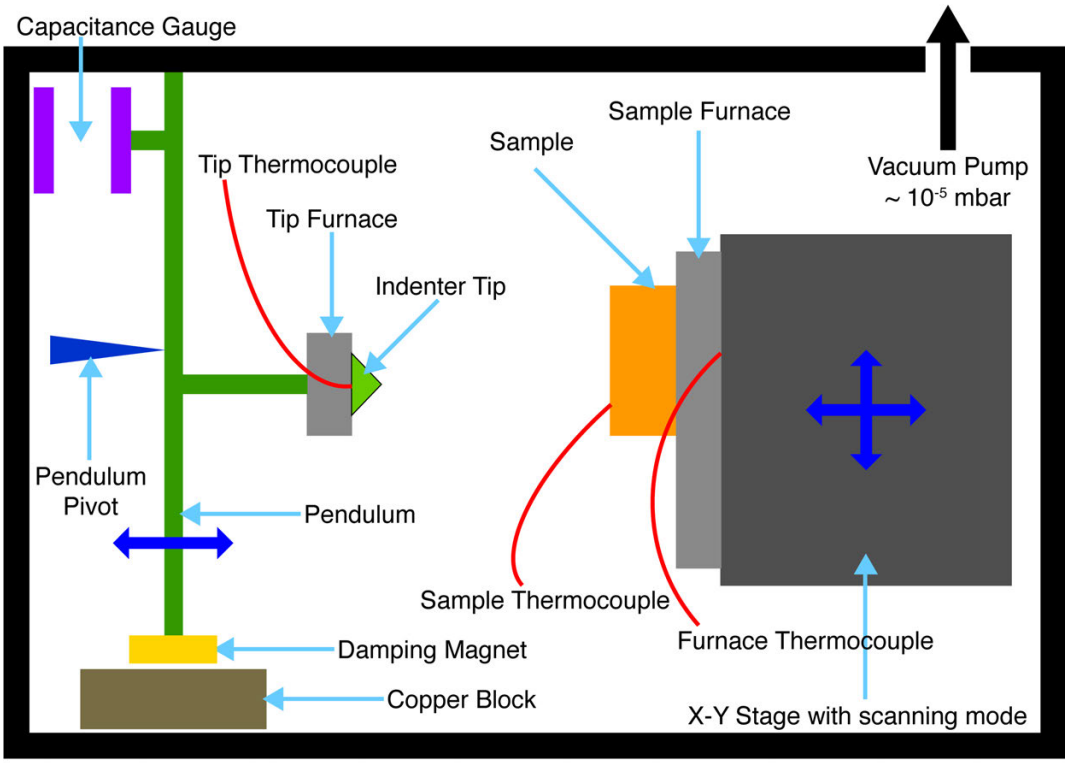

(a) Schematic representation (not to scale).

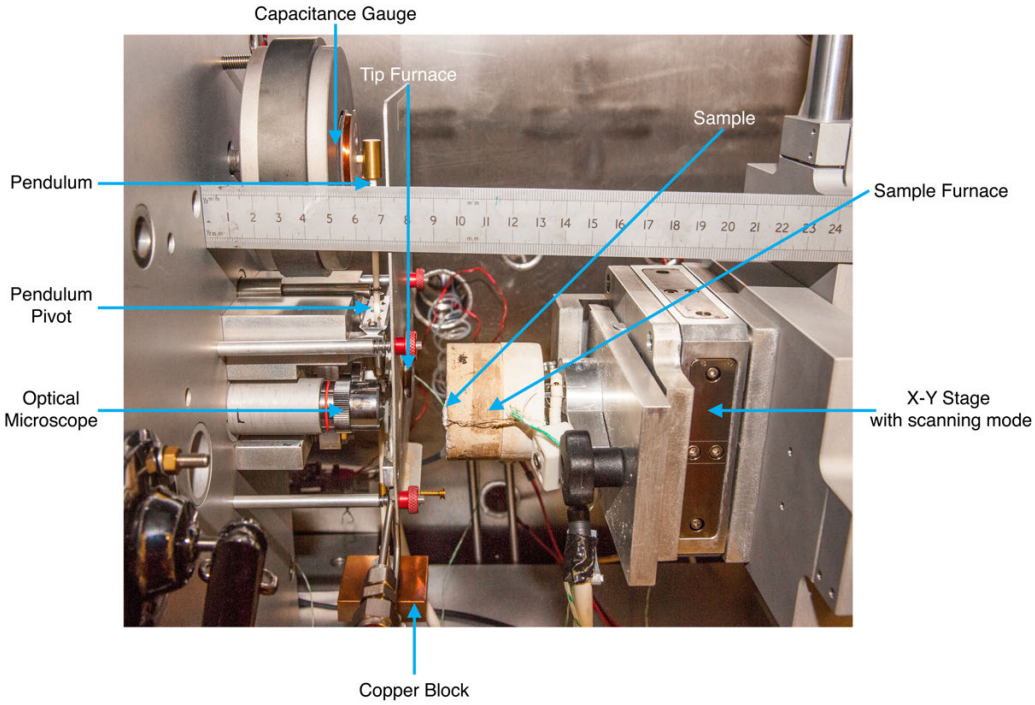

(b) Photo inside the vacuum chamber.

Figure 3.3: The MicroMaterials High-Temperature Vacuum Nanoindenter.

The system also features a nanopositioning stage, allowing profilometry to be carried out on samples. However, the system does not allow for CSM indentation, therefore all hardness-depth data were obtained by a series of load-partial unload indents using the methods described in section 3.4.

Samples were mounted on a furnace using high-temperature cement (Forta Fix Autostic FC6), a water-based product containing alkali silicate glass and inorganic oxides. The temperatures of the tip and sample furnace are individually controlled in order to allow isothermal contact to be obtained.

Initially, the system was developed with a purging system so that testing took place under various inert atmospheres: argon, a reducing He-5%H mix and argon with a zirconium getter. Tungsten samples held at 750°C for five hours are shown in figure 3.4(a) - 3.4(c), all of which show significant oxidation. However, the tungsten sample held at 750°C in vacuum for 75 hours shows no oxidation (figure 3.4(d)).

(a) Tungsten under pure argon.

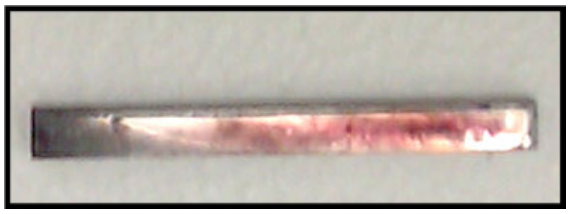

(b) Tungsten under a He-5%H atmosphere.

(c) Tungsten under pure argon with a zirconium 'getter'.

(d) Tungsten under a vacuum level of 10^{-5} mbar.

Figure 3.4: Tungsten samples held at 750°C for five hours in various 'inert' atmospheres. Only sample 3.4(d) shows no oxidation.

While testing in vacuum removes the issue of oxidation for the material, the actual nanoindentation is made significantly more difficult. As seen in this thesis and elsewhere,[192, 195] isothermal contact to <1°C is necessary to produce drift rates low enough for accurate hardness data to be obtained, as a thermal fluctuation of this magnitude can lead to a drift displacement of ∼100 nm.[174]

By removing convective heating (as this requires an atmosphere), equilibrating sample and tip temperatures relies on heating both components to identical temperatures. Sufficient time must then be allowed for thermal gradients within the system to disappear. Thermal equilibration due to conduction between sample and tip should be avoided, as due to the changing contact area of a pyramidal indenter with depth the tip heating and drift would vary with depth. This prevents any drift correction without computational modelling of the contact.[192,195] As such, careful control of tip and sample temperatures is necessary in order to prevent significant drift rates.

The method developed during this thesis for isothermal contact was as follows:

1. Position tip 500 μm from sample surface, to prevent thermal expansion of the sample damaging the tip.
2. Heat both tip and sample to desired sample temperature.
3. Wait ~6 hours for sample temperature to stabilise.
4. Position tip 25 μm from sample surface.
5. Tip temperature will increase due to radiative heating from the sample.
6. Set tip temperature to the current temperature.
7. Perform series of trial indents to determine drift rates and variation of tip temperature with depth.
8. Adjust tip temperature up or down as necessary based on drift rate.
9. Once drift rate is low enough (typically <0.1 nm/s, i.e. comparable to room temperature drift rates), begin array of load-partial unload indentations.

The choice of tip material becomes important when testing at elevated temperatures. Due to the propensity of tungsten to form carbides at elevated temperatures a typical diamond indenter tip was not used. Sapphire (Al_2O_3) - another popular tip material - was not considered as its hardness (~11.5 GPa) and modulus (~400 GPa)[234] are too low; comparible to the properties of tungsten.

Two tips were trialled: one silicon carbide (SiC) and one cubic boron nitride (cBN). Figure 3.5 shows the results of testing using each tip, which plots the projected contact area of the tip against the penetration depth. This curve describes the shape of the tip and is used to convert the depth data into indent area (see section 3.4). In the as-received condition, the SiC tip is sharper (smaller projected area with depth) and produces a more uniform curve compared with the cBN tip. However, it can be easily seen that the tip rapidly blunts, with degradation occurring roughly four times faster than the cBN indenter.

To demonstrate this effect on hardness, the same load-unload hysteresis data were analysed using the new and used tip profiles to produce the data in table 3.1. At the shallow depths where the effects of ion-implantation are determined, the blunting causes a difference of 4-10 GPa. This is up to five times larger than the hardening due to ion implantation, thus tip wear would cause significant errors in the results unless corrected for. Although tip wear can be corrected for by running regular tip calibrations, this is not practical when used a heated vacuum system as cooling the system, venting the chamber, running a calibration and then restoring the previous state takes around three days. This process also causes thermal fatigue of the mounting cement, potentially affecting the sample mounting and hence the sample compliance. As such, a cBN indenter tip was used for the experiments, with a tip calibration performed before and after the full hardness-temperature set of experiments. The calibrations were very close, but the second, post-indentation calibration was used to determine hardness values.

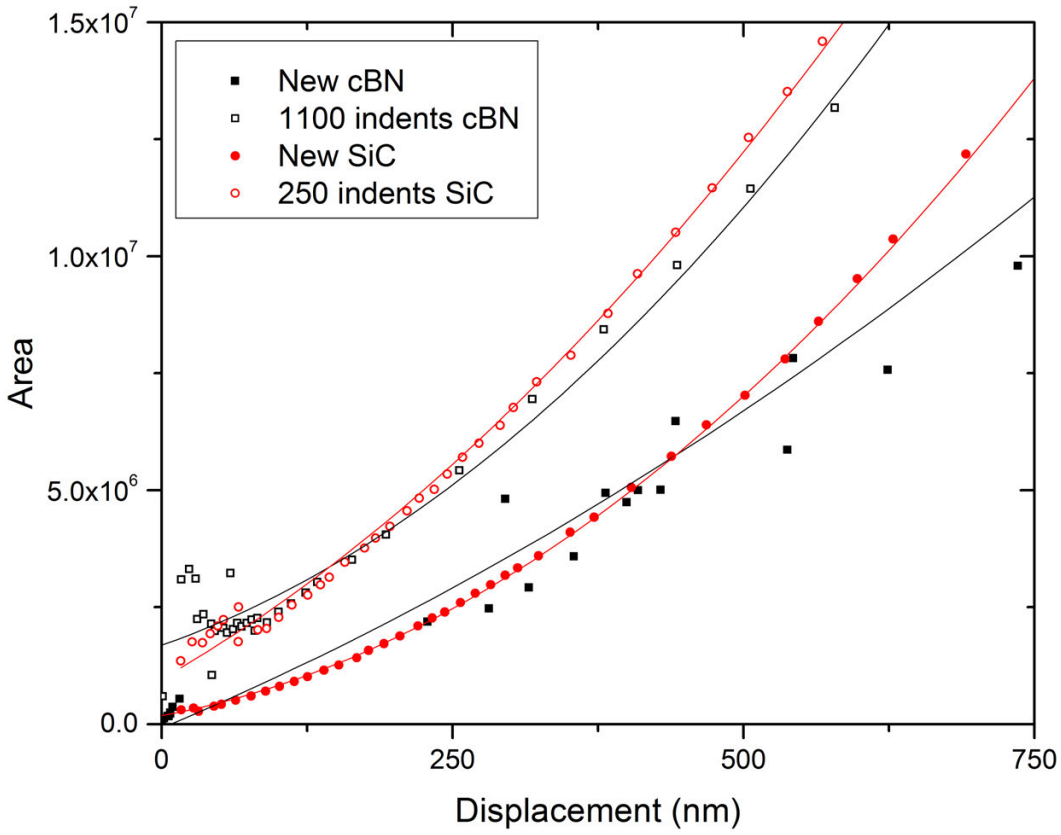

Figure 3.5: Area functions of a silicon carbide and cubic boron nitride indenter tip in the as received condition and after a number of indents at a range of typical temperatures (20-700°C). The SiC tip is initially sharper, but blunts extremely rapidly.

Depth (nm)	H (GPa) (New SiC)	H (GPa) (Used SiC)
69	14.9	4.9
162	12.9	5.0
262	11.4	5.0
363	10.7	5.2
463	10.2	5.4
559	9.8	5.6
1023	8.4	5.9
1458	7.8	6.2
1792	7.5	6.4

Table 3.1: Hardness with depth for load-unload hysteresis data analysed using the new and used SiC tip profile. The hardness values - particularly below 500 nm where ion-irradiated values are taken from - vary by up to three times between the calibrations.

3.4 Nanoindentation Data Analysis

The data from the nanoindenter is in the form of load-displacement curves. This needs to be converted to values of hardness and elastic modulus with indentation depth. The Oliver-Pharr method by which this occurs was discussion in the literature review (section 2.11.1, page 40). The modulus is determined from the unloading slope of the load-displacement curve while accounting for instrument and tip compliances.

The hardness is given by the maximum load divided by the contact area. As the indents are too small to image quickly and accurately, the contact area is determined by producing an array of indents in a material of known mechanical properties; fused silica in this work. As the hardness and modulus of fused silica are known, an experimental curve that describes the contact area (figure 3.5) can be produced. This allows the calculation of the contact area at any indentation depth. This tip calibration was said to be accurate when the hardness and modulus calculated for fused silica were within 5% of literature values. Additionally, the produced modulus-depth curves should be flat, outside of surface roughness and noise at shallow depths. This is shown in figure 3.6.

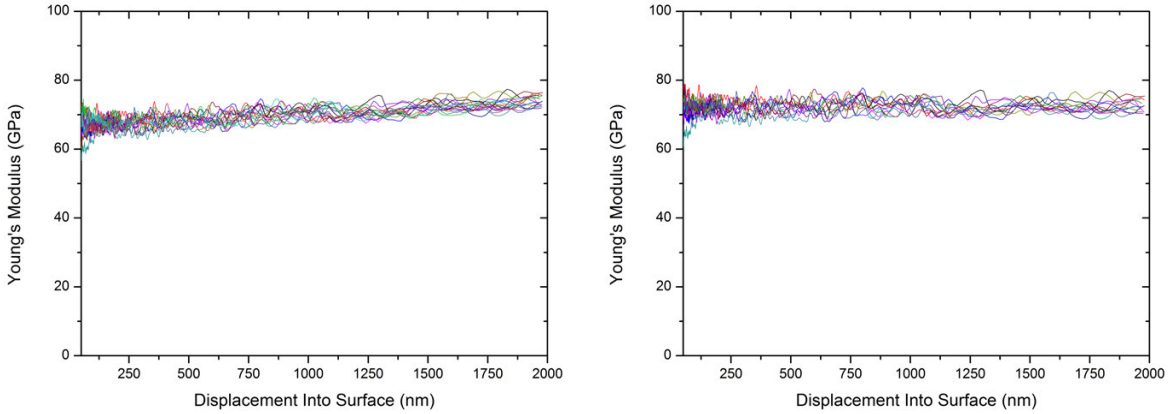

(a) Poor tip calibration.

(b) Good tip calibration.

Figure 3.6: A poor tip calibration produces a modulus-depth curve that varies with indentation depth (a). A well-calibrated tip lacks this variation (b), and is closer to the given value of 72 GPa. Modulus-depth plots for several indents are shown in order to demonstrate the scatter within each array.

Thermal drift can lead to inaccuracies in the measured displacements. The indentation area and therefore hardness and modulus depends on accurate measurements of indentation depth. Therefore, thermal drift during indentation must be measured and corrected for. Drift was measured during a 60 s hold period at the end of each indent (and prior to each indent at elevated temperatures). This thermal drift rate (averaged for elevated temperatures) is used to correct the measured displacement into a true displacement from which hardness and modulus can be calculated.

For the room-temperature indents, rates are typically below 0.05 nm/s over an indentation time of around 180 s. This corresponds to a total displacement of 9 nm, meaning the effects of drift at room temperature are minimal. For the micro-cantilever tests test times can be up to 1000 s in duration. However, this is still only a $\sim$2% error in the absence of thermal drift correction.

At high temperature, drift rates are harder to control and test times are much longer due to the load-partial unload indents performed, up to 1200 s. For the unimplanted and helium implanted samples, indents were discarded if the average drift rate was >0.15 nm/s. This corresponds to a maximum allowable total drift of 180 nm, or 9% of the total indent depth. Therefore errors due to thermal drift are minimal in these samples even if drift were not corrected. Drift levels were higher in the tungsten-implanted sample tested due to failure of the air conditioning in the lab, but test times were also shorter due to the improved load-partial unload program. In this case, 66% of the indents at 550°C were below 0.25 nm/s (165 nm total drift with an overall error of 8%) and 72% of the indents at 650°C were below 1.2 nm/s (790 nm total drift with an overall error of 40%). Although much of this displacement is corrected for, it still leads to greater uncertainty in the calculated values of hardness hence larger error bars on the data.

3.5 Ion Implantation

Four beam lines were used for the ion-implantation used in this work. The National Ion Beam Centre at the University of Surrey is a 2 MV beam line operating at temperatures up to 800°C. W^+ ions are accelerated in the tandem Van de Graaff accelerator and focused into the target chamber. They strike the sample perpendicular to its surface. Temperature calibrations performed by Hardie[235] indicate the range of uncertainty to be $\pm$50°C. The dose and dose rate were controlled by four Faraday cups located at the four corners of the sample holder. Implantation is performed

at a background pressure 10^{-6} Pa.

IPP Garching is an 3 MV tandem accelerator. Typical ion currents for the 18 MeV W^{6+} implantation are around 20 nA. In order to obtain a homogeneous flux over the sample surface, the ion beam is swept vertically and horizontally over the target. Beam position, ion flux, and fluence are controlled by an arrangement of four small-diameter Faraday cups located at the corners of the sample mask. Damage rates of a few 10^{-4} dpa/s are typically achieved for tungsten self-implantation. Radiative heating is applied for implantation up to 800°C. The sample temperature is measured by a thermocouple attached to the sample or a two wavelength pyrometer. Implantation is performed at a background pressure of 10^{-5} Pa.

The accelerator used at the HZDR, Rossendorf, Germany is very similar to that present at Garching. It is also a 3 MV Tandetron accelerator that rasters the beam over the samples. This facility was used to generate the samples to match the neutron irradiation as no other facility would implant at 900°C. A typical beam current of 4 nA corresponds to a fluence of 1.6×10^{10} ions/cm^2/s.

JANNuS (Joint Accelerators for Nano-science and Nuclear Simulation) couples a 3 MV Pelletron accelerator (Épiméthée) equipped with a multi-charged ECR ion source and a 2.5 MV single ended Van de Graaff accelerator (Yvette). In the dual-beam implantations, tungsten ions are handled by Épiméthée and light ions by Yvette. As with IPP Garching, high-energy implantations are carried out by higher-charged ions. Beam currents decrease strongly past W^{6+}, therefore W^{12+} was the highest charge used.

At Surrey, HZDR and IPP Garching, the beam is rastered over the sample and a flat damage profile is created by successive ion implantations from high accelerating voltages to lower voltages. At JANNuS, the beam is defocussed so that the entire sample is implanted simultaneously. Additionally, the damage profile is produced by a set of six rotating degrader foils so the damage throughout the sample is generated more continuously as each depth range is hit in succession between foils. Both these factors may have an effect of the resultant damage structure, although this effect in tungsten is currently unknown. Preliminary studies by Hewitt[236] showed that in both pure iron and in an iron-chromium alloy known to be dose-rate sensitive,[90] the nanoindentation hardness is unchanged between the defocussed and rastered beams at the same average dose rates. Therefore, it is likely that no effect is seen in tungsten either.

All ion implantations were performed into high purity (99.99%), polycrystalline tungsten. Table

3.2 below provides a complete list of irradiations completed, with the ion dose converted to dpa values (see section 3.6). These values will be used throughout this thesis. The specific combinations of fluence and energy (or degrader thickness) are given in table 3.3

Implanted Ion	Implantation Energy (MeV)	Temperature (°C)	Damage Level	Dose Rate (dpa/s)	Beamline
W	20 MeV	500	1.5 dpa	10^{-4}	Garching
He	2 MeV	500	600 appm	10^{-6}	Surrey
W	20 MeV	800	1.5 dpa	10^{-4}	Garching
W	36 MeV	800	1.5 dpa	10^{-4}	JANNuS
He	2 MeV	800	600 appm	10^{-6}	JANNuS
W + He	36 + 2 MeV	800	1.5 dpa and 600 appm	10^{-4}	JANNuS
W	15 MeV	900	4.5 dpa	5×10^{-5}	HZDR

Table 3.2: Irradiated Materials

Beamline	Implantation Energy (MeV)	Degrader Thickness (μm)	Fluence (ions/m^2)
Garching (W-Ion)	20	-	2.6×10^{18}
	10	-	7.4×10^{17}
	5.5	-	1.9×10^{17}
	4	-	4.1×10^{17}
	1	-	4.6×10^{17}
HZDR (W-Ion)	15	-	1×10^{19}
	10	-	6×10^{17}
	8	-	7.5×10^{17}
	5.5	-	7.5×10^{17}
	4	-	3.5×10^{17}
	2	-	5×10^{17}
	1	-	7.5×10^{17}
JANNuS (W-Ion)	36	5	5×10^{18}
	36	3	5×10^{18}
	36	2	5×10^{18}
	36	0.8	5×10^{18}
	36	0	5×10^{18}
	36	0	5×10^{18}
Surrey (He-Ion)	2	-	1.59×10^{19}
	1.8	-	1.38×10^{19}
	1.6	-	1.38×10^{19}
	1.4	-	1.06×10^{19}
	1.2	-	1.06×10^{19}
	1.0	-	1.06×10^{19}
	0.8	-	1.06×10^{19}
	0.6	-	1.06×10^{19}
	0.4	-	1.17×10^{19}
	0.2	-	1.17×10^{19}
JANNuS (He-Ion)	36	5	1.21×10^{20}
	36	3	1.21×10^{20}
	36	2	1.21×10^{20}
	36	0.8	1.21×10^{20}
	36	0	1.21×10^{20}
	36	0	1.21×10^{20}

Table 3.3: Specific conditions used at each beamline

3.6 Calculation of Damage

Damage profiles for each implantation were calculated using SRIM2008.03 using the quick (Kinchin-Pease) cascade option as recommended by Stoller.[237] The displacement threshold energy (E_d) used for the dpa level estimation was an average over all crystallographic directions. Armstrong[143] uses a value of 68 eV in his work, and the same value is used here for comparison. ASTM standards recommend a value between 40 and 90 eV.[238]

The SRIM output 'VACANCY.txt' provides the number of displaced target atoms per Angstrom depth per implanted ion. The data in the output file consist of the displacements due to the incident ion and the displacements due to recoils. As 'full cascades' inaccurately calculates the levels of damage,[237, 239] replacement collisions are not considered. However, these collisions were found to be typically <10% of the total number of vacancies generated, and thus do not significantly contribute to the overall damage calculation.

The number of vacancies due to the incident ion and recoils are summed to give N_{SRIM} and converted from Angstroms to cm. This value is converted to dpa by multiplying by the impinging ion fluence (Γ_r) and dividing by the atomic density of tungsten (6.33×10^{22} atoms / cm^3).

$$N_{dpa} = \frac{N_{SRIM} \times \Gamma_r}{6.33 \times 10^{14}} \tag{3.6.1}$$

Using equation 3.6.1, the following damage profiles can be generated for each implantation facility.

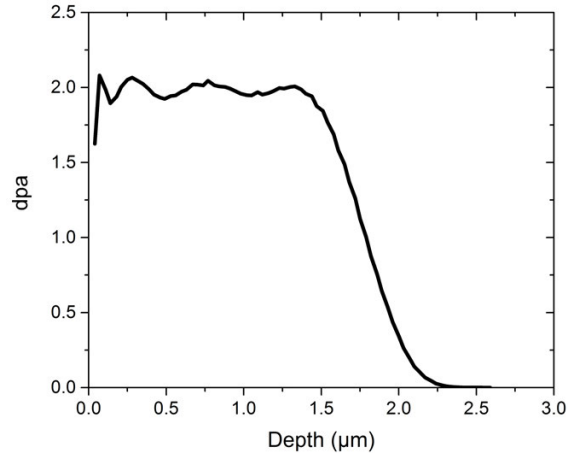

(a) IPP Garching, W-ion

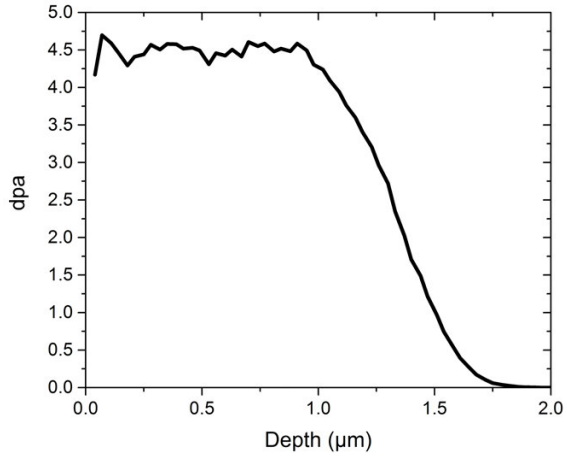

(b) Rossendorf, W-ion

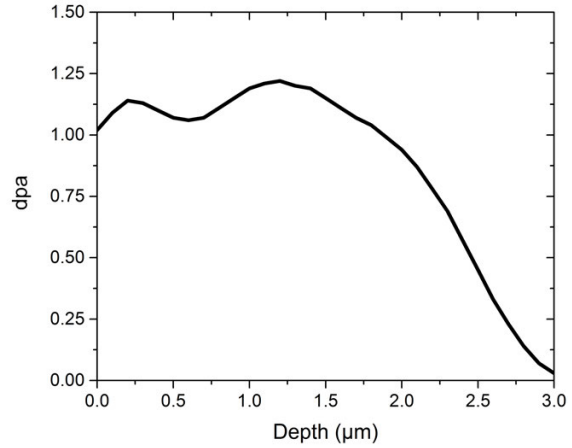

(c) JANNuS, W-ion

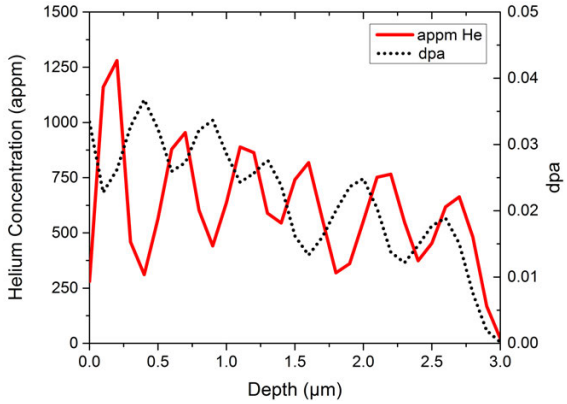

(d) JANNuS, He-ion

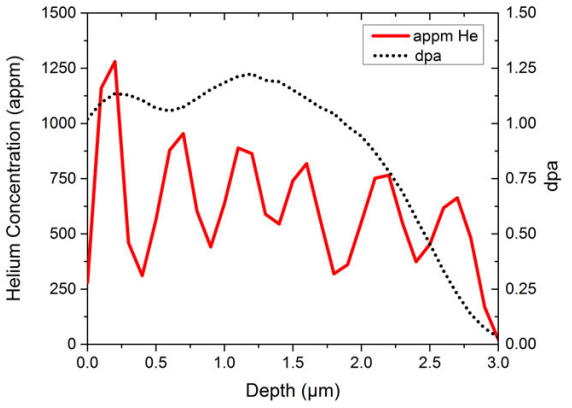

(e) JANNuS, W+He ions

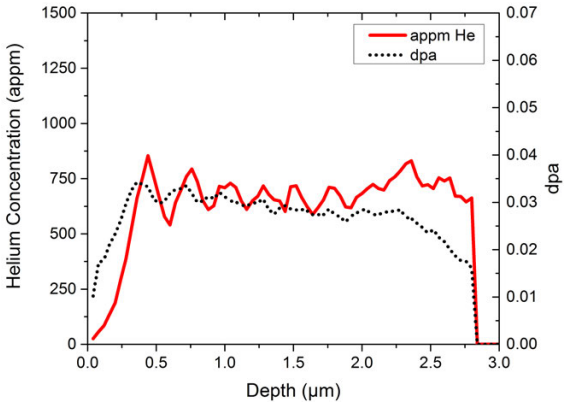

(f) Surrey, He-ion

Figure 3.7: Predicted profiles for the implantation performed using SRIM.

3.7 Neutron Irradiation

Irradiation was performed under the Extremat II campaign at the high flux reactor in Petten, Netherlands. The irradiation was performed at 900°C to an average dose of 4 dpa (stainless steel equivalent) with a peak dose of 4.7 dpa (stainless steel equivalent). The irradiation time was 282 days, giving an average dose rate of 1.63×10^{-7} dpa/s, roughly three orders of magnitude slower than the ion irradiations.

The four-point bend beams were prepared by Giannattasio, who also carried out the original tests on the unirradiated material.[40,54] The beams were 1 × 1 × 11 mm in size, polished to a diamond finish on each side with a ∼60 μm notch in one side.

3.8 Sample Preparation

The material was obtained from Metal Crystals and Oxides, Cambridge, UK in the form of a 99.99% pure arc-melted rod. No chemical analysis was performed, therefore this purity value is that given by the manufacturer. This rod was cut using electric discharge machining (EDM) into small 'matchsticks', approximately 1.2 mm × 1.2 mm × 12 mm. These samples were ground with silicon carbide paper to a 2500 grit finish, followed by 3 μm diamond paste. One side of each sample was then finished using 40 nm colloidal silica and this face was used for the ion implantations. The samples were prepared to match those prepared by Giannattasio[40,54] and therefore provide the best comparison with the neutron-irradiated material. As such, the material was used in the as-received condition, with no annealing carried out.

The grain structure of the material as imaged by EBSD is shown in figure 3.8, which has been analysed to produce the grain distribution in figure 3.9. The surface quality is poor as the colloidal silica polish introduced surface relief around some grains, preventing EBSD patterns from being obtained. The sample was therefore re-polished prior to these scans being taken which introduced some scratches due to the difficulty of polishing a single 1 mm wide specimen. A higher-resolution EBSD scan of the sample produces the data shown in figure 3.11, which shows the presence of many smaller sub-grains within each larger grain. These sub-grains have a misorientation of ∼1° and an average size of 4 μm.

The material has an average grain size of 30 μm with no overall texture (figure 3.10), although the grains are slightly elongated in the axis of the rod. As such, both nanoindentation and micro-mechanical tests will be largely unaffected by the crystallography of the system. This is helped by the elastic isotropy of tungsten (the anisotropy coefficient at 24°C is only 1.010[240]), and means that the effect of grain orientation can be neglected when interpreting mechanical property data.

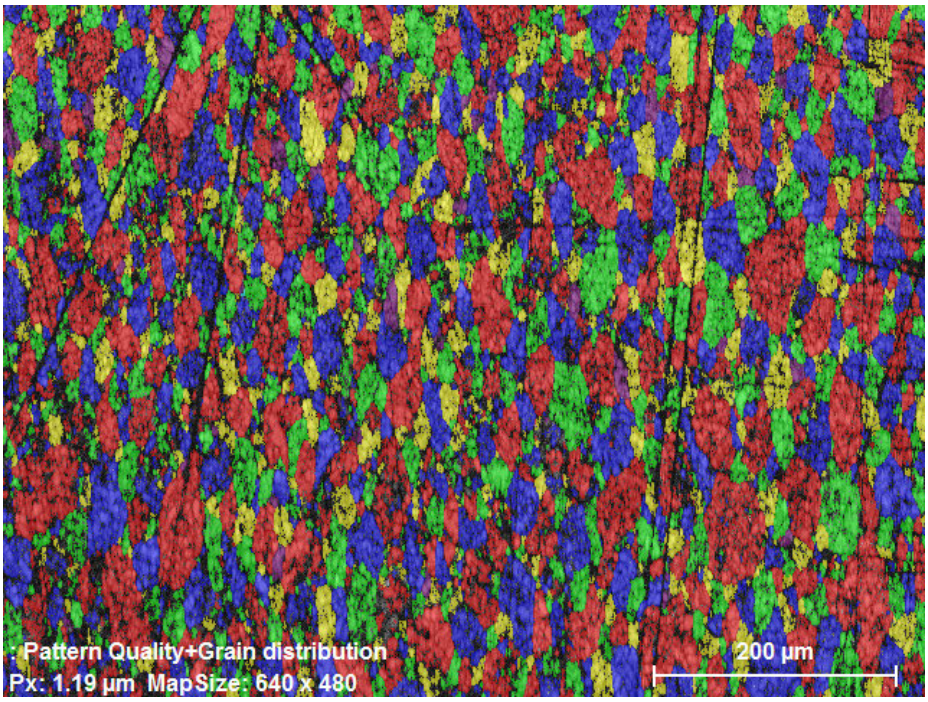

Figure 3.8: Large area of sample with grains highlighted. A grain boundary misorientation of 12° was used to define each grain. The colours do not refer to any crystallographic information, they simply highlight different grains. A slight grain elongation can be seen along the axis of the rod, oriented vertically in this image.

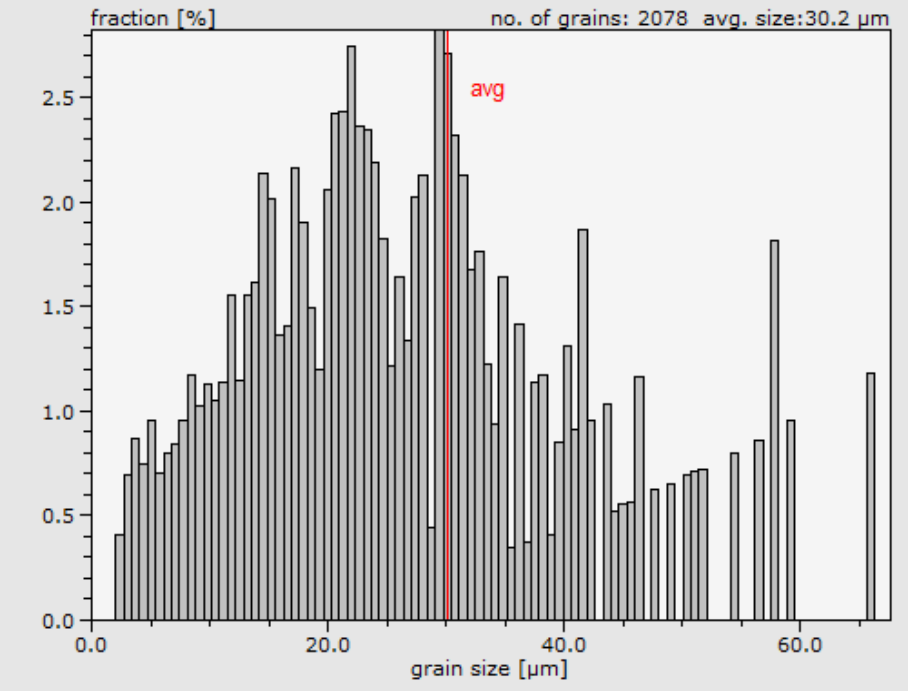

Figure 3.9: Grain size distribution from the data in figure 3.8. The average grain size is 30.2 μm.

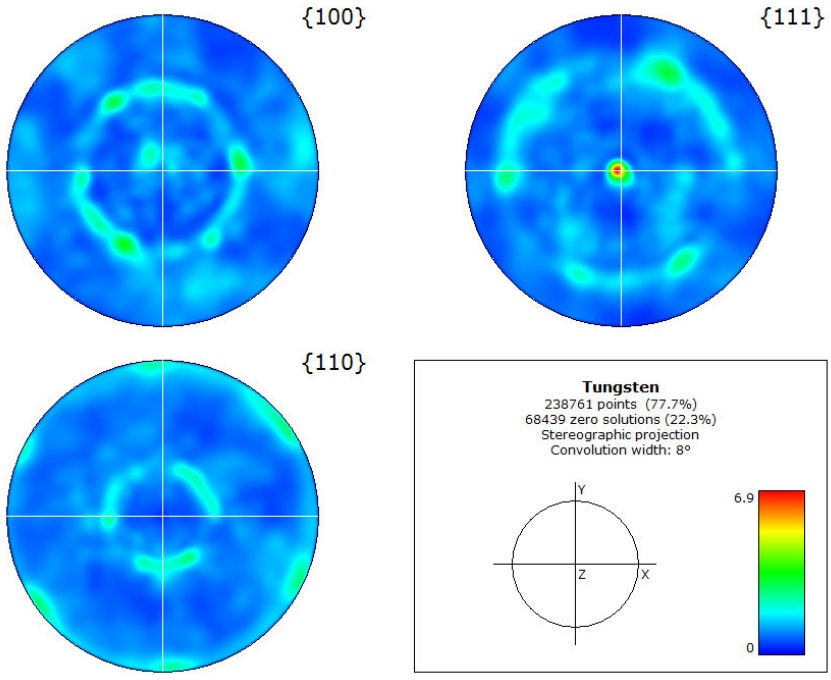

Figure 3.10: Texture analysis from the data in figure 3.8. No significant texture is present.

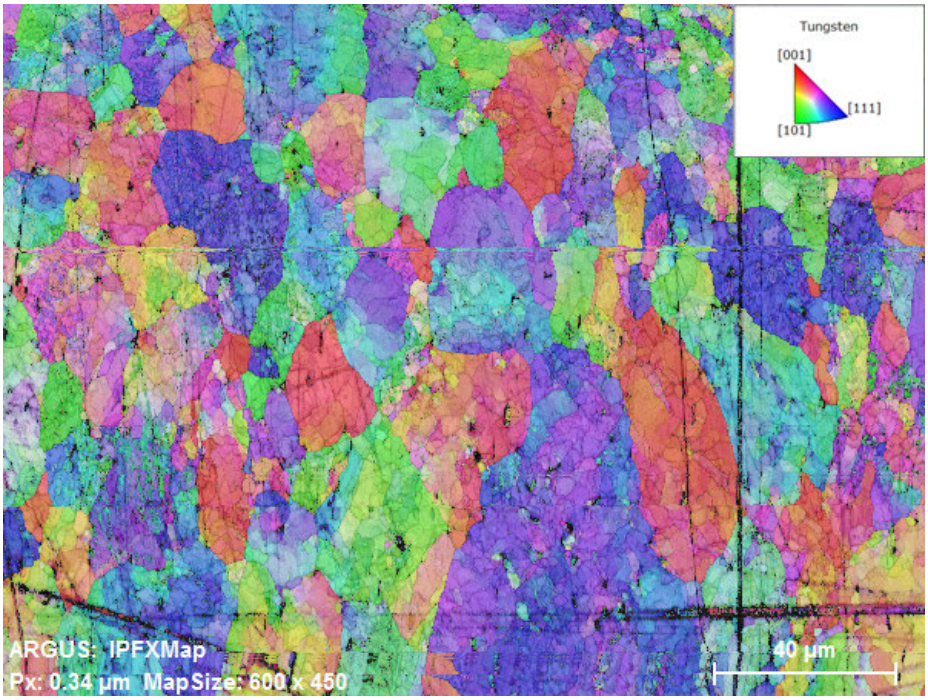

Figure 3.11: Higher-resolution EBSD scan combining crystallographic information with pattern quality. A sub-grain structure is visible within each grain.

Chapter 4

Nanoindentation

4.1 Introduction

Ion irradiation is widely used to study the fundamental effects of radiation damage. As such, ion irradiations have been performed using various combinations of ion species and temperature - detailed in section 3.5, page 67 - in order to capture the varying behaviour of radiation damage. Unlike testing with micro-mechanical methods, nanoindentation is a quick and simple method of obtaining mechanical property data and was therefore performed on all the irradiated samples.

4.2 Method

The room temperature nanoindentation method as described in section 3.2, page 59 was performed on all the samples. The nanoindenter was operated in continuous stiffness mode in order to measure hardness and modulus as a function of depth. An array of one hundred indents was performed on each sample, an example of which is shown in figure 4.1. A strain rate target of 0.05 s^{-1} was used to a depth of 2000 nm. The CSM oscillation was operated at a frequency of 39 Hz with a displacement target of 2 nm.

It was noted very early in nanoindentation experiments[173] that inaccuracies in the definition of tip geometry may lead to large errors in the determined values of hardness and modulus. As such, all the experiments reported here calibrated the tip shape according to the method proposed by Oliver and Pharr.[234] This involves producing a small array in a material of known mechanical behaviour - sixteen indents in fused silica in this work - and determining the tip geometry from these data. This was done prior to each 100-indent array.

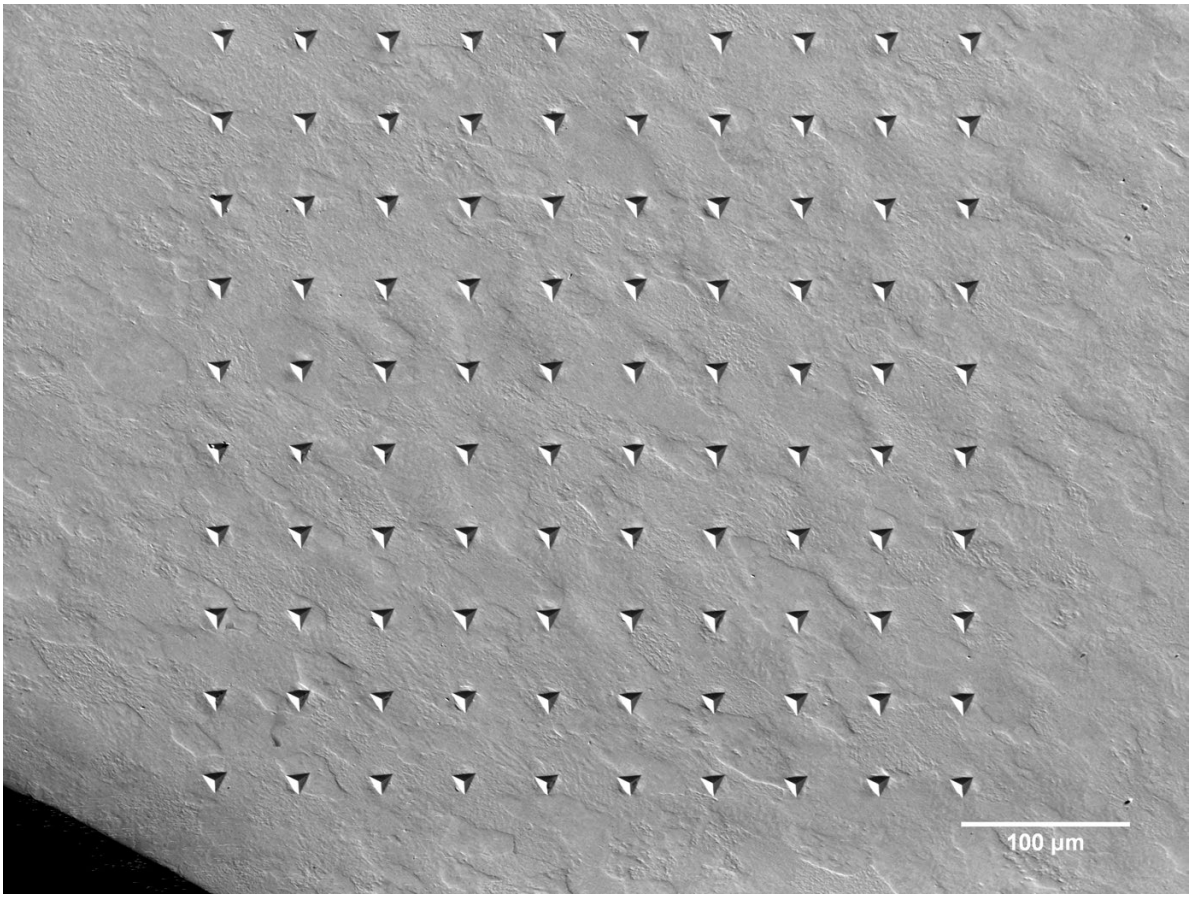

Figure 4.1: SEM image of a typical one hundred indent array, shown here in unimplanted tungsten. The array spans multiple grains. Therefore, hardness and modulus data will give a representative average of the material properties.

4.3 Results

The projected contact area assumes no pile up during an indentation. If pile up is present, the measured hardness and modulus will be higher than the true values[119] because of the larger contact area than expected. Therefore, before the effects of implantation can be discussed it is necessary to determine if any pile up has occurred. Figure 4.2 shows an image of an indent in each material at 54°, an AFM-like scan of the indent using the nanoindenter and the resultant depth profiles from the scan. These data can be used to determine the level of pile-up present in each indent array. Minimal - if any - pile up is seen in any of the implantation conditions, therefore hardness and modulus values will solely determined by the implanted damage.

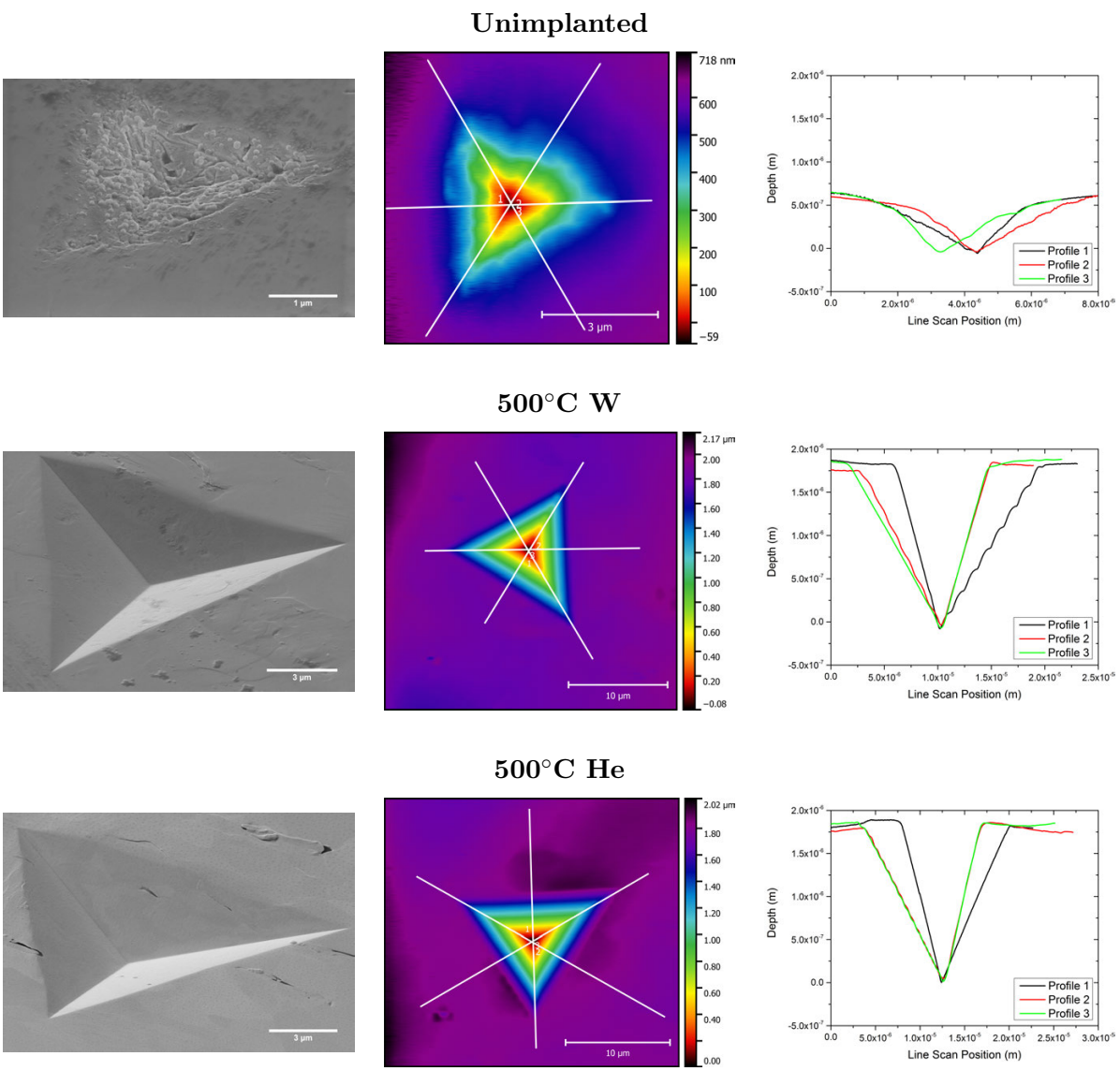

Figure 4.2: Image of an indent, an AFM-like scan using the nanoindenter and the resultant profile used to judge the degree of pile-up. In all cases, this is minimal, therefore hardness and modulus data will be representative of the radiation damage. The 'unimplanted' data were taken after the sample was polished for the EBSD scan in figure 3.11, hence the degraded edges.

Indent Image	Nanoindenter Scan	Indent Profile

800°C W

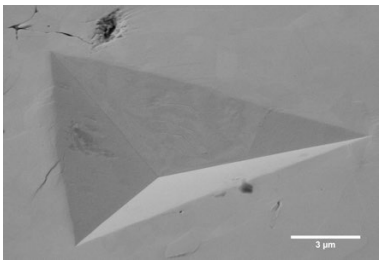

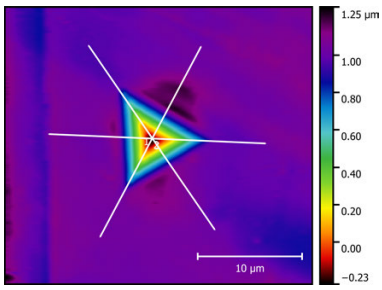

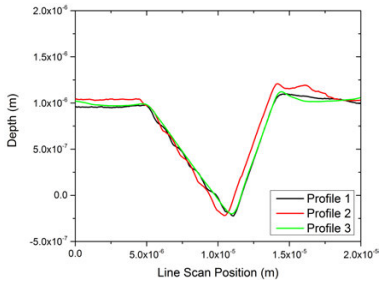

800°C He

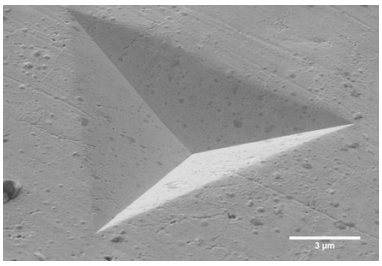

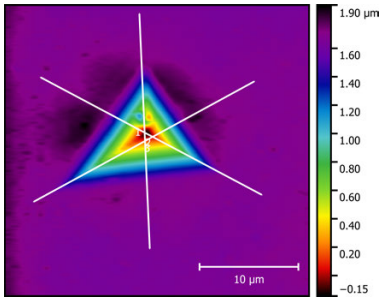

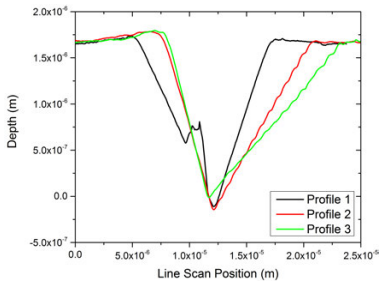

800°C WHe

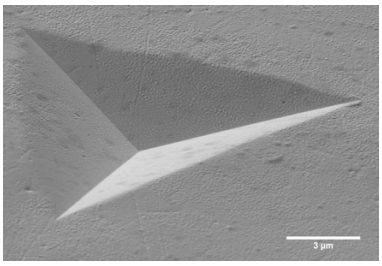

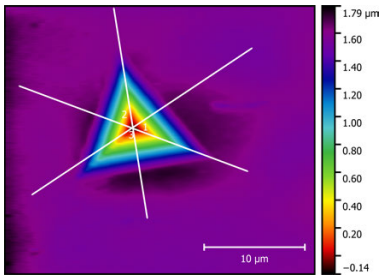

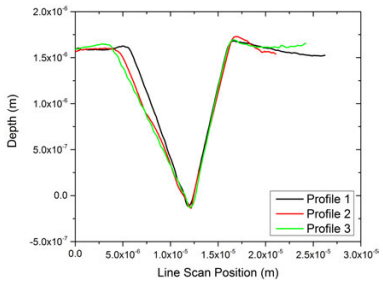

900°C W

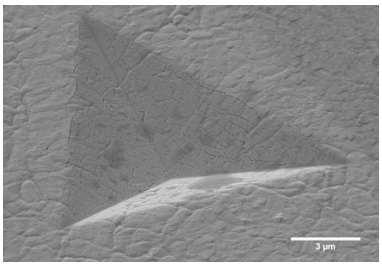

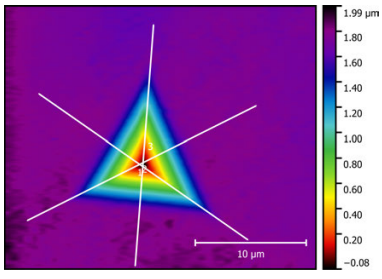

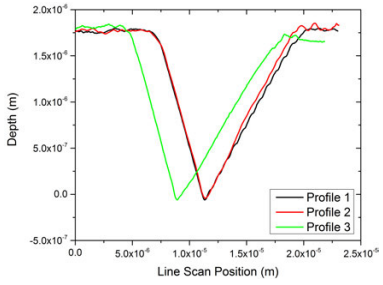

Figure 4.2: Image of an indent, an AFM-like scan using the nanoindenter and the resultant profile used to judge the degree of pile-up. In all cases, this is minimal, therefore hardness and modulus data will be representative of the radiation damage (cont.)

Figure 4.3 shows the variation in hardness with depth for the samples irradiated at JANNuS at 800°C. The implanted layer is around 3 μm thick, so the hardness of this layer should be evaluated up to approximately $\frac{\text{Implanted Depth}}{7}$, i.e. 400 nm.[143, 182] The dual beam implantation hardens the material by 2 GPa, far more than the 1.2 GPa from the W-ions and 0.73 GPa from the He-ions. However, the overall level of hardness is roughly comparable to the sum of each individual implantation. As there has not been any TEM characterisation of this material, it is unclear if this is because the microstructure consists of small dislocation loops and helium-vacancy clusters, i.e. consists of the same damage present in the single beam samples found by Xi[143] (W-implanted) and Beck[154] (He-implanted). As helium interacts with vacancies formed in the displacement cascades very strongly, it is likely that there is a synergistic effect in the damage formation and the resultant hardness is coincidentally equal to the sum of both the helium clusters and displacement damage. It is not clear why the hardening from the ion-implanted layer is still affecting the data at 2000 nm, unlike the other implantations.

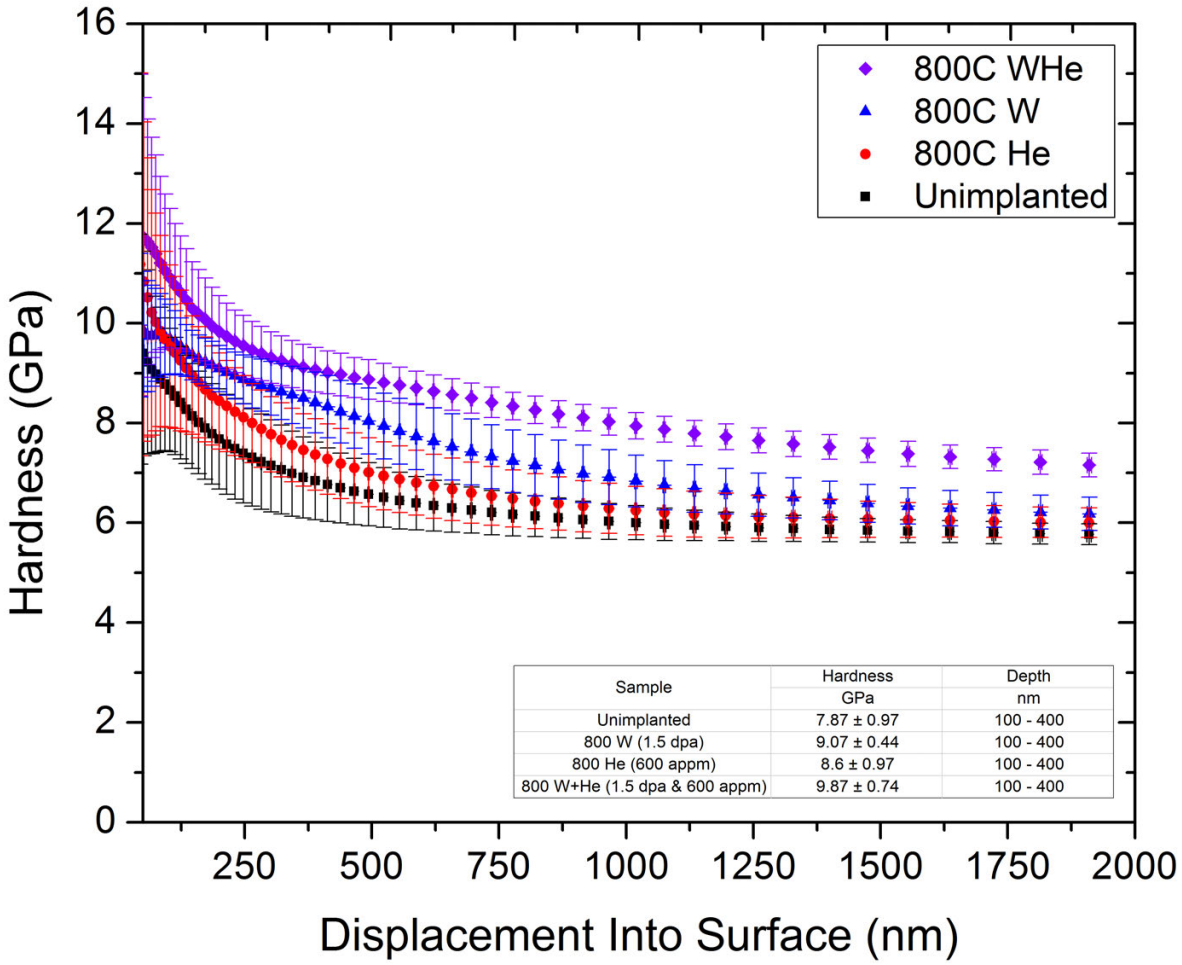

Figure 4.3: Hardness with depth for JANNuS samples, all produced at 800°C. The hardness values are taken from 100-400 nm in depth so as to avoid strong size effects and only sample the implanted layer.

These data examining the interaction of tungsten ion and helium ion implantation can be compared with Armstrong's work[120] on sequential self-ion and helium-ion implantation. Although Armstrong implanted at 300°C, he showed that tungsten implanted to 13 dpa (with the same 8.35 GPa hardness as a 1.2 dpa sample[143]) that was then implanted with 300 appm helium showed no increase in hardness compared to the sample that was only implanted with 13 dpa of self-ions. This was attributed to helium trapping at dislocation loops. The loop volume number density does not change significantly between 1.2 dpa and 33 dpa - 2.16×10^{22} to 1.61×10^{23} - nor does the hardness - 8.35 GPa to 8.55 GPa.[143] Therefore it is likely that the 13 dpa sample has a similar loop density to the 1.2 dpa sample, which therefore means the same helium-absorbing effect would

be seen. Even if the densities are different, a slight reduction in hardness - 11 GPa to 10.5 GPa - is also seen for a 0.4 dpa self-ion implanted sample with 5.6×10^{22} loops / m^3 subsequently implanted with 300 appm helium.

This helium-trapping effect is clearly not present in this work: the dual-beam sample is 0.8 GPa harder than the self-ion sample. Although the implantation temperatures are substantially different, it is reasonable to conclude that sequential ion implantation does not result in the same damaged microstructure as a dual-beam implanted sample. Given the strong interaction of helium and vacancies, it is probable that the helium is having a significant effect on the damage structure formed. Therefore, the microstructure in the dual-beam sample contains an increase in size or number density of helium-vacancy clusters compared to those present in the single-beam, helium-implanted material.

If the helium-vacancy clusters harden via an Orowan mechanism (equation 4.4.2), the 1.27 GPa increase in hardening between the dual-beam and helium-ion specimens corresponds to a 2.7 times increase in radius, assuming constant defect density. SRIM predicts 47.3 vacancies per ion for the 2 MeV helium implantation compared with 43591 vacancies per ion for the 36 MeV tungsten implantation. Mason[241] shows that the number of point defects N in a vacancy cluster in tungsten is given by equation 4.3.1. Therefore, a 2.7 times increase in r requires 19.7 times the number of vacancies, well below the 922 times more vacancies created during the implantation. It is therefore trivial for large clusters to be formed during the dual-beam implantation, if the increased hardening is due to an increased cluster size.

$$r = a_0 \left(\frac{3N}{8\pi} \right)^{\frac{1}{3}} \tag{4.3.1}$$

This increase in cluster size seems more likely than an increase in cluster density. Helium-vacancy clusters formed during a 300°C implantation contain two helium atoms based on DFT modelling and the measured elastic strains.[119] The higher implantation temperature favours larger complexes with fewer helium atoms,[156] therefore the clusters formed at 800°C likely only contain one or two helium atoms. The increased hardening of the dual-beam specimen compared to the helium implanted specimen requires nearly three times the number of defects, which is not possible.

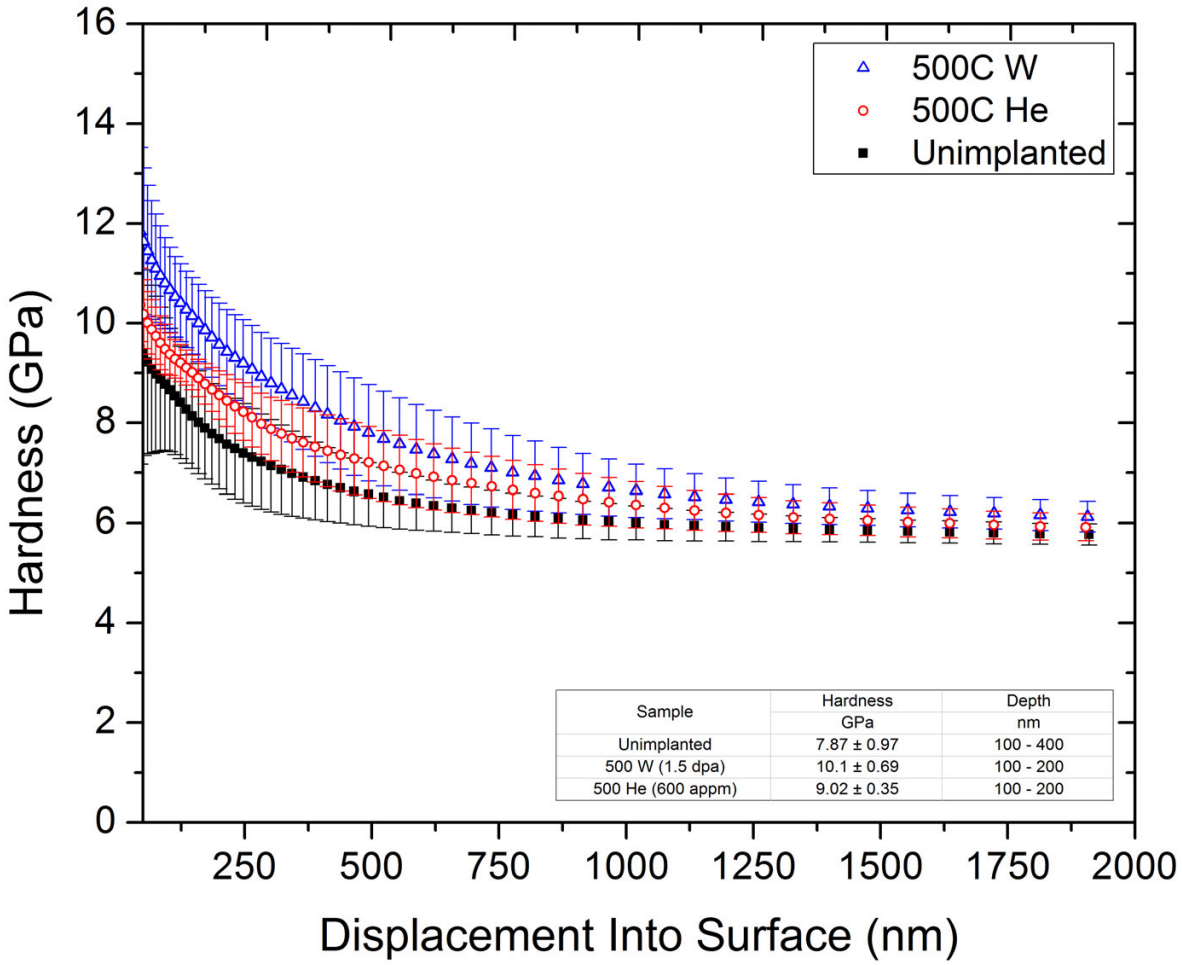

Figure 4.4: Hardness with depth for samples produced at 500°C at Surrey (He) and IPP Garching (W). The thinner damaged layers from these beam lines mean hardnesses are evaluated from 100-200 nm. The same trends as the 800°C data are seen: self-ion damage produces a greater hardening effect than helium damage.

Figure 4.4 shows the variation in hardness with depth for samples irradiated at 500°C. The same behaviour as the 800°C data is seen: a small increase in hardness due to the helium-ion implantation (1.15 GPa) and a larger increase with self-ions (2.23 GPa). These data and the complete hardness-depth curves in figure 4.5 allows a comparison between tungsten irradiated at 500°C and 800°C. The samples from each temperature are extremely close in hardness. The helium-implanted samples differ by 0.4 GPa with an average error of 0.66 GPa. The difference between the tungsten samples is 1.03 GPa with an average error of 1.15 GPa, and the slight difference between the tungsten-implanted samples below 250 nm - 0.5 GPa at 125 nm - is likely due to a slight

difference in the specific tip area function as the values are very close elsewhere. These results are not unsurprising; vacancies are relatively mobile at both temperatures[116,242] and thus the damage structures formed are likely to be similar.

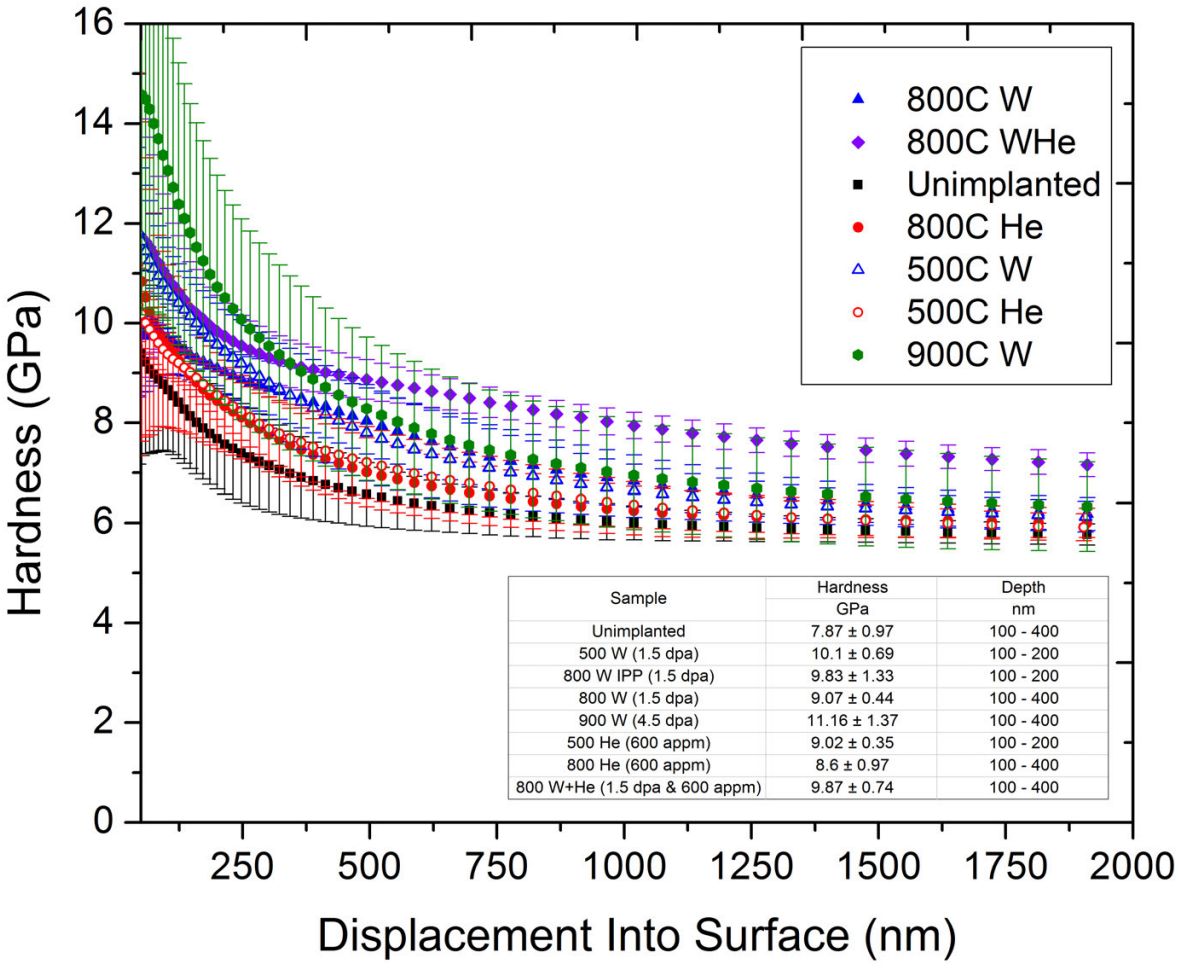

Sample	Hardness GPa	Depth nm
Unimplanted	7.87 ± 0.97	100 - 400
500 W (1.5 dpa)	10.1 ± 0.69	100 - 200
800 W IPP (1.5 dpa)	9.83 ± 1.33	100 - 200
800 W (1.5 dpa)	9.07 ± 0.44	100 - 400
900 W (4.5 dpa)	11.16 ± 1.37	100 - 400
500 He (600 appm)	9.02 ± 0.35	100 - 200
800 He (600 appm)	8.6 ± 0.97	100 - 400
800 W+He (1.5 dpa & 600 appm)	9.87 ± 0.74	100 - 400

Figure 4.5: Hardness with depth for all samples. The 500°C and 800°C data for each ion match closely, likely due to similar vacancy mobilities at these temperatures.

Two separate 800°C self-ion irradiations were performed. The data shown above are from the JANNuS irradiations, however an additional ion-irradiation was required to produce several samples for high-temperature nanoindentation. This was carried out at IPP Garching, and the comparison between the two beamlines is shown in figure 4.6. There could potentially be a difference between the degrader-based and defocussed beam at JANNuS and the multiple energy-based and rastered implantation at Garching. However, within error bars (0.89 GPa) there is no difference in hardness and Hewitt[236] shows the same behaviour in pure iron as that seen here: no change between rastered and defocussed beams.

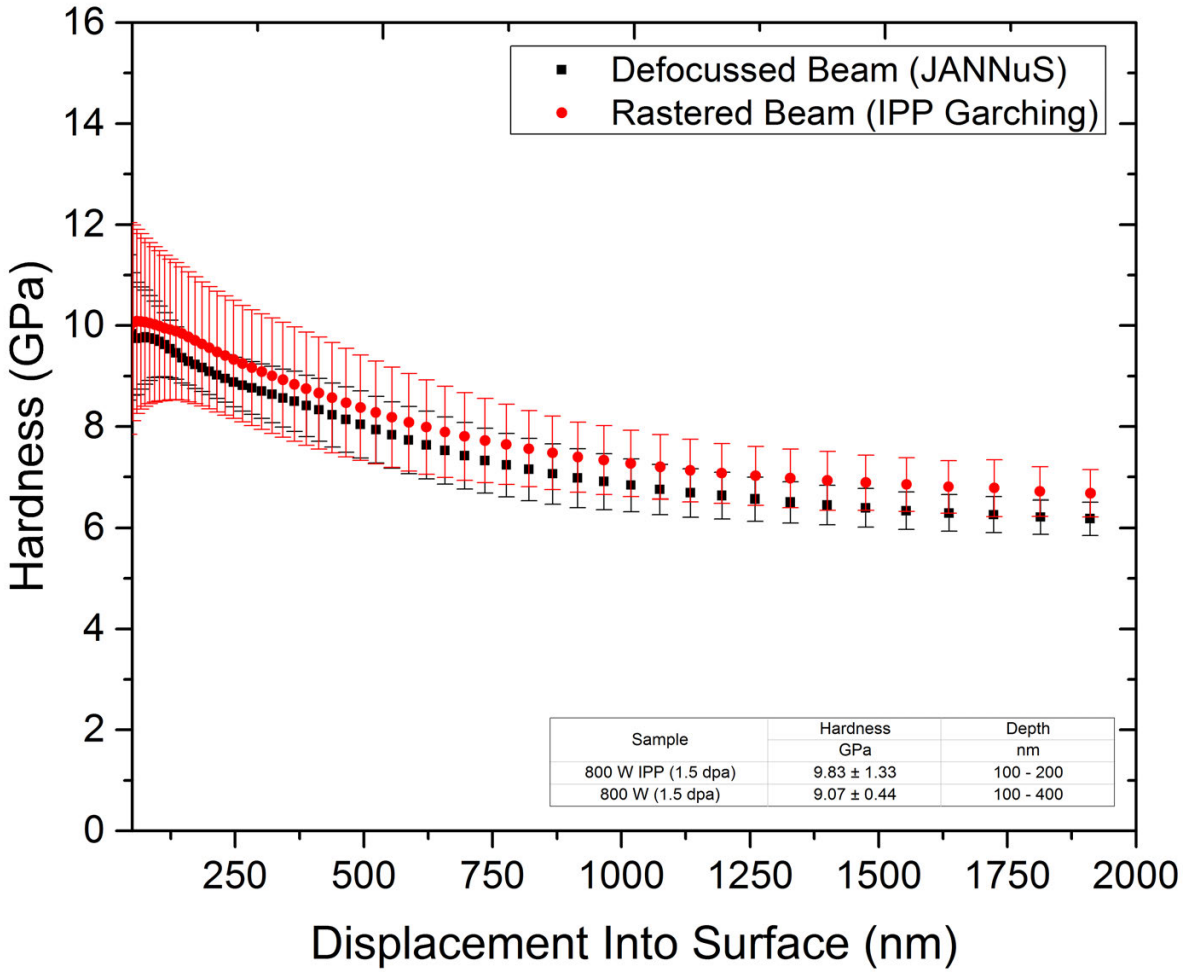

Figure 4.6: Hardness with depth for self-ion irradiated tungsten at IPP Garching and JANNuS. No difference is present within error bars, indicating that the damage produced by rastered and defocussed ions beams is the same in pure tungsten.

Finally, an interesting effect of irradiation temperature is seen in figure 4.7, which shows the hardness of self-ion implanted tungsten for implantations at 500°C, 800°C and 900°C. There is a clear increase in hardness with damage level, with all the 1.5 dpa samples (at 500°C and both 800°C implantations) showing similar levels of hardness; 9-10 GPa. The IPP-implanted specimen is not shown for clarity, but it has already been seen that both 800°C implantations are identical. This can again be compared with Armstrong's implantations at 300°C:[143] these show a saturation in hardness at approximately 0.4 dpa with an increase in hardness of 0.82 GPa. His 1.2 dpa sample shows a hardness increase of 0.73 GPa. In this work, the increase in hardness of the 1.5 dpa specimens is ∼1.7 GPa, slightly higher than Armstrong. However, a significant difference is seen in the 4.5 dpa sample with a hardness increase of 3.3 GPa. Figure 4.8 shows a FIB cross-section of the surface of the sample. No surface oxide is seen, confirmed by the determined modulus of 381 GPa. Therefore this significant increase in hardness is only due to the implanted damage.

In TEM characterisation by Yi,[79] a 300°C, 1.5 dpa implantation produces dislocation loops of which 60% are below 3 nm in size. At 500°C or 750°C the size distribution increases slightly, with 60% of loops below 4 nm. The near-identical loop size distribution at 500°C and 750°C explains the similar values of hardness measured in this work.

Between 1.5 dpa and 4.5 dpa at 500°C a small increase in the frequency of <3 nm loops is observed. No significant changes are seen in the larger loops. As the largest loops harden more than the smaller loops, the hardening in the 900°C, 4.5 dpa material is very likely due to an increase in loop size rather than loop number density. Resistivity measurements during annealing of neutron-irradiated tungsten[243] show a step around 900°C. A similar step is seen around 400°C where vacancy mobility becomes significant. Therefore, the increased atomic mobility at 900°C - also seen by the thermal grooving in figure 4.2 - may facilitate the formation of larger loops, even though no change in loop size is seen between 500°C and 750°C. However, additional damage and therefore hardening mechanisms such as void formation may be present at these higher temperatures. TEM characterisation of the material would be required in order to conclusively determine the mechanism.

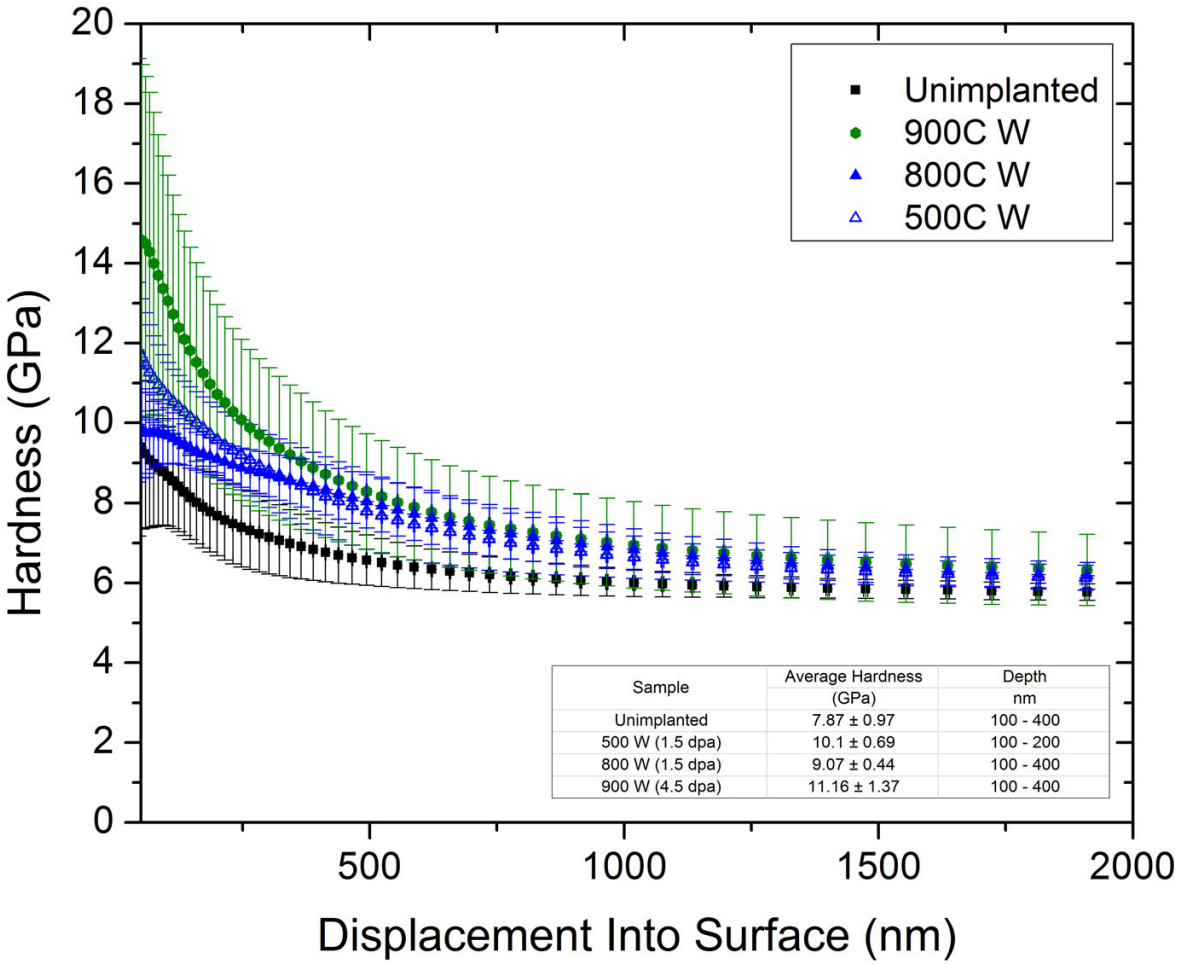

Figure 4.7: Hardness with depth for all self-ion irradiated samples. There is a significant increase in the hardness of tungsten irradiated to 4.5 dpa at 900°C of 3.3 GPa.

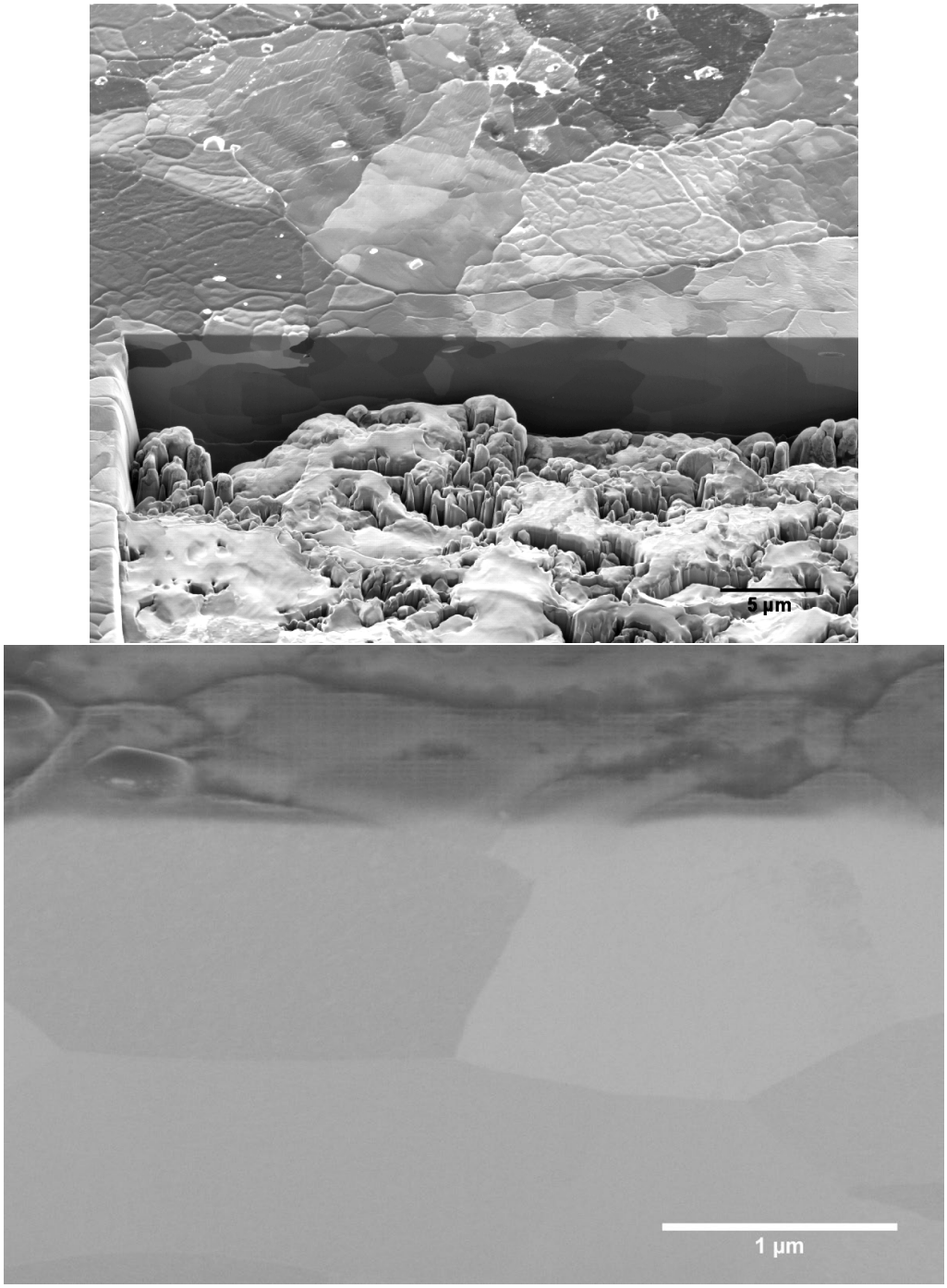

Figure 4.8: FIB cross-section at low and high magnification showing no evidence of surface oxide. This, and the sensible value of elastic modulus means the significant hardening measured in this sample is therefore just due to the implanted damage.

By examining the irradiation hardening for all the samples irradiated (figure 4.9), it can be seen that overall hardness levels for the 500 and 800°C samples are fairly similar, with 600 appm He producing comparable hardening to 1.5 dpa of irradiation damage.

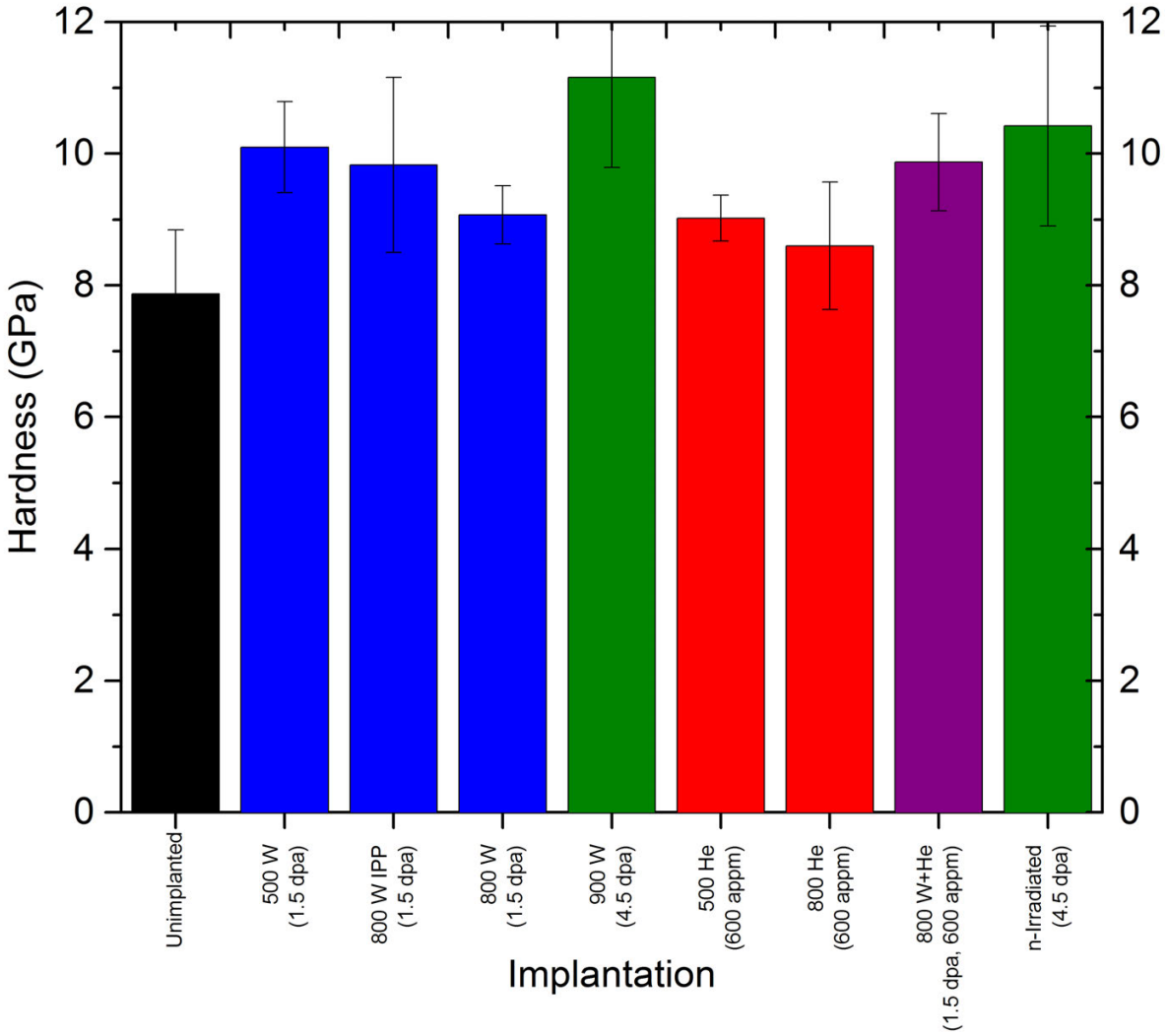

Figure 4.9: Hardness for all ion irradiated samples. Values shown are averaged from the depths detailed in the previous hardness-depth curves, typically 100-400 nm.

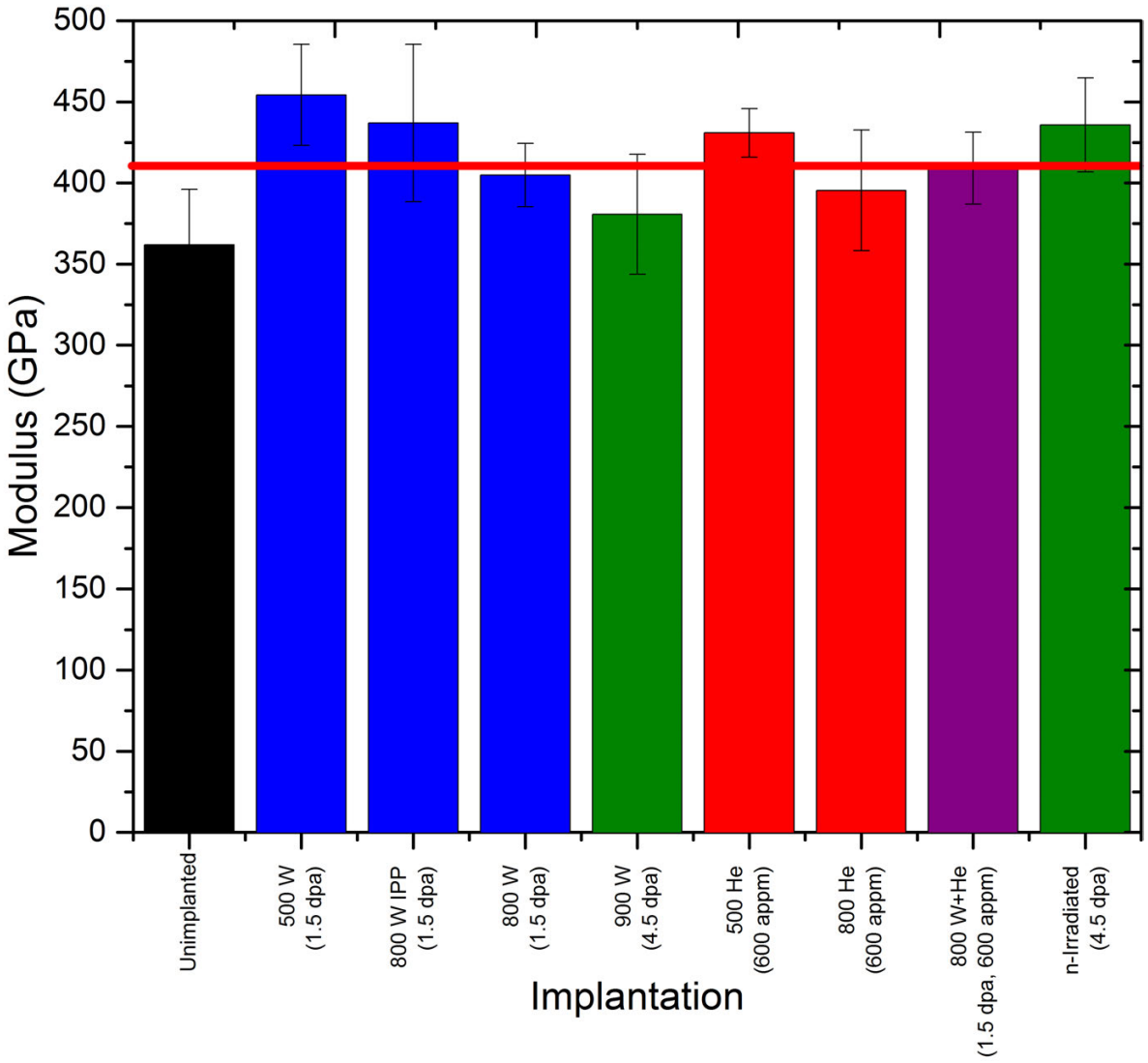

Figure 4.10: Modulus for all ion irradiated samples. The average value is 416 GPa, very close to literature values.

Figure 4.10 shows the modulus data for all the indentations. It can be seen that all the data are fairly similar, and close to the literature value of 410 GPa. This indicates that the damage is not affecting the elastic modulus of tungsten. To confirm, a one-sample z-test can be performed. This takes the form of equation 4.3.2, where $\bar{x}$ is the sample mean (determined modulus), μ_0 the value to be tested (the literature value of modulus), σ the standard deviation (32 for these indents) and n is equal to 1.

$$t = \frac{\bar{x} - \mu_0}{\frac{\sigma}{\sqrt{n}}} \tag{4.3.2}$$

The determined z values are given in table 4.1. As the determined modulus could be higher or lower than the literature, a two-tailed test is used at a 90% confidence interval to give the p values. None of the determined p values are below 0.05, therefore the differences from the literature value of 410 GPa are not considered statistically significant.

Irradiation Condition	z Value	p Value
Unimplanted	-1.51	0.13
500°C W (1.5 dpa)	1.38	0.17
800°C W IPP (1.5 dpa)	0.84	0.40
800°C W (1.5 dpa)	-0.16	0.87
900°C W (4.5 dpa)	-0.92	0.36
500°C He (600 appm)	0.65	0.51
800°C He (600 appm)	-0.46	0.65
800°C W+He (1.5 dpa, 600 appm)	-0.03	0.98
900°C Neutron (4.5 dpa)	0.81	0.42

Table 4.1: Determined z values, comparing the determined moduli with the literature value of 410 GPa.

A Nix-Gao[208] size effect analysis can be applied to the nanoindentation data. This model states that the hardness of a material (H) varies according to equation 4.3.3, where H_0 is the hardness at infinite indentation depth, h^* is the characteristic length depending on the hardness, indenter profile and shear modulus, and h is the indentation depth. As CSM provides multiple values of H with h, this model can be fitted to individual indents. This has been carried out for unimplanted tungsten and the three implantations performed at JANNuS. These results are shown in table 4.2.

$$H = H_0\sqrt{1 + \frac{h^*}{h}} \tag{4.3.3}$$

Irradiation Condition	Bulk Hardness (H_0) (GPa)	Characteristic Length (h^*) (nm)
Unimplanted	**6.12** ± 0.55	**71.89** ± 36.58
1.5 dpa W (JANNuS)	**8.24** ± 0.43	**74.39** ± 42.11
600 appm He (JANNuS)	**6.11** ± 0.73	**176.94** ± 100.07
W & He (JANNuS)	**8.78** ± 0.53	**74.82** ± 61.88

Table 4.2: NixGao analysis from CSM data, using the MATLAB code of S. Connolly[225] to fit indentation size effect curves. The values of bulk hardness are close to, but slightly lower than, those determined from the 100-400 nm data. The characteristic lengths are reasonably close and match well with literature data.

The data in table 4.2 show a small size effect in the data obtained from the indentations (figure 4.3) of 22% (1.5 GPa). The trends in the values of H_0 follow the behaviour of the indentation data. The characteristic lengths obtained for all but the helium implantation are very similar, although there are large error bars on the helium data. The characteristic length of ∼100 nm matches well with Armstrong's indentation data,[143] and shows that the indentation size effect does not significantly change with irradiation.

4.4 Discussion

Nanoindentation has been used on all the ion-irradiated samples. The effect of temperature on irradiation-induced hardening appears to be minimal for samples irradiated at 500°C and 800°C for both self-ion and helium-ion irradiation. As vacancy mobility will have a strong influence on the damage structure, it is not surprising that this is true as vacancy mobility becomes significant about 430°C.[116,242]

Keys and Moteff[243] suggest the 500°C recovery temperature ($0.15T_m$) is due to 'a mobile self-interstitial, immobile vacancy, recovery process'. The additional recovery temperatures at $0.22T_m$ and $0.33T_m$ (750°C and 1050°C) are suggested to be divacancy migration and monovacancy migration, respectively. While their data clearly shows a recovery at these temperatures, their assigned mechanisms are suspect. Other authors[79,116] suggest that it is vacancy migration that occurs at ∼500°C. Indeed the energy for ⟨111⟩ dumbbell migration is so low: 0.004-0.022eV[244,245] that interstitials are mobile at almost all finite temperatures. Thus it is likely that the difference in irradiation behaviour between Armstrong's 300°C specimens and those detailed above are due

to vacancy mobility.

If it is assumed that the irradiation-induced defects harden via an Orowan (dislocation-bowing) mechanism, then the strength of the irradiation-induced obstacles can be analysed in two similar ways: the dislocation breakaway angle from the defect, and the increase in hardness due to the presence of the defect.

The breakaway angle is given by equation 4.4.1.[246] G is the bulk modulus (161 GPa), b the Burgers' vector (0.22 nm), L is the obstacle spacing, $\Delta\tau$ is change in shear yield stress due to obstacles (approximately $\frac{\Delta H}{6}$).

$$\phi_c = 2arccos(\frac{Gb}{L\Delta\tau}) \tag{4.4.1}$$

The obstacle spacing - to a first approximation - is given by the cube root of the inverse of the obstacle density. In the self-ion implanted material this is the loop number density. For the 1.5 dpa samples, the loop number density is 1.8×10^{22} m^{-3} at 750°C, based on observations in [100] grains.[79] The loop size distribution shows of 45% of loops are >4 nm in diameter at 750°C. It is assumed that the largest loops (4 nm) dominate the hardening process (see section 5.4) then the breakaway angle in this material is 148°.

In the helium-implanted material it is assumed that the helium sits in small He_nV_m clusters (with $n < 4$), as the high irradiation temperature favours large complexes with lower helium content when compared to low temperatures where vacancies are not mobile.[156] The obstacle density is therefore calculated by distributing the 600 helium atoms among 5×10^5 tungsten unit cells each of volume 3.16×10^{-29} m^3. For $1 \leq n \leq 4$, ϕ_c varies between 178° and 179°, i.e. each helium-vacancy cluster is an extremely weak obstacle.

The increase in yield stress ($\Delta\sigma_{Orowan}$) due to the presence of the defect is given by equation 4.4.2,[247] where G is shear modulus, b is Burgers' vector ν is Poisson's ratio, M is Taylor factor used to convert shear strength to uniaxial yield strength (3.06), r_s is the average radius of cross section of clusters on the slip planes, r is the mean radius of the clusters and λ is the inter-particle spacing.

$$\Delta\sigma_{Orowan} = M\frac{0.83Gb}{2\pi(1-\nu)^{0.5}}\frac{1}{\lambda}ln(\frac{2r_s}{4b})$$
$$r_s = \sqrt{\frac{2}{3}}r \tag{4.4.2}$$

Equation 4.4.2 gives $\Delta\sigma_{Orowan}$ as 0.97 GPa for the 1.5 dpa self-ion implanted sample. This predicts a 2.91 GPa increase in hardness after self-ion irradiation, approximately 2.5 times more than the experimental increase of 1.2 GPa. This implies that the dislocation loops are weaker obstacles than those described by an Orowan mechanism, which may therefore mean that loops are hardening via their associated stress field rather than being hard obstacles to dislocation motion.

In the helium-implanted material, $\Delta\sigma_{Orowan}$ depends very strongly on the defect size. As the helium-vacancy clusters cannot be observed in the the TEM,[154] it shall be assumed for the purposes of the calculation that the defects are 1 nm in diameter, based on work in iron.[248] $\Delta\sigma_{Orowan}$ thus varies from 4.6 to 2.9 GPa for $1 \leq n \leq 4$, i.e. the hardness should increase by up to 14 GPa after helium implantation. Clearly this is not observed experimentally and the assumption that the helium-vacancy clusters can be described using an Orowan-Ashby model is likely to be false. Instead, their hardening effect must be due to another mechanism. Given the size of the clusters, a mechanism more similar to that of a Cotrell atmosphere seems more plausible.

Alsabbagh[247] carried out a similar analysis to the above calculations in more detail in work on neutron-irradiated stainless steel, which included additional possible strengthening mechanisms after irradiation. Four main mechanisms contribute to the increased strength in irradiated materials: grain size (GS), solid solution (SS), atomic clustering (Clu) and dislocation hardening (Dis). This can be written as:

$$\Delta\sigma_{irr} = \Delta\sigma_{GS} + \Delta\sigma_{SS} + \Delta\sigma_{Clu} + \Delta\sigma_{Dis} \tag{4.4.3}$$

No change in grain size was observed before and after the irradiations. Pure tungsten was investigated, hence no solid solution strengthening is possible. As such, equation 4.4.3 can be written as:

$$\Delta\sigma_y = \sigma_{\text{after}} - \sigma_{\text{before}} = \Delta\sigma_{Clu} + \Delta\sigma_{Dis} \tag{4.4.4}$$

The strength increase due to irradiation-induced clusters - Mn-Si clusters in Alsabbagg's work - can be described using an Orowan-Ashby model given by equation 4.4.2. Although this model is commonly used for incoherent precipitates such that dislocation bowing occurs, previous studies[249, 250] on different ferrous alloys showed that hardening due to nano-clusters modelled by Orowan is capable of explaining the observed increase in yield stress. In this work, the damage is either in the form of helium-vacancy clusters or dislocation loops where it has been shown that this model is not fully applicable.

$$\Delta\sigma_{dis} = \alpha MGb(\sqrt{\rho_{irr}} - \sqrt{\rho_{unirr}}) \tag{4.4.5}$$

Where ρ is the dislocation density, α is a strengthening coefficient (0.4 for BCC metals).

Hence:

$$\Delta\sigma_y = \Delta\sigma_{Orowan} + \Delta\sigma_{dis} = M\frac{0.83Gb}{2\pi(1-\nu)^{0.5}}\frac{1}{\lambda}ln(\frac{2r_s}{4b}) + \alpha MGb(\sqrt{\rho_{irr}} - \sqrt{\rho_{unirr}}) \tag{4.4.6}$$

In the self-ion irradiated material, the unirradiated dislocation density is estimated to be 5×10^9 m^{-2} based on Giannattasio's calculations on the same material.[54] ρ_{irr} is calculated as 2.7×10^{12} m^{-2}, i.e. a plausible increase of around 500 times. The loop number density from Yi for an 800°C irradiation is 2.1×10^{15} m^{-2}, much higher than ρ_{irr}. The loops are therefore likely to dominate the hardening of self-ion irradiated tungsten.

For the helium-implanted material, again assuming a 1 nm defect size, ρ_{irr} is calculated as 2.3×10^{15} m^{-2}, roughly a 10^5 times increase above the unimplanted density. This is a significant increase, but is likely erroneous due to the aforementioned problems with the calculation of $\Delta\sigma_{Orowan}$.

Looking at the effect of temperature in self-ion implanted material, the loop density at 750°C falls to 33% of the 300°C value.[79] Despite this, the hardening is 233% higher, implying the larger loops are roughly 700% stronger obstacles. This is significant given the loops only double in size, with the stress field around a dislocation scaling proportional to b. The modest change in

dislocation breakaway angle between the 2 nm defects at 300°C and that calculated above (13%) also casts doubt on this implication. Therefore, it is possible another hardening mechanism such as void formation is taking place here during high-temperature implantation. Alternatively, the formation of loop strings or loop rafts at higher temperatures and damage levels[79] may increase the amount of hardening the implanted damage is able to achieve.

Examining the results for helium-implanted tungsten, Hofmann et al. have done extensive characterisation of a 300°C, 3000 appm helium-implanted W-1%Re alloy[119] that demonstrates the significant elastic strains from implanted helium. They use micro-Laue diffraction to measure an out-of-plane lattice strain of 1.5×10^{-3} that results in a hydrostatic strain of 2.620×10^{-3}. This gives in-plane stresses of 0.32 GPa and out-of-plane stress of 0.81 GPa due to the implanted defects and in the in-plane case also the boundary condition requiring continuity of the material at the interface between the implanted layer and the substrate. These significant stresses likely explain the significant hardening seen in indentation experiments.[120] Using DFT, they also show that the helium-vacancy clusters likely contain a pair of helium atoms.

The hardness increase for 300°C implantations are 1.2 GPa for 300 appm in pure tungsten[120] and 5.56 GPa after 3000 appm helium implantation for W-1% Re.[154] Here, 600 appm produces a hardening of 0.73 GPa at 800°C and 1.13 GPa at 500°C. Figure 4.11 shows that based upon these results and those from Armstrong and Beck that the increase in hardness with helium concentration appears to be linear, regardless of implantation temperature or slight changes in alloy composition. This is in stark contrast to the self-ion results that show an saturation in hardening at 300°C that is not present above 800°C. Mason[241] shows that the number of point defects N in a $\frac{1}{2}\langle 111 \rangle$ loop in tungsten is given by equation 4.4.7. A 2 nm loop with $a_0 = 2.86 \times 10^{-10}$, requires 265 point defects increasing to 1062 defects for a 4 nm loop. The significantly higher defect requirement for loops to form may explain why the smaller helium-vacancy clusters show this different behaviour with temperature.

$$r = a_0 \sqrt{\frac{N}{\pi\sqrt{3}}} \tag{4.4.7}$$

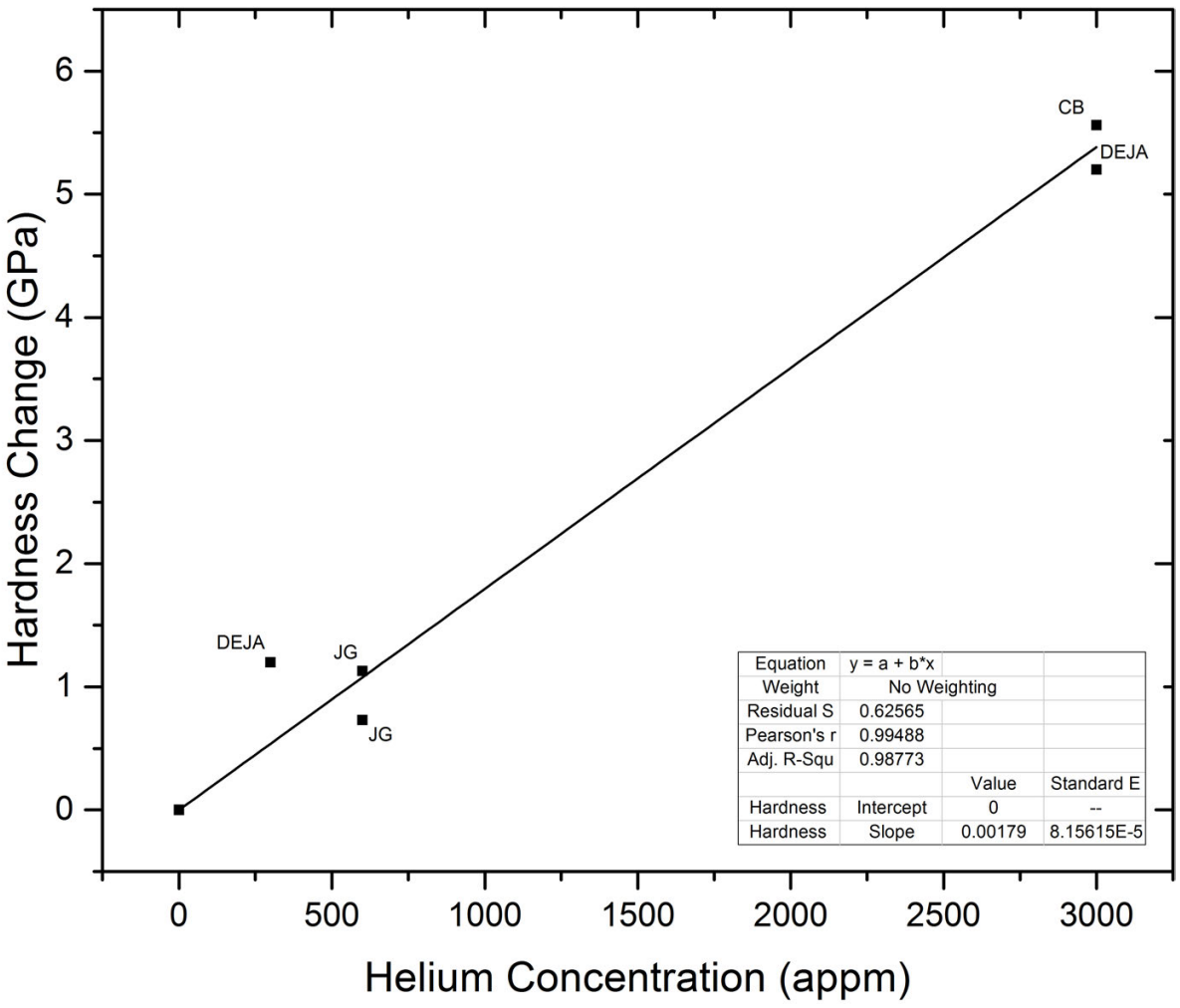

Figure 4.11: Increase in indentation hardness for a given implanted helium concentration. Values from Armstrong (DEJA)[120] and Beck (CB)[154] are also used. The increase in hardness from helium implantation seems to only depend on the injected helium concentration, as other implantations were performed at 300°C.

4.5 Summary

Nanoindentation has been performed on samples irradiated under tungsten and helium ion beams at 500°C and 800°C. There are no effects of implantation temperature or beam rastering on the hardness of the implanted samples. The hardness of the self-ion implanted samples does not appear to saturate, unlike implantations performed at 300°C. However, the hardness of helium-implanted tungsten appears to only depend on the injected helium concentration. It is likely that these differences are due to the greater number of defects required required to form a dislocation loop compared to a helium-vacancy cluster.

Neither helium-vacancy clusters nor dislocation loops can be described as Orowan-like obstacles. Given the size of helium-vacancy clusters, it is likely that dislocations are pinned via a Cotrell atmosphere mechanism. This implies that the increased hardening seen at room temperature in the dual-beam irradiated sample is due to an increase in defect density rather than defect size.

The Nix-Gao size effect analysis demonstrates that there is no change in the indentation size effect after irradiation. During indentation, the size effect at small scales is still determined by the work hardening due to geometrically necessary dislocations. The amount of induced defects by the irradiation is not significant enough to cause additional hardening in this regime.

Chapter 5

Hot Nanoindentation

5.1 Introduction

Chapter 4 showed the importance of vacancy mobility in mechanical behaviour. As a result, and because tungsten will not be in service at room temperature, it is necessary to assess how the mechanical properties of tungsten change with temperature in the presence of radiation damage.

Some of the samples analysed in chapter 4, namely tungsten irradiated with tungsten or helium ions at 800°C were indented in the high-temperature nanoindenter described in section 3.3.

5.2 Method

Unlike the room temperature nanoindenter systems, the MicroMaterials instrument does not have a CSM indentation option. In order to obtain the values of hardness with indentation depth required to analyse the effect of the ion-implanted damage, load partial-unload indents must be performed.

The unimplanted and helium-implanted material was analysed using the load partial-unload indent profile shown in figure 5.1. A software upgrade later allowed specific depths to be targeted to produce the load profile in figure 5.2, which was used to test the tungsten-implanted sample. This reduced the amount of time - and hence overall drift - for each indent. Loading and unloading was conducted at a rate of 1.5 mN/s, with a 15 s hold at the peak load for each cycle. At least 36 indents were performed at each temperature.

The initial load-unload profile (figure 5.1) was determined by specifying a depth target of 2000 nm that was divided into twenty segments in order to obtain data every ∼100 nm. CSM data at room temperature shows that for these implantations, data for the ion-implanted layer should be extracted from 100-400 nm, and bulk data from >1500 nm. This profile therefore allows approximately four values of hardness to be averaged to give an ion-implanted hardness and bulk hardness for each indent in the array. Data from partial unloads outside this depth range were discarded. The updated load-unload curve (figure 5.2) was constructed in a similar way: unload

portions every ∼100 nm to measure the ion-implanted layer, and three deeper unloads in order to evaluate the bulk hardness.

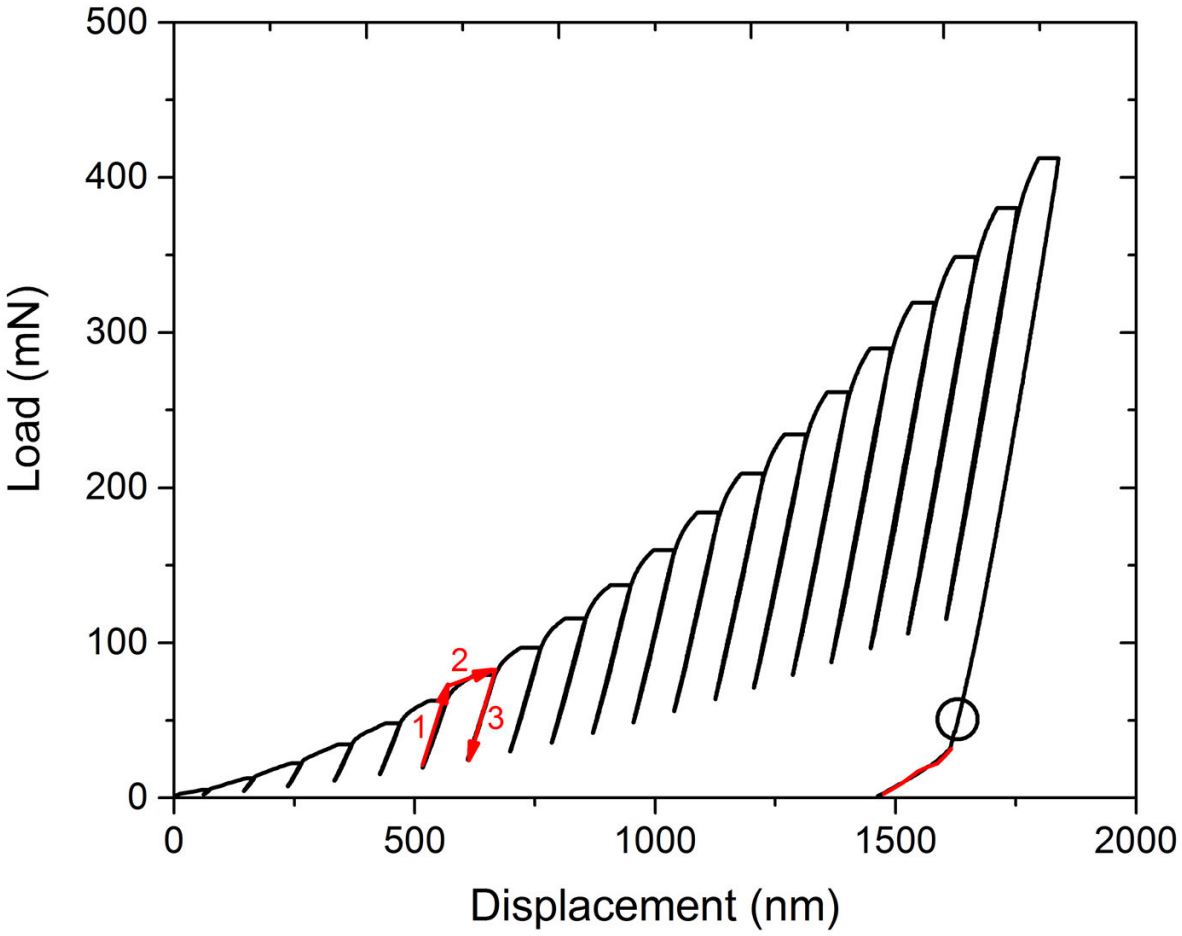

Figure 5.1: Example load-partial unload for determining hardness with depth. Each load-unload segment consists of three parts: (1) A loading portion; (2) a hold period, typically 15 s; (3) an unload portion. The load is then increased, and the lack of any hysteresis further demonstrates the tight control of thermal drift. The circled part of the curve indicates the measurement of thermal drift post-indentation. The anomaly present after the thermal drift measurement - highlighted in red - is discussed below and is likely due to tip roughness.

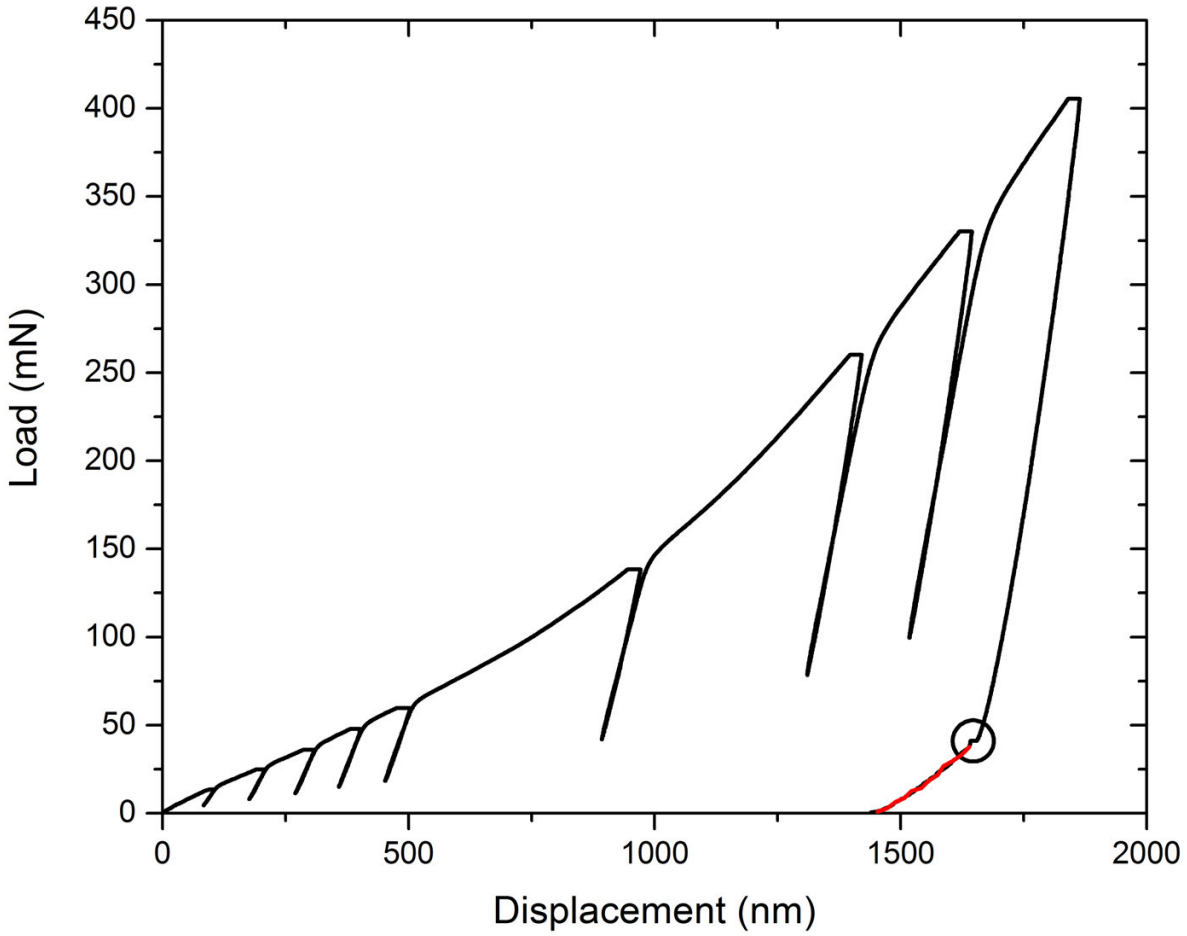

Figure 5.2: Better load-partial unload for determining hardness with depth, accessible after a software upgrade. The load-hold-unload behaviour of each segment is identical to that shown in figure 5.1. The circled part of the curve indicates the measurement of thermal drift post-indentation. The anomaly present after the thermal drift measurement - highlighted in red - is discussed below and is likely due to tip roughness.

Both figure 5.1 and 5.2 show a possible artefact in the curve after the post-indentation thermal drift measurement. The thermal drift measurement is circled in figures 5.1 and 5.2, with the artefact highlighted in red. In the G200 this part of the curve would have the same slope at the final unload, whereas here it clearly does not. This feature is present in the vast majority of the load-displacement curves collected, and is seen in other work on the MicroMaterials indenter.[251, 252] It does not appear to be due to thermal drift or creep, as it is present both at room temperature and despite the very low levels of thermal drift. This part of the curve is not used for the calculation of hardness, so it should not have an effect on the final data. Discussions with MicroMaterials suggest

that it could be due to a difference in surface roughness between the tip suppliers and hence a small degree of mechanical keying. This is supported by the fact the G200 uses a diamond tip and the MicroMaterials indenter a cBN tip. If a diamond tip is used in the MicroMaterials system at room temperature this effect is significantly reduced, as shown in figure 5.3.

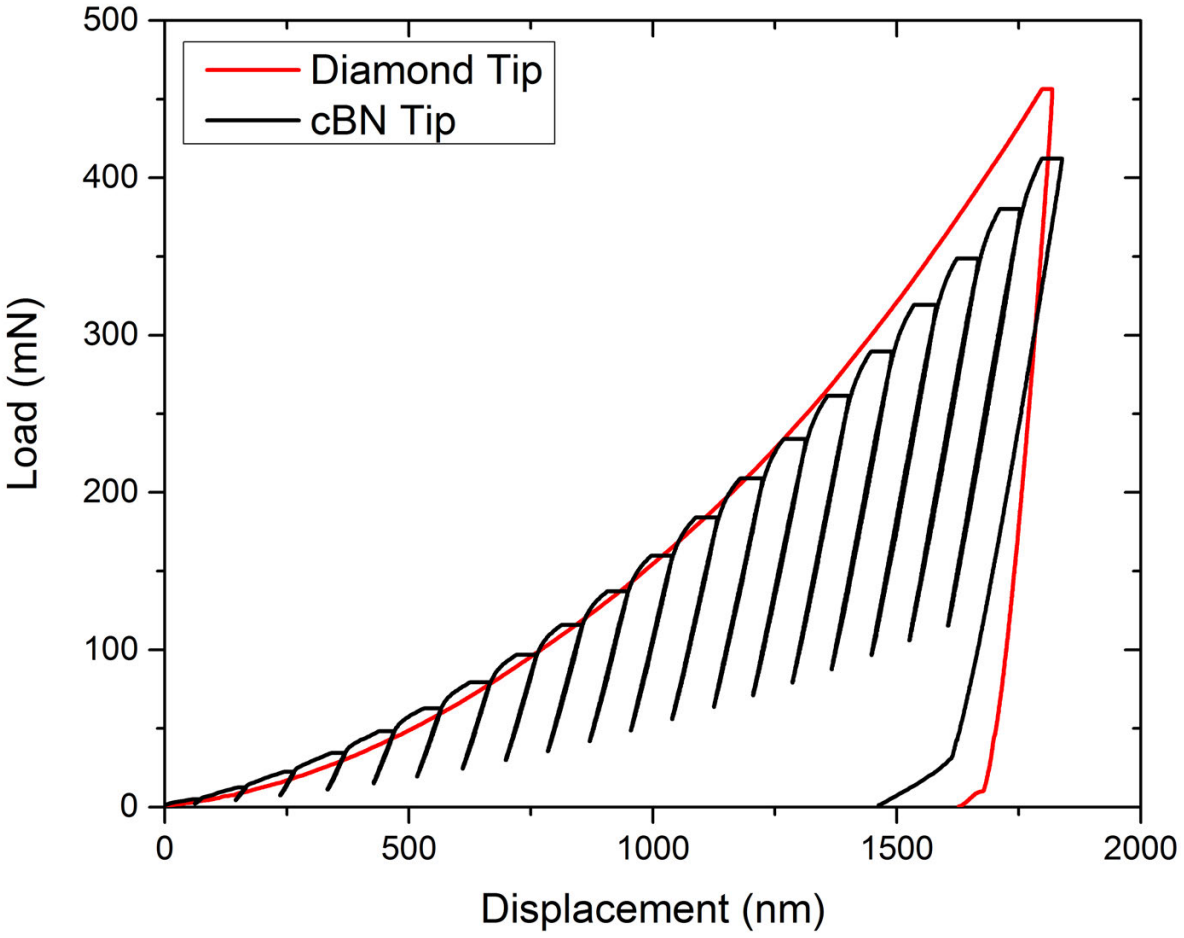

Figure 5.3: Comparison of indents made with a diamond tip and a cBN tip at room temperature. The artefact present after the thermal drift measurement is significantly reduced by using a diamond tip.

A thermocouple was cemented to the surface of the sample to monitor the temperature of the material in contact with the indenter. A second thermocouple in the indenter was used to obtain an isothermal contact. Prior to the start of each indentation, the tip was brought into contact with the sample for 120 s in a thermalisation step. Drift rates were measured pre-indentation (after the thermalisation step) and after the final unload cycle at a load of 30% of the peak load. In each case, these drift rates were measured for 60 s.

Samples were heated from 50°C to 750°C in 100°C increments, with indents performed at each temperature. The sample was heated at a rate of 2°C/min. The system was then left to stabilise for at least six hours before performing tests. For the helium-implanted sample, once a set of indentations had been performed at 750°C, the sample was cooled at 2°C/min and indentation was also performed successively at 550°C, 350°C, 50°C and 20°C. At each of these temperatures the six hour stabilisation was also carried out. This was done to assess the hardening behaviour after the sample had been held at an elevated temperature, determining the stability of the helium-induced damage. No softening was seen in the self-ion implanted sample, thus indents were only performed on the 'heating' cycle.

It is necessary to minimise thermal drift in the system in order to produce accurate data, especially for the long contact times (∼25 minutes) required for a complete load-partial unload indentation. This is done by matching the temperature of the tip with the temperature of the sample to <1°C, as a thermal fluctuation of this magnitude can lead to a drift displacement of ∼100 nm.[174]

Temperature matching was accomplished by initially matching the temperature measured by the indenter thermocouple with that measured by the thermocouple mounted to the sample before testing. This was done with the tip in close proximity (∼20 μm) to the sample. At these distances, the tip temperature is strongly influenced by radiative heating from the sample. In order to produce a stable tip temperature and prevent drift during the experiment, the input power from the heater must balance the contributions from both the radiative heating and conduction when the tip is in contact with the sample. The temperature-matching process is further complicated due to the tip thermocouple being positioned closer to the heater than the actual Berkovich tip, leading to uncertainty in the actual tip temperature.

A series of single indents were thus performed in order to confirm temperature stability by measuring drift rates and observing the shape of the load-displacement curve. If drift levels were too high, the tip temperature was varied based on the measured drift rates and more single indents were performed to check the drift rates. Once stability was confirmed within the system, the load-partial unload array began.

5.3 Results

5.3.1 Thermal Drift

As mentioned earlier, the control of thermal drift is critical in producing accurate, quantitative data. It is also the biggest challenge in high-temperature nanoindentation, and the reason why the hardness-temperature behaviour for each condition (unimplanted, helium implanted, self-ion implanted) takes up to four weeks to collect. Comparable data from the G200 at room temperature requires only one hour.

Figure 5.4 shows pre-indentation thermal drift data for indents performed at 50°C, 350°C and 750°C on the helium-implanted sample. Pre-indentation drift is a good measure of the stability of the system as the data are not convoluted with creep effects from the sample. The scatter of the data increase with temperature, however all three drift rates are below 0.01 nm/s, comparable with drift rates obtained at room temperature. This thermal stability therefore allows quantitative, repeatable values of hardness to be measured.

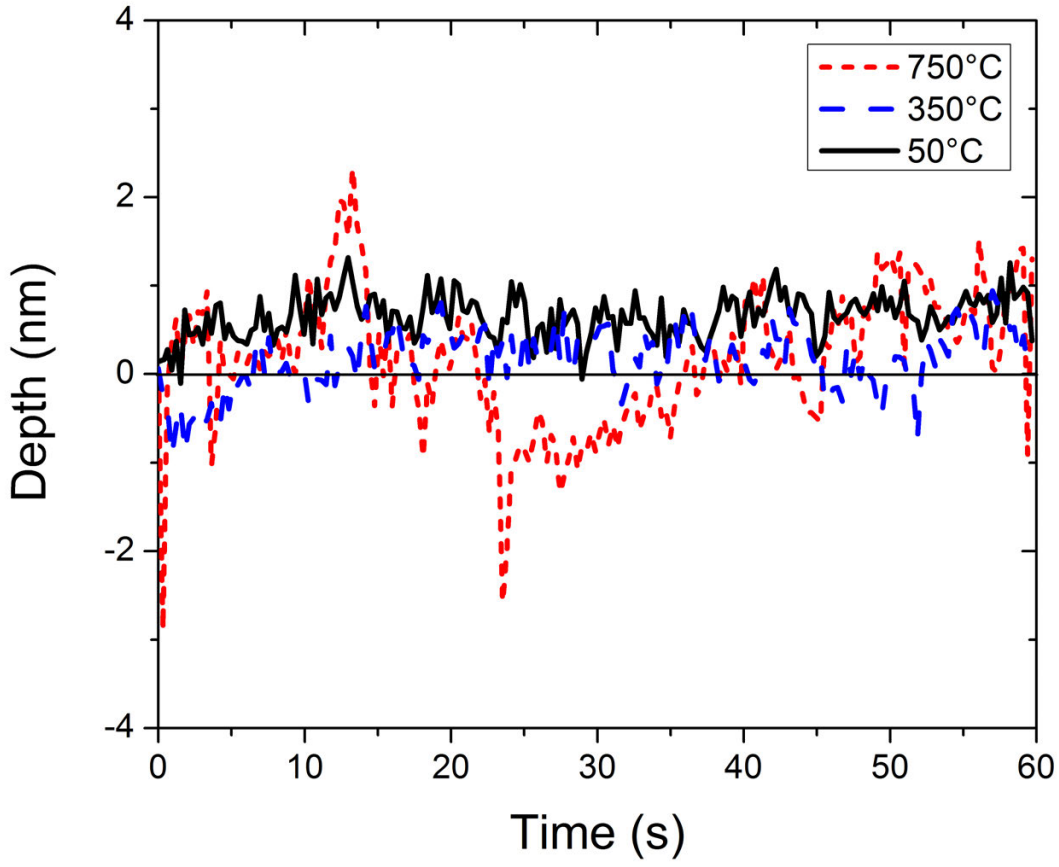

Figure 5.4: Pre-indentation thermal drift data for indents performed at 50°C, 350°C and 750°C. The 750°C indentation shows greater scatter, but all three drift rates are below 0.01 nm/s.

The load-displacement data are corrected using the average (pre and post-indentation) thermal drift measurements before values of hardness are calculated. The average thermal drift for each indent array is given in table 5.1. For the unimplanted and helium implanted samples, indents were discarded if the average drift rate was >0.15 nm/s. This corresponds to a maximum allowable total drift of 180 nm, or 9% of the total indent depth. Drift levels were higher in the tungsten-implanted sample tested due to failure of the air conditioning in the lab, but test times were also shorter due to the improved load-partial unload program. In this case, 66% of the indents at 550°C were below 0.25 nm/s (165 nm total drift with an overall error of 8%) and 72% of the indents at 650°C were below 1.2 nm/s (790 nm total drift with an overall error of 40%). Although much of this displacement is corrected for, it still leads to greater uncertainty in the calculated values of hardness hence larger error bars on the data.

Temperature	% Indents With Drift (nm/s)					
	<0.15	<0.05	<0.15	<0.05	<0.15	<0.05
	Unimplanted		He-Implanted		W-Implanted	
50	100	57	100	62	100	56
150	100	47	100	97	96	72
250	80	40	97	51	100	23
350	100	47	99	57	62	0
450	100	85	100	6	80	15
550	100	29	89	39	23	0
650	97	53	96	64	0	0
750	100	57	93	58	-	-

Table 5.1: Average values of thermal drift over the full indent array for each of the three samples tested. The levels of thermal drift in the tungsten-implanted sample are very high due to failure of the air conditioning. This directly leads to the large error bars in the hardness data.

5.3.2 Unimplanted Tungsten

In unimplanted tungsten, the hardness of the bulk material decreases rapidly in hardness from 5.5 GPa at 50°C to 2.5 GPa at 250°C which is retained up until 750°C. There is a small size effect in the unimplanted material: the hardness of the material 150-400 nm from the surface is roughly 16% (0.5 GPa) higher than the bulk (>1500 nm data) when averaged over all temperatures. The full behaviour of the size effect with temperature is detailed in table 5.2, with an example hardness-depth curve shown in figure 5.5 that shows a 24% size effect at 75°C. It is therefore possible to separate the hardening effect of the implanted ions from the size effect present during nanoindentation, as the indentation size effect does not change with implanted damage (see the Nix-Gao analysis in figure 4.2, page 93).

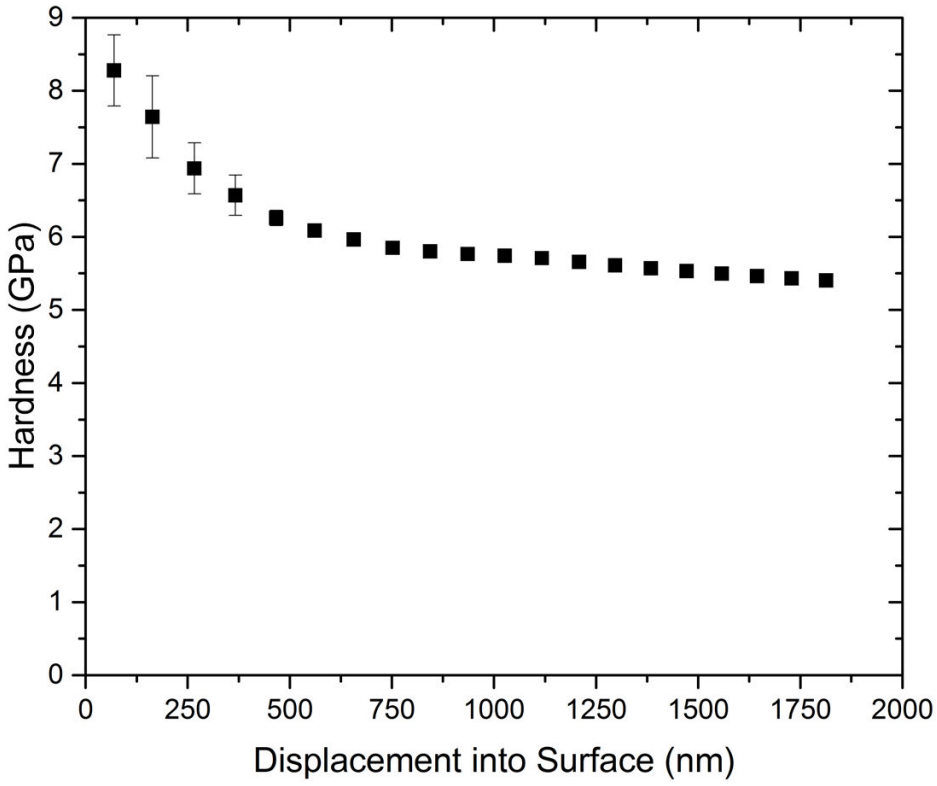

Figure 5.5: Hardness with indentation depth for tungsten at 75°C, showing the indentation size effect seen in the high-temperature nanoindentation curves. Each point is from one unload segment of the load-partial unload curve.

Temperature	Δ Hardness (GPa)	% Hardness
22	0.98	18
50	0.55	9
75	0.94	24
100	0.13	3
150	0.47	15
250	0.84	36
350	0.55	24
450	0.49	18
550	0.91	37
650	0.03	1
750	-0.36	-14
Average	0.5	16

Table 5.2: Increase in hardness due to size-dependent behaviour below 400 nm, expressed in GPa and as a percentage. The size effect on the whole does not appear to change with temperature.

In BCC micropillar compression,[253, 254] tungsten shows a weaker size effect than other BCC metals due to its high critical temperature (525°C[253]). Above the critical temperature in molybdenum,[254] the size dependence of pillars follows FCC behaviour with a power law exponent of 0.6, which is reduced to 0.35 below the critical temperature. Thus the increase in hardening due to the size effect is expected to increase with increasing temperature, but remain constant above 525°C. This is not evident in these data, although thermal drift has the greatest effect at shallow depths evidenced by the apparent decrease in hardness at 750°C.

The difference between these data and the results in the literature are likely due to the significant difference in test geometry between indentation and micropillar compression, namely the strong influence of the free surface in micropillars. In these pillars, dislocation kinks - that are the limiting step for dislocation motion in tungsten - can easily nucleate at the pillar surface. Additionally, there is no neutral axis and therefore little pile up of dislocations. In indentation, the characteristic lengths scales are much smaller and are dominated by work-hardening of dislocations. The strains in the indents are the same at each temperature, therefore the degree of work-hardening due to geometrically necessary dislocations is the same. This means the size effect during nanoindentation is not expected to change.

5.3.3 Helium Implanted Tungsten

The hardness of helium-implanted tungsten with temperature is shown in figure 5.6. The hardness of the >1500 nm depth load-unload curves for the irradiated and unirradiated material matches closely. This match in hardness shows the reproducibility of the results, and further shows that thermal drift can be controlled over different samples. It also shows the validity of the conclusion from the room temperature CSM data; that the hardness derived from data >1500 nm in depth has little influence from the implanted layer.

The hardening effect of the implanted helium, visible from the 150-400 nm load-unload depths, is up to 2.5 GPa at low temperatures, a significant increase in hardness. The hardening effect decreases with increasing temperature and is not significantly present above 450°C. When the sample is cooled from 750°C and indents are performed at lower temperatures, the hardening effect is the same at a given temperature as for tests performed during the heating cycle. If the decrease in hardness at high temperature was due to helium desorption from the implanted layer or diffusion

into the bulk, then the reduction in obstacle density would result in a lower hardness on cooling compared to the previous indents.

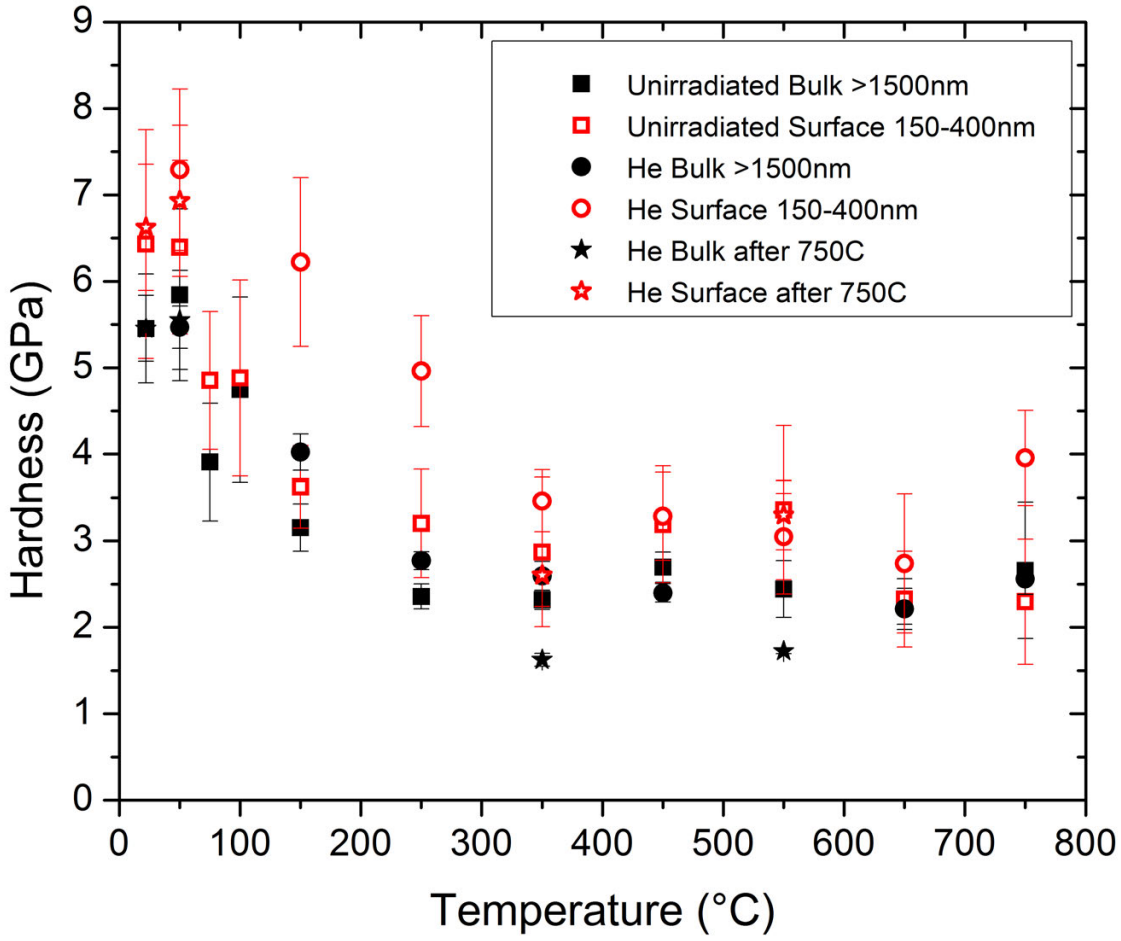

Figure 5.6: Indentation hardness as a function of temperature for the 800°C helium-implanted sample. Points denoted with a star indicate data obtained on cooling after the indentations performed at 750°C. Error bars indicate one standard deviation in the measured hardness. The hardening effect of the helium is negligible above 450°C, but returns to its previous level at each temperature once the sample is cooled.

The retention of the helium matches with results from thermal desorption spectroscopy of tungsten implanted with high-energy helium ions.[255] The TDS showed that helium is trapped in mono-vacancies and helium-vacancy clusters up until 1500-1600 K. This conclusion is supported by TEM of helium-implanted tungsten that shows no visible bubbles, suggesting the helium is trapped in vacancies below the resolution limit of the microscope.[154] Finally, modelling of helium-irradiated tungsten[256] shows almost complete retention of the helium at He_nv_m clusters for irradiation at 700 K.

5.3.4 Self-Ion Implanted Tungsten

The self-ion implanted material shows strikingly different behaviour with temperature to the helium-implanted sample. Figure 5.7 shows that the hardening effect of the 1.5 dpa of self-ion damage is 1.41 GPa at 50°C, very close to the 1.2 GPa measured at room temperature in chapter 4. This hardening does not decrease with increasing temperature, likely due to the increased size of the irradiation-induced obstacles compared with those produced by helium-ion implantation. As a result, no 'cooling' indents were performed.

The greater degree of thermal drift present in these tests has not affected the results too significantly. Although it has led to greater error bars on the data, it has been corrected enough that the trend in hardness with temperature is still easily visible. This is demonstrated by the close match in hardness for the 'bulk' portions of the data, where the test has been proceeding for the longest and thus the accumulated drift would be the largest.

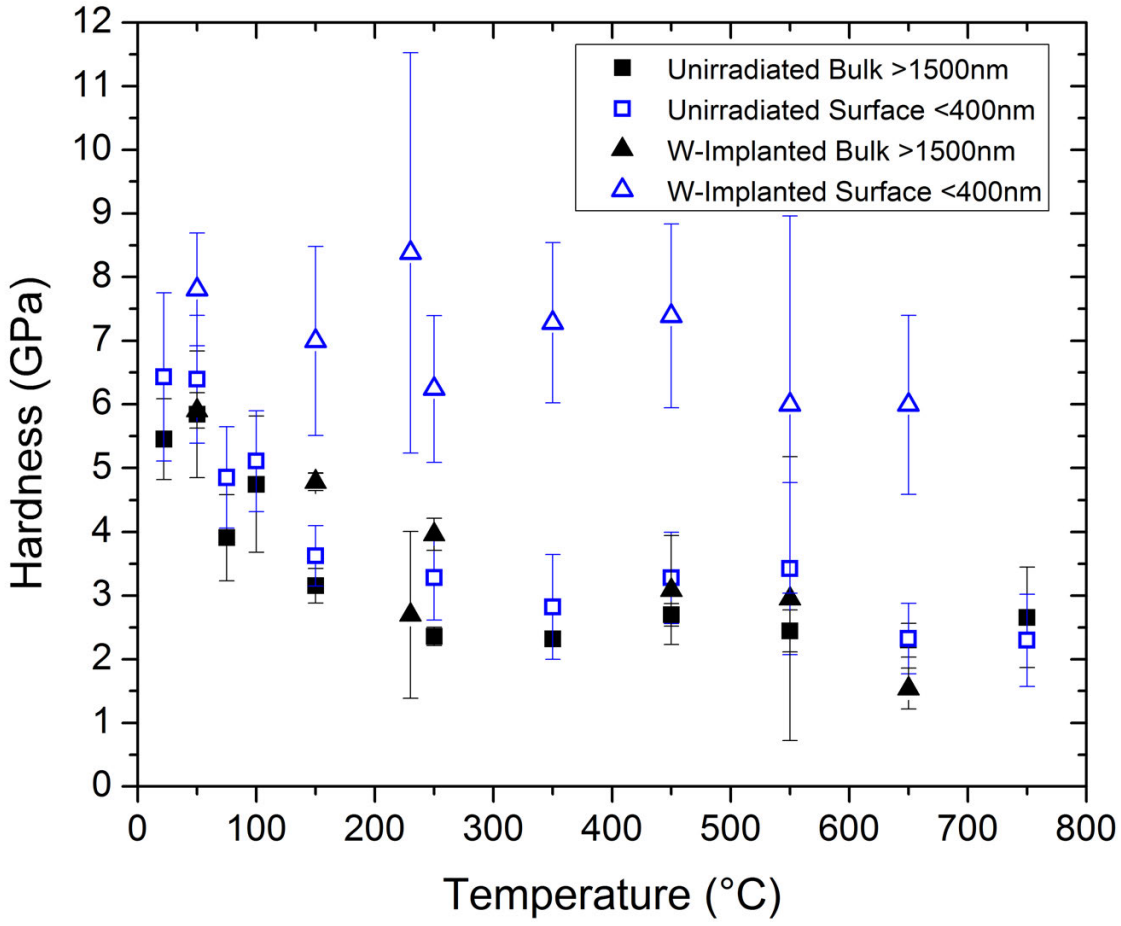

Figure 5.7: Hardness with temperature for the 800°C tungsten-implanted sample. Error bars indicate one standard deviation in the measured hardness. No reduction in hardness is seen as the temperature is increased up until the maximum test temperature of 650°C.

In self-ion implanted tungsten, Yi[79] has shown that annealing at 800°C rapidly reduces the loop number density of a UHP, 1 dpa sample from 6.5×10^{15} m^{-2} to 3×10^{15} m^{-2} simply during the ramp phase of the heater. However, after this point the loop population is relatively stable, only decreasing to 2.1×10^{15} m^{-2} after two hours at 800°C. The subsequent loop size distribution shows that the initial, significant loss of loop density is due to the coalescence of small (<3 nm) loops. 23.7% of the initial loop distribution was >4 nm, increasing to 49.7% after two hours at 800°C. Yi calculates that loop loss to the surface only occurs within 5 nm of the surface, and therefore 'the denuded zones do not exceed 20% of the total displacement damage [region] and that the extraction of bulk damage properties may still be considered valid.'

5.4 Discussion

The decrease in hardness with increasing temperature in the helium-implanted sample is due to the helium-vacancy complexes generated during ion implantation becoming weaker obstacles to plastic deformation at increased temperatures. The low damage levels produced during the implantation (∼0.02 dpa) and relatively high helium levels (∼600 appm) favour the production of these small defects that are easy to overcome via cross-slip and climb. Since near-surface hardness values are the same at a given temperature on both heating and cooling cycles, the decrease in hardness with increasing temperature in the helium-implanted sample must be due to the helium-vacancy complexes generated during ion implantation becoming weaker obstacles to plastic deformation at increased temperatures, rather than to any thermal removal of helium or damage.

The strength of the defects was analysed in section 4.4 and showed the dislocation breakaway angle for the helium-implanted sample was between 178° and 179° for He_nV_m clusters (with $n < 4$) at room temperature. The rapid drop in irradiation-induced hardening with increasing temperature is due to the already low obstacle strength falling to negligible values as thermally activated bypass mechanisms become increasingly operative.

Modelling indicated that the critical resolved shear stress for an edge dislocation to overcome a helium-vacancy complex in α-Fe decreases only slightly ($\sim 10\%$) between 100 K and 600 K.[257] This is a similar homologous temperature range to that investigated here: 0.06-0.33 in iron and 0.09-0.20 here. The authors do not give any indication as to why the obstacle strength decreases with temperature as the dependence is weak. The elastic modulus from the modelled stress-strain curves does not change over this temperature range. Whatever the reason, it is unlikely to be significant enough to explain the ∼50% drop in hardening seen here. Therefore, the majority of the drop is likely to be due to thermally-activated mechanisms for dislocations to bypass obstacles: increased cross-slip of screw dislocations[258] and climb of edge dislocations.[259] It is clear that the mobility of dislocations increases over this temperature range due to the significant drop in hardness of tungsten seen in macro-indentation.[260][261]

In the self-ion irradiated sample, it is safe to assume that this sample is in the stable regime observed by Yi and that any small loops will have disappeared by the time hardness measurements are made. This is due to the long thermal stabilisation times required for high-temperature nanoinden-

tation. Given the high-temperature measurements are close to that of the room-temperature hardness values, this implies that the large loops dominate the hardening mechanism in ion-irradiated tungsten. This gives greater credibility to the assumptions used to calculate the Orowan strengthening of loops in section 4.4 (page 93).

The stress field around a dislocation loop scales with b,[262] and the Orowan strengthening of an obstacle as $ln(r)$. Based on these equations it is therefore unusual that the largest loops dominate the hardening of tungsten. It is possible that the appearance of very large loops (>10 nm) that were not widely present post-irradiation but form during the in-situ annealing provide enough hardening to counteract the reduction in loop density and loss of smaller loops. This would require a better knowledge of the hardening mechanics of loops to prove, but a 10 nm loop would harden between three and five times more than a 2 nm loop based on the Orowan and stress field scaling. Approximately 1.3×10^{15} 2 nm loops are lost after two hours at 800°C, but 2×10^{14} 10 nm loops are gained. Therefore each 10 nm loop is six times stronger, the same order of magnitude as predicted and it could be said that these large loops are controlling the hardening. However, the real material with its size distribution is more complex: comparing 8 nm loops instead of 10 nm requires 40 times stronger loops, therefore the small loops must contribute.

It is difficult to find literature data that relates a loop size distribution to the measured hardness of a material after irradiation. Armstrong[143] and Nagasaka[263] have shown that the loop number density correlates well with changes in hardness in irradiated tungsten and zirconium, respectively. Neither of these works calculate a size distribution, so the dominance or otherwise of large loops is unknown. Qiangmao et al. have analysed the hardness and loop size distribution of A508 steel (also with a BCC structure) after proton irradiation at room temperature.[264] Based on their loop size distribution they calculate an expected hardness increase that increases linearly with the average loop size as the number density does not strongly increase. Finally, Gan et al. have compared a number of neutron and proton irradiated steels along with an extensive literature comparison.[265] Some of their samples: CP 316 SS and CP 304 SS both irradiated at 360°C show a change in yield strength from Vickers indentation that increases linearly with loop diameter. As many of the defects were too small to be accurately measured, this loop diameter is representative of the larger loops.

Overall it is difficult to say whether the largest loops dominate the hardness or not given the

scatter of the hardness data, but it seems unlikely given the possible strengthening mechanisms of dislocation loops. Instead, it seems that the increased hardening from the increase in average loop size is enough to counteract the softening from a reduction in loop density.

Finally, hardnesses measured by the high-temperature equipment match well with micro-indentation data.[137] However, for the three samples tested, the hardness values from the MicroMaterials system are on average 1.3 GPa lower than as measured in the G200 (see figure 5.8). The data from fused silica is close to literature values in both hardness and modulus, and the difference between the two systems is consistent between samples. This difference is therefore likely due to the strain rates used and the strain-rate sensitivity of BCC tungsten. The G200 was operated at a constant strain rate of 0.05 s^{-1}. Here, testing was performed under a constant loading rate of 1.5 mN/s. Each indent here took up to 25 minutes, compared to 3 minutes in the G200. Even accounting for the unloading portion of the curves, the tests here were conducted at a much slower strain rate, producing the apparently softer materials.

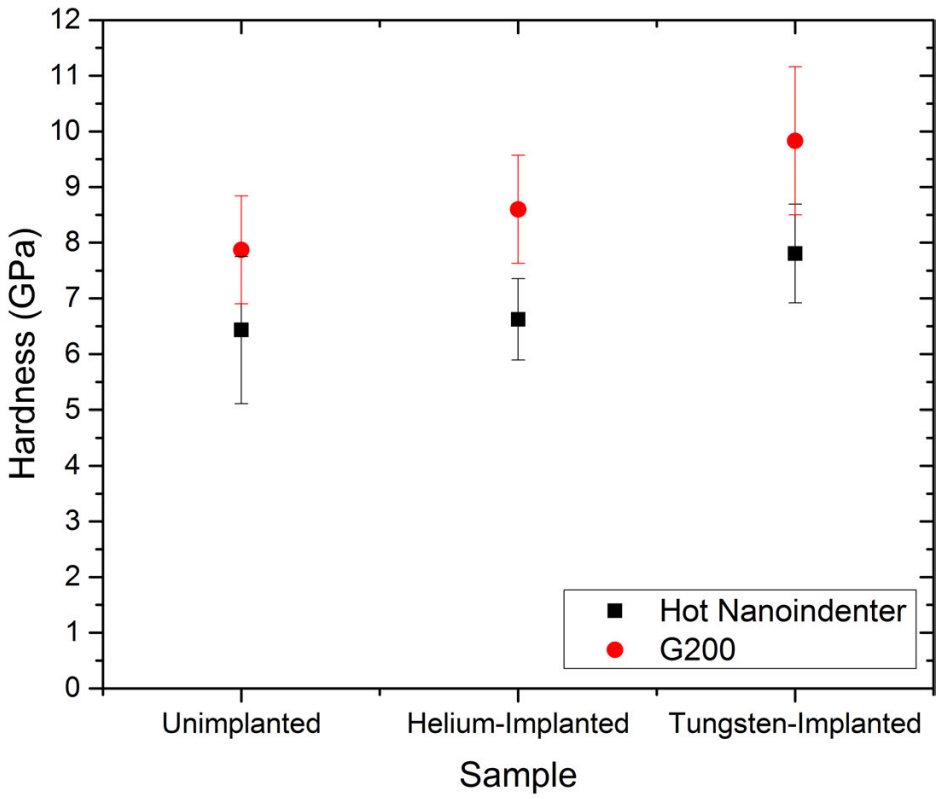

Figure 5.8: Comparison of hardness determined for each of the three materials tested at room temperature in the G200 and the MicroMaterials system. The G200 produces higher values of hardness due to the higher strain rates used.

5.5 Summary

Values of hardness determined by high-temperature nanoindentation compare well to micro-indentation data and literature behaviour of the hardness of tungsten with temperature. The absolute values of hardness require care in comparing with other systems - particularly the G200 used in chapter 4 - due to the influence of strain rate.

The hardening from implanted helium is negligible above 450°C, likely due to dislocations being able to bypass small obstacles via cross-slip and climb. In contrast, the self-ion implanted material retains its hardness up to the maximum test temperature of 650°C. This is either due to the largest loops dominating the hardening of tungsten or the overall increase in average loop size balancing the reduction in loop density.

Chapter 6

Micro-Mechanical Testing

6.1 Introduction

While nanoindentation is a quick, simple and effective method of determining mechanical properties, it only produces data for hardness and modulus. These are useful parameters, and give a good indication of the mechanical behaviour of the material, but they do not describe every aspect. In particular, fracture toughness cannot be measured as tungsten is too ductile for cracks to be induced by indentation. It is also prudent to measure yield stress directly, rather than estimate it through the typical $\frac{H}{3}$ relationship that is unvalidated in tungsten.

All the materials in this chapter were implanted out at the JANNuS facility, as this was the only beam line with sufficient energy to produce a deep enough damage profile ($\sim$3 μm) for cantilevers to be manufactured. Cantilevers were manufactured using the method of Di Maio[168] in each of the three implanted samples (self-ion, helium-ion and dual-ion), and in the ends of the samples that did not see the ion beam in order to determine data on unimplanted tungsten that had seen the same temperature profile as the implanted material. A G200 nanoindenter was used to apply the bending load and measure the critical value at which each beam failed. The beams were loaded to failure under displacement control at a rate of 5 nm/s, corresponding to a strain rate of approximately 3×10^{-5} s^{-1}. The beams are all of a similar size, therefore the strain rate does not significantly vary; the smallest 1.3 μm beam was tested at 8.6×10^{-5} s^{-1}

Figure 6.1 shows example images of cantilevers with a triangular or pentagonal cross-section used for elastic-plastic or fracture toughness measurements, respectively. A constant cross-section is required to simplify the calculation of K_{1c}. The region of constant cross-section was therefore manufactured within the ion-damaged layer. Notches were made $\sim$1 μm from the fixed end of the beam at a beam current of 10 pA to produce a sharp notch approximately 400 nm in depth. The notch width is approximately 100 nm, hence the notch radius is estimated as 50 nm. The pentagonal cross-section is more complicated to produce compared to a simple triangle because a symmetrical

cross-section is required so as not to introduce torsion into the beam. For the elastic-plastic tests where a region of constant cross-section is not required, triangular beams were produced so as to simplify the manufacturing process.

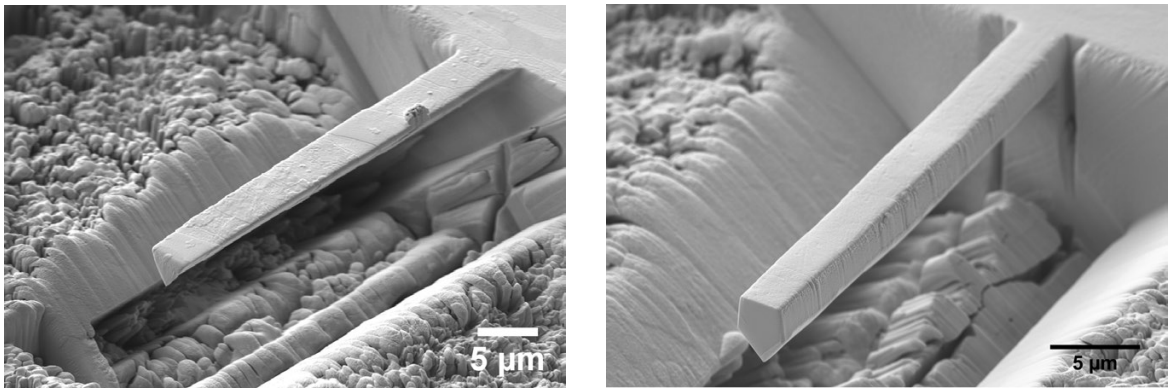

(a) Triangular beam for elastic-plastic tests. (b) Pentagonal beam for fracture tests.

Figure 6.1: Typical micro-cantilevers produced by FIB-machining.

6.2 Method

6.2.1 Finite Element Modelling of Cantilevers

The compliance, S, of a FIB-machined cantilever with length L, i.e. a beam whose fixed end is not fully constrained, is given by equation 6.2.1,[266] where E is the elastic modulus, I the second moment of area, θ_{mo} and δ_{mo} the slope and displacement at the fixed end due to unit shear force, θ_{po} and δ_{po} the slope and displacement at the fixed end due to unit bending moment.

$$S = \frac{\delta_L}{P} = \frac{1}{3EI}L^3 + \theta_{mo}L^2 + (\theta_{po} + \delta_{mo})L + \delta_{po} \tag{6.2.1}$$

Armstrong has shown that an aspect ratio (length / depth) of greater than six is required for accurate determination of Young's modulus.[72] This allows the L^3 term from the beam to dominate the calculation of compliance. However, for beams required for the size effect study (section 6.2.2, below) that are up to 8 μm in depth, this requires a significant amount of FIB-milling to remove material around a large beam. Additionally, wide trenches are required around the beam to undercut the beam sufficiently to allow testing until yield. Due to the limitations

of available FIB-time, it is not possible to manufacture a complete set of cantilevers required for a size-effect study if simple beam theory is to be used. By using short beams, such that the L^3 term no longer dominates, the calculation of modulus becomes more complex but the experimental requirements lessen.

To allow for short beams, finite element modelling was used to model the displacement of the fixed end of the cantilever and therefore determine accurate modulus values. An FE model was constructed for each cantilever so as to capture its specific geometry, measured dimensions and loading position. The model captured all of the cantilever beam and some of the material to which it was attached at the fixed end, as shown in figure 6.2. The programmed element type was a 20 node quadratic brick. The boundary conditions were that the surfaces of the model that adjoin additional material in the real sample are 'encastré': fixed with zero displacement or rotation.

The fixed end of the cantilever causes the discrepancy between simple beam theory and literature values of modulus. Simple beam theory assumes no displacement at the fixed end of the beam. However, as the beam is made of the same material to which it is attached, a displacement of the free end of the beam results in a small deflection at the fixed end. This extra deflection increases the measured strain, therefore decreasing the determined Young's modulus. By including the 'fixed' end in the finite element calculation, the strain at this end can be determined and accounted for leading to more accurate measurements of Young's modulus.

The stress in simple beam theory is given by equation 6.2.2 where σ is stress, M is the bending moment, y the distance to the neutral axis and I the second moment of area. This equation is only valid while the bending is elastic: once plasticity occurs, stress no longer varies linearly with y. The post-yield behaviour shown in figure 6.3 and elsewhere simply (and erroneously) ignores this. As such, the finite element calculation is required to describe the post-yield stress-strain behaviour of the beam as well as to determine an accurate modulus.

$$\sigma = \frac{My}{I} \tag{6.2.2}$$

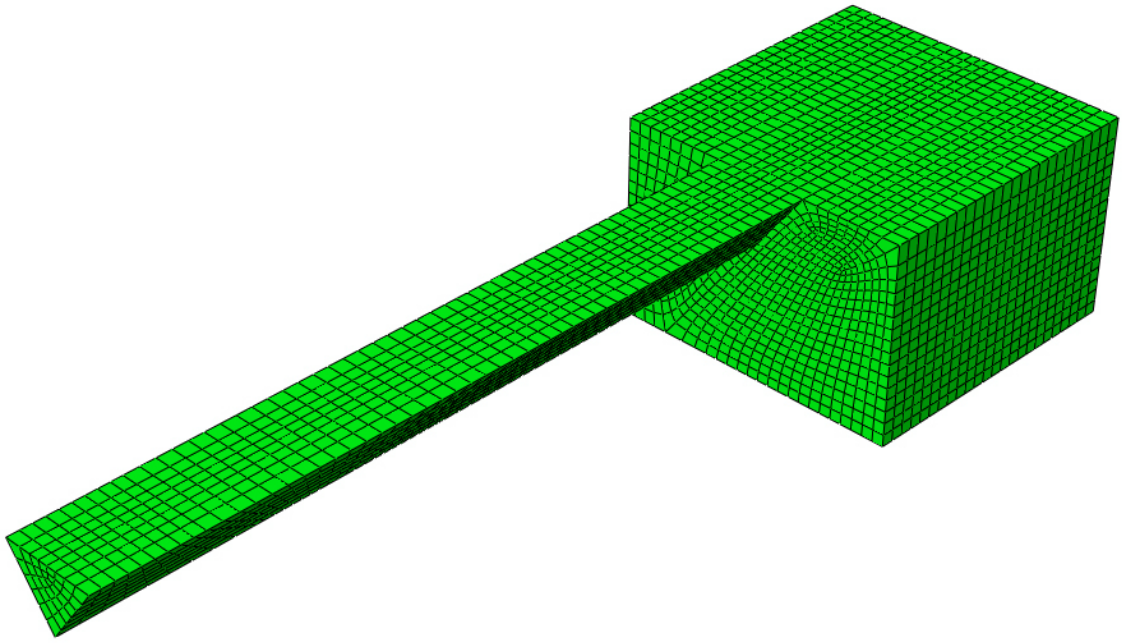

Figure 6.2: Finite element model of a cantilever constructed in ABAQUS, representing the exact geometry of a tested beam and material at the 'fixed' end into which the strain field in the cantilever penetrates. It is this fixed end that causes the discrepancy between simple beam theory and literature values of modulus.

Matching between the model and experiment was carried out using an automated curve-matching MATLAB code developed by Hardie.[90] This iteratively sets potential material parameters (Young's modulus and yield stress), displaces the free end of the cantilever beam, compares the ABAQUS and experimental load-displacement curves, adjusts the material parameters and repeats until the theoretical curve is within 2% of the experimental curve.

ABAQUS allows multiple values of yield stress during an experiment to allow for work hardening after plastic deformation. The load-displacement data after the yield point are split evenly into several plastic increments by the MATLAB code and a yield stress determined for each increment via the curve-matching process. Two values of yield stress are allowed during the curve matching process in order to account for work hardening.

An example of the matching is shown in figure 6.3 with the determined material parameters. The FEA-derived modulus (389 GPa) is close to the literature value of 410 GPa, with simple beam theory producing an underestimation of 9.9% with a value of 354 GPa. In the simple beam

analysis, the yield stress is determined using a similar method to Armstrong[266] by defining the point at which the local elastic modulus drops to 98% of the initial modulus as the yield point. It is therefore difficult to compare the two values, but this likely explains why the simple beam yield stress is higher despite the lower calculated Young's modulus.

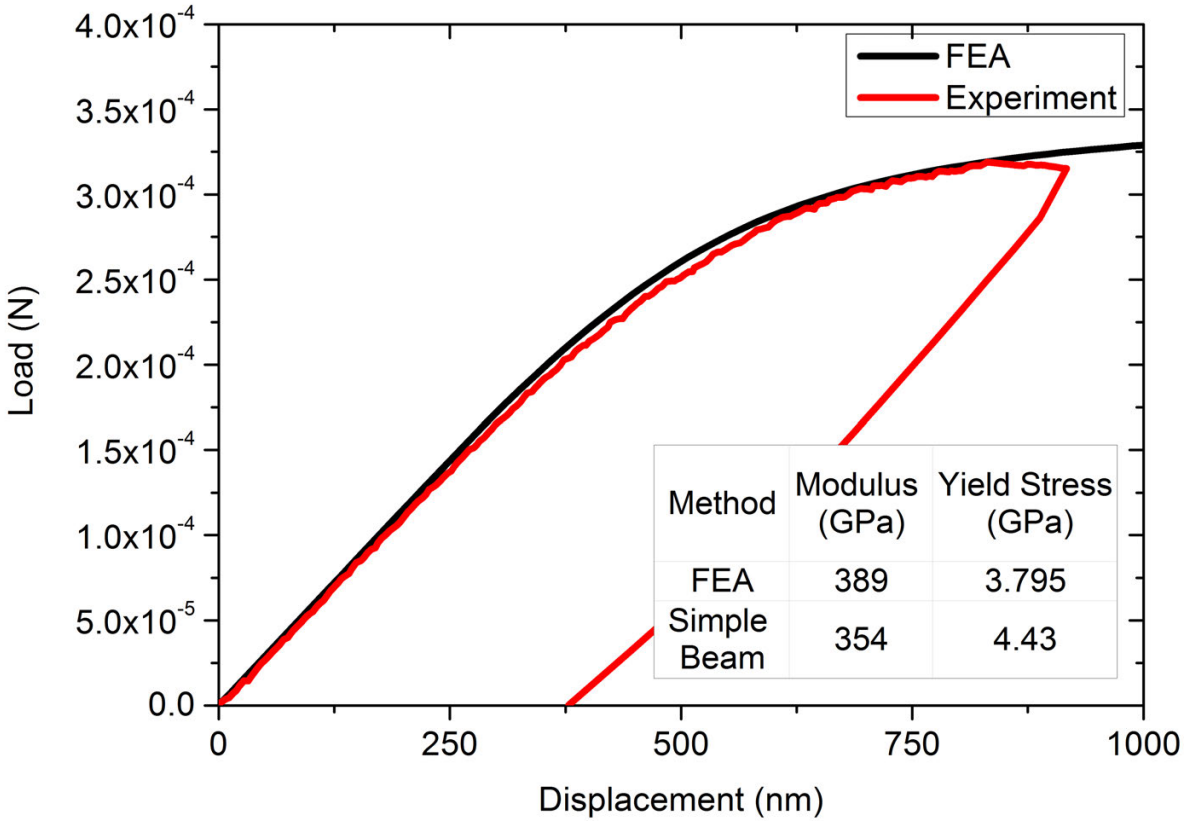

Figure 6.3: Matched load-displacement curve for a beam produced by ABAQUS and a comparison with the experimental curve. The beam modelled here is 1.68 μm long, hence the high values of yield stress. An aspect ratio of 3.5 results in a 9.9% underestimation of Young's modulus when using simple beam theory.

6.2.2 Size Effects In Cantilevers

As cantilevers are subject to the typical 'smaller is stronger' behaviour,[90, 266] it is necessary to determine the effects of specimen size on plasticity. A series of cantilevers of varying depth were manufactured in an unimplanted sample. The yield stresses and moduli of the beams were calculated using the finite element model described in section 6.2.1.

It can be seen from figure 6.4 that there is no influence of specimen size on Young's modulus.

This is expected behaviour as modulus is an entirely elastic phenomenon and is thus not influenced by dislocation density. Although there is some scatter, particularly at small beam depths due to the difficulty in precise measurements of beam dimensions, the average value is in line with literature data.

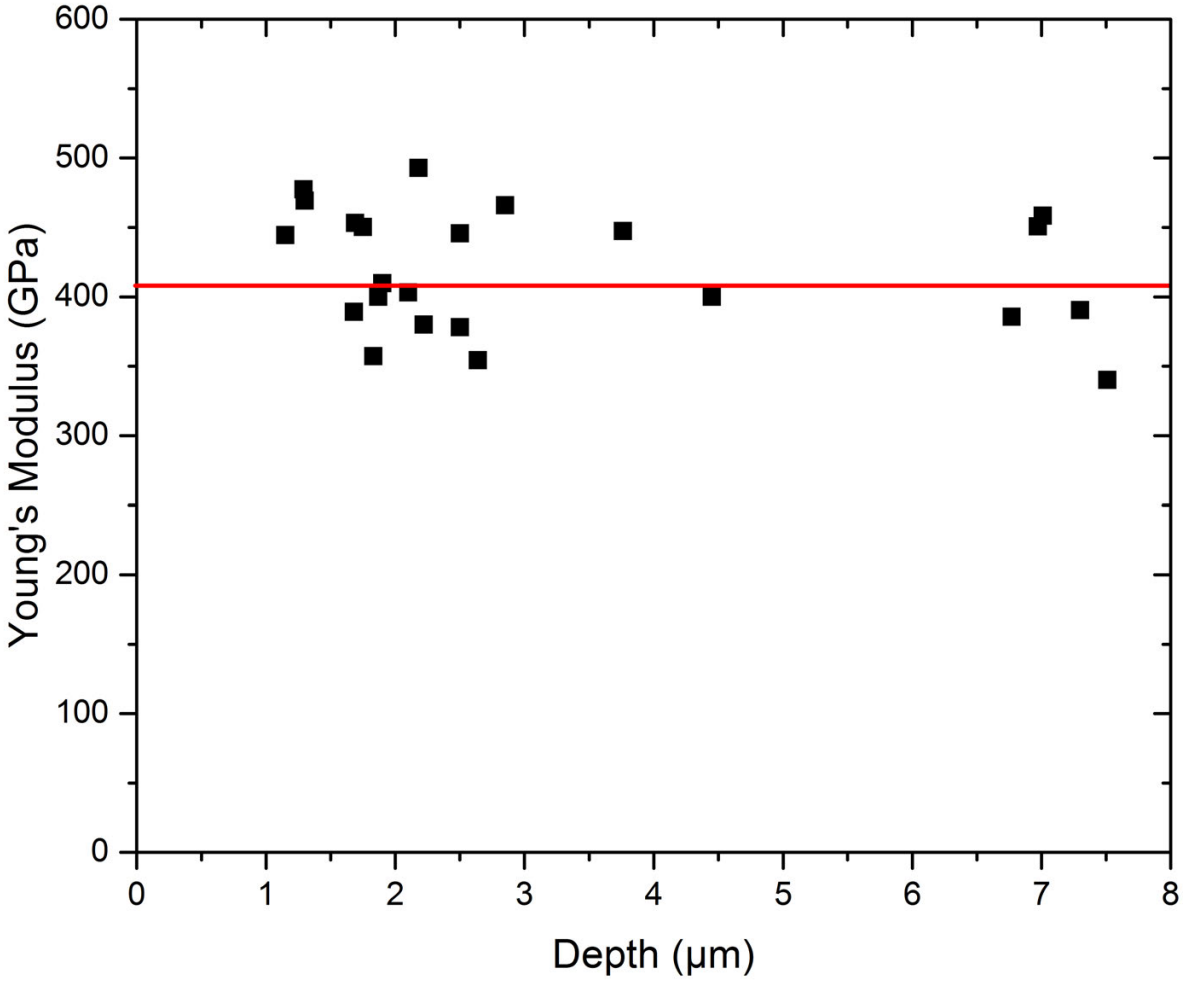

Figure 6.4: Measured Young's modulus with depth for cantilevers in pure, unimplanted tungsten, calculated using a finite element model. The red line marks the literature value of 410 GPa.[234] No size effect is seen as modulus is an entirely elastic phenomenon.

The measured yield stress, shown in figure 6.5, is seen to strongly increase below $\sim 3\ \mu m$ in depth, comparable with the sub-grain size as measured by EBSD (figure 3.11, page 76). This behaviour must be accounted for when measuring the properties of ion-irradiated tungsten as the implanted layers are approximately 3 μm thick. Size effects in unimplanted cantilevers are controlled by a variety of factors, including dislocation source density, strain gradients and grain size. As the size

of cantilevers is reduced, the number of dislocation sources in each beam decreases. This gives rise to greater scatter in smaller beams: if the beam happens to contain a source near the fixed, stressed end then the yield stress will be lower. The strain gradients mean that the operating sources will result in dislocation pile-up at the neutral axis of the beam that are larger for smaller beams leading to work hardening and a higher yield stress.

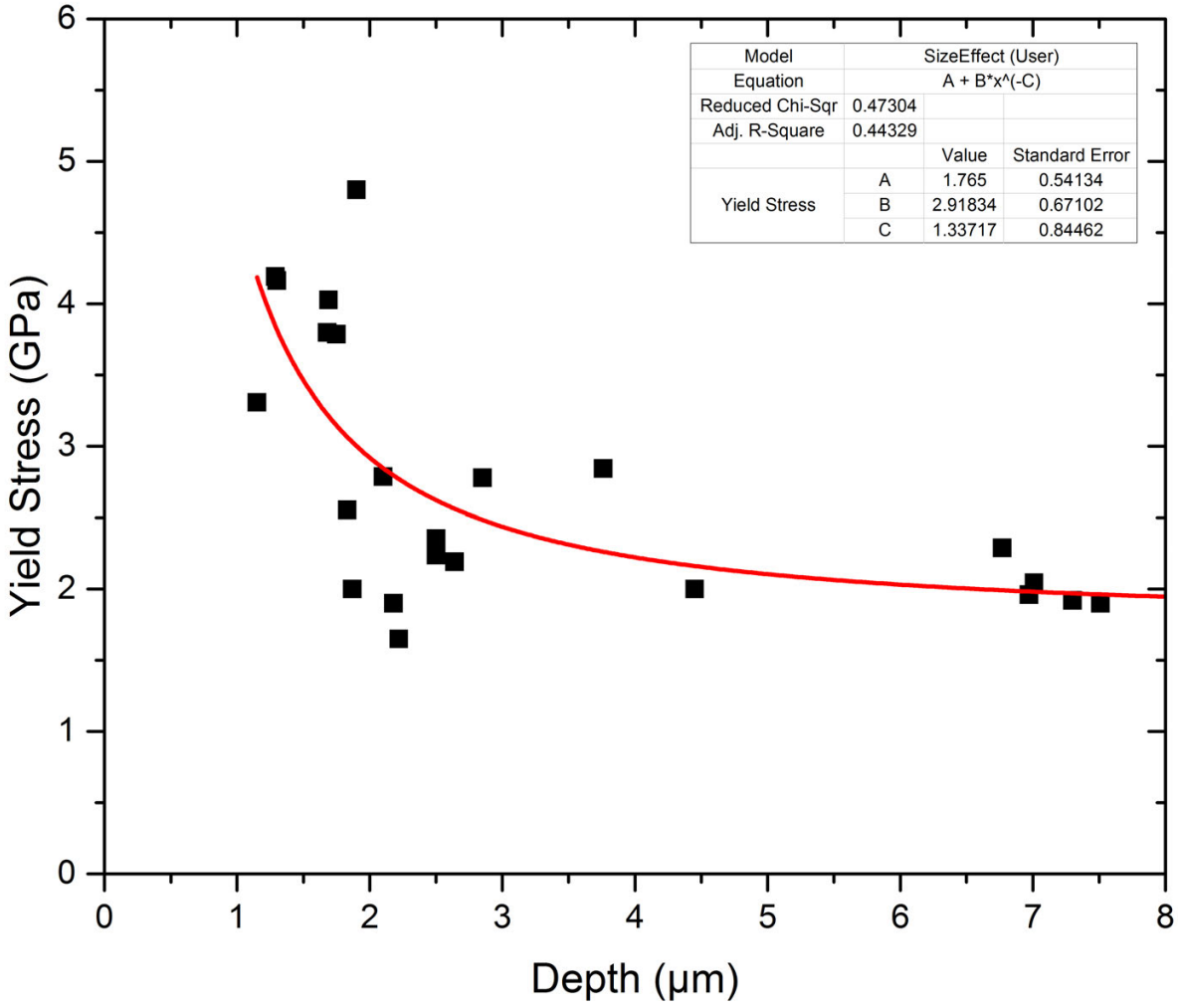

Figure 6.5: Apparent yield stress with depth for cantilevers in pure, unimplanted tungsten, calculated using a finite element model. The size effect becomes significant below $\sim 3\ \mu m$ in depth. The power law fitted to the data is given by equation 6.2.3.

A power law is fitted to the data in figure 6.5. This takes the form of equation 6.2.3, where σ_y is the measured yield stress, σ_0 the yield stress for the bulk crystal, k and n are constants and D is the beam depth.

$$\sigma_y = \sigma_0 + kD^{-n} \tag{6.2.3}$$

When this equation is fitted, σ_0 is determined to be 1.77 GPa, close to macro-scale tests[267, 268] that determine a value of ∼1.5 GPa. The size effect exponent, n has a value of +1.34, which is very different to the -0.6 seen in FCC micropillars.[269] Schneider[254] shows that the power law exponent is reduced in BCC materials due to the increased contribution of lattice resistance below their critical temperature, where dislocation mobility has a thermal component. Schneider determines a value of -0.20-0.25 for single-crystal tungsten at room temperature depending on crystal orientation.

It is not fully clear why the value for n determined here is so different from the value from Schneider, despite the significant error bars. It is unusual that the values of n determined by Schneider for all the investigated materials (W, Mo, Ta and Nb) are all negative. Values in the literature are typically between 0.2 and 1,[270] i.e. positive. It may be that Schneider's values should instead be positive, reducing the discrepancy. Additionally, the test geometries are very different because of the work-hardening and strain gradients due to a neutral axis that are present in cantilevers compared to micro-pillar experiments. Schneider showed a reduction in n due to lattice resistance. The work hardening present in these beams also increases the lattice resistance that would therefore further decrease the value of n.

Greer[271] in a review of size effects, including those present in poly-crystalline materials also notes that in bi-crystalline Al micropillars the data 'suggest the presence of a grain boundary inside [the pillar] contributes to dislocation storage at that boundary, leading to a pronounced increase in both the strain-hardening rate and the attained flow stresses.' As the materials from Schneider were single-crystal, this may also explain the lower values of n compared to that determined here.

The value of n found here can be better compared to cantilever size effect studies in a variety of materials, detailed in table 6.1. The value of n in tungsten of +1.34 is very close to that determined in other polycrystalline BCC materials, in particular Fe-6%Cr of +1.16 and Eurofer of +1.35. This close match means that these data will be useful in separating the effects of specimen size and radiation damage.

Material	n	Author
Single-Crystal Copper (FCC)	+0.71	Armstrong[266]
Single-Crystal Titanium (HCP)	+0.87	Tarleton[270]
Poly-Crystal Fe-6%Cr (BCC)	+1.16	Hardie[90]
Poly-Crystal Eurofer (BCC)	+1.35	Jones[272]
Poly-Crystal ODS-Eurofer (BCC)	+3.11	Jones[272]
Poly-Crystal Tungsten (BCC)	+1.34	Gibson (This work)

Table 6.1: Size effect exponents n for a range of materials from micro-cantilever bending.

6.3 Results

6.3.1 Elastic-Plastic Behaviour

	Irradiation Condition			
	Unimplanted (7 Beams)	W ion (16 Beams)	He ion (13 Beams)	W and He ion (7 Beams)
Avg. Depth (μm)	3.9	3.2	2.1	3.0
Young's Modulus (GPa)	**418** ± 86	**438** ± 62	**482** ± 49	**496** ± 90
	0%	4.8 ± 1.2%	15.4 ± 2.7%	18.8 ± 5.2%
Yield Stress (GPa)	**2.7** ± 0.4	**3.0** ± 0.7	**3.1** ± 0.7	**3.0** ± 1.2
	0%	11.0 ± 3.2%	15.2 ± 2.6%	18.6 ± 5.1%
$\frac{\text{Hardness}}{3}$ (GPa)	**2.6** ± 0.3	**3.0** ± 0.1	**2.9** ± 0.3	**3.3** ± 0.2
	0%	5.1 ± 0.7%	3.1 ± 0.4%	8.5 ± 1.2%

Table 6.2: Comparison of modulus and yield stress for the materials tested. One standard deviation of the scatter is given as an indication of the error in the results. The percentage increase above the unimplanted material is also shown.

The micro-mechanical tests on the unimplanted material shown in table 6.2 compare favourably with literature values for the modulus (410 GPa[234]) and hardness (7.62 GPa[143]) of tungsten. A small size effect is seen in the yield stress measured here above the 1.5 GPa measured in macro-scale tests[267, 268] even at an average beam depth of 4 μm. The equation describing the size-dependent behaviour from the size effect study (figure 6.5) does not approach 1.5 GPa until >10 μm. Although this is likely an overestimation of the depth required to remove size effects, it does explain why size effects are still seen even in these relatively deep beams.

In both the unirradiated and ion-irradiated conditions the elastic moduli are similar whether determined by micro-cantilevers or nanoindentation, shown in figure 6.6. This demonstrates that cantilevers are capable of measuring values of elastic modulus in these materials. Radiation damage could affect the bonding and average atomic distance in tungsten, leading to changes in elastic modulus. Although a small increase is possibly seen here after irradiation, within error bars all the elastic moduli are close to the literature value of 410 GPa. Additionally, Hofmann et al. showed little change in modulus after helium implantation[119] and therefore it is likely that the modulus is indeed unchanged here.

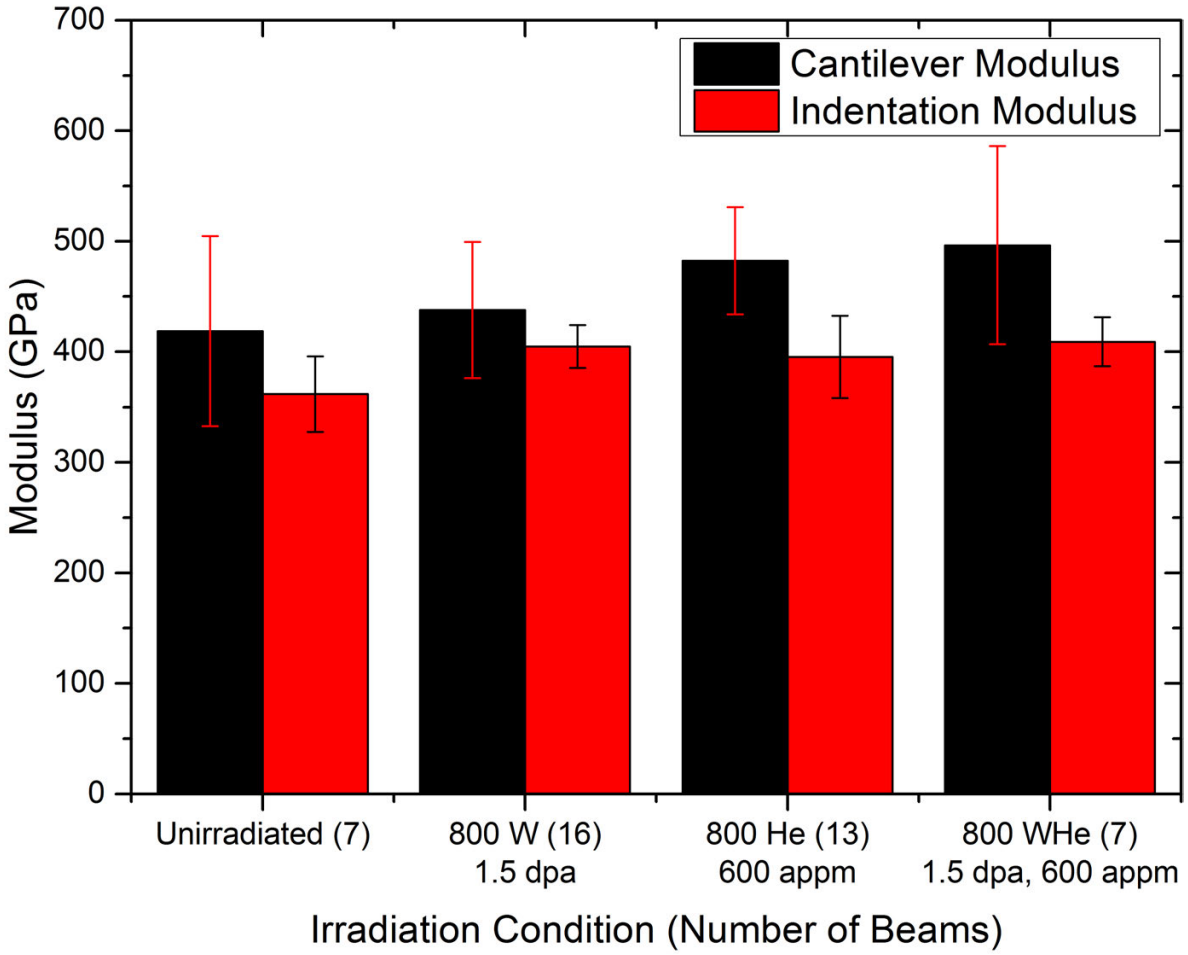

Figure 6.6: Comparison of Young's modulus determined from cantilevers and nanoindentation. The values are comparable and close to literature values regardless of technique or irradiation condition.

Figure 6.7 shows a comparison between the yield stress as measured from the cantilevers and one-third of the indentation hardness from chapter 4. After irradiation, a difference in the plastic flow stress measured by the micro-cantilevers and nanoindentation is seen. The yield stress of all the samples increases by around 11% after irradiation, while the irradiation hardening predicts an increase of between 3.1% in the helium-implanted sample and 8.5% in the dual-beam irradiated sample. Chapter 4 demonstrated no significant changes from pile up effects in these materials, therefore the cantilevers are indeed overestimating the yield stress.

It is likely that due to the size of the beams produced in the material ($\sim$2-3 μm) that the plastic behaviour of the micro-cantilevers is dominated by small-scale effects, rather than being representative of changes due to radiation damage. The increase in hardness between the unimplanted

material and the hardest, dual-beam material is 2.0 GPa, corresponding to a yield stress increase of 0.67 GPa. In comparison, the increase from the 'bulk' (5 μm thick beams) yield stress to 2 μm thick beams results in an increase in yield stress of 0.82 GPa, from 2.10 to 2.92 GPa. The increase in yield stress simply from the size effect is therefore larger than the largest measured increase due to irradiation hardening. The hardness of the dual beam material (9.87 GPa) corresponds to a yield stress of 3.3 GPa, well within the scatter of micro-cantilever data.

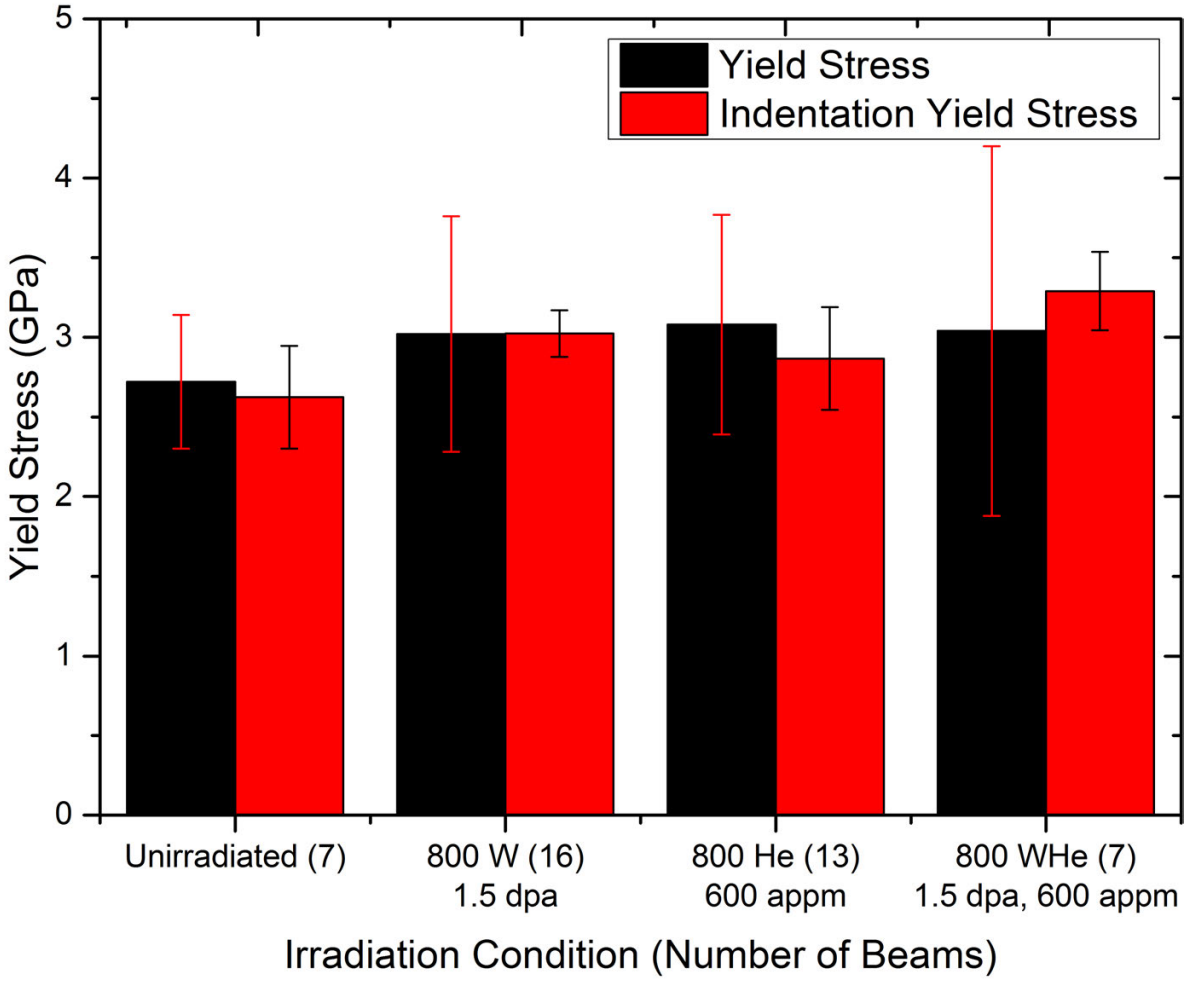

Figure 6.7: Comparison of yield stress determined from cantilevers and one-third of the corresponding indentation hardness. The scatter from the indentation data is much smaller. The trends in yield stress - particularly the helium-implanted sample - do not follow the trends in hardness likely due to size-effects dominating in the cantilevers.

The nanoindentation hardnesses from chapter 4 have been approximated to yield stresses using two different conversion factors. The first, the typical $\frac{\text{Hardness}}{3}$ scaling produces values that are reasonably close to the yield stresses determined from the micro-cantilever tests. These data are those shown in figure 6.7. However, it was shown in the size effect study (figure 6.5) that these cantilevers are still subject to some degree of a size effect. It is preferable to determine the effects of radiation damage on the bulk properties of tungsten. Therefore, an attempt was made to scale the 'indentation yield stress' and yield stress from the cantilevers to be representative of bulk properties.

The nanoindentation hardnesses were therefore also scaled using $\frac{\text{Hardness}}{3.935}$, to correct for small-scale effects by producing a yield stress of 2.0 GPa in the unimplanted material, as 2.0 GPa is the value to which the yield stress tends to in the largest cantilevers. Although this is higher than the literature data, is allows a comparison between the two techniques in the same material so as to better compare the scaling of small-scale mechanical data. The nanoindentation data can be scaled using the same factor as the size effect does not change between implantation conditions. The ion-irradiated cantilever data is scaled using equation 6.3.1, i.e. a simple rearrangement of the power law used to fit the data in the size effect study. This is given by the 'Scaled σ_y' row.

$$\sigma_y(\text{Bulk}) = \sigma_y(\text{Measured}) - kD^n \tag{6.3.1}$$

These bulk yield stresses are shown in table 6.3. These data still agree within error bars, implying the scaling to bulk values is successful. Interestingly, the unimplanted cantilevers scale to a yield stress above that determined by the size effect study. As mentioned, this is likely due to the power law not fully describing the size-dependent behaviour of the beams.

	Irradiation Condition			
	Unimplanted (7 Beams)	W ion (16 Beams)	He ion (13 Beams)	W and He ion (7 Beams)
Avg. Depth (μm)	3.9	3.2	2.1	3.0
σ_y (GPa)	**2.7** $\pm$ 0.4	**3.0** $\pm$ 0.7	**3.1** $\pm$ 0.7	**3.0** $\pm$ 1.2
$\frac{\text{Hardness}}{3.935}$ (GPa)	**2.0** $\pm$ 0.2	**2.3** $\pm$ 0.3	**2.2** $\pm$ 0.2	**2.5** $\pm$ 0.1
Scaled σ_y (GPa)	**2.3** $\pm$ 0.4	**2.4** $\pm$ 0.7	**1.9** $\pm$ 0.7	**2.4** $\pm$ 1.1

Table 6.3: Nanoindentation hardness and cantilever yield stresses scaled to try to remove the influence of small-scale effects.

Ideally, nanoindentation hardness could be used to determine the effect of irradiation on the bulk yield stress of tungsten. Although it is difficult to say conclusively due to the scatter in the data, overall the predicted yield stress from the hardness data is close to that measured by the cantilevers, implying that indentation data can indeed be used to predict changes in yield stress. The effect of radiation damage on the yield stress of tungsten is therefore very similar to that determined in chapter 4. At these damage levels, the changes in yield stress are minimal, probably due to the extremely high initial yield stress of tungsten. Helium implantation at these concentrations (600 appm) only has a small effect on the yield stress. Self-ion and dual-ion implantation produces a scaled yield stress that is only 5% greater than the unimplanted value.

In summary, the elastic behaviour of the materials is unchanged between irradiations or testing techniques. Due to the sensitivity to changes in hardness, nanoindentation appears to be better at investigating the effects of radiation damage on plasticity. The high stresses under the indenter tip will activate any present dislocation sources, or homogeneously nucleate one. Therefore the hardness will be controlled by the propagation of dislocations through the damaged microstructure even with the presence of size effects at small indentation depths. In the cantilevers, activation of dislocation sources within the beam is much more difficult as the stresses are lower, therefore the mechanical properties of these beams is dominated by the source activation. This means size effects are much more dominant and the radiation damage is less influential. However, there is some

indication that the properties of cantilevers and nanoindentation can be scaled so as to remove the influence of size effects, but many cantilevers over a range of depths are required.

6.3.2 Fracture

Although nanoindentation is more sensitive to the plastic behaviour of irradiated tungsten, tungsten is too ductile to fracture during indentation. It was observed during testing of the triangular beams used for elastic-plastic measurements that some beams in the dual-beam irradiated material underwent brittle failure. Therefore, some cantilevers were manufactured to measure the fracture toughness of the dual-beam implanted material.

Fracture toughness for these pentagonal beams is given by K_{1c} in equation 6.3.2.[168] P is the failure load; L the distance between the loading point and the notch; a the notch depth; b the depth of the constant cross-section; and w the beam width.

$$K_{1c} = \frac{PLy\sqrt{\pi a}}{I} F\left(\frac{a}{b}\right)$$

$$F\left(\frac{a}{b}\right) = 1.85 - 3.38\left(\frac{a}{b}\right) + 13.24\left(\frac{a}{b}\right)^2 - 23.26\left(\frac{a}{b}\right)^3 + 16.8\left(\frac{a}{b}\right)^4$$

$$I = \frac{wb^3}{12} + \left(y - \frac{b}{2}\right)^2 bw + \frac{w^4}{288} + \left[\frac{b}{6} + (b - y)\right]^2 \frac{w^2}{4} \tag{6.3.2}$$

$$y = \frac{\frac{b^2 w}{2} + \frac{w^2}{4}\left(b + \frac{w}{6}\right)}{bw + \frac{w^2}{4}}$$

Many of the cantilevers tested failed plastically, as shown by the stress-strain curve and SEM image in figure 6.8. With these beams, P is given by the load at yield to give a lower bound of fracture toughness. The yield stress is determined using the method of Armstrong[266] by defining the point at which the local elastic modulus drops to 98% of the initial modulus as the yield point. For beams that failed in a brittle fashion, as shown by the stress-strain curve and SEM in figure 6.9, P is simply given by the peak load before failure.

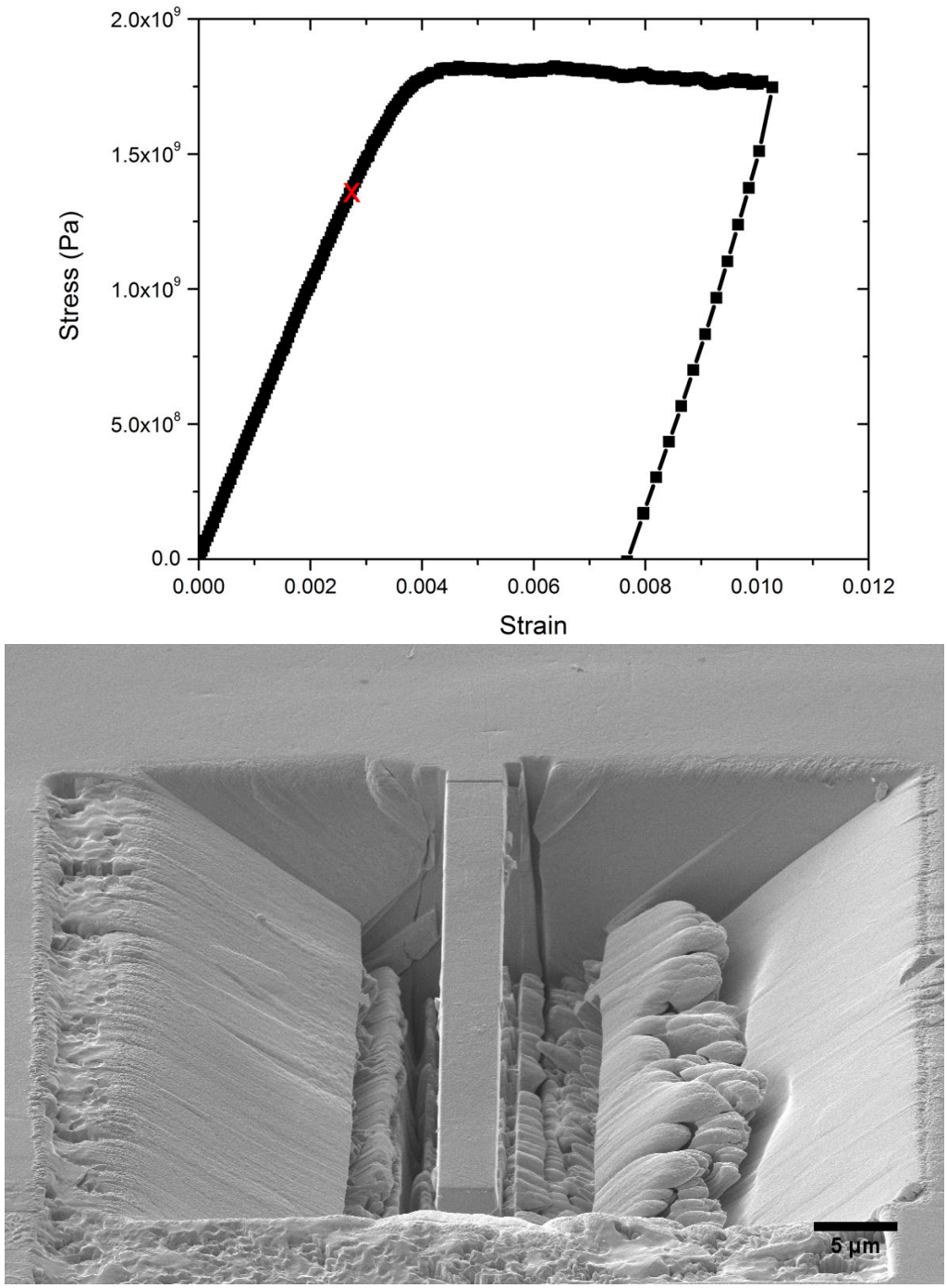

Figure 6.8: Typical stress strain curve and SEM image of a cantilever that failed plastically. The yield point is marked with an 'X', at the point where the local elastic modulus has fallen to 98% of the initial modulus. This load is used in the calculation of fracture toughness.

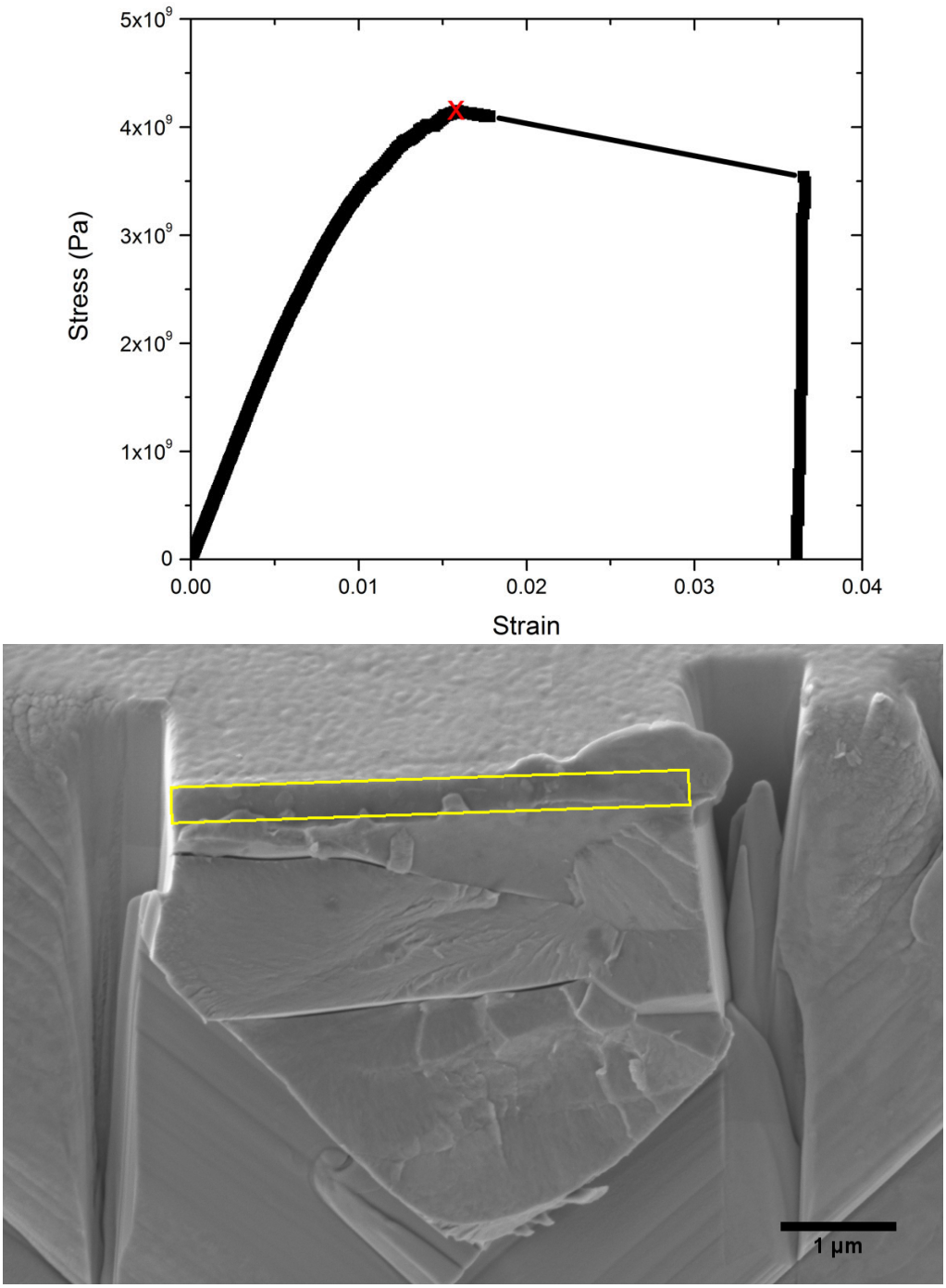

Figure 6.9: Typical stress-strain curve (using simple beam theory) and SEM image for a micro-cantilever that failed in a brittle manner. The failure point is marked with an 'X', this is the maximum load used for the calculation of fracture toughness. The rest of the curve is generated automatically by the nanoindenter tip moving downwards to the maximum programmed displacement. A data point is created every 0.8 s. The notch of the fracture surface is marked in yellow.

The calculated values of fracture toughness in the dual-beam irradiated material are detailed in table 6.4. In bulk samples, the fracture toughness of this material has been measured at 5-10 MPa$\sqrt{m}$.[54] Therefore, the fracture behaviour recorded here appears to be in line with the bulk behaviour of the unirradiated material, despite the increase in hardness and yield stress. To compare fracture on the micro-scale, pentagonal cantilevers were also manufactured in unimplanted material and material of a similar hardness to the dual-beam sample: the W-ion implanted material. The self-ion implanted material was used to determine whether the increase in hardness after irradiation corresponds to an increase in embrittlement. These values of fracture toughness are given in tables 6.5 and 6.6, respectively.

Beam	Failure Mode	Fracture Toughness (MPa$\sqrt{m}$)
1	Plastic	>2.4
2	Plastic	>2.7
3	Plastic	>2.9
4	Plastic	>8.5
5	Plastic	>7.1
6	Plastic	>4.2
7	Plastic	>2.4
8	Plastic	>1.8
9	Plastic	>4.1
10	Plastic	>3.7
11	Plastic	>8.1
12	Plastic	>6.5
13	Brittle	5.5
14	Brittle	10.1
Average		5.0 ± 2.6

Table 6.4: Failure of fracture-testing cantilevers in the 1.5 dpa, 600 appm W-He implanted material. For beams that have failed plastically, the lower bound of fracture toughness has been calculated using the load recorded at yield.

Beam	Failure Mode	Fracture Toughness (MPa$\sqrt{m}$)
1	Plastic	>2.5
2	Plastic	>2.0
3	Plastic	>1.9
4	Plastic	>2.1
5	Plastic	>2.4
6	Plastic	>1.8
7	Plastic	>1.7
8	Plastic	>3.2
9	Plastic	>1.0
10	Brittle	3.1
Average		2.2 ± 0.6

Table 6.5: Failure of fracture-testing cantilevers in the unimplanted material. For beams that have failed plastically, the lower bound of fracture toughness has been calculated using the load recorded at yield.

Beam	Failure Mode	Fracture Toughness (MPa$\sqrt{m}$)
1	Plastic	>8.0
2	Plastic	>9.1
3	Plastic	>9.1
4	Plastic	>5.4
5	Plastic	>2.4
6	Plastic	>2.2
Average		>6.0 ± 2.9

Table 6.6: Failure of fracture-testing cantilevers in the 1.5 dpa self-ion implanted material. For beams that have failed plastically, the lower bound of fracture toughness has been calculated using the load recorded at yield.

Somewhat surprisingly, fracture toughness appears to increase in the implanted materials from 2.2 MPa$\sqrt{m}$ to over 5 MPa$\sqrt{m}$. In the implanted materials, the radiation damage results in a higher yield stress, shown in figure 6.10 and also table 6.2. As the majority (90%) of the cantilevers tested yielded rather than fractured, this increased yield stress results in an increased failure load and hence the increased lower bound of fracture toughness measured.

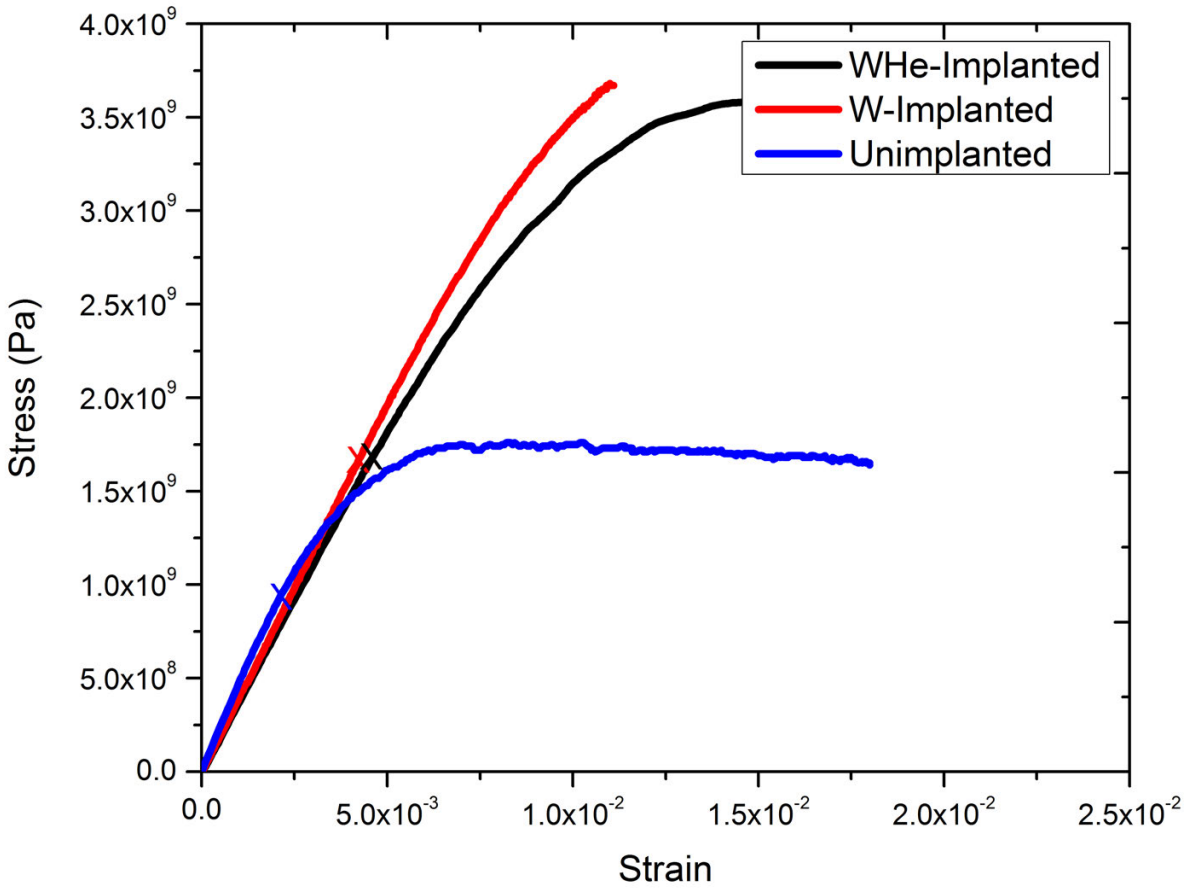

Figure 6.10: Typical load-displacement curves for pentagonal cantilevers, with the yield stresses marked to show the points used for the calculation of fracture toughness. The irradiation hardening leads to higher values of yield stress in the implanted materials. The tests were stopped when the cantilevers impacted the bottom of the trench, rather than through brittle failure.

In order to check whether this result is erroneous due to the use of yield stress in the calculation of fracture toughness, the work of deformation was also calculated for all the beams at the point of yield and at 1% strain. 1% was used as this allows most of the beams tested to be included in the analysis. The plot of the work of deformation at 1% strain is shown in figure 6.11. As the elastic modulus of tungsten does not change after implantation, the work of deformation calculated at yield shows the exact same trend the fracture toughnesses calculated above: the work of deformation increases due to the hardening from radiation damage and is therefore not shown here.

The work of deformation at 1% strain of the W-He implanted material shows more scatter, but the average is 3.9 times higher than the unimplanted material. This shows the implanted material still requires more energy to deform. It is possible that if these tests are applicable to the macro-

scale then the increased hardening seen in the nanoindentation does not correspond to increased embrittlement from a reduction in the fracture toughness.

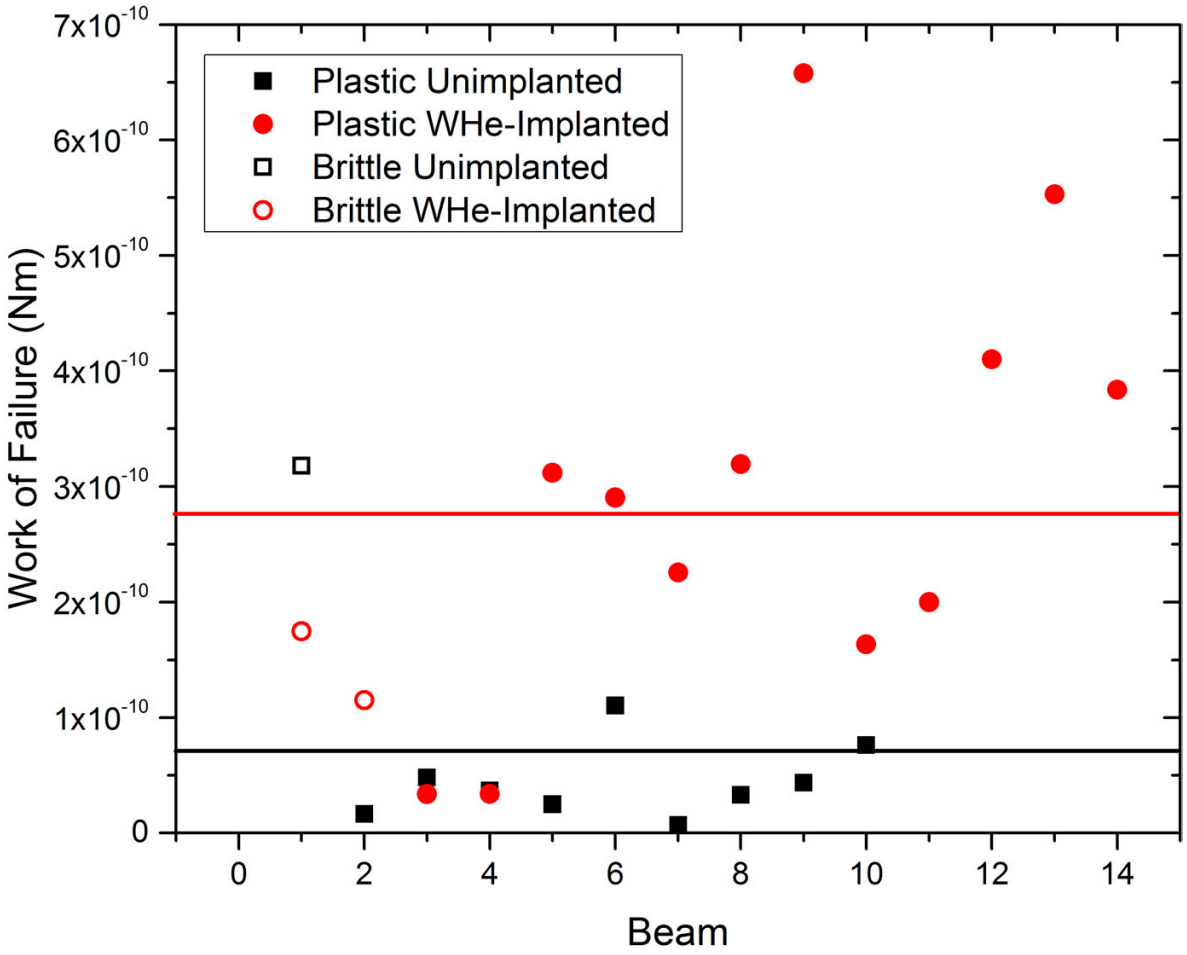

Figure 6.11: Work of deformation for unimplanted and 1.5dpa, 600appm W-He implanted cantilevers up to 1% strain. The black and red lines give the average values for the unimplanted and implanted material, respectively. The work of deformation in the implanted material is 3.9 times higher than the unimplanted material.

6.4 Discussion

6.4.1 Elastic-Plastic

In the scaling of the cantilever data to macro-scale values (table 6.3), the assumption has been that the size effect takes the same form in both the unirradiated and irradiated conditions. This assumption is worth investigating. The curve fitted to the size effect study is from Schneider[254] (equation 6.4.1) in the analysis of size effects in BCC micropillars. A very similar equation is used by Tarleton in a discrete dislocation plasticity study of the size effect in micro-cantilevers.[270]

$$\sigma = \sigma_0 + A' d^{-n'} \tag{6.4.1}$$

This work shows that n is reduced in BCC materials due to lattice resistance, i.e. how steeply the size-effect curve increases at small depths. If there is a significant amount of lattice resistance from radiation damage, this may also reduce the size effect exponent. Therefore, applying the unimplanted size effect scaling to a heavily-irradiated material would produce an irradiated yield stress that is lower than the true yield stress. That does not appear to have happened with these data. The bulk yield stress has increased in all cases, and the scaled cantilever yield stress is close to the values predicted from the nanoindentation data. The Nix-Gao analysis of the nanoindentation data (figure 4.2, page 93) demonstrated that there was no change in the indentation size effect after irradiation, therefore the nanoindentation hardnesses can be scaled by the same factor to predict the yield stress after irradiation. In ∼1 dpa proton-irradiated copper microcompression tests,[273] samples below 400 nm in diameter displayed the same yield stress dependence on size. It was only above this diameter, by which time the yield stress had dropped, that the influence of radiation damage was seen and the irradiated yield stress remains constant. This supports the argument that as long as size-dependent plasticity is dominant, radiation damage will not change the size effect exponent.

Figure 6.12 plots the yield stress against cantilever depth for all the implantation conditions and the full size-effect study. The same curve from the size effect study is fitted while allowing the bulk yield stress to vary. The amount of scatter between the beams and the small range in cantilever depths in the implanted conditions mean it is difficult to extrapolate these data to bulk

values to draw conclusions. Although the 'bulk' values of the self-ion and dual-ion implantations are reasonably different (0.5 GPa higher than the unimplanted value), it is within the 0.7-1.2 GPa of scatter in the as-measured yield stresses. Therefore, the changes in yield stress cannot be measured by cantilevers of this depth. Higher energy implantations, or a different irradiating species (e.g. protons) would be required for size-effect free data to be determined.

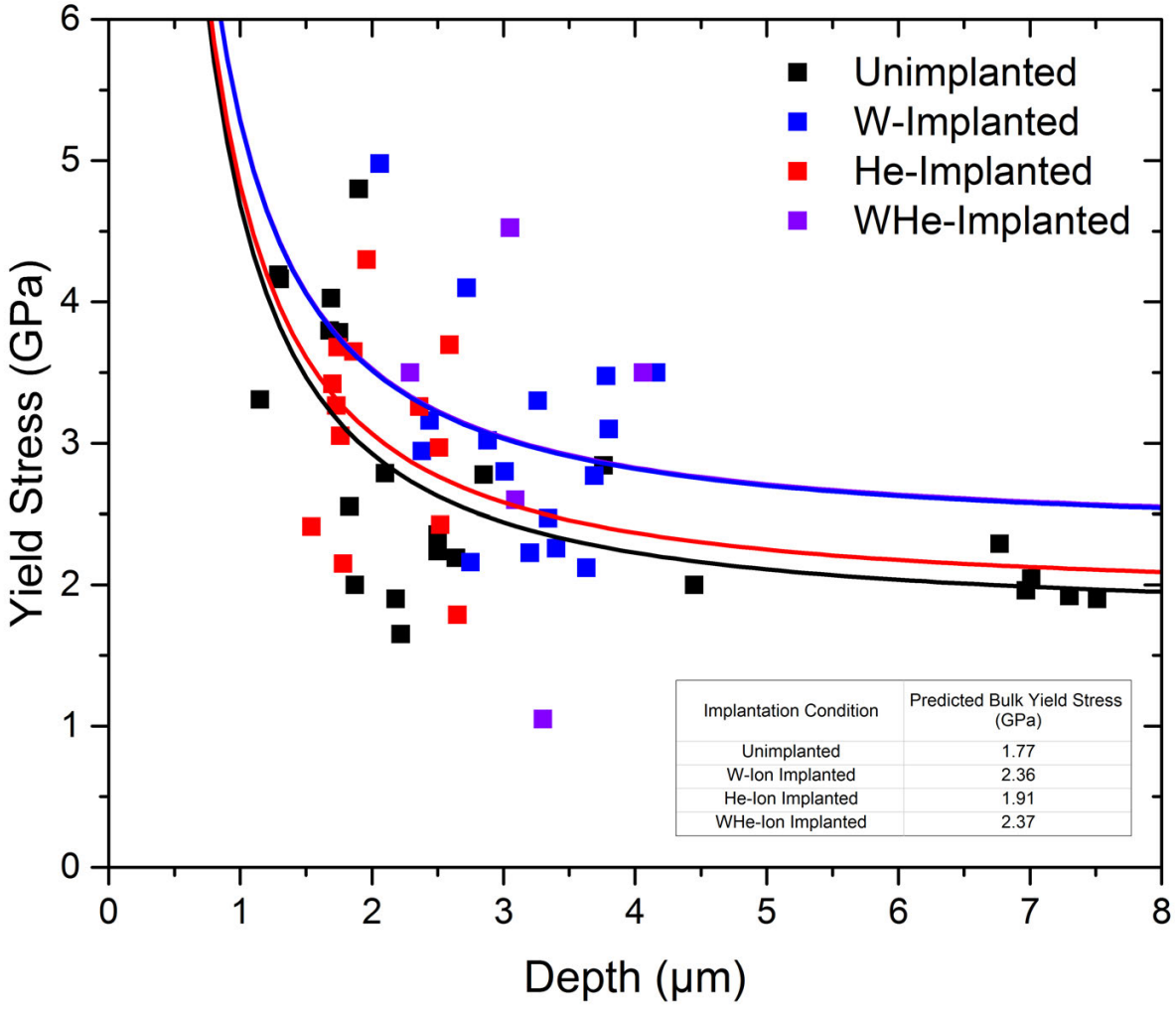

Figure 6.12: All the tested cantilevers plotted with the size-effect curve fitted to the data to extrapolate to a bulk yield stress.

6.4.2 Fracture

Fracture is rarely seen in the notched pentagonal beams, likely due to the size of the plastic zone around the pre-notch. Irwin's estimation of plastic zone size, for a uniformly stressed beam under

plane stress is given by equation 6.4.2, where r_y is the plastic zone radius, K_{1c} is the fracture toughness of the material and σ_y the yield stress. The plain strain estimate is given by equation 6.4.3, which gives a smaller, more conservative estimate of fracture toughness and is therefore the condition under which these beams would ideally be tested.

$$r_y = \frac{1}{2\pi}\left(\frac{K_{1c}}{\sigma_y}\right)^2 \tag{6.4.2}$$

$$r_y \sim \frac{1}{6\pi}\left(\frac{K_{1c}}{\sigma_y}\right)^2 \tag{6.4.3}$$

These equations are for uniformly stressed beams, but bending causes a change in stress from tension to compression moving from the notched face to the bottom of the beam. This could reduce the size of the plastic zone meaning these values are upper bounds. An ABAQUS model of a pentagonal cantilever similar to those used for the fracture toughness tests, including a 400 nm notch, is shown in figure 6.13. The maximum principle stress penetrates a similar depth into the beam and the predicted Tresca yield surface shows the neutral axis of the beam is approximately central; despite the pentagonal cross-section of the beam, the maximum principle and shear stresses are reasonably even. Therefore, the plastic zone would have to be larger than 1.4 μm for the plastic zone size predicted by equation 6.4.2 or 6.4.3 to be reduced. At this point, plasticity would be present throughout the thickness of the beam meaning fracture would not be seen.

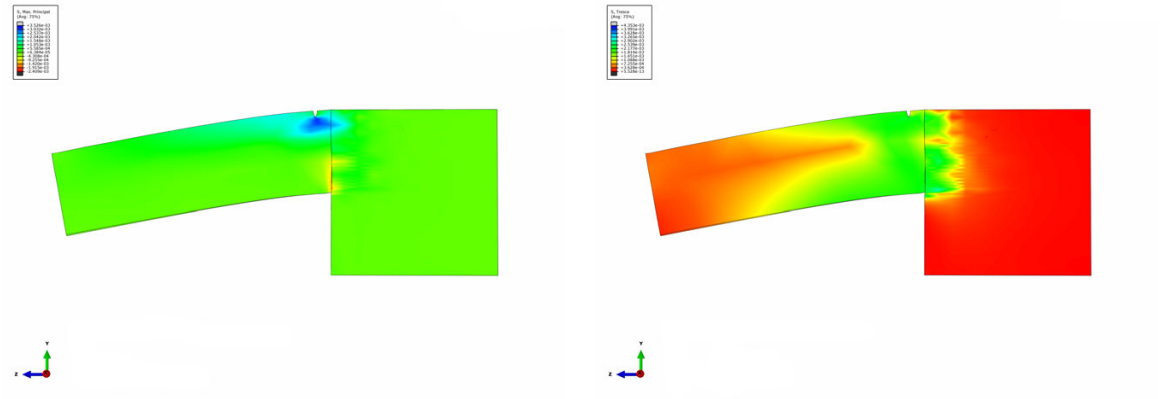

Figure 6.13: ABAQUS model of a pentagonal cantilever with the free end displaced 1 μm, showing the maximal principle stress (left) and Tresca stress (right). The size of the plastic zones around the notch and base of the cantilever are roughly equal in size with the neutral axis approximately in the centre of the beam.

Using literature values for K_{1c} and σ_y of 5-10 MPa$\sqrt{m}$ and 1.5 GPa, respectively, r_y under plane stress falls between 1.8-7.0 μm. The beams are typically 3 μm thick meaning fracture is unlikely to be seen unless failure occurs along weak grain boundaries.

For irradiated materials, the irradiation hardening increases the yield stress to approximately 2 GPa. A plain strain state occurs when the plastic zone is around $\frac{1}{15}$ of the material thickness, i.e. 200 nm. For a material with a yield stress of 2 GPa and r_y of 200 nm, K_{1c} is equal to 2.25 MPa$\sqrt{m}$. Using the measured value of K_{1c} of 5.0 and 6.0 MPa$\sqrt{m}$, r_y is determined as 1.0-1.4 μm. These data are summarised in table 6.7.

K (MPa$\sqrt{m}$)	σ_y (GPa)	r_y (μm)	Data From
5	1.5	7.0	Literature Values[32,33,54]
10	1.5	1.8	
5	2.0	1.0	Measured Values
6	2.0	1.4	
2.25	2.0	0.2	Required for plain strain and valid LEFM

Table 6.7: Calculations of Irwin's plastic zone size for various combinations of unirradiated and irradiated properties. A fracture toughness of 2.25 MPa$\sqrt{m}$ and yield stress of 2 GPa are required for plain strain conditions.

The calculations of fracture toughness shown in tables 6.4 and 6.6 show that the hardest implanted materials result in a fracture toughness of ~5 MPa$\sqrt{m}$, and are therefore not sufficiently embrittled so as to reduce r_y to a level at which fracture would routinely be seen in beams 3 μm deep. Standard fracture toughness tests require the specimen dimensions to be greater than $2.5\left(\frac{K_1}{\sigma_y}\right)^2$. Using the measured values, beams would need to be around 19 μm deep for valid plain strain conditions. This is not possible with self-ion irradiation, as it requires a 1.5 GeV self-ion irradiation to produce damage to this depth. 3 MeV protons penetrate to around 25 μm, so this irradiation could potentially be used but the low damage levels and extreme amounts of FIB time required would make it laborious.

Micro-cantilever fracture is typically seen for macro-scale fracture toughnesses under 3 MPa$\sqrt{m}$,[201] around one half of the tungsten investigated here[54] and close to plain strain conditions based on the calculations in table 6.7. The cantilevers were tested at a strain rate of around 5×10^{-5} s^{-1}, therefore testing at -50°C or 20 times faster should reduce K_{1c} to a level at which fracture would routinely be seen, based upon the macro-scale fracture toughness data.[40,54]

As the lack of fracture is a small-scale artefact, calculating a lower bound of K_{1c} for the beams that failed plastically can be attempted using the point of yield. Therefore, these tests imply that although tungsten can be significantly hardened after irradiation, it does not necessarily lead to increased embrittlement; the experiments are inconclusive. However, it must be noted that fracture in tungsten is generally intergranular and these beams incorporate only a few sub-grains per beam. They may therefore not be fully representative of the bulk properties. In particular, these tests indicate that there is no segregation of helium to the grain boundaries causing embrittlement, supported by the stability of the helium-vacancy clusters during the high temperature nanoindentation in chapter 5. However, helium would be more likely to segregate to the more open structure of high-angle grain boundaries, and given the grain size is of the order of the cantilever size (30 μm) means it is very unlikely that many of these boundaries were tested. Therefore the lack of helium embrittlement, while likely, has not been shown conclusively.

The results and previous discussion have referred to the data determined from the pentagonal cantilevers as 'fracture toughness', despite 90% of the beams failing to fracture. These ductile failures and the plastic zone size being comparable to the dimensions of the beam mean that strictly 'fracture toughness' is not being determined. Instead, the values can be more accurately described as a 'stress intensity factor at yield' or 'lower bound fracture toughness'. As above, while this means that it is likely that the ion-implantation has not lead to dramatic embrittlement, it was not possible to quantitatively determine fracture toughness data from these ion-implanted layers.

Finally, 'embrittlement' can also include a shift in the BDTT as well as a reduction in fracture toughness, indeed this is what is seen in the neutron-irradiated material in chapter 7. Although K_{1c} has not changed significantly, tests on these beams were only conducted at one temperature and strain rate and therefore cannot show any changes in the BDTT.

6.5 Summary

Micro-cantilever tests produce values of Young's modulus and yield stress that are comparable with nanoindentation data and literature data. However, the scatter between tests and the laborious process of producing specimens means that nanoindentation is probably better for investigating the effect of radiation damage on plasticity. Nevertheless, both indentation and micro-cantilevers give comparable plastic data in the as-measured and scaled conditions, implying nanoindentation can be used to predict changes in the bulk yield stress.

Cantilevers allow fracture behaviour to be investigated, which is not possible using indentation in tungsten. It is difficult for fracture to occur in cantilevers due to the size of the plastic zone. The radiation damage does not reduce the lower bound of fracture toughness as calculated from the yield stress. Instead, the measured value increases and therefore fracture is not routinely seen after irradiation. This lack of fracture, along with the calculated work of deformation, demonstrates that the ion irradiations do not lead to significant embrittlement despite the measured increases in hardness. The size of the beams means that few grain boundaries - particularly high-angle boundaries - were tested, therefore grain boundary embrittlement cannot conclusively be ruled out using these tests.

Chapter 7

Neutron Irradiation

7.1 Introduction

Fission neutrons are arguably the best analogue for fusion neutrons due to the close match in dose rate and large penetration depths allowing size effects to be neglected. While the spectra for fission and fusion neutrons differs slightly (see figure 2.5), the damage produced with PKA energy is closer between fission and fusion neutrons than for ions (figure 2.8).

From 2008 to 2009, a number of four-point bend specimens - 73 polycrystalline and 36 single-crystal - were prepared by Giannattasio and irradiated at the HFR, Petten for 282 days to an average damage level of 4 dpa (peak 4.7 dpa). The samples were not previously accessed as the material had to cool and access to the samples was severely delayed due to staff turnover in the ExtreMat project and in Petten. Once retrieved, these beams were tested in collaboration with colleagues at KIT, Germany as they have the facilities to decontaminate the specimens and test them in a controlled area. The residual activity levels were low enough that a specimen can be handled in person rather than remotely, greatly simplifying the testing process. Near the end of the project, KIT had also installed a FIB-SEM in the controlled area, allowing micro-mechanical test specimens to be manufactured.

7.2 Results

7.2.1 Macro-Mechanical Tests

The four-point bend beams were prepared by Giannattasio, who also carried out the original tests on the unirradiated material.[40,54] The beams were 1 × 1 × 11 mm in size, polished to a diamond finish on each side and subsequently electropolished, with a ∼40 μm notch in one side.

The BDTT in tungsten is sensitive to and increases with strain rate. Therefore, a slow surface strain rate to match one of Giannattasio's original tests was chosen as 3.33×10^{-5} s^{-1} so the BDTT would (hopefully) lie within the capabilities of the furnace (<1000°C) in the four-point bend testing rig. Due to time constraints, this was the only strain rate used during the tests.

Single-Crystal

Five beams in the single crystal material were tested to give the load-displacement curves shown in figure 7.2(a). Figure 7.2(b) shows the initial part of the curves more clearly. The sample tested at 900°C shows good ductility with a displacement extending to 1200 μm, equivalent to 14% surface strain.

The sample tested at 230°C appears to show some limited ductility, but subsequent fractography (figure 7.3(b)) revealed this was due to crack deflection, not plastic flow. The crack did not travel straight through the specimen parallel to the pre-notch direction but instead travelled a short distance perpendicular to the notch, and this increased crack path length produces the illusion of ductility. The 300°C curve (shown in green) clearly shows no ductile failure. Given the slight curvature of the load-displacement curve for the 600°C test, it is likely that the BDTT in this material lies slightly above this temperature.

Some non-linear behaviour can be seen in the curves up to ∼40 μm. This is a common occurrence in mechanical testing due to settling and compliance of the four-point bend rig. Although this compliance affects any subsequently determined strains, it does not affect the measured loads and hence fracture toughnesses or BDTT. A linear extrapolation backwards from the elastic region, and the known value of elastic modulus, can be used to more accurately determine strains if necessary.

Figures 7.3(a) to 7.3(d) are representative SEM images of the fracture surface for each specimen. No image was taken of the 900°C sample as it did not fracture. The fracture surface at 600°C (figure 7.3(d)) is similar to that seen in molybdenum at elevated temperatures that were still below the BDTT (figure 7.1).[274] This was attributed to stable crack growth caused by shielding dislocations near the crack tip. These dislocation concentrations induce small microcracks that run back into the main crack thus causing it to advance. It is likely a similar mechanism is occurring here given the close proximity to the BDTT.

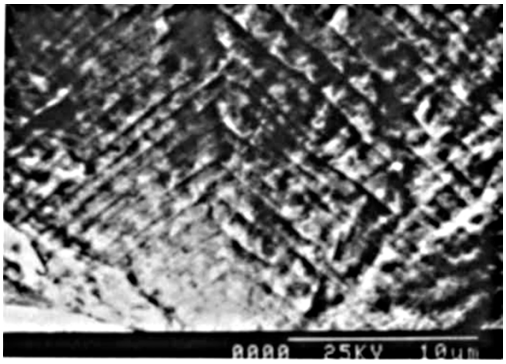

Figure 7.1: Fracture surface of molybdenum at a slow strain rate, showing steps similar to those seen here in tungsten at 600°C. From[274]

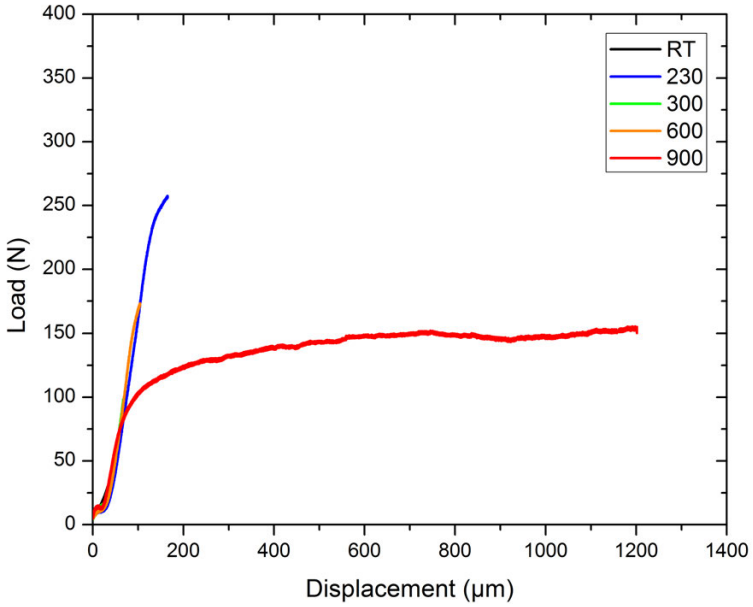

(a) Load-displacement curves for neutron-irradiated, single-crystal tungsten at a strain rate of 3.33×10^{-5} s^{-1}. The sample tested at 900°C shows significant ductility before failure. Although the sample tested at 230°C appears to show some limited ductility, subsequent fractography (figure 7.3(b)) revealed this was due to crack deflection, not ductility. The 300°C curve (shown in green) clearly shows no ductile failure.

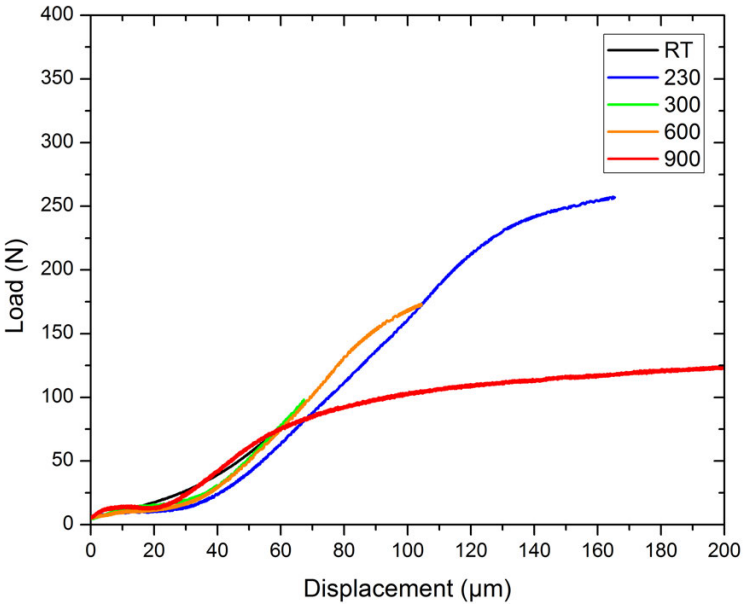

(b) Load-displacement curves for neutron-irradiated, single-crystal tungsten, enlarged to show the initial part of the curves more clearly. Some initial ductility is seen in the 600°C curve, indicating that the BDTT likely lies slightly above this temperature.

Figure 7.2: Load-displacement curves for neutron-irradiated, single-crystal tungsten tested at 3.33×10^{-5} s^{-1}.

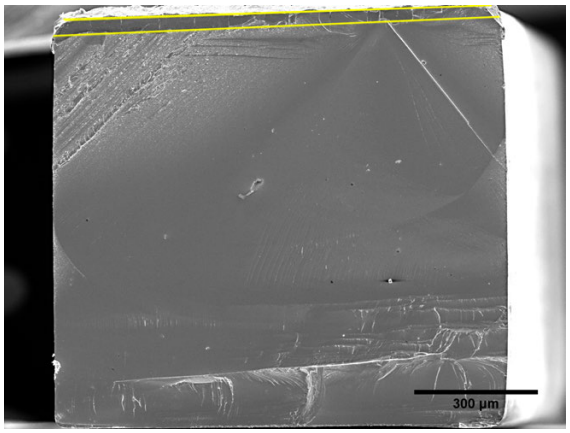

(a) 25°C fracture surface. Fracture proceeds cleanly across the whole specimen.

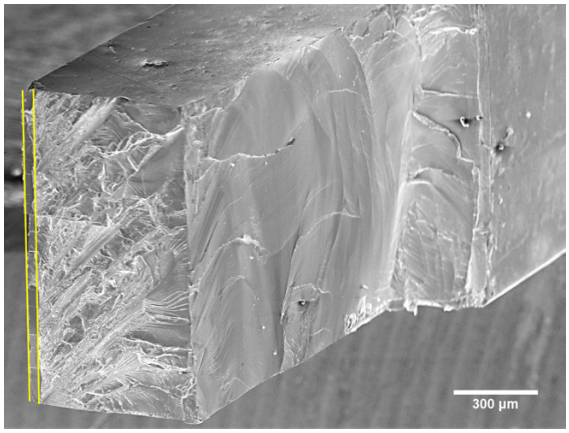

(b) 230°C fracture surface. The crack proceeds across most of the specimen before deflecting. This leads to the pseudo-ductility seen in the load-displacement curve.

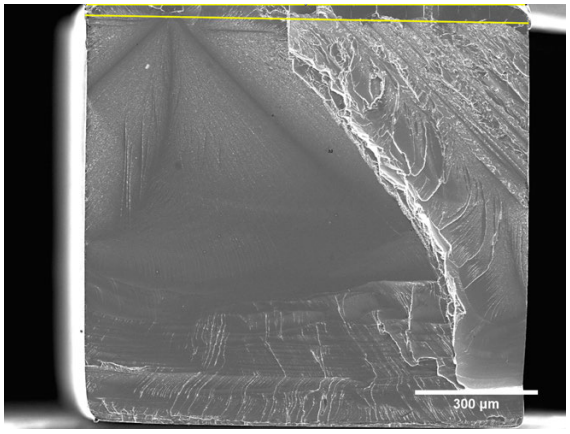

(c) 300°C fracture surface. Fracture proceeded cleanly across the specimen from the notch, indicating that the crack deflection seen at 230°C is what led to the anomalous load-displacement behaviour.

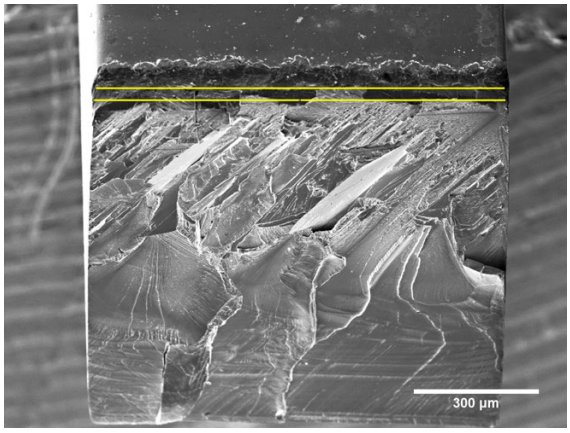

(d) 600°C fracture surface. The multiple features on the fracture surface may be indicative of dislocation mobility.

Figure 7.3: Fracture surfaces for neutron-irradiated, single-crystal tungsten tested at 3.33×10^{-5} s^{-1}. In all cases the notch is highlighted.

Poly-Crystal

The poly-crystal specimens were prepared and tested in the same way as the single-crystal beams. The load-displacement curves are shown in figures 7.4(a) with an enlarged view shown in figure 7.4(b).

Ductility is seen in the specimens tested at 300°C and above. A slight deviation from elastic deformation is seen at 230°C past ∼120 μm (1.4% strain), although the fracture surface (figure 7.5(c)) shows some crack deflection. Therefore the BDTT lies between 230°C and 300°C.

The fracture surfaces of each of the tested specimens are shown in figure 7.5.

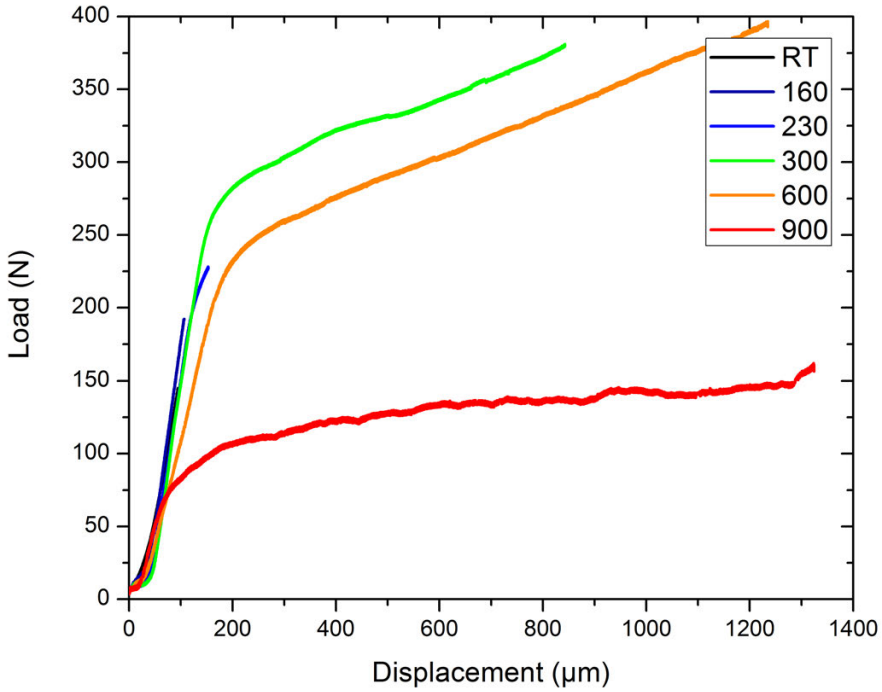

(a) Load-displacement curves for neutron-irradiated, poly-crystal tungsten.

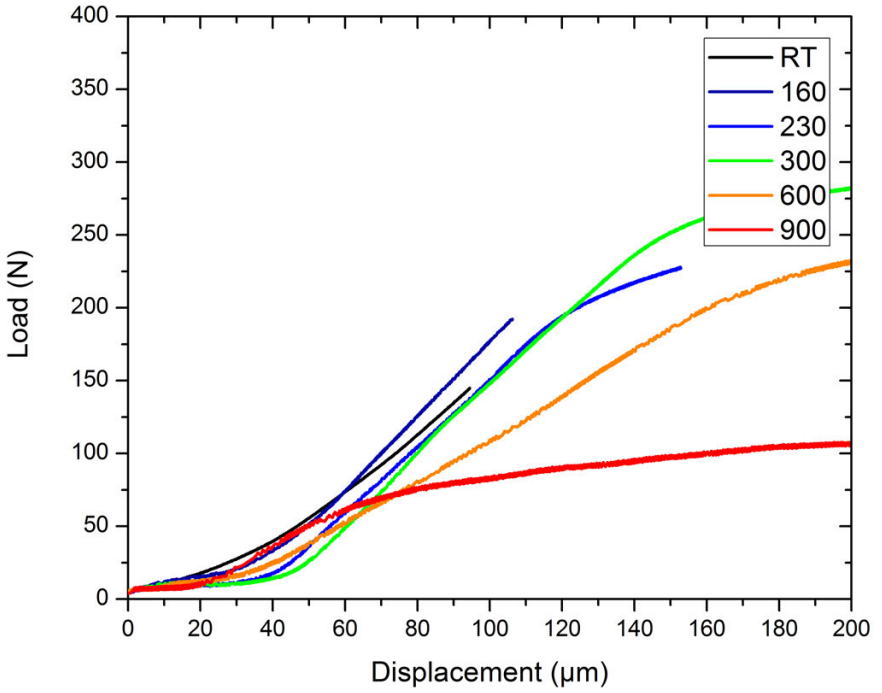

(b) Load-displacement curves for neutron-irradiated, poly-crystal tungsten, enlarged to show the initial part of the curves more clearly.

Figure 7.4: Load-displacement curves for neutron-irradiated, single-crystal tungsten tested at 3.33×10^{-5} s^{-1}.

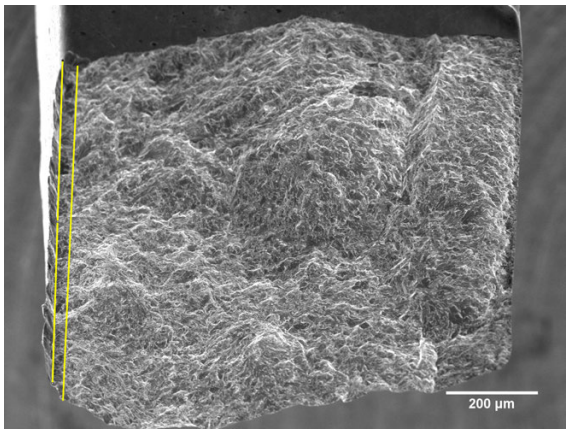

(a) 25°C fracture surface.

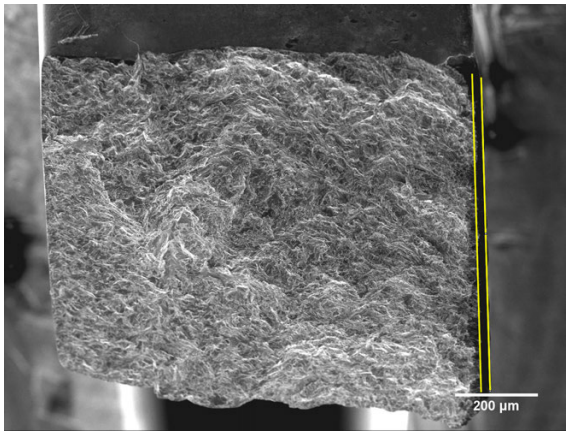

(b) 160°C fracture surface.

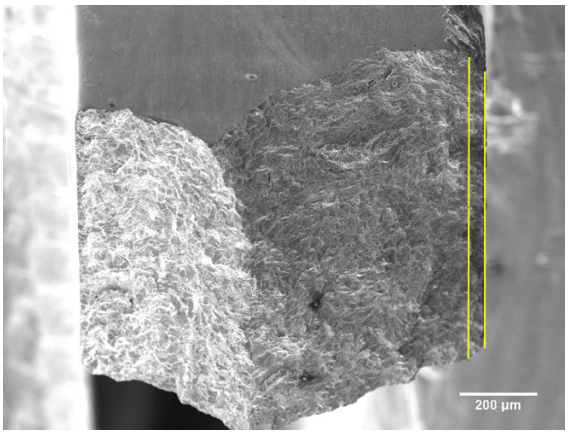

(c) 230°C fracture surface.

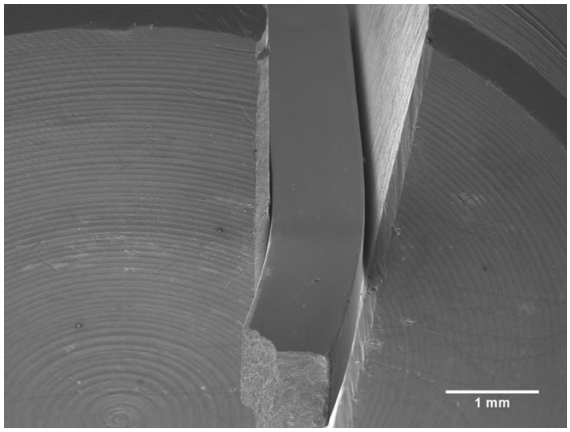

(d) 300°C bend specimen. Despite the obvious fracture of the specimen, significant bending of the beam is seen both here and in the load-displacement curve.

Figure 7.5: Fracture surfaces for neutron-irradiated, poly-crystal tungsten tested at 3.33×10^{-5} s^{-1}. In all cases the notch is highlighted.

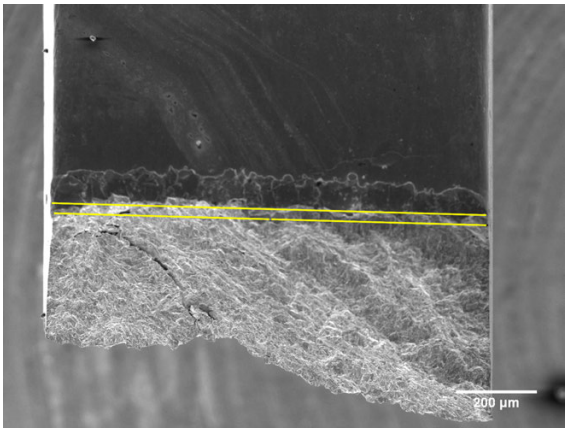

(e) 300°C fracture surface. Intergranular failure is seen through the beam.

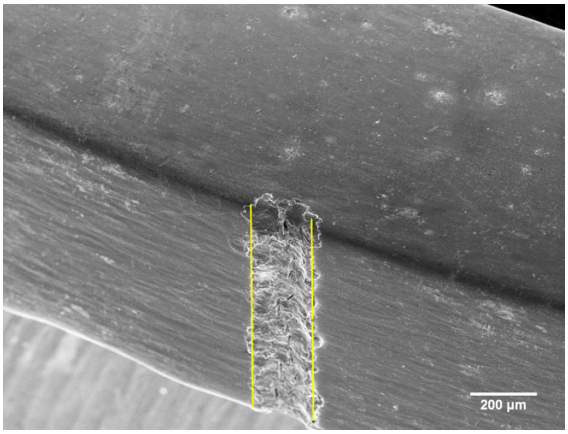

(f) 600°C specimen. No cracks are seen from the notch.

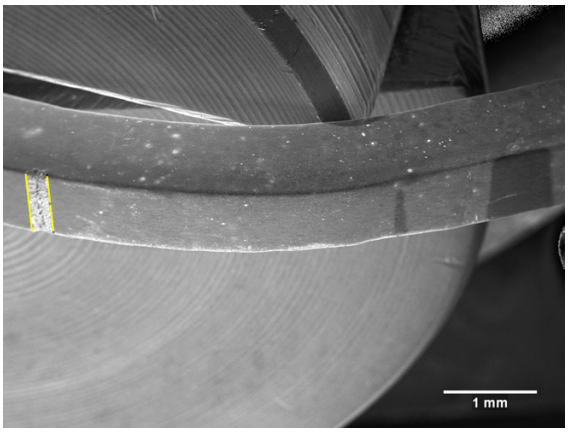

(g) 900°C surface with the notch highlighted. No cracks are seen near the notch and significant deformation of the beam is visible.

Figure 7.5: Fracture surfaces for neutron-irradiated, poly-crystal tungsten tested at 3.33×10^{-5} s^{-1}. In all cases the notch is highlighted. (cont.)

Figure 7.6 shows the fracture toughnesses determined for all the neutron-irradiated specimens tested from the maximum load during testing. Also plotted are the unirradiated fracture toughness values from the Giannattasio[40,54] at the same strain rate. As the unirradiated data are taken from the literature, the 'ductile' values of fracture toughness are the stress intensity factor at yield, hence their decrease above the BDTT. The reported values of fracture toughness for the specimens that did not fail are strictly a lower bound for the fracture toughness of the material, as was true for the pentagonal micro-cantilever tests. The micrographs of the sample clearly show no crack propagation, therefore the data cannot be referring to a fracture process.

In the unirradiated condition there is no difference between the fracture toughness of the single-crystal and poly-crystal material: 5-10 MPa$\sqrt{m}$ depending on the exact strain rate. Nor is there a difference in the calculated E_{BDT} of 1.0 eV (see equation 2.2.1) indicating that the controlling process for the BDTT is the nucleation of kink-pairs in screw dislocations in both materials. As testing only occurred at a single strain rate, it is not possible to determine a value of E_{BDT} for the neutron irradiated material.

After neutron-irradiation the values of fracture toughness are increased due to the increased hardness of the material. This was also observed in the fracture testing of the micro-cantilevers (section 6.3.2). However, the BDTT at this strain rate (3.33×10^{-5} s^{-1}) rises from ~120°C in the unirradiated condition to ~230°C in the polycrystalline material and ~600°C in the single-crystal material.

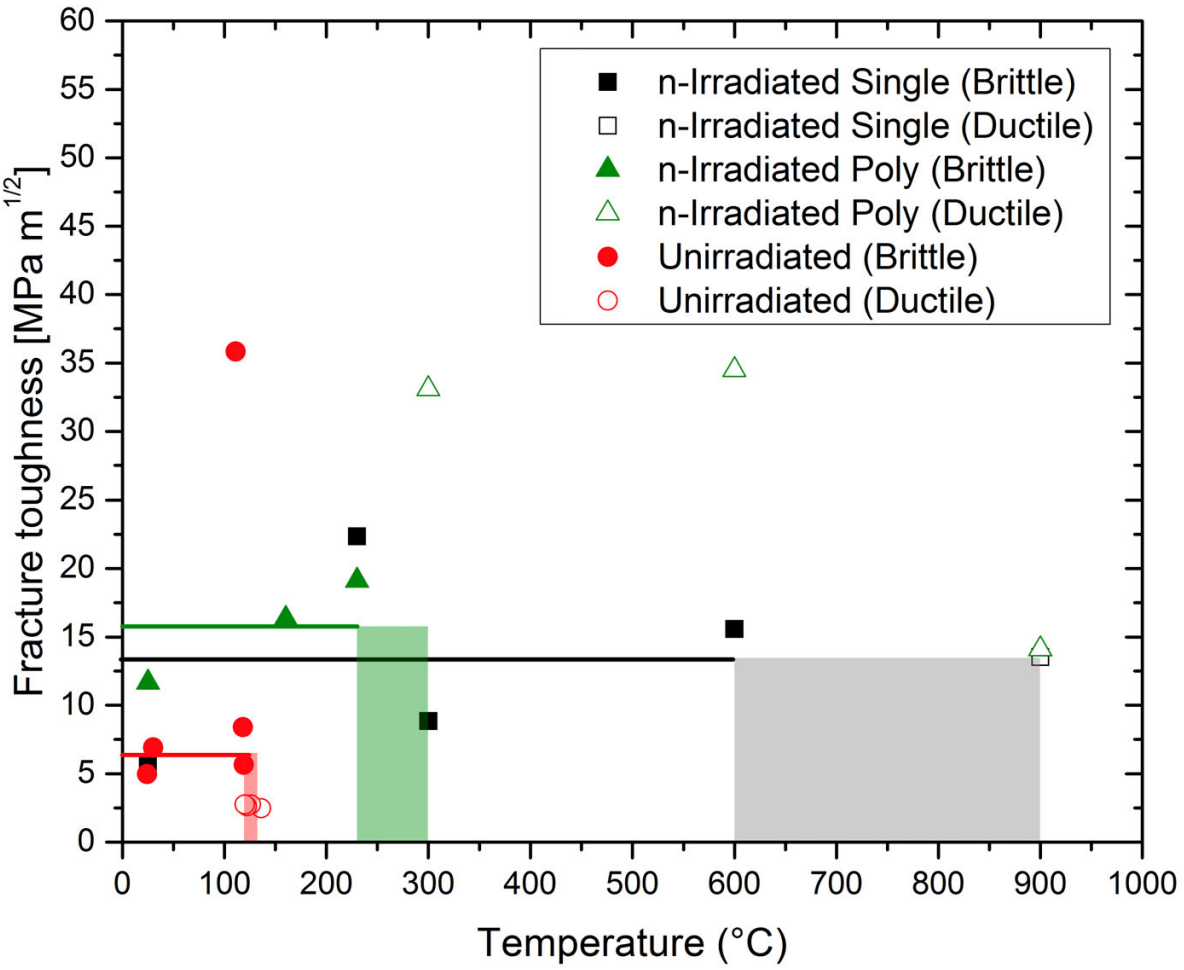

Figure 7.6: Fracture toughness of the neutron-irradiated four point bend specimens, and a comparison with unirradiated material.[40,54] The lines mark the average values for the fracture toughness of the brittle specimens, and the shaded area the potential range of the BDTT. The irradiation hardening leads to higher values of K_c in the neutron-irradiated specimens, however the BDTT increases as a result. In the unirradiated condition, there is no difference between single-crystal and poly-crystal behaviour. Here, the BDTT of the single-crystal material increases to ~600°C, while the poly-crystal only increases to ~230°C.

Sample	Failure Stress (MPa)	Notch Depth (μm)	K_{1c} (MPa$\sqrt{m}$)
Single-Crystal 25°C	470	36	5.6
Single-Crystal 230°C	1900	40	22.4
Single-Crystal 300°C	700	43	8.8
Single-Crystal 600°C	1200	43	15.6
Single-Crystal 900°C	610	40	7.5
Poly-Crystal 25°C	1000	34	11.7
Poly-Crystal 160°C	1400	38	16.3
Poly-Crystal 230°C	1700	37	19.1
Poly-Crystal 300°C	1700	40	20.1
Poly-Crystal 600°C	1500	40	17.2
Poly-Crystal 900°C	420	40	5.3

Table 7.1: Calculated values of fracture toughness of neutron-irradiated tungsten beams used to calculate the data in figure 7.6. For beams that did not fail an average value of notch depth for the specimens was used.

7.2.2 Micro-Mechanical Tests

Cantilevers were manufactured in the neutron-irradiated material using an FEI Scios FIB-SEM and tested ex-situ at KIT using an Agilent G200 nanoindenter. Nanoindentation was also performed on the same instrument using a standard Berkovich indenter, calibrated on fused silica.

The nanoindentation results are shown in figure 7.7 along with data for unimplanted material and material irradiated by self-ions to a level of 4.5 dpa that was carried out to match the damage in the neutron-irradiated samples. The implanted layer is 1 μm thick and shown in figure 3.7(b). The effect of the unimplanted substrate can therefore be seen in the ion-irradiated data, with hardness values trending back to the unimplanted curve at deep indentation depths. As the neutron damage extends through the specimen, the hardening due to the neutron damage can be calculated as 3.0 GPa in the absence of size effects by averaging the data from 500-1500 nm in depth. Between 100-400 nm where the ion-irradiated data (see chapter 4) can be examined the hardness from the ion and neutron irradiated material is very similar: 10.5-11.1 $\pm$ 1.4 GPa, an increase of also around 3 GPa.

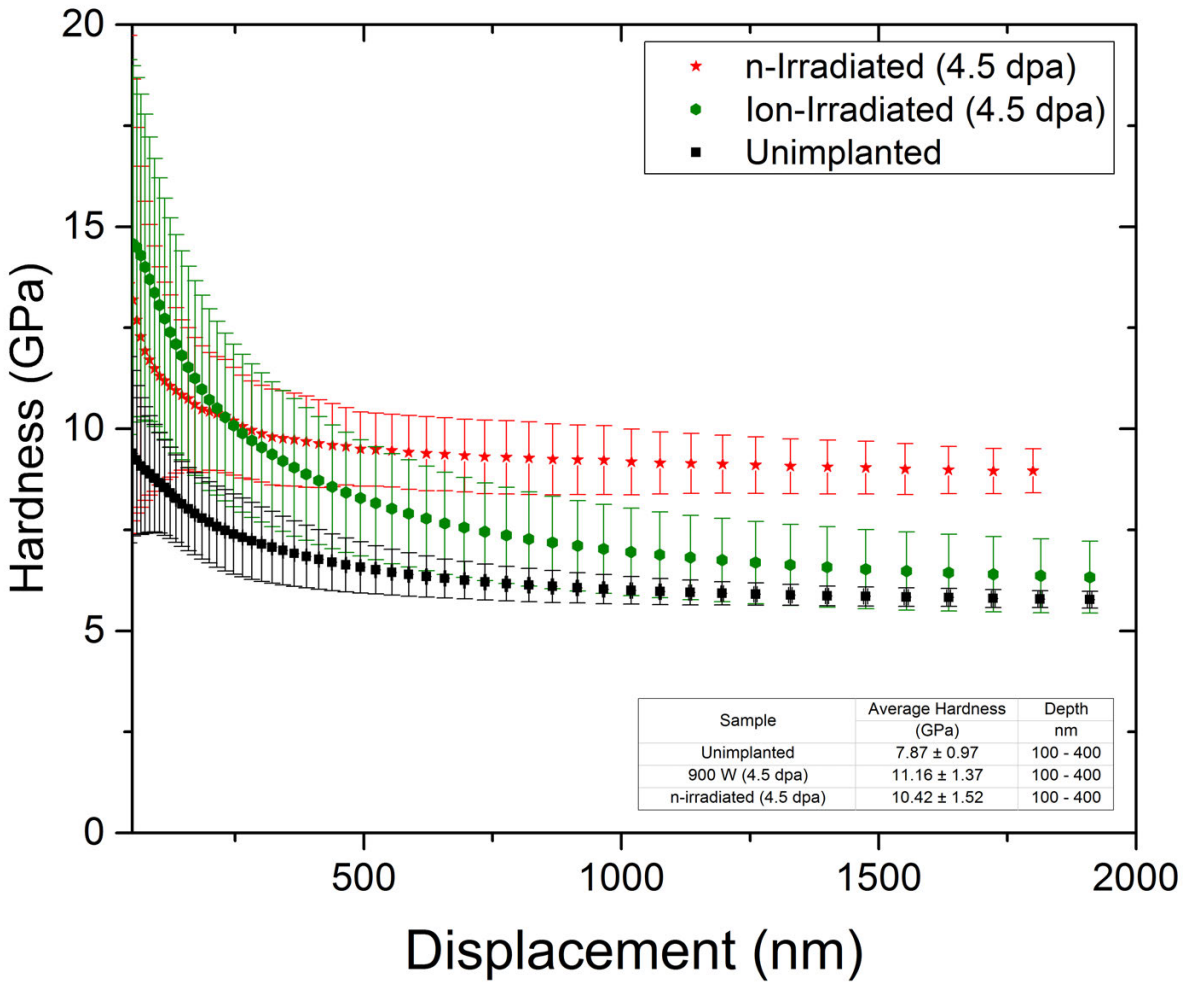

Figure 7.7: Indentation hardness of neutron-irradiated tungsten, and a comparison with ion-irradiated tungsten damaged to the same dpa. Although the effect of the unimplanted substrate are clearly visible in the ion-irradiated material, the average hardness between 100-400 nm matches closely.

Cantilevers were manufactured in the neutron-irradiated material to be at least 3 μm deep. This allows a comparison with the beams made in the 1.5 dpa ion implanted material (see chapter 6), but also limits the effects of small-scale plasticity on the data obtained. The cantilevers can be seen in figure 7.8, along with the significant thermal grooving seen in the sample. Optical images of the beams before and after testing are shown in figure 7.9. Two cantilevers - 2B and 3A in figure 7.10 - have clearly fractured. The testing of the other two beams was stopped shortly after yield to avoid any potential contamination of the nanoindenter. The stress-strain curves for the beams are shown in figure 7.10. These curves were produced using simple beam theory, however

the load-displacement curves underwent the same FEA analysis as described in section 6.2.1 to produce the values of yield stress detailed in table 7.2.

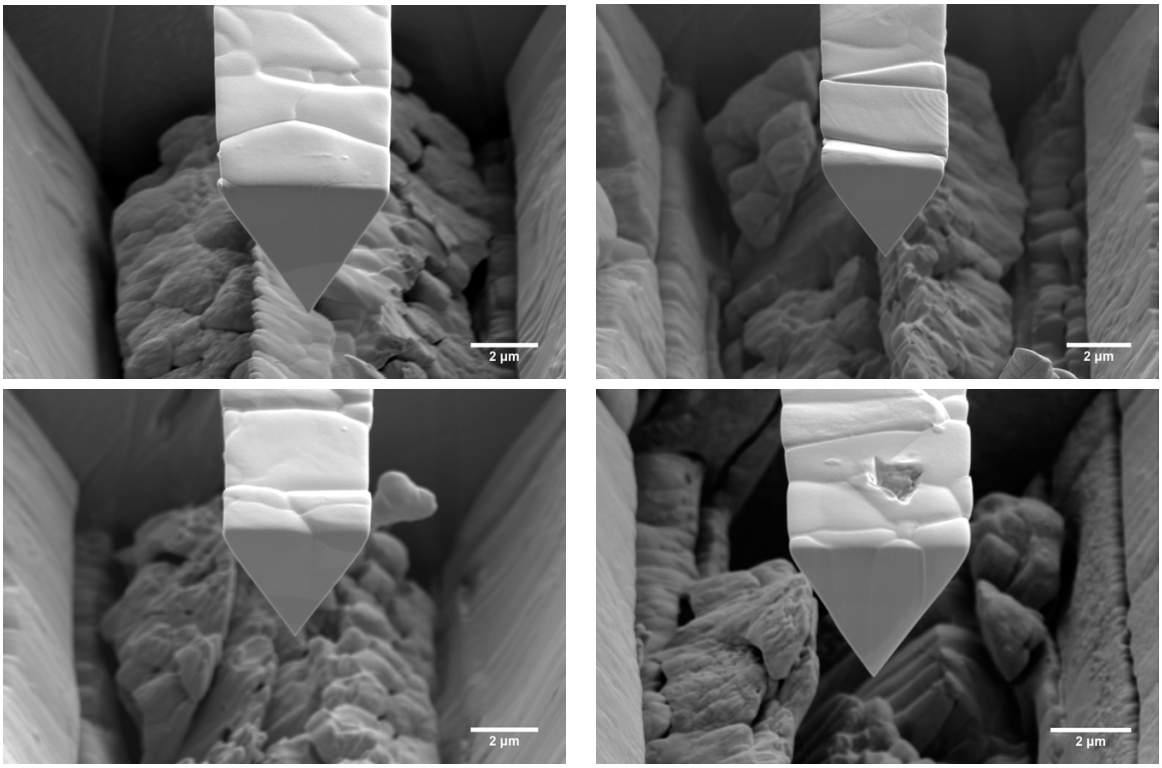

Figure 7.8: Cantilevers manufactured in the neutron-irradiated tungsten. All the beams are >3 μm deep, where size effects in the unimplanted material are minimal.

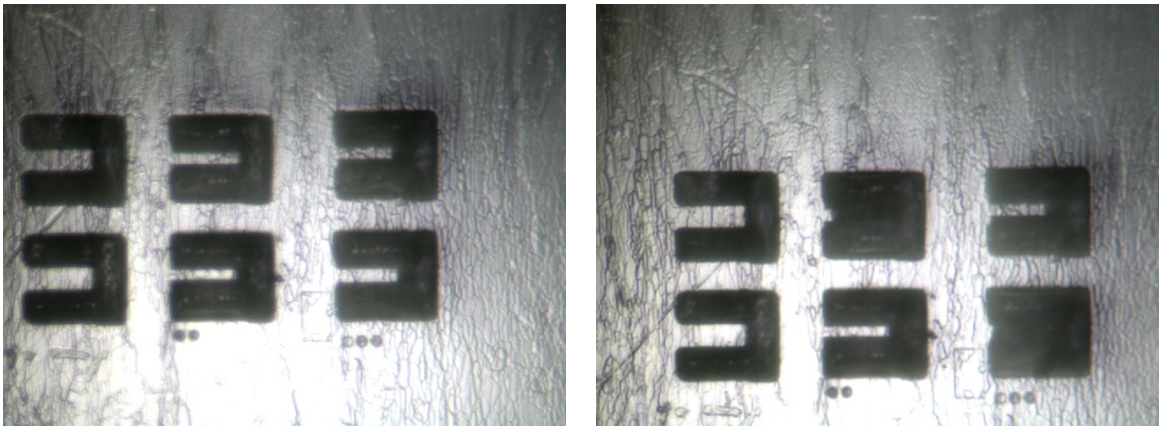

Figure 7.9: Optical image of the cantilevers before (left) and after (right) testing in the G200. Two beams appear to have fractured along the grain boundaries, despite the lack of pre-notch and triangular shape of the beam.

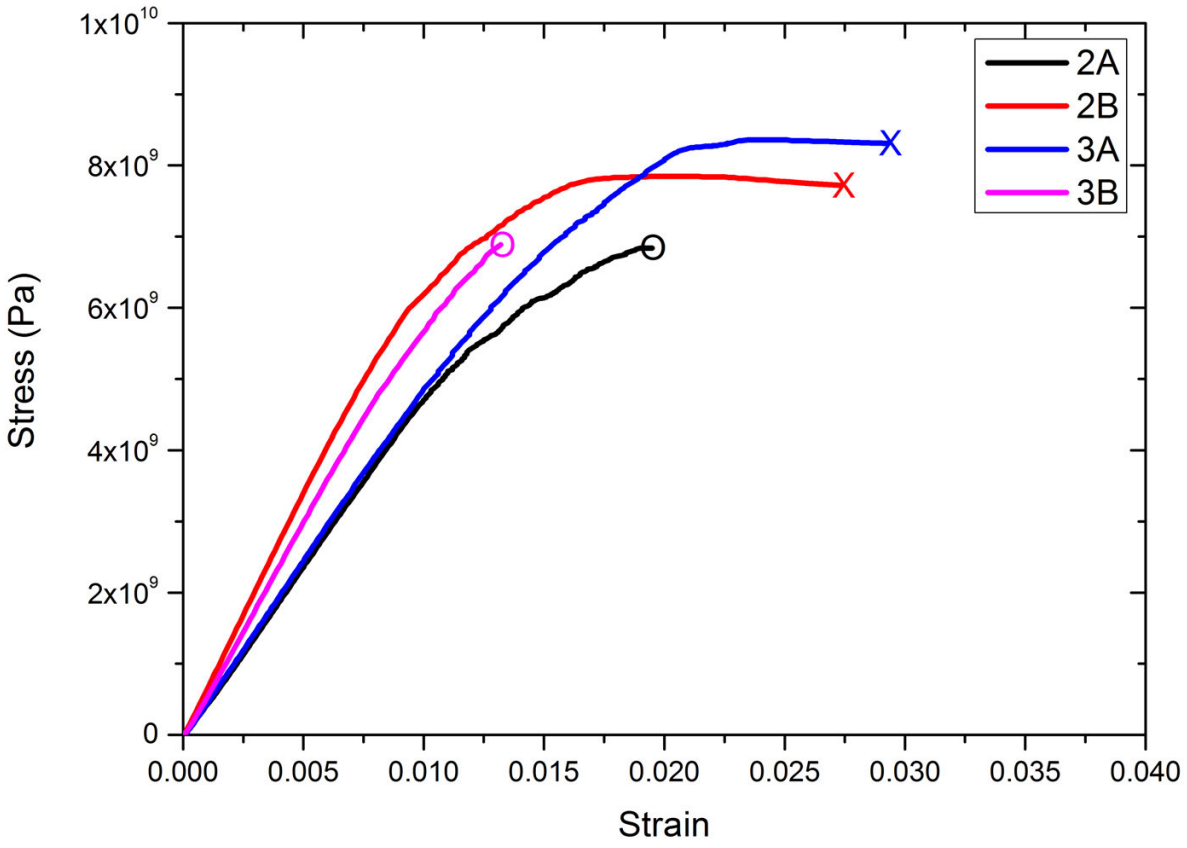

Figure 7.10: Stress-strain curves for the four beams tested, calculated using simple beam theory. Beams 2B and 3A are the beams that fractured (marked with an X); the other two tests were stopped early (marked with an O). The curves for the fractured beams show a significant degree of plastic deformation before fracture occurred.

	Unirradiated	W-Ion (1.5 dpa)	W-Ion (4.5 dpa)	n-irradiated (4.5 dpa)
Hardness (GPa)	**7.9** ± 0.97	**9.1** ± 0.44	**11.2** ± 1.37	**10.4** ± 1.52
% Above Unirradiated	0	15.2	41.7	32.1
$\frac{\text{Hardness}}{3}$ (GPa)	**2.6**	**3.0**	**3.7**	**3.5**
Cantilever Yield Stress (GPa)	**2.7** ± 0.4	**3.0** ± 0.7	-	**3.2** ± 0.2
% Above Unimplanted	0	10.2	-	16.7

Table 7.2: Micro-mechanical data from ion and neutron-irradiated tungsten. The ion-irradiated layer for the 4.5 dpa implantation is ~1 μm thick. Therefore cantilevers could not be formed in this sample as the size effect would have dominated the mechanical properties.

The rate of hardness increase with damage begins to slow at the damage levels shown in table 7.2: the increase in hardness and yield stress in the neutron-irradiated material is roughly twice that of the increase in the 1.5 dpa ion-irradiated sample. Armstrong[143] sees saturation in the hardness increase at 0.4 dpa in his work at 300°C. The difference is most likely due to the lower temperature of Armstrong's implantations as vacancy mobility is only significant above 430°.[116, 242]

There is a close agreement in hardness between the two 4.5 dpa specimens, demonstrating that the self-ions are simulating the effect of neutrons on the mechanical properties of pure tungsten very closely. Cantilevers could not be made in the 4.5 dpa ion-irradiated sample due to the shallow depth of the implanted layer, around 1 μm. The increase in hardness doubles between the 4.5 dpa and 1.5 dpa samples, as does the yield stress. This implies that the increase in yield stress follows the same trend as the increase in hardness, i.e. micro-mechanical determinations of yield stress in ion-irradiated material are very likely to produce the same values of yield stress in a neutron-irradiated specimen.

7.3 Discussion

In the macro-mechanical tests a difference between the single-crystal and poly-crystal neutron-irradiated material is seen with the BDTT of the single-crystal material ∼300°C higher. Intergranular failure is significant in these samples on both the macro- and micro-scale. Therefore it is likely that the grain boundary behaviour results in the observed difference.

Giannattasio[40] showed similar fractography in the unirradiated material. Single-crystal material shows a smooth surface with no dislocation activity at low temperatures, and 'river lines' along <110> directions at higher temperatures. Poly-crystal material shows dominantly brittle intergranular fracture at low temperatures with small amounts of transgranular fracture present at temperatures near the BDTT. This is also seen in these specimens.

In the single-crystal samples, the BDTT is entirely controlled by dislocation mobility. In the poly-crystal samples, failure can - and does - also occur along grain boundaries. If the grain boundaries have been significantly weakened from the segregation of trace impurities then failure along them should be present until higher temperatures, i.e. the BDTT should also be higher. The opposite effect is seen, therefore the boundaries must instead be acting as sinks for the displacement

damage responsible for the embrittlement. This consequently reduces the amount of damage present and hence the BDTT is closer to the unirradiated value. Armstrong[148] has shown this effect in nanostructured W-5wt%Re with a decrease in radiation hardening resistance when the material is annealed and the grain size is increased.

The difference of nearly 400°C in the BDTT between the single-crystal and poly-crystal data means that the amount of defect absorption must be substantial. Armstrong[148] sees the effect in material with a grain size of 75-200 nm, much smaller than the 2-3 μm seen in the neutron-irradiated material[54] and the 3 μm sub-grain size seen in the material investigated elsewhere in this thesis (figure 3.11). However, his irradiations were at 300°C while the neutron irradiation was carried out at 900°C; 0.32 T_m. This can be compared with neutron irradiations in molybdenum at 600°C[275] and 700°C;[276] 0.30-0.34 T_m. Here, a 1 μm zone denuded of dislocation loops was observed at the grain boundaries using TEM.

Additionally, DFT modelling[277] shows that above ∼800°C crowdion motion in tungsten becomes three-dimensional, i.e. diffusion is very rapid. It has already been stated that vacancy mobility is significant above 430°C.[116, 242] As a result, it is likely that the denuded zones in tungsten are similar to those in molybdenum and therefore it is not inconceivable that a significant fraction of the irradiation damage is absorbed by the grain boundaries; around 72% using Gianattasio's grain size (2.9 μm) and assuming spherical grains (equation 7.3.1). This matches well with the BDTT data: the single-crystal results show an increase in the BDTT of ∼100°C / dpa. If only 28% of the damage is present in the poly-crystal material, then a BDTT increase of 130°C is expected. This is very close to the 110°C measured, although it depends on the simplistic assumption that the BDTT scales linearly with dpa.

$$\begin{aligned}
\text{Denuded Zone Volume} &= \frac{4}{3}\pi(2.9^3 - 1.9^3) \\
\text{Fraction Absorbed} &= \frac{\text{Denuded Zone Volume}}{\text{Grain Volume}} \\
\text{Fraction Absorbed} &= \frac{\frac{4}{3}\pi(2.9^3 - 1.9^3)}{\frac{4}{3}\pi 2.9^3} \\
\text{Fraction Absorbed} &= 72\%
\end{aligned} \tag{7.3.1}$$

Unfortunately, due to issues with the four-point bend tests - other experiment priorities and failures in the vacuum system - testing only occurred at one strain rate: 3.33×10^{-5} s^{-1}. Therefore, it is not possible to determine an activation energy for the BDTT in the neutron-irradiated samples. If future testing occurs to determine the BDTT over a range of strain rates, then the resultant activation energy may be higher for the single-crystal than the poly-crystal specimens if this theory is true. As E_{BDT} is a measure of dislocation mobility, then the increased loop density leads to less mobile dislocation in the more damaged single-crystal material. Additionally, due to time constraints at KIT only poly-crystal material was examined via micro-mechanical methods, so as to better compare with that examined in chapters 4 and 6. The hardness of single-crystal neutron-irradiated tungsten should be higher if damage is not being absorbed at grain boundaries.

There is therefore a potential conflict between the micro-cantilevers and the four point bend tests. The micro-cantilevers would suggest significant grain boundary embrittlement; fracture is seen in the irradiated cantilevers that is not present in the unirradiated beams. The BDTT of the four-point bend tests suggests otherwise, as embrittled grain boundaries would result in a higher BDTT than the single-crystal material. As poly-crystalline tungsten fails intergranularly, embrittled and weak grain boundaries would lead to failure at higher temperatures, which is not seen in practice. Due to the size of the cantilevers, it is possible that the thermal grooving of the grain boundaries is acting to significantly concentrate the stresses near the fixed end of the beam, much like a pre-notch in fracture testing.

In the absence of a standard stress intensity factor for notched beams with a triangular cross-section, the fracture toughness is best estimated using the equation for a single edge-notched beam

(equation 7.3.2[41]). P is the failure load, S the beam length, B the beam width, W the beam depth, and a the notch depth. The notch depth, as estimated from the thermal grooving in the SEM images of the cantilevers is 150 nm. Equation 7.3.2 thus evaluates to 0.4 MPa$\sqrt{m}$, compared with 15 MPa$\sqrt{m}$ as measured macro-mechanically. The cantilever fracture toughness is lower, which supports the theory of grain boundary embrittlement. However, it is difficult to evaluate the values too exactly given the estimates made in the calculation.

$$K = \frac{PS}{BW^{\frac{3}{2}}} F\left(\frac{a}{W}\right)$$

$$F\left(\frac{a}{W}\right) = \frac{3\left(\frac{a}{W}\right)^{0.5}}{2(1+2\left(\frac{a}{W}\right))(1-\frac{a}{W})^{1.5}} \times \left[1.99 - \left(\frac{a}{W}\right)\left(1-\frac{a}{W}\right)(2.15 - 3.93\left(\frac{a}{W}\right) + 2.7\left(\frac{a}{W}\right)^2\right] \tag{7.3.2}$$

In the micro-mechanical tests the nanoindentation hardness values of the neutron-irradiated and 4.5 dpa ion-irradiated material are extremely close (10.5 to 11.1 GPa ± 1.4 GPa), indicating that the ions are probably well-representing the neutron damage. This is very promising, showing that the difference in dose rates does not affect the mechanical properties of tungsten at these moderate damage levels. However, the promising result can probably be linked to the fact that only pure tungsten was investigated. Hardie[90] used atom probe tomography to show that the dose-rate effect on the hardness of Fe-6%Cr was due to the difference in the size and number density of the chromium clusters formed after irradiation. As no elemental clustering is possible in pure tungsten, no dose rate dependence is seen. However, this will probably not be true for W-Re and W-Re-Os alloys investigated by others to determine the effect of transmutation elements.

Grain boundary embrittlement is strongly influenced by impurity segregation. It is reasonable to assume that any impurities present will have segregated to the grain boundaries after 282 days at 900°C. In Fe-Cr alloys, Hardie[90] also showed traces of nitrogen in the regions of chromium enrichment, but no evidence of segregation of other elements including carbon. As such, the lack of any dose rate effect here is not evidence that the carbon has not diffused to the grain boundaries. Therefore carbon-mediated grain boundary embrittlement is still possible, although unlikely for the reasons given above. Additionally, grain boundary segregation of carbon does not have a strong

effect on the failure of grain boundaries in tungsten.[50]

The failed micro-cantilever beams show a reasonable amount of plastic deformation (3%) before fracture occurred. If it is assumed that the thermally-grooved grain boundaries are acting as stress concentrators then this behaviour is much like the previous micro-fracture tests in section 6.3.2 that were hampered by the large plastic zone around the notch.

Finally, the nanoindentation and micro-cantilever data for the neutron-irradiated tungsten show similar trends. The yield stress of the beams does not increase by as large a proportion above the unirradiated value as the indentation hardness. This is not too surprising given the beams are still subject to a small size effect. This, and the scatter in the yield stress due to the small number of specimens leads to the reduced sensitivity of cantilevers to hardness changes, as was shown in chapter 6.

In the cantilevers, values of fracture toughness rose 270% from 2.2 MPa$\sqrt{m}$ in the unirradiated material to 6 MPa$\sqrt{m}$ after 1.5 dpa of self-ion irradiation. After neutron irradiation, values from four-point bend tests rose 220% on average from 6.5 MPa$\sqrt{m}$ to 14.5 MPa$\sqrt{m}$. This unirradiated value discounts the anomalously high 35 MPa$\sqrt{m}$ point as it is probable that some plastic deformation is occurring given the close proximity to the BDTT, therefore the value is not truly representative of brittle fracture.

Given the behaviour of the yield stress and hardness, the predicted value of fracture toughness from cantilevers produced in 4.5 dpa irradiated material is 6.6 MPa$\sqrt{m}$, a 300% increase above the unirradiated value. This is higher than the observed increase in the fracture toughness of the neutron-irradiated material. Given the close match in hardnesses, it would be unusual if the ions were poorly representing neutrons in this case. Instead, there are a number of explanations as to why the neutron-irradiated material is less brittle than predicted.

Firstly, as already mentioned when determining the values of fracture, most of the values were calculated using the yield stress as the peak load as it is assumed that the lack of fracture event is due to the large plastic zone around the notch. It may be that this assumption is incorrect and the peak load would be higher. Even if were true, this should affect the unirradiated and self-ion irradiated material equally, as no difference in the size effect was seen in indentation or the cantilevers. Secondly, relatively few grains are tested in micro-cantilevers. Grain boundary failure is predominant in tungsten (discussed in chapter 2), and the weaker grain boundaries will

naturally be 'selected' during the fracture of a four-point bend beam. It could be that not enough grain boundaries were sampled in the cantilevers and fracture toughness is artificially high as a result. Thirdly, it was seen in the first fracture tests in silicon cantilevers that the calculated fracture toughnesses were slightly (∼20%) higher than literature values.[168] This was attributed to 'the extra load needed to nucleate a sharp crack at the bottom of the notch'. This could again contribute to the cantilever-predicted fracture toughness values exceeding the bulk values, and will also tend to induce crack tip plasticity rather than fracture. It is difficult to say what influence these last two factors have on the data, given the lack of fracture events that occurred.

Finally, it could simply be insignificant within error: the scaling of fracture toughness with the increase in yield stress ($\Delta K_{1c} \times 1.167$) is $302\% \pm 11.5\%$ compared with the four point bend tests of $224\% \pm 96\%$. The large error bar is due to the degree of scatter in the neutron-irradiated material as the fracture toughness is an average of only seven values. The true value fracture toughness of the neutron-irradiated tungsten would have to lie near the extreme of this range for the data to match, but it is possible.

7.4 Summary

The four-point bend tests show an increase in the BDTT of neutron-irradiated poly-crystalline tungsten of ∼100°C and for single-crystal tungsten an increase of ∼500°C. This difference is potentially due to the grain boundaries acting as sinks for the displacement damage produced by the neutrons. The fracture toughness may be lower than that predicted by scaling micro-cantilever data. If true, this is likely due to an overestimation of the fracture toughness in micro-cantilevers due to the small number of grain boundaries tested and the extra load needed to nucleate sharp cracks.

Nanoindentation of a poly-crystalline sample produces very a similar hardness to an ion-irradiated sample. The lack of dose-rate sensitivity present is likely due to the lack of solute segregation possible. Cantilevers also show an increase in yield stress, but also fracture along grain boundaries. It is likely this is due to thermal grooving simply increasing the stress in that region.

Chapter 8

Overall Conclusions and Future Work

8.1 Summary of Key Results

- Pure tungsten at 500°C and 800°C was implanted with self-ions to 1.5 dpa or helium ions to 600 appm. An additional implantation of simultaneous tungsten and helium helium ions was performed at 800°C to 1.5 dpa and 600 appm. A 900°C, 4.5 dpa self-ion irradiation was performed to match the conditions of a neutron irradiation campaign on the same material.

- Nanoindentation was performed at room temperature on all the samples. There is no effect of implantation temperature on the hardness of the material. The hardness of self-ion implanted tungsten increases with increasing damage level and has not saturated by 4.5 dpa, unlike implantations at 300°C. The hardness of helium-implanted tungsten appears to only depend on the concentration of injected helium, likely due to the smaller defect size.

- The strength of the irradiation-induced defects is poorly described by Orowan hardening. Dislocation loops are ∼40% of the predicted strength and helium-vacancy clusters are ∼95% weaker than predicted. Due to the size of helium-vacancy clusters, it is likely a different hardening mechanism is taking place.

- The Nix-Gao indentation size effect does not change after irradiation, indicating that work hardening from GNDs dominates the hardness of shallow indents

- High-temperature nanoindentation up to a maximum of 750°C was performed on unimplanted tungsten and samples self-ion or helium-ion irradiated at 800°C. The thermal drift during these tests was reduced to levels comparable with room-temperature indentation, allowing quantitative hardness measurements to be obtained.

- In unimplanted tungsten, the hardness drops rapidly from 5.5 GPa to 2.5 GPa at 250°C, after which it is relatively constant up to 750°C. In the helium-implanted material, the small defect size means the hardening measured at room temperature drops with increasing temperature

and is negligible above 450°C. In contrast, the larger dislocation loops in the self-ion irradiated material mean that the hardness does not change up to 650°C. The larger defects are unable to be bypassed by thermally-activated dislocation processes such as cross-slip or climb.

- Indents performed on cooling the helium-implanted sample show that the helium is trapped in the helium-vacancy clusters as the hardening returns to the same level as when the sample is heated. In-situ annealing experiments show that small (<2 nm) dislocation loops are lost on heating. This implies that either the larger (∼4 nm) loops dominate the hardening in ion-implanted material or the overall increase in loop size counteracts the overall reduction in loop density.

- Micro-cantilevers were manufactured in self-ion, helium-ion and dual-beam implanted tungsten from an 800°C implantation to measure Young's modulus, yield stress and fracture toughness.

- Young's modulus is comparable with nanoindentation and literature values, and does not change after implantation. The yield stress is dominated by size-dependent hardening and the scatter from the dislocation source distribution. Nanoindentation is therefore more sensitive in picking up changes in hardness after irradiation. Fracture is difficult to measure due to the large (∼2 μm) plastic zone size around the pre-notch. No increase in fracture is seen after irradiation, and the irradiation hardening acts to increase the apparent fracture toughness by 270% and work of deformation of the material by 390%. This implies that the measured increases in irradiation hardening are not corresponding to an increase in embrittlement.

- Tungsten neutron-irradiated at 900°C to 4.5 dpa has been investigated by four-point bend tests, nanoindentation and micro-cantilever bending. The four-point bend tests show an increase in the BDTT from 120°C in the unirradiated condition to 230°C in poly-crystal material and 600°C in the single-crystal material. No difference in the BDTT exists between single and poly-crystal in the unirradiated condition.

- This difference implies that the grain boundaries are acting to absorb the defects produced in the displacement cascade, due to the 2-3 μm grain size and high irradiation temperature.

This reduces the levels of damage in the poly-crystalline material and therefore the shift in BDTT is lower.

- Nanoindentation shows comparable levels of hardness to a self-ion irradiated specimen, demonstrating that self-ions match the damage produced by neutrons in pure tungsten as there are no dose-rate dependent solute segregation effects.

- Micro-cantilevers show an increase in yield stress that can be predicted given other small-scale tests. Fracture is seen around 3% strain along grain boundaries. Given the lower BDTT in the poly-crystal material, it is likely that this is not due to grain boundary embrittlement, but instead due to thermally-grooved grain boundaries acting as stress concentrations.

- The fracture toughness from micro-cantilevers is expected to predict a higher fracture toughness than measured by four-point bending. If true, this is likely due to the few grains tested in each cantilever and an increased load necessary to nucleate a sharp crack in the beam.

8.2 Outlook

This work set out to provide insight into the ability of small-scale tests on ion-irradiated material as a way to measure the mechanical properties of neutron-irradiated, bulk-scale tungsten. In this regard, the close match in hardness between the ion-irradiated and neutron-irradiated material is very promising.

To measure additional parameters requires the use of micro-mechanics. The data from the micro-cantilevers are heavily influenced by size effects, severely restricting their ability to measure yield stress and fracture toughness. If deeper implantations can be performed either from a higher-energy facility or a different irradiating species such as protons then the cantilevers produced can be 4-5 μm in depth where size effects are minimal. Extrapolating the values of yield stress and fracture toughness to bulk values is difficult due to the multiple competing factors affecting size effects and the scatter in the data. Therefore it would be best to produce deep enough damage that they can simply be avoided.

Despite the complications due to size effects, there is some indication that the hardness data from nanoindentation can be scaled to determine values close to the bulk yield stress. As nanoindentation

is significantly faster to perform than micro-mechanical tests, this bodes well for future materials testing. Additionally, nanoindentation can be performed routinely at elevated temperature allowing data reactor-relevant data in both scale and temperature to be obtained.

Chapter 7 demonstrated that due to the increase in fracture toughness after irradiation the biggest concern with the use of tungsten in a fusion environment is the shift in the BDTT. Unfortunately, the fracture data from the micro-mechanics is inconclusive. More work is needed, using faster strain rates, lower temperatures or novel geometries such as chevron notches in order to produce reliable fracture data on the micro-scale.

8.3 Future Work

Firstly, and most simply, the testing of the remaining neutron-irradiated four point bend specimens should be completed. These tests should determine the BDTT over a range of strain rates so that the activation energy of the BDTT can be calculated. This will help explain the difference in the BDTT between the single-crystal and poly-crystal material that is not seen in the unirradiated condition.

It was seen in the neutron-irradiated cantilevers that fracture readily occurred, despite the triangular shape of the beams. Preliminary examination shows that this fracture proceeded along the grain boundaries. Fracture testing in the ion-irradiated material was carried out on a sample irradiated to 1.5 dpa, not the 4.5 dpa present in the neutron-irradiated tungsten. Although fracture was rarely seen, the hardness of the material increases with increasing damage. Therefore, it cannot be assumed that fracture would not occur in the ion-irradiated material and it is therefore also not clear whether the radiation hardening is leading to embrittlement, rather than oxidation, impurity segregation to grain boundaries or thermal grooving causing a stress concentration.

As such, it is necessary to carry out an annealing of the same material under the same conditions that the specimens were initially irradiated: 282 days at 900°C in high-purity argon. This will separate the effects of the thermal ageing and the radiation damage. Additionally, it may be worthwhile to carry out a 4.5 dpa, 900°C W-ion implantation at JANNuS or a similar facility to produce a deep ion-irradiated layer to compare micro-fracture of ion-implanted and neutron-irradiated material.

Similarly, the most important parameter when considering the use of tungsten in a fusion environment is the BDTT. It would be extremely useful if the BDTT of ion-irradiated cantilevers matched the BDTT of neutron-irradiated material. The deep implantation detailed above in combination with the high-temperature nanoindenter system could be used to investigate whether this is the case. Even though fracture is difficult to obtain, with a high enough strain rate and given the system supports sub-zero temperatures, it should be possible to routinely obtain fracture. This subsequently allows E_{BDT} to be calculated which describes the BDTT behaviour for the irradiation condition.

TEM by Yi[79] and Beck[154] has proved instrumental in relating the change in mechanical properties to the modification of the tungsten microstructure after irradiation. However, that work was performed on annealed material with a large grain size. As grain boundaries act as sinks for radiation damage, it would be prudent to perform TEM on the samples investigated here to ensure that the conclusions drawn are still valid. Additionally, no TEM has been performed on the dual-beam implanted material, thus the form of the radiation damage is unknown. Finally, it would be interesting to form TEM lamella from indents - potentially using ones made over a range of temperatures - in order to observe directly the interaction between dislocations and radiation damage.

Only one dual-beam implantation was performed. The indentation hardening is equal to the sum of the hardening of the component parts. This is very different to sequential implantations at 300°C, where the dislocation loops act as sinks for the helium thus reducing its hardening effect. However, it is not known whether the increased hardening seen here is a result of the dual-beam implantation (i.e. a synergistic effect) or simply the higher implantation temperature. It would be interesting to see if such a synergistic effect exists, and whether additional synergy is present when hydrogen is also simultaneously implanted.

Bibliography

[1] BP. *BP Statistical Review of World Energy: June 2011*. Web Page, 2011. http://www.bp.com/content/dam/bp-country/de_de/PDFs/brochures/statistical_review_of_world_energy_full_report_2011.pdf.

[2] Hurst, T. *China's Massive Coal-Fired Power Plant Boom Visualized*. Web Page, 2010. http://ecopolitology.org/2010/08/26/chinas-massive-coal-fired-power-plant-boom-visualized/.

[3] World Nuclear News. *Another Drop in Nuclear Generation*. Web Page. http://www.world-nuclear-news.org/EE_Another_drop_in_nuclear_generation_0505102.html.

[4] Greenpeace. *Nuclear Safety Campaign*. Web Page, 2014. http://www.greenpeace.org/international/en/campaigns/nuclear/safety/.

[5] Watch, N.W. *National Wind Watch Frequently Asked Questions*. Web Page, 2015. https://www.wind-watch.org/faq-output.php.

[6] Matlack, C. *Sahara Solar Energy Could Power Europe*. Web Page, 2010. http://www.bloomberg.com/bw/magazine/content/10_38/b4195012469892.htm.

[7] Mendick, R., et al. *True Cost of Britain's Wind Farm Industry Revealed*, 2013. http://www.telegraph.co.uk/news/earth/energy/windpower/10122850/True-cost-of-Britains-wind-farm-industry-revealed.html.

[8] Wald, M. *Wind Drives Growing Use of Batteries*. Web Page, 2010. http://www.nytimes.com/2010/07/28/business/energy-environment/28storage.html?_r=0.

[9] EFDA. *JET's Maximum Achieved Parameters*. Web Page, 2008. http://www.jet.efda.org/wp-content/uploads/JET-main-features.pdf.

[10] Miyazawa, J. *Fusion Triple Product and the Density Limit of High-Density Internal Diffusion Barrier Plasmas in LHD*. 35th EPS Conference on Plasma Physics, 32D:1076, 2008.

[11] ITER Organization. *ITER and Beyond*. Web Page, 2015. https://www.iter.org/proj/iterandbeyond.

[12] ITER Organization. *The ITER divertor.* Web Page, 2015. `https://www.iter.org/mach/divertor`.

[13] Nygren, R. *Making Tungsten Work.* Journal of Nuclear Materials, 417(1-3):451, 2011.

[14] Bolt, H., et al. *Materials for the plasma-facing components of fusion reactors.* Journal of Nuclear Materials, 329-333(1-3 PART A):66, 2004.

[15] Merola, M., et al. *ITER plasma-facing components.* Fusion Engineering and Design, 85(10-12):2312 , 2010.

[16] Riccardi, B., et al. *Preliminary results of the experimental study of PFCs exposure to ELMs-like transient loads followed by high heat flux thermal fatigue.* Fusion Engineering and Design, 86(9-11):1665 , 2011.

[17] Norajitra, P., et al. *Progress of He-cooled divertor development for DEMO.* Fusion Engineering and Design, 86(9-11):1656, 2011.

[18] Lindau, R. *ODS-EUROFER - A Reduced Activation Ferritic-Martensitic ODS-Steel for Application in Advanced Blanket Concepts.* Web Page, 2014. `http://bibliothek.fzk.de/zb/veroeff/62596.pdf`.

[19] Cheng, E. *Assessment of low activation materials.* In *Fusion Engineering, 1991 Proceedings., 14th IEEE/NPSS Symposium on*, 621.

[20] Zinkle, S., et al. *Operating temperature windows for fusion reactor structural materials.* Fusion Engineering and Design, 51-52:55, 2000.

[21] Singheiser, L., et al. *Plasma-facing materials for thermo-nuclear fusion devices.* Transactions of the Indian Institute of Metals, 62(2):123, 2009.

[22] Munsat, T. *High-temperature carbon-irradiation issues for the Sombrero ICF reactor.* Fusion Engineering and Design, 54(2):249 , 2001.

[23] Loarer, T. *Tritium Inventory in ITER: Laboratory data and extrapolation from tokamaks.* In *6th EU PWI TF Meeting Madrid.* 2007.

[24] Pestchanyi, S., et al. *Estimation of carbon fibre composites as ITER divertor armour.* Journal of Nuclear Materials, 329-333, Part A(0):697 , 2004.

[25] Roth, J. *Tritium inventory in ITER plasma-facing materials and tritium removal procedures.* Plasma Physics and Controlled Fusion, 50(10):103001, 2008.

[26] Brooks, J.N., et al. *Plasma-surface interaction issues of an all-metal ITER.* Nuclear Fusion, 49(3), 2009.

[27] Bolt, H., et al. *Plasma facing and high heat flux materials - Needs for ITER and beyond.* Journal of Nuclear Materials, 307-311(1 SUPPL.):43, 2002.

[28] Khripunov, B. *Accumulation of deuterium in radiation-damaged tungsten.* Journal of Surface Investigation, 5(2):272, 2011.

[29] Winter, M. *Tungsten: Physical Properties.* Web Page, 2015. `http://www.webelements.com/tungsten/`.

[30] Pitts, R.A., et al. *A full tungsten divertor for ITER: Physics issues and design status.* Journal of Nuclear Materials, 438, Supplement(0):S48, 2013.

[31] Kukushkin, A.S., et al. *ITER tungsten divertor: Initial operation at low power.* In *40th EPS Conference on Plasma Physics, EPS 2013*, vol. 1, 289–292.

[32] Gumbsch, P. *Brittle fracture and the brittle-to-ductile transition of tungsten.* Journal of Nuclear Materials, 323(2-3):304, 2003.

[33] Margevicius, R.W., et al. *Fracture toughness of polycrystalline tungsten under mode I and mixed mode I-II loading.* Materials Science and Engineering A, 270(2):197, 1999.

[34] Tran-Huu-Loi, et al. *Brittle fracture of polycrystalline tungsten.* Journal of Materials Science, 20(1):199, 1985.

[35] Barabash, V., et al. *Neutron irradiation effects on plasma facing materials.* Journal of Nuclear Materials, 283-287(Part 1):138, 2000.

[36] Gorynin, I., et al. *Effects of neutron irradiation on properties of refractory metals.* Journal of Nuclear Materials, 191-194(PART A):421, 1992.

[37] International Tungsten Industry Association. *Tungsten uses*. Web Page, 2011. `http://www.itia.info/about-tungsten.html`.

[38] Gumbsch, P., et al. *Controlling factors for the brittle-to-ductile transition in tungsten single crystals*. Science, 282(5392):1293, 1998.

[39] Mutoh, Y., et al. *Effect of rhenium addition on fracture toughness of tungsten at elevated temperatures*. Journal of Materials Science, 30(3):770, 1995.

[40] Giannattasio, A., et al. *Strain-rate dependence of the brittle-to-ductile transition temperature in tungsten*. Philosophical Magazine, 87(17):2589, 2007.

[41] Hertzberg, R.W. *Deformation and fracture mechanics of engineering materials*. John Wiley & Sons, 1996.

[42] Murphy, J.D., et al. *Characterisation of plastic zones around crack-tips in pure single-crystal tungsten using electron backscatter diffraction*. IOP Conference Series: Materials Science and Engineering, 3:6, 2008.

[43] Hirth, J.P., et al. *Theory of dislocations*. Wiley, 1982.

[44] Qiao, Y., et al. *Brittle-to-ductile fracture transition in Fe-3wtcrystals by thermal crack arrest*. Mechanics of Materials, 35(9):903, 2003.

[45] Hull, D., et al. *Introduction to Dislocations*. Butterworth-Heinemann, 2001.

[46] Dieter, G., et al. *Mechanical Metallurgy*. McGraw-Hill Education, 1989.

[47] Cottrell, A.H., et al. *Dislocation Theory of Yielding and Strain Ageing of Iron*. Proceedings of the Physical Society. Section A, 62(1):49, 1949.

[48] Gilman, P., et al. *Mechanical Alloying*. Annual Review of Materials Science, 13:279, 1983.

[49] Grujicic, M., et al. *Atomistic simulation of Sigma-3 (111) grain boundary fracture in tungsten containing various impurities*. International Journal of Refractory Metals and Hard Materials, 15(5-6):341 , 1997.

[50] Gludovatz, B., et al. *Influence of impurities on the fracture behaviour of tungsten.* Philosophical Magazine, 91(22):3006, 2011.

[51] Gludovatz, B., et al. *A study into the crack propagation resistance of pure tungsten.* Engineering Fracture Mechanics, 100:76, 2013.

[52] Petch, N.J. *The Cleavage Strength of Polycrystals.* Journal of the Iron and Steel Institute, 174:25, 1953.

[53] Hall, E.O. *The Deformation and Ageing of Mild Steel: III Discussion of Results.* Proceedings of the Physical Society B, 64:747, 1951.

[54] Giannattasio, A., et al. *Brittle-ductile transitions in polycrystalline tungsten.* Philosophical Magazine, 90(30):3947, 2010.

[55] Noto, H., et al. *Effect of grain orientation and heat treatment on mechanical properties of pure W.* Journal of Nuclear Materials, 455(13):475, 2014.

[56] Romaner, L., et al. *Effect of rhenium on the dislocation core structure in tungsten.* Physical Review Letters, 104(19):195503, 2010.

[57] Rieth, M., et al. *Influence of microstructure and notch fabrication on impact bending properties of tungsten materials.* International Journal of Refractory Metals and Hard Materials, 28(6):679, 2010.

[58] Gibson, J., et al. *Tungsten for Fusion Power Applications.* Part II thesis, University of Oxford, 2011.

[59] Du, J., et al. *Shear debonding behavior of a carbon-coated interface in a tungsten fiber-reinforced tungsten matrix composite.* Journal of Nuclear Materials, 417(1-3):472, 2011.

[60] Du, J., et al. *Interfacial fracture behavior of tungsten wire/tungsten matrix composites with copper-coated interfaces.* Materials Science and Engineering A, 527(6):1623, 2010.

[61] He, G., et al. *Preparation of tungsten fiber reinforced-tungsten/copper composite for plasma facing component.* Journal of Nuclear Materials, 455(1-3):225, 2014.

[62] Kurumada, A., et al. *Evaluation of the integrity of divertor models of tungsten or SiC/SiC composites joined with copper.* Journal of Nuclear Materials, 313-316(SUPPL.):245, 2003.

[63] Reiser, J., et al. *Tungsten foil laminate for structural divertor applications - Basics and outlook.* Journal of Nuclear Materials, 423(1-3):1, 2012.

[64] Nmeth, A.A.N., et al. *The nature of the brittle-to-ductile transition of ultra fine grained tungsten (W) foil.* International Journal of Refractory Metals and Hard Materials, 50(0):9, 2015.

[65] Saito, S., et al. *Mechanical properties of HIP bonded W and Cu-alloys joint for plasma facing components.* Journal of Nuclear Materials, 307-311(2 SUPPL.):1542, 2002.

[66] Kalin, B., et al. *Development of brazing foils to join monocrystalline tungsten alloys with ODS-EUROFER steel.* Journal of Nuclear Materials, 367-370 B(SPEC. ISS.):1218, 2007.

[67] Kallenbach, A., et al. *Divertor power load feedback with nitrogen seeding in ASDEX Upgrade.* Plasma Physics and Controlled Fusion, 52(5):055002, 2010.

[68] Battabyal, M., et al. *W-2wt%Y2O3 composite: Microstructure and mechanical properties.* Materials Science and Engineering A, 538:53, 2012.

[69] Veleva, L. *Contribution to the production and characterisation of W-Y, W-Y2O3 and W-TiC materials for fusion reactors.* Phd thesis, 2011.

[70] Fan, J., et al. *Micro/nano composited tungsten material and its high thermal loading behavior.* Journal of Nuclear Materials, 455(13):717, 2014.

[71] Bushby, A., et al. *Nanoindentation investigation of ion-irradiated Fe-Cr alloys using spherical indenters.* Journal of Materials Research, 27(1):85, 2012.

[72] Armstrong, D.E.J., et al. *Measuring anisotropy in Young's modulus of copper using micro-cantilever testing.* Journal of Materials Research, 24(11):3268, 2009.

[73] Wiffen, F. *Effects of Irradiation on Properties of Refractory Alloys With Emphasis on Space Power Reactor Applications.* In *Symposium on refractory alloy technology for space nuclear power applications*, 252–277.

[74] Ciupinski, L., et al. *TEM observations of radiation damage in tungsten irradiated by 20 MeV W ions.* Nuclear Instruments and Methods in Physics Research Section B: Beam Interactions with Materials and Atoms, 317, Part A(0):159 , 2013.

[75] Yi, X., et al. *In situ study of self-ion irradiation damage in W and W-5Re at 500C.* Philosophical Magazine, 93(14):1715, 2013.

[76] Hardie, C.D., et al. *Effects of irradiation temperature and dose rate on the mechanical properties of self-ion implanted Fe and Fe-Cr alloys.* Journal of Nuclear Materials, 439(1-3):33 , 2013.

[77] Zheng, Y., et al. *Investigation of Radiation Damage in Stainless steel, Tungsten and Tantalum by Heavy Ion Irradiations.* Nuclear Physics A, 834(1-4):761c, 2010.

[78] Troev, T., et al. *Simulation of defects in fusion plasma first wall materials.* Journal of Physics: Conference Series, 516(1), 2014.

[79] Yi, X. *Electron Microscopy Study of Radiation Damage in Tungsten and Alloys.* DPhil thesis, University of Oxford, 2013.

[80] Vladimirov, P., et al. *Comparison of material irradiation conditions for fusion, spallation, stripping and fission neutron sources.* Journal of Nuclear Materials, 329-333(1-3 PART A):233, 2004.

[81] Ryazanov, A., et al. *Radiation damage formation in fusion structural materials due to elastic and inelastic processes.* Journal of Nuclear Materials, 417(1-3):1074 , 2011.

[82] Stoller, R.E. *The role of cascade energy and temperature in primary defect formation in iron.* Journal of Nuclear Materials, 276(1-3):22 , 2000.

[83] Sawan, M. *Damage parameters of structural materials in fusion environment compared to fission reactor irradiation.* Fusion Engineering and Design, 87(5-6):551, 2012.

[84] JANNUS. *JANNuS: Joint Accelerators for Nano-science and Nuclear Simulation.* Web Page, 2014. `http://jannus.in2p3.fr`.

[85] Serruys, Y., et al. *JANNUS: experimental validation at the scale of atomic modelling.* Comptes Rendus Physique, 9(3-4):437 , 2008.

[86] Shimada, M. *Overview of the US-Japan collaborative investigation on hydrogen isotope retention in neutron-irradiated and ion-damaged tungsten.* Fusion Engineering and Design, 87(7-8):1166, 2012.

[87] Yabuuchi, K. *Dose dependence of irradiation hardening of binary ferritic alloys irradiated with Fe 3+ ions.* Journal of Nuclear Materials, 417(1-3):988, 2011.

[88] Wang, S. *Irradiation-induced amorphization: Effects of temperature, ion mass, cascade size, and dose rate.* Physical Review B - Condensed Matter and Materials Physics, 63(2):241051, 2001.

[89] Garner, F.A., et al. *Implications of Neutron-Spectrum and Flux Differences on Fission-Fusion Correlations at High Neutron Fluence.* Radiation Effects and Defects in Solids, 113(1-3):229, 1990.

[90] Hardie, C. *Micro-Mechanics of Irradiated Fe-Cr Alloys for Fusion Reactors.* DPhil thesis, University of Oxford, 2013.

[91] Westmoreland, J.E., et al. *Flux (Dose Rate) Effects for 2.8 MeV 58Ni Irradiations of Pure Ni*, book section 51, 663–674. Springer US, 1974.

[92] Noda, T., et al. *Transmutation and induced radioactivity of W in the armor and first wall of fusion reactors.* Journal of Nuclear Materials, 258263, Part 1(0):934, 1998.

[93] Yoshida, N., et al. *Impact of low energy helium irradiation on plasma-facing metals.* Journal of Nuclear Materials, 337-339:946 , 2005.

[94] Oya, Y. *Correlation between deuterium retention and microstructure change for tungsten under triple ion implantation.* Physica Scripta T, T138:14051, 2009.

[95] Hinoki, T. *DuET Facility and Charged Particle Research for Fusion.* Web Page. `http://www.iae.kyoto-u.ac.jp/zero_emission/file/kyoudoukenkyu/device_list.pdf`.

[96] Kolitsch, D.A. *HZDR Ion Beam Centre*. Web Page, 2014. `https://www.hzdr.de/db/Cms?pNid=141`.

[97] Iwakiri, H., et al. *Effects of helium bombardment on the deuterium behavior in tungsten*. Journal of Nuclear Materials, 307-311(Part 1):135 , 2002.

[98] Becquart, C., et al. *Solute-point defect interactions in BCC systems: Focus on first principles modelling in W and RPV steels*. Current Opinion in Solid State and Materials Science, 16(3):115 , 2012.

[99] Greuner, H., et al. *Surface morphology changes of tungsten exposed to high heat loading with mixed hydrogen/helium beams*. Journal of Nuclear Materials, 455(13):681, 2014.

[100] Sekimura, N., et al. *Synergistic effects of hydrogen and helium on microstructural evolution in vanadium alloys by triple ion beam irradiation*. Journal of Nuclear Materials, 283-287, Part 1(0):224 , 2000.

[101] Hamada, S., et al. *Effect of triple beam irradiation on microstructural evolution in austenitic stainless steel*. Radiation Physics and Chemistry, 50(6):555, 1997.

[102] Gilbert, M., et al. *An integrated model for materials in a fusion power plant: transmutation, gas production, and helium embrittlement under neutron irradiation*. Nuclear Fusion, 52(8):083019, 2012.

[103] Kajita, S., et al. *Sub-ms laser pulse irradiation on tungsten target damaged by exposure to helium plasma*. Nuclear Fusion, 47(9):1358, 2007.

[104] Liu, Y., et al. *Effect of He on the structure and bonding properties of W: A first-principles computational tensile test*. Nuclear Instruments and Methods in Physics Research, Section B: Beam Interactions with Materials and Atoms, 267(18):3193, 2009.

[105] Gonzlez, C., et al. *Migration mechanisms of helium in copper and tungsten*. Journal of Materials Science, 49(23):8127, 2014.

[106] Amano, J., et al. *Diffusivity of 3He Atoms in Perfect Tungsten Crystals*. Journal of Applied Physics, 56(4):983, 1984.

[107] Becquart, C., et al. *Migration energy of He in W revisited by Ab initio calculations.* Physical Review Letters, 97(19), 2006.

[108] Becquart, C.S., et al. *Modelling radiation damage and He production in tungsten.* Physica Scripta, 2011(T145):014048, 2011.

[109] Li, X.C., et al. *Molecular dynamics simulation of helium cluster diffusion and bubble formation in bulk tungsten.* Journal of Nuclear Materials, 455(13):544, 2014.

[110] Yang, L., et al. *First-principles study of the migration of helium in tungsten.* International Journal of Modern Physics B, 23(8):2077, 2009.

[111] Debelle, A., et al. *First temperature stage evolution of irradiation-induced defects in tungsten studied by positron annihilation spectroscopy.* Journal of Nuclear Materials, 376(2):216, 2008.

[112] Barashev, A.V., et al. *The behavior of small helium clusters near free surfaces in tungsten.* Journal of Nuclear Materials, 454(13):421, 2014.

[113] Hashimoto, N., et al. *Microstructural analysis on helium retention of ion-irradiated and annealed tungsten foils.* Journal of Nuclear Materials, 347(3):307, 2005.

[114] Debelle, A., et al. *Helium behaviour and vacancy defect distribution in helium implanted tungsten.* Journal of Nuclear Materials, 362(2-3):181, 2007.

[115] Ziegler, J., et al. *SRIM - The Stopping and Range of Ions in Matter*, 2010. `http://www.srim.org`.

[116] Takamura, S. *The recovery stage of vacancies in Mo, W and Fe studied by doping experiments.* Radiation Effects Letters, 43(2):69, 1979.

[117] Gilliam, S., et al. *Retention and surface blistering of helium irradiated tungsten as a first wall material.* Journal of Nuclear Materials, 347(3):289, 2005.

[118] Iwakiri, H., et al. *Microstructure evolution in tungsten during low-energy helium ion irradiation.* Journal of Nuclear Materials, 283-287, Part 2(0):1134 , 2000.

[119] Hofmann, F., et al. *Lattice swelling and modulus change in a helium-implanted tungsten alloy: X-ray micro-diffraction, surface acoustic wave measurements, and multiscale modelling.* Acta Materialia, 89(0):352 , 2015.

[120] Armstrong, D.E.J., et al. *Effects of sequential tungsten and helium ion implantation on nano-indentation hardness of tungsten.* Applied Physics Letters, 102(25), 2013.

[121] El-Atwani, O., et al. *Ultrafine tungsten as a plasma-facing component in fusion devices: Effect of high flux, high fluence low energy helium irradiation.* Nuclear Fusion, 54(8), 2014.

[122] Brass, A., et al. *Helium 3 precipitation in AISI 316L stainless steel induced by radioactive decay of tritium: Microstructural study of helium bubble precipitation.* Metallurgical and Materials Transactions A, 25(10):2117, 1994.

[123] Oya, Y., et al. *Comparison of deuterium retention for ion-irradiated and neutron-irradiated tungsten.* Physica Scripta, 2011(T145):014050, 2011.

[124] Gilbert, M., et al. *Neutron-induced transmutation effects in W and W-alloys in a fusion environment.* Nuclear Fusion, 51(4), 2011.

[125] Cottrell, G.A., et al. *Transmutation and phase stability of tungsten armor in fusion power plants.* Fusion Science and Technology, 50(1):89, 2006.

[126] Herschitz, R., et al. *Radiation-induced precipitation in fast-neutron irradiated tungsten-rhenium alloys: An atom-probe field-ion microscope study.* Nuclear Instruments and Methods in Physics Research Section B: Beam Interactions with Materials and Atoms, 7-8, Part 1(0):137 , 1985.

[127] Tanno, T., et al. *Effects of transmutation elements on neutron irradiation hardening of tungsten.* Material Transformations, 48:2399, 2007.

[128] Fukuda, M., et al. *Microstructural development of tungsten and tungstenrhenium alloys due to neutron irradiation in HFIR.* Journal of Nuclear Materials, 455(13):460, 2014.

[129] Young-Won, K., et al. *An annealing study of thermal neutron irradiated tungsten.* Journal of Nuclear Materials, 69-70(C):680, 1978.

[130] Tanno, T., et al. *Microstructure development in neutron irradiated tungsten alloys.* Materials Transactions, 52(7):1447, 2011.

[131] Hasegawa, A., et al. *Neutron irradiation effects on tungsten materials.* Fusion Engineering and Design, 89(78):1568, 2014.

[132] Armstrong, D.E.J., et al. *Mechanical properties of ion-implanted tungsten 5-wt% tantalum.* Physica Scripta, 2011(T145):014076, 2011.

[133] Liu, C., et al. *Micro-structure and micro-hardness of ODS steels after ion irradiation.* Journal of Nuclear Materials, 417(1-3):270 , 2011.

[134] Kurishita, H., et al. *Development of ultra-fine grained W-(0.25-0.8)wt%TiC and its superior resistance to neutron and 3 MeV He-ion irradiations.* Journal of Nuclear Materials, 377(1):34, 2008.

[135] Fukuda, M., et al. *Property change of advanced tungsten alloys due to neutron irradiation.* Journal of Nuclear Materials, 442(13, Supplement 1):S273, 2013.

[136] Hutchinson, J.W. *Plasticity at the micron scale.* International Journal of Solids and Structures, 37(12):225, 2000.

[137] Gibson, J.S.K.L., et al. *High temperature indentation of helium-implanted tungsten.* Materials Science and Engineering: A, 625(0):380, 2015.

[138] Hasegawa, A., et al. *Property change mechanism in tungsten under neutron irradiation in various reactors.* Journal of Nuclear Materials, 417(1-3):491, 2011.

[139] Steichen, J. *Tensile properties of neutron irradiated TZM and tungsten.* Journal of Nuclear Materials, 60(1):13 , 1976.

[140] Brunner, D., et al. *Plastic properties of high-purity W single crystals.* Materials Letters, 42(5):290, 2000.

[141] Krautwasser, P., et al. *Influence of fast neutron fluence on the DBTT of tungsten, W-10Re and W-3.4Ni-1.6Fe.* High Temp.-High Press., 22:25, 1976.

[142] Nelson, S., et al. *The use of ion accelerators to simulate fast neutron-induced voidage in metals.* Journal of Nuclear Materials, 37(1):1, 1970.

[143] Armstrong, D.E.J., et al. *Hardening of self ion implanted tungsten and tungsten 5-wt% rhenium.* Journal of Nuclear Materials, 432(1-3):428, 2013.

[144] Bull, S.J. *Nanoindentation of coatings.* Journal of Physics D: Applied Physics, 38(24):R393, 2005.

[145] Hanna, L. *Atom Probe Tomography of Fusion Materials.* Part II thesis, University of Oxford, 2014.

[146] Battabyal, M., et al. *Effect of ion-irradiation on the microstructure and microhardness of the W-2Y2O3 composite materials fabricated by sintering and hot forging.* Fusion Engineering and Design, 88(9-10):1668 , 2013.

[147] Battabyal, M., et al. *Investigation of microstructure and microhardness of pure W and W-2Y 2O3 materials before and after ion-irradiation.* International Journal of Refractory Metals and Hard Materials, 46:168, 2014.

[148] Armstrong, D.E.J., et al. *Effect of dislocation density on improved radiation hardening resistance of nano-structured tungsten-rhenium.* Materials Science and Engineering: A, 611(0):388, 2014.

[149] Arsenlis, A., et al. *A dislocation dynamics study of the transition from homogeneous to heterogeneous deformation in irradiated body-centered cubic iron.* Acta Materialia, 60(9):3748 , 2012.

[150] Arkhipov, I., et al. *Deuterium trapping in ion-damaged tungsten single crystal.* Journal of Nuclear Materials, 363-365(0):1168 , 2007.

[151] Frank, R.C., et al. *The trapping of deuterium in argon-implanted nickel.* Journal of Applied Physics, 57(3):845, 1985.

[152] Nagata, S., et al. *Hydrogen accumulation in the helium implanted surface of Mo single crystals.* Journal of Alloys and Compounds, 356-357(0):326 , 2003.

[153] Ogorodnikova, O., et al. *Deuterium retention in tungsten exposed to low-energy pure and helium-seeded deuterium plasmas.* Journal of Applied Physics, 109(1):013309, 2011.

[154] Beck, C.E., et al. *Effect of alloy composition & helium ion-irradiation on the mechanical properties of tungsten, tungsten-tantalum & tungsten-rhenium for fusion power applications.* In *2012 MRS Fall Meeting*, vol. 1514, 99–104.

[155] Thompson, D.O., et al. *Effects of neutron irradiation upon the young's modulus and internal friction of copper single crystals.* Journal of Applied Physics, 27(7):713, 1956.

[156] Ou, X., et al. *The role of helium implantation induced vacancy defect on hardening of tungsten.* Journal of Applied Physics, 115(12):123521, 2014.

[157] Tanigawa, H., et al. *Radiation induced phase instability of precipitates in reduced-activation ferritic/martensitic steels.* Journal of Nuclear Materials, 367-370, Part A(0):132 , 2007.

[158] Greer, J., et al. *Size dependence of mechanical properties of gold at the micron scale in the absence of strain gradients.* Acta Materialia, 53(6):1821, 2005.

[159] Uchic, M., et al. *Sample dimensions influence strength and crystal plasticity.* Science, 305(5686):986, 2004.

[160] Motz, C., et al. *Mechanical properties of micro-sized copper bending beams machined by the focused ion beam technique.* Acta Materialia, 53(15):4269, 2005.

[161] Kiener, D., et al. *Determination of mechanical properties of copper at the micron scale.* Advanced Engineering Materials, 8(11):1119, 2006.

[162] Gong, J., et al. *Micro-cantilever testing of $\langle a \rangle$ prismatic slip in commercially pure Ti.* Philosophical Magazine, 91(7-9):1137, 2011.

[163] Gong, J., et al. *Anisotropy in the plastic flow properties of single-crystal alpha-titanium determined from micro-cantilever beams.* Acta Materialia, 57(19):5693 , 2009.

[164] Kiener, D., et al. *A further step towards an understanding of size-dependent crystal plasticity: in-situ tension experiments of miniaturized single-crystal copper samples.* Acta Materialia, 56(3):580 , 2008.

[165] Bei, H., et al. *Compressive strengths of molybdenum alloy micro-pillars prepared using a new technique.* Scripta Materialia, 57(5):397, 2007.

[166] Shim, S., et al. *Effects of focused ion beam milling on the compressive behavior of directionally solidified micropillars and the nanoindentation response of an electropolished surface.* Acta Materialia, 57(2):503, 2009.

[167] Armstrong, D.E.J., et al. *Measuring Local Mechanical Properties Using FIB Machined Microcantilevers.* Probing Mechanics at Nanoscale Dimensions, 1185:7, 2009.

[168] Di Maio, D., et al. *Measuring fracture toughness of coatings using focused-ion-beam-machined microbeams.* Journal of Materials Research, 20(2):299, 2005.

[169] Takashima, K., et al. *Fatigue and fracture of a Ni-P amorphous alloy thin film on the micrometer scale.* Fatigue & Fracture of Engineering Materials & Structures, 28(8):703, 2005.

[170] Chuang, W., et al. *Characterization of mechanical properties of silicon nitride thin films for space applications.* In *Materials Research Society Symposium - Proceedings*, vol. 782, 193–198.

[171] Greenwood, J. *Constriction resistance and the real area of contact.* British Journal of Applied Physics, 17(12):1621, 1966.

[172] Mulhearn, T. *The deformation of metals by Vickers-type pyramidal indenters.* Journal of the Mechanics and Physics of Solids, 7(2):85, 1959.

[173] Pethica, J., et al. *Hardness Measurement at Penetration Depths as Small as 20nm.* Philosophical Magazine A: Physics of Condensed Matter, Structure, Defects and Mechanical Properties, 48(4):593, 1983.

[174] Schuh, C.A., et al. *Nanoindentation and contact-mode imaging at high temperatures.* Journal of Materials Research, 21(3):725, 2006.

[175] Gouldstone, A., et al. *Indentation across size scales and disciplines: Recent developments in experimentation and modeling.* Acta Materialia, 55(12):4015, 2007.

[176] Peralta, P., et al. *Characterization of surface deformation around Vickers indents in monocrystalline materials.* Metallurgical and Materials Transactions A: Physical Metallurgy and Materials Science, 35 A(8):2247, 2004.

[177] Roberts, S., et al. *Hardness anisotropies: A new approach.* Materials Science and Engineering, 105-106(PART 1):19, 1988.

[178] Oliver, W.C., et al. *Measurement of hardness and elastic modulus by instrumented indentation: Advances in understanding and refinements to methodology.* Journal of Materials Research, 19(1):3, 2004.

[179] Herbert, E.G., et al. *On the measurement of stressstrain curves by spherical indentation.* Thin Solid Films, 398399(0):331, 2001.

[180] Li, X., et al. *Fracture mechanisms of thin amorphous carbon films in nanoindentation.* Acta Materialia, 45(11):4453, 1997.

[181] Featherston, F., et al. *Elastic Constants of Tantalum, Tungsten, and Molybdenum.* Phys. Rev., 130:1324, 1963.

[182] Jung, Y.G., et al. *Evaluation of elastic modulus and hardness of thin films by nanoindentation.* Journal of Materials Research, 19:3076, 2004.

[183] King, R., et al. *The effect of temperature on the mechanical properties and the friction of plastics.* Proceedings of the Physical Society. Section B, 66(9):728, 1953.

[184] Suzuki, T., et al. *Ultra-microindentation of silicon at elevated temperatures.* Philosophical Magazine A, 74(5):1073, 1996.

[185] Xia, J., et al. *Hot-stage nano-characterisations of an iron aluminide.* Materials Science and Engineering A, 354(1-2):112, 2003.

[186] Lund, A., et al. *Incipient plasticity during nanoindentation at elevated temperatures.* Applied Physics Letters, 85(8):1362, 2004.

[187] Yang, B., et al. *Thermal activation in Au-based bulk metallic glass characterized by high-temperature nanoindentation.* Applied Physics Letters, 90(6):061911, 2007.

[188] Sawant, A., et al. *High temperature nanoindentation of ni-base superalloys.* In *Proceedings of the International Symposium on Superalloys*, 863–871.

[189] Sawant, A., et al. *High temperature nanoindentation of a Re-bearing single crystal Ni-base superalloy.* Scripta Materialia, 58(4):275, 2008.

[190] Rathinam, M., et al. *Nanoindentation of aluminum (100) at various temperatures.* Journal of Mechanical Science and Technology, 23(10):2652, 2009.

[191] Ruffell, S., et al. *Nanoindentation-induced phase transformations in silicon at elevated temperatures.* Nanotechnology, 20(13):135603, 2009.

[192] Trenkle, J.C., et al. *Hot nanoindentation in inert environments.* Review of Scientific Instruments, 81(7):, 2010.

[193] Gavendova, P., et al. *Nanohardness of grains of electrotechnical steel at elevated temperature.* Acta Metallurgica Slovaca, 18(4):156, 2012.

[194] Lotfian, S., et al. *High-temperature nanoindentation behavior of Al/SiC multilayers.* Philosophical Magazine Letters, 92(8):362, 2012.

[195] Korte, S., et al. *High temperature microcompression and nanoindentation in vacuum.* Journal of Materials Research, 27(1):167, 2012.

[196] Sharma, G., et al. *High temperature mechanical behavior of nanocrystalline Ni.* Materials Science and Engineering: A, 576(0):69 , 2013.

[197] Gan, B., et al. *Influence of pre-deformation on jerky flow in Ni-10Pd during high-temperature instrumented indentation.* Philosophical Magazine Letters, 93(6):371, 2013.

[198] Yoshida, K. *Thickness Dependence of Plastic Behaviors of Copper Whiskers.* Journal of the Physical Society of Japan, 24(5):1099, 1968.

[199] Young, F. *Yield stress of copper crystals.* Journal of Applied Physics, 33(3):963, 1962.

[200] Bailey, J.E. *The dislocation density, flow stress and stored energy in deformed polycrystalline copper.* Philosophical Magazine, 8(86):223 , 1963.

[201] Wurster, S., et al. *Characterization of the fracture toughness of micro-sized tungsten single crystal notched specimens.* Philosophical Magazine, 92(14):1803, 2012.

[202] Massel, S., et al. *Investigation of fracture properties of magnetron-sputtered TiN films by means of a FIB-based cantilever bending technique.* Acta Materialia, 57(6):1768, 2009.

[203] Armstrong, D., et al. *Micro-mechanical measurements of fracture toughness of bismuth embrittled copper grain boundaries.* Philosophical Magazine Letters, 91(6):394, 2011.

[204] Beaber, A., et al. *Smaller is tougher.* Philosophical Magazine, 91(7-9):1179, 2011.

[205] Fan, M., et al. *Generalized Irwin plastic zone correction for a Griffith crack near a coated-circular inclusion.* International Journal of Damage Mechanics, 2014.

[206] Maloy, S.A., et al. *The effect of 800 MeV proton irradiation on the mechanical properties of tungsten at room temperature and at 475C.* Journal of Nuclear Materials, 343(1-3):219, 2005.

[207] Stelmashenko, N., et al. *Microindentations on W and Mo oriented single crystals: An STM study.* Acta Metallurgica Et Materialia, 41(10):2855, 1993.

[208] Nix, W., et al. *Indentation size effects in crystalline materials: A law for strain gradient plasticity.* Journal of the Mechanics and Physics of Solids, 46(3):411, 1998.

[209] Qing, M., et al. *Size dependent hardness of silver single crystals.* Journal of Materials Research, 10(4):853, 1995.

[210] Kiener, D., et al. *Microstructural evolution of the deformed volume beneath microindents in tungsten and copper.* Acta Materialia, 54(10):2801 , 2006.

[211] McElhaney, K., et al. *Determination of indenter tip geometry and indentation contact area for depth-sensing indentation experiments.* Journal of Materials Research, 13(5):1300, 1998.

[212] Pharr, G., et al. *The indentation size effect: A critical examination of experimental observations and mechanistic interpretations.* Annual Review of Materials Research, 40:271, 2010.

[213] Chen, S., et al. *Size effect in micro-scale cantilever beam bending.* Acta Mechanica, 219(3-4):291, 2011.

[214] Ehrler, B. *Grain size and sample size interact to determine strength in a soft metal.* Philosophical Magazine, 88(25):3043, 2008.

[215] Shrotriya, P., et al. *On the measurement of the plasticity length scale parameter in LIGA nickel foils.* Mechanics of Materials, 35(3-6):233, 2003.

[216] Lam, D., et al. *Experiments and theory in strain gradient elasticity.* Journal of the Mechanics and Physics of Solids, 51(8):1477, 2003.

[217] Haque, M.A., et al. *Strain gradient effect in nanoscale thin films.* Acta Materialia, 51(11):3053, 2003.

[218] Soler, R., et al. *Understanding size effects on the strength of single crystals through high-temperature micropillar compression.* Acta Materialia, 81(0):50, 2014.

[219] Sharma, G., et al. *Study of the effect of alpha irradiation on the microstructure and mechanical properties of nanocrystalline Ni.* Acta Materialia, 61(9):3257 , 2013.

[220] Mayo, M., et al. *A micro-indentation study of superplasticity in Pb, Sn, and Sn-38 wt% Pb.* Acta Metallurgica, 36(8):2183 , 1988.

[221] Maier, V., et al. *Nanoindentation strain-rate jump tests for determining the local strain-rate sensitivity in nanocrystalline Ni and ultrafine-grained Al.* Journal of Materials Research, 26(11):1421, 2011.

[222] Peykov, D., et al. *Evaluation of strain rate sensitivity by constant load nanoindentation.* Journal of Materials Science, 47(20):7189, 2012.

[223] Varam, S., et al. *Strain rate sensitivity studies on bulk nanocrystalline aluminium by nanoindentation.* Journal of Alloys and Compounds, 585(0):795 , 2014.

[224] Wang, Y., et al. *Temperature-dependent strain rate sensitivity and activation volume of nanocrystalline Ni.* Acta Materialia, 54(10):2715 , 2006.

[225] Connolly, S. *Micromechanical deformation of ODS alloys.* Part II thesis, University of Oxford, 2014.

[226] Gong, J., et al. *A microcantilever investigation of size effect, solid-solution strengthening and second-phase strengthening for $\langle a \rangle$ prism slip in alpha-Ti.* Acta Materialia, 59(15):5970, 2011.

[227] McCarthy, J., et al. *FIB micromachined sub-micron thickness cantilevers for the study of thin film properties.* Thin Solid Films, 358(1-2):146 , 2000.

[228] Maass, R., et al. *Time-resolved Laue diffraction of deforming micropillars.* Physical Review Letters, 99(14):145505, 2007.

[229] Hutsch, J., et al. *The influence of focused-ion beam preparation technique on microcompression investigations: Lathe vs. annular milling.* Scripta Materialia, 77:49, 2014.

[230] Seliger, R., et al. *A high-intensity scanning ion probe with submicrometer spot size.* Applied Physics Letters, 34(5):310, 1979.

[231] Young, R.J. *Micro-machining using a focused ion beam.* Vacuum, 44(3-4):353 , 1993.

[232] Langford, R., et al. *Preparation of transmission electron microscopy cross-section specimens using focused ion beam milling.* Journal of Vacuum Science and Technology, Part A: Vacuum, Surfaces and Films, 19(5):2186, 2001.

[233] Li, X., et al. *A review of nanoindentation continuous stiffness measurement technique and its applications.* Materials Characterization, 48(1):11, 2002.

[234] Oliver, W., et al. *Improved technique for determining hardness and elastic modulus using load and displacement sensing indentation experiments.* Journal of Materials Research, 7(6):1564, 1992.

[235] Hardie, C.D. *Dose rate effects in FeCr*, 2011. Personal Communication.

[236] Hewitt, L., et al. *Dose-Rate Effects in Fe and Fe-Cr Alloys*, 2014. Unpublished Work.

[237] Stoller, R.E., et al. *On the use of SRIM for computing radiation damage exposure.* Nuclear Instruments and Methods in Physics Research, Section B: Beam Interactions with Materials and Atoms, 310:75, 2013.

[238] ASTM. *Standard Practice for Measurement of Mechanical Properties During Charged-Particle Irradiation*, 2009.

[239] Bratchenko, M., et al. *Comments on DPA calculation methods for ion beam driven simulation irradiations.* Problems of Atomic Science and Technology, (2):11, 2013.

[240] Lassner, E., et al. *Tungsten: Properties, Chemistry, Technology of the Elements, Alloys, and Chemical Compounds.* Springer US, 1999.

[241] Mason, D.R., et al. *Elastic trapping of dislocation loops in cascades in ion-irradiated tungsten foils.* Journal of Physics Condensed Matter, 26(37), 2014.

[242] Xu, A., et al. *Ion-irradiation-induced clustering in WRe and WReOs alloys: A comparative study using atom probe tomography and nanoindentation measurements.* Acta Materialia, 87(0):121, 2015.

[243] Keys, L.K., et al. *Neutron irradiation and defect recovery of tungsten.* Journal of Nuclear Materials, 34(3):260, 1970.

[244] Chen, L., et al. *Stability and diffusion properties of self-interstitial atoms in tungsten: A first-principles investigation.* Science China: Physics, Mechanics and Astronomy, 55(4):614, 2012.

[245] Wang, J., et al. *A modified W-W interatomic potential based on ab initio calculations.* Modelling and Simulation in Materials Science and Engineering, 22(1), 2014.

[246] Soboyejo, W. *Mechanical Properties of Engineered Materials.* CRC Press, 2002.

[247] Alsabbagh, A., et al. *Microstructure and mechanical behavior of neutron irradiated ultrafine grained ferritic steel.* Materials Science and Engineering A, 615:128, 2014.

[248] Gai, X., et al. *Helium Bubbles in Fe: Equilibrium Configurations and Modification by Radiation.* MRS Online Proceedings Library, 1514:21, 2013.

[249] Lambrecht, M., et al. *On the correlation between irradiation-induced microstructural features and the hardening of reactor pressure vessel steels.* Journal of Nuclear Materials, 406(1):84, 2010.

[250] Bergner, F., et al. *Application of a three-feature dispersed-barrier hardening model to neutron-irradiated FeCr model alloys.* Journal of Nuclear Materials, 448(13):96, 2014.

[251] Beake, B., et al. *High-temperature nanoindentation testing of fused silica and other materials.* Philosophical Magazine A: Physics of Condensed Matter, Structure, Defects and Mechanical Properties, 82(10 SPEC.):2179, 2002.

[252] Beake, B.D., et al. *Nanoscale materials testing under industrially relevant conditions: high-temperature nanoindentation testing.* Zeitschrift fr Metallkunde, 94(7):798, 2003.

[253] Schneider, A.S., et al. *Correlation between Critical Temperature and Strength of Small-Scale bcc Pillars.* Phys. Rev. Lett., 103:105501, 2009.

[254] Schneider, A.S., et al. *Influence of test temperature on the size effect in molybdenum small-scale compression pillars.* Philosophical Magazine Letters, 93(6):331, 2013.

[255] Lhuillier, P.E., et al. *Helium desorption in 3He implanted tungsten at low energy.* Journal of Nuclear Materials, 417(1-3):504, 2011.

[256] Rivera, A., et al. *Effect of ion flux on helium retention in helium-irradiated tungsten.* Nuclear Instruments and Methods in Physics Research, Section B: Beam Interactions with Materials and Atoms, 303:81, 2013.

[257] Yang, L., et al. *Effects of temperature on the interactions of helium-vacancy clusters with gliding edge dislocations in α-Fe.* Journal of Nuclear Materials, 441:6, 2013.

[258] Cheng, J., et al. *A unified constitutive model for strain-rate and temperature dependent behavior of molybdenum.* Mechanics of Materials, 33(11):603, 2001.

[259] Osetsky, Y.N., et al. *Atomic-scale mechanisms of void hardening in BCC and FCC metals.* Philosophical Magazine, 90(7-8):945, 2010.

[260] Pisarenko, G.S., et al. *The effect of temperature on the hardness and modulus of elasticity of tungsten and molybdenum (20-2700C).* Soviet Powder Metallurgy and Metal Ceramics, 1(5):371, 1964.

[261] Lee, M., et al. *Hardness of polycrystalline tungsten and molybdenum oxides at elevated temperatures.* Journal of the American Ceramic Society, 73(7):2117, 1990.

[262] Langdon, N. *Explicit expressions for stress field of a circular dislocation loop.* Theoretical and Applied Fracture Mechanics, 33(3):219, 2000.

[263] Nagasaka, T., et al. *Recovery of Hardness, Impact Properties and Microstructure of Neutron-Irradiated Weld Joint of a Fusion Candidate Vanadium Alloy.* Materials Transactions, 46(3):498, 2005.

[264] WAN, J., et al. *Study on the Microstructure Evolution of A508 Steel Under Proton Irradiation.* Acta Metallurgica, 48(8):929, 2012.

[265] Gan, J., et al. *Microstructure evolution in austenitic Fe-Cr-Ni alloys irradiated with protons: Comparison with neutron-irradiated microstructures.* Journal of Nuclear Materials, 297(2):161, 2001.

[266] Armstrong, D.E.J. *Measuring Elastic, Plastic and Fracture Properties using Micro-Cantilever Testing.* DPhil thesis, University of Oxford, 2009.

[267] Dummer, T., et al. *Effect of strain rate on plastic flow and failure in polycrystalline tungsten.* Acta Materialia, 46(17):6267 , 1998.

[268] Li, M., et al. *Fracture mechanical analysis of tungsten armor failure of a water-cooled divertor target.* Fusion Engineering and Design, 2014.

[269] Uchic, M.D., et al. *Plasticity of micrometer-scale single crystals in compression.* In *Annual Review of Materials Research*, vol. 39, 361–386. 2009.

[270] Tarleton, E., et al. *A discrete dislocation plasticity study of the micro-cantilever size effect.* Acta Materialia, 88(0):271, 2015.

[271] Greer, J.R., et al. *Plasticity in small-sized metallic systems: Intrinsic versus extrinsic size effect.* Progress in Materials Science, 56(6):654, 2011.

[272] Jones, C. *Micro-Mechanics of Fusion Relevant ODS Alloys.* DPhil thesis, University of Oxford, 2015.

[273] Kiener, D., et al. *In situ nanocompression testing of irradiated copper.* Nature Materials, 10(8):608, 2011.

[274] Hirsch, P.B., et al. *Dislocation-driven stable crack growth by microcleavage in semi-brittle crystals.* Scripta Metallurgica et Materialia, 27(12):1723, 1992.

[275] Brimhall, J.L., et al. *Thermal stability of radiation produced defects in molybdenum.* Acta Metallurgica, 16(6):781, 1968.

[276] Rau, R.C., et al. *Neutron damage in molybdenum irradiated at high temperatures.* Philosophical Magazine, 21(171):441, 1970.

[277] Derlet, P.M., et al. *Multiscale modeling of crowdion and vacancy defects in body-centered-cubic transition metals.* Physical Review B - Condensed Matter and Materials Physics, 76(5), 2007.